



University of  
**Nottingham**  
UK | CHINA | MALAYSIA

**Cost-Effective and Eco-Friendly  
Manufacture of Titanium  
Components via the  
Near-Net-Shape Electrochemical  
Metallisation Process**

by Aleksei Dolganov, BEng

*Supervised by: Dr. Di Hu and Prof. George Chen*

Thesis submitted to The University of Nottingham

for the degree of Doctor of Philosophy, June 2020

# Contents

<b>Abstract</b>	<b>ix</b>
<b>List of Figures</b>	<b>xiii</b>
<b>List of Tables</b>	<b>xix</b>
<b>Nomenclature</b>	<b>xxi</b>
<b>Acknowledgements</b>	<b>xxiv</b>
<b>1 Introduction</b>	<b>1</b>
1.1 Statement of Problem . . . . .	1
1.1.1 Titanium . . . . .	1
1.1.2 Applications . . . . .	2
1.1.3 Manufacture . . . . .	3
1.1.4 Environmental Impact . . . . .	6
1.2 Research Question . . . . .	7
1.3 Aims and Objectives . . . . .	7
1.3.1 Development of the Near-net-shape Electrochemical Metallisation Process . . . . .	8

1.3.1.1	Rapid Fabrication of Titanium Oxide Precursors with Complex Shapes (fabrication aspect) . . . . .	8
1.3.1.2	Direct Metallisation of Titanium Oxide Precursors via the FFC-Cambridge Process (extraction aspect) . . . . .	9
1.4	Statement of Novelty . . . . .	9
	References of Chapter 1 . . . . .	16
<b>2</b>	<b>Literature Review</b>	<b>17</b>
2.1	Background . . . . .	17
2.2	Production of Titanium and Its Alloys . . . . .	19
2.2.1	Conventional Extraction Processes . . . . .	19
2.2.1.1	Metallothermic Processes . . . . .	19
2.2.1.2	Electrochemical Process . . . . .	26
2.2.1.3	Combined Process . . . . .	28
2.2.2	Summation . . . . .	30
2.3	Fabrication of Titanium and Its Alloys . . . . .	31
2.3.1	Conventional Fabrication Methods . . . . .	32
2.3.1.1	Metal Forging . . . . .	32
2.3.1.2	Casting . . . . .	33
2.3.1.3	Machining . . . . .	34
2.3.2	Near-net-shape Methods . . . . .	35
2.3.2.1	Selective Melting/Sintering . . . . .	35
2.3.2.2	Shaped Metal Deposition . . . . .	37

2.3.2.3	Hot Isostatic Pressing . . . . .	38
2.3.2.4	Metal Injection Moulding . . . . .	39
2.3.2.5	Field Assisted Sintering Technology Forging . . . . .	40
2.3.2.6	Binder Jetting Printing . . . . .	41
2.3.3	Summation . . . . .	41
2.3.4	Powder Spheradisation . . . . .	42
2.3.4.1	Direct Powder Production . . . . .	42
2.3.4.2	Hydride-Dehydride . . . . .	43
2.3.4.3	Advanced Techniques . . . . .	43
2.3.5	Summation . . . . .	44
2.4	Fabrication of Titanium Oxide Precursors . . . . .	44
2.4.1	Shaping of Ceramics . . . . .	45
2.4.1.1	Slip Casting . . . . .	45
2.4.1.2	Direct Ink Writing . . . . .	47
2.4.1.3	Indirect Methods . . . . .	48
2.4.1.4	Selective Laser Sintering . . . . .	49
2.4.1.5	Stereolithography . . . . .	51
2.4.1.6	Binder Jetting Printing . . . . .	52
2.4.2	Summation . . . . .	52
2.5	Conclusion . . . . .	52
	References of Chapter 2 . . . . .	54

<b>3</b>	<b>Equipment and Methods</b>	<b>66</b>
3.1	Manufacturing Routes . . . . .	66
3.1.1	Direct Ink Writing . . . . .	66
3.1.1.1	Ink Preparation . . . . .	67
3.1.1.2	3D Printing . . . . .	67
3.1.1.3	Drying . . . . .	73
3.1.2	The Electrochemical Reduction Process . . . . .	73
3.1.2.1	Preparation . . . . .	73
3.1.2.2	Electrolysis . . . . .	81
3.1.2.3	Post-Metallisation Treatment . . . . .	81
3.2	Analytical Techniques . . . . .	82
3.2.1	Rheological Tests . . . . .	82
3.2.1.1	Theory of Rheology . . . . .	82
3.2.1.2	Methodology of Rheological Tests. . . . .	88
3.2.2	Scanning Electron Microscope and Energy-Dispersive X-Ray Spectroscopy . . . . .	90
3.2.2.1	Theory of SEM and EDS . . . . .	90
3.2.2.2	Methodology of SEM and EDS . . . . .	93
3.2.3	X-Ray Defraction . . . . .	93
3.2.3.1	Theory of XRD . . . . .	93
3.2.3.2	Methodology of XRD . . . . .	96
3.2.4	Cyclic Voltammetry . . . . .	96

3.2.4.1	Theory of CV . . . . .	97
3.2.4.2	Methodology of CV . . . . .	99
3.2.5	Oxygen Analysis . . . . .	100
3.2.5.1	Theory of Oxygen Analysis . . . . .	100
3.2.5.2	Methodology of Oxygen Analysis . . . . .	101
3.2.6	Compressive Strength Testing . . . . .	102
3.2.6.1	Theory of the Compressive Strength Testing . . . . .	102
3.2.6.2	Methodology of the Compressive Strength Testing . . . . .	102
3.2.7	Life Cycle Assessment . . . . .	103
3.2.7.1	Theory of the Life Cycle Assessment . . . . .	103
3.2.7.2	Methodology of the Life Cycle Assessment . . . . .	104
	References of Chapter 3 . . . . .	110
<b>4</b>	<b>Direct Ink Writing of Titania</b>	<b>111</b>
4.1	Introduction . . . . .	111
4.2	Ink Loading Technique . . . . .	112
4.2.1	Established Technique . . . . .	113
4.2.2	Upgraded Technique . . . . .	114
4.3	3D Printer Modification . . . . .	115
4.3.1	Original Design . . . . .	116
4.3.2	Screw-head Design . . . . .	117
4.3.3	Updated Design . . . . .	119
4.3.3.1	Nozzle Change . . . . .	119

4.3.3.2	Pressure Relief System . . . . .	121
4.4	Ink Preparation and Analysis . . . . .	125
4.4.1	Experimental . . . . .	125
4.4.1.1	Feedstock . . . . .	125
4.4.1.2	Rheological Tests . . . . .	126
4.4.1.3	Extrudability . . . . .	127
4.4.2	Results and Discussion . . . . .	128
4.4.2.1	Effect of Additives . . . . .	128
4.4.2.2	Rheological Evaluation . . . . .	130
4.4.2.3	Extrudability . . . . .	134
4.4.2.4	Investigation of the Best Performing Ink . . . . .	136
4.4.2.5	Further Optimisation . . . . .	138
4.4.3	Effects of Additives . . . . .	139
4.4.4	Drying Behaviour . . . . .	142
4.4.5	Summation . . . . .	144
4.5	Conclusion . . . . .	145
	References of Chapter 4 . . . . .	148

## **5 Optimisation of the Near-net-shape Electrochemical Metallisation**

	<b>Process</b>	<b>152</b>
5.1	Introduction . . . . .	152
5.2	Characterisation of Feedstock . . . . .	154
5.2.1	Electrochemical Characterisation . . . . .	154

5.2.2	SEM . . . . .	157
5.2.2.1	Powder . . . . .	157
5.2.2.2	DIW . . . . .	161
5.3	Sintering and Porosity . . . . .	164
5.4	Deformation . . . . .	166
5.5	Product Tests . . . . .	175
5.6	Financial Analysis . . . . .	177
5.6.1	Data Collection . . . . .	178
5.6.2	Cost Break Down . . . . .	183
5.7	Critical Evaluation . . . . .	186
5.8	Conclusion . . . . .	190
	References of Chapter 5 . . . . .	194
<b>6</b>	<b>Environmental Assessment of the NEM Process</b>	<b>200</b>
6.1	Introduction . . . . .	201
6.2	Methodology . . . . .	204
6.2.1	Goal and Scope . . . . .	204
6.2.2	Case Study . . . . .	206
6.2.2.1	The NEM Process . . . . .	206
6.2.2.2	The Kroll Process-Electron Beam Melting . . . . .	209
6.2.3	Life Cycle Inventory . . . . .	212
6.2.4	Interpretation . . . . .	213
6.2.5	Impact Assessment and Categories . . . . .	213

6.3	Results and Discussion . . . . .	217
6.3.1	Contribution Analysis . . . . .	217
6.3.2	Parametric and Sensitivity Analysis . . . . .	222
6.3.3	Comparison of Conventional Kroll - EBM Route and the NEM Process . . . . .	225
6.3.4	Legislations . . . . .	228
6.4	Conclusion . . . . .	230
	References of Chapter 6 . . . . .	232
<b>7</b>	<b>Conclusions and Future Work</b>	<b>242</b>
7.1	Concluding Remarks . . . . .	242
7.2	Significance in the Field . . . . .	249
7.3	Future Work . . . . .	250
7.3.1	Fabrication of Other Metallic and Inter-metallic Materials . .	250
7.3.2	Enhancement of the Properties of the Product . . . . .	251
7.3.3	Development of the 4D Printing . . . . .	251
7.3.4	Reduction of the Surface Area of the Produced Metal . . . . .	251
7.3.5	Computer Simulation of the Deformation . . . . .	252
	<b>Appendix</b>	<b>253</b>
	<b>A Life Cycle Inventory for the Kroll Process</b>	<b>253</b>
	<b>B Matlab Scrip for G-code Modification</b>	<b>256</b>

# Abstract

Titanium is an outstanding material, due to its unique set of properties, which is sought after in almost every industry. However, with great properties comes a great price, which for titanium is the ironic statement as it is the 9<sup>th</sup> most abundant element in the Earth's crust. The price, instead, comes from the extraction and fabrication conventionally adopted by the industry.

The extraction of titanium is currently done via the Kroll Process, which was established in 1940 and has almost reached saturation in its development and optimisation. Due to this, many novel extraction techniques have emerged, such as the FFC-Cambridge Process; an electrolytic reduction process conducted in molten salt. This process has been shown to reduce the cost associated with the production of titanium and has been intensively investigated since its development.

As previously stated, the fabrication of titanium is another problematic area due to the low heat dissipation, low Young's modulus and high reactivity of titanium. Therefore, titanium is required to be treated in an inert atmosphere and when shaped the additional coolant needs to be supplied, which still does not remove the increased wear of milling tools that is common to titanium forming.

These obstacles were reported to be overcome by utilising the unique solid-state

transformation seen in the FFC-Cambridge Process, which results in the near-net-shaped reduction of the precursor into a metallic product. Previous studies covered the use of slip casting to shape the precursor, which reduces the versatility of the process due to the low variety of possible products. In this project for the first time, the combination of the FFC-Cambridge Process with the ceramic 3D Printing was decided to be investigated and optimised, creating a new additive manufacture technique named the Near-net-shape Electrochemical Metallisation (NEM) Process.

The first step of the NEM Process was Direct Ink Writing (DIW), which allowed the viscous ink to be extruded in layers that built up the 3D structure. Optimisation of DIW for titanium dioxide printing was conducted, along with some of the modification to the mechanics of the process. The initial study on the formulation of the titanium dioxide ink was facilitated by the extrudability and rheological tests. These tests indicated that among the wide variety of inks, the one containing Polyethylene Glycol (PEG) was performing the best on a small scale. When the size of the products was increased, the inconsistency of flow became more distinct. This change was found to be caused by a complex interaction within the components of the ink at higher shear rates, which was overcome by the addition of surface lubricant. The high-quality products were achieved from DIW with the titanium dioxide ink that contained the following components in the weight ratio: 1 of  $\text{TiO}_2$ , 0.9 of 10% aqueous solution of PEG and 0.1 of mixed oil.

The next step of the NEM process focuses on the electrochemical metallisation of these titanium dioxide components via the constant voltage electrolysis in 900

°C  $\text{CaCl}_2$ , which resulted in a noticeable deformation of the titanium product. It is important to highlight that this phenomenon has not previously been reported before and, thus, required an in-depth investigation. Following results showed the dependencies between salt temperature, pre-sintering and design with the deformation. It was noted that the temperature of the salt during the electrolysis affected the sintering of the produced titanium parts, causing products to shrink by up to 40% and dramatically deform. This, however, was found to be mitigated to some degree by the sintering of the precursors for 1 hour at 1100 °C. The resulted product had a suitable density and porosity to be successfully reduced to metallic titanium with compressive strength of 111.4 MPa and Young's modulus of 1.39 GPa that was reported to be similar to the conventionally produced titanium foams with similar porosity (around 50%). In addition to that, the oxygen content was recorded to be as low as 1000 PPM, another sign of the successful reduction to metallic titanium, but it was found to be depended on the geometry of the product. Moreover, some attention was given to deformations that were caused by the design flaws, which unfortunately were not possible to predict and could be eliminated only by the iteration in the design.

Finally, a lot of work was done to evaluate the feasibility of the NEM Process in both cost and environmental aspects. Conducted cost evaluation demonstrated an incredible cost reduction compared to conventional additive manufacture technique, measuring a cost reduction of up to 4 times. In addition to that, the cost breakdown was found to be heavily dependent on the labour cost, which reached 56% of the

cost of one tooth implant.

The environmental impact of the NEM Process was assessed on the gate-to-gate principle using the Life Cycle Assessment (LCA) following the established international standard. This evaluation was done in two parts, first was the investigation of the main contributors towards the environmental impact, pointing out two major contributors that were argon consumption and electrode materials. Due to this a few possible optimisations to the process were proposed such as “smart” argon consumption and the need for reusable electrode materials. Implementing both showed a possible reduction of the overall environmental impact of 10-15%.

The second part of the LCA was comparative analysis where the NEM Process was compared against the commercially used Kroll - Electron Beam Melting (EBM) process. This showed that the overall impact of the NEM Process was lower than the Kroll - EBM Process by around 67%. Additionally, acquired data were also applied to the legislations that mainly monitor  $\text{NO}_x$ ,  $\text{SO}_2$ ,  $\text{PM}_{2.5}$  and  $\text{CO}_2$ , the emission of which was found to be more than 70% lower for the NEM Process.

This project resulted in the development of a feasible and green manufacturing route of titanium components in a safe and relatively fast way. Along with that numerous new ideas and discoveries were made that deserve further research and have the potential to improve our quality of life.

# List of Figures

1.1	Comparison of the conventional and proposed routes for AM of titanium components. . . . .	10
2.1	Process flow diagram of the Kroll process. . . . .	21
2.2	Cost break down of the Kroll process. . . . .	23
2.3	Process flow diagram of the Armstrong process. . . . .	24
2.4	Process flow diagram of the Armstrong process for Ti-64. . . . .	25
2.5	Process description of the PRP. . . . .	26
2.6	Experimental set up for the PRP. . . . .	27
2.7	Schematic of the CaO <sub>2</sub> shell formation around Ti particle. . . . .	29
2.8	Schematic of the experimental rig used for the OS process. . . . .	30
2.9	Examples of the sheet forming techniques. . . . .	33
2.10	Schematic of Selective Laser Sintering (SLS) process. . . . .	36
2.11	Schematic of the laser shaped metal deposition process. . . . .	38
2.12	Schematic of the Hot Isostatic Pressing process. . . . .	39
2.13	Schematic of the Metal Injection Moulding (MIM) process. . . . .	40

2.14 Schematic of the Direct Ink Writing of ceramics and waxy mixture extrusion. . . . .	48
2.15 Production of porous moulds via 3D printing for slip casting of ceramics.	49
3.1 Schematic of the ChiTu V 3.9 FDM 3D Printer motherboard. . . . .	69
3.2 Schematic of the DIW 3D printer. . . . .	72
3.3 Cell set up for a stainless steel crucible. . . . .	76
3.4 Cell set up for an aluminium oxide crucible. . . . .	77
3.5 Cell set up for a graphite crucible. . . . .	78
3.6 Experimental set up of the molten salt reduction. . . . .	80
3.7 Typical examples of the shear rate vs viscosity plots. . . . .	84
3.8 Typical reaction of a tested materials in the creep and recovery test. .	85
3.9 Main parameters found on a creep and recovery graphs. . . . .	86
3.10 Typical examples of the shear rate vs shear stress plots. . . . .	87
3.11 Schematic drawing of the Kinexus rheometer KNX2100. . . . .	88
3.12 Types of loading states of a sample. . . . .	89
3.13 Scattering of electrons and production of X-rays during SEM and EDS analysis. . . . .	91
3.14 Cross-section of the area of interaction of primary electron beam and sample. . . . .	92
3.15 Example of four types of Bravais lattices. . . . .	95
3.16 The Wheatstone bridge. . . . .	101

4.1	Ink loading technique proposed by the manufacturer of the 3D printer.	113
4.2	Different ink loading technique. . . . .	114
4.3	After loading homogenisation step. . . . .	116
4.4	Artefacts caused by uninterrupted extrusion of paste. . . . .	117
4.5	Schematic drawing of the screw head Direct Ink Writing 3D printer. .	118
4.6	Drawing of analysed nozzles. . . . .	120
4.7	Schematic drawing of the modified Direct Ink Writing 3D printer. . .	122
4.8	Delayed deposition of material compared with the programmed path.	123
4.9	Schematic drawing of the screw head Direct Ink Writing 3D printer. .	124
4.10	Flow diagram for the experimental set-up. . . . .	125
4.11	Shear stress vs shear rate comparison for PEG and PVA containing water-based TiO <sub>2</sub> slurries. . . . .	129
4.12	Shear rate vs Viscosity for water, PEG and PVA based inks. . . . .	130
4.13	Creep and recovery test for water, PEG and PVA based inks. . . . .	132
4.14	Shear rate vs shear stress plots for water, PEG and PVA based inks. .	134
4.15	The effect of solution content on the storage and loss moduli. . . . .	136
4.16	Shear rate vs viscosity comparison of ink (PEG 1:0.9) with and with- out boundary lubricant. . . . .	139
4.17	Result of the implementation of a surface lubricant on the quality of a product . . . . .	140
4.18	The effect of PEG onto the ink. . . . .	141
4.19	The migration of water under the applied pressure in the unstable ink.	142

4.20	The effect of the drying-induced shrinkage on the support. . . . .	143
5.1	CV of the notched Mo electrode loaded with TiO <sub>2</sub> , recorded at the scan rate of 1 mV/sec. . . . .	155
5.2	The SEM image of the powdered TiO <sub>2</sub> . . . . .	158
5.3	The SEM image of Ti derived from 60 nm TiO <sub>2</sub> . . . . .	158
5.4	The optical images of the whole titanium sponge and the individual crystals. . . . .	159
5.5	The SEM images of Titanium and Perovskite spikes. . . . .	161
5.6	The SEM images of the precursor after the DIW process and the reduced precursor. . . . .	162
5.7	The SEM image of the internal surface of the reduced hollow titanium sphere. . . . .	163
5.8	SEM images of ceramic samples sintered at different temperature and their consecutive morphology after reduction. . . . .	165
5.9	Examples of the precursors and the respective titanium counterparts produced via the NEM Process. . . . .	168
5.10	Product deformation comparison after 24h reduction with different degree of sintering. . . . .	170
5.11	Oxygen content of titanium impellers produced via the NEM Process from TiO <sub>2</sub> precursors sintered at 900 °C, 1100 °C or 1300 °C. . . . .	171

5.12	The effect of electrolysis temperature on the integrity of titanium turbines. . . . .	172
5.13	The effect of reduction temperature on complex deformation. . . . .	173
5.14	Design depended defects. . . . .	174
5.15	The XRD spectra of titanium dioxide feedstock and consequently reduced titanium. . . . .	176
5.16	The EDX results for the bulk and the surface of the reduced sample.	177
5.17	Cost break down of a titanium tooth implant produced by the NEM Process on the Lab-scale. . . . .	184
5.18	Cost break down of the optimised production of a titanium tooth implant produced by the NEM Process. . . . .	185
5.19	An example of the G-code predefined problem areas. . . . .	188
5.20	The reduction ability of samples with different thickness. . . . .	189
5.21	Examples of the titanium products produced via the NEM process. .	190
6.1	Manufacture routes of an additively produced (i.e. 3D-printed) titanium product. . . . .	205
6.2	Detailed material and energy flow within the boundary A (the NEM Process). . . . .	207
6.3	The NEM Process, showing the two stages used for fabricating a titanium impeller from raw titanium dioxide. . . . .	209

6.4	The AM-assisted Kroll Process, showing the three stages used for fabricating a titanium impeller from raw titanium dioxide. . . . .	211
6.5	Impact analysis of contribution of the sub-processes for the NEM Process. . . . .	218
6.6	Environmental impact contribution for the impeller production by the NEM Process. . . . .	219
6.7	Environmental impact contributors for the DIW process. . . . .	220
6.8	Endpoint comparison of the replacement material candidates. . . . .	222
6.9	Parametric and Sensitivity Analysis. . . . .	223
6.10	Endpoint comparison of the Kroll - EBM and the NEM Process. . . . .	226
6.11	Midpoint comparison for the Kroll and the FFC-Cambridge Processes for titanium extraction only. . . . .	227
6.12	Midpoint comparison of the NEM Process with the Kroll - EBM route.	228

# List of Tables

3.1	Crystal systems and their existing Bravais lattices. . . . .	94
4.2	Extrudability results from a 0.5 mm nozzle. . . . .	135
4.3	The ink composition and its relative Yield and Flow points. . . . .	137
5.1	The measurement of porosity for titanium and titanium oxide samples produced via the NEM Process. . . . .	166
5.2	Electricity related calculation. . . . .	179
5.3	Price of the raw materials. . . . .	180
5.4	Data collected for the calculation of the prices of miscellaneous ma- terials. . . . .	181
5.5	Prices of the used equipment. . . . .	182
6.1	Life cycle inventory for the NEM Process to produce one titanium impeller. . . . .	214
6.2	Life cycle inventory for Kroll - EBM Process. . . . .	215

6.3	List of abbreviations used int the life cycle assesment of the NEM	
	Process. . . . .	216
6.4	Legislation cantered emissions . . . . .	229
A.1	Life cycle inventory for the Kroll process. . . . .	255

# Nomenclature

BCC Body-centered cubic

BSE Back Scattered Electron

Ca Calcium

CaO Calcium oxide

CMT Combined Motor Transducer

CRT Cathode Ray Tube

CV Cyclic voltammetry

EDS Energy-Dispersive X-Ray Spectroscopy

FDM Fused Deposition Modelling

FE Freshwater eutrophication

FeCl<sub>3</sub> Iron chloride

FET Freshwater ecotoxicity

FPMF Fine particulate matter formation

FRS Fossil resource scarcity

GW Global warming

HCT Human carcinogenic toxicity

HPC Hexagonal closed-packed

HT Human non-carcinogenic toxicity

IR Ionizing radiation

ITP International Titanium Powder LLC

LCA Life Cycle Assesment

LCIA Life Cycle Inventory Analysis

LU Land use

ME Marine eutrophication

MET Marine ecotoxicity

Na Sodium

NaCl Sodium chloride, salt

NaCl Sodium chloride, salt

OD Stratospheric ozone depletion

OFHH Ozone formation, Human health

OFTE Ozone formation, Terrestrial ecosystems

OS The Ono-Suzuki process

PE Primary Electron

PEG polyethylene glycol

PRP Preform reduction process

PVA poly vinyl alcohol

RES Mineral resource scarcity

SE Secondary Electron

SEM Scanning Electron Microscope

SS Stainless steel

TAC Terrestrial acidification

TET Terrestrial ecotoxicity

Ti64 Titanium alloy containing 6 % aluminium, 4 % vanadium and 90 % titanium

TiCl<sub>4</sub> Titanium tetrachloride

UI User Interface

WC Water consumption

# Acknowledgements

I acknowledge everyone who made this project possible and who helped me to get through this research!

Polina Trofimova

Di Hu

George Chen

Matthew Jasmine Thomas Bishop

Mingchan Ma

Dong Zhao

Biyash Bhattacharya

Kate Yuan

Jason Wang

Jane Zhang

Julian Zhu

My Mum: Dolganova Vera Victorovna

My Dad: Dolganov Oleg Vladimirovich

Bamidele Akinwolemiwa

Chaohui Wei

Jorge Mendez Astudillo

Marco Tomatis

Michael Paul Stevens

Craig Andrew Simon

Magdalena Rybarczyk

Wyatt Michael Moss Wellington

Sophia Harris

Chuang Gao

Eraln Dzhumaliev

Daniil Tsikin

Zeping Wang

My fat cat: Rainbow

My small cat: Milky

# Chapter 1

## Introduction

### 1.1 Statement of Problem

#### 1.1.1 Titanium

Metals are one of the most used types of the engineering materials, due to strength, ductility and weight they pose a valuable set of physical and chemical properties [1]. Most of the development associated with metals is allocated to the discovery of new alloys and more efficient extraction and fabrication techniques [2].

The most striking example of a widely used engineering metal is titanium. It is known that titanium and its alloys are the most desired materials used across all the existing industries from food to aerospace [3]. The use of titanium, however, faces a massive price that limits its application. The irony of this is the fact that titanium is 9<sup>th</sup> most abundant element on the Earth [4]. This means that the extraction and

fabrication of this metal is an extremely difficult and dangerous process [5].

Therefore, titanium draws a lot of attention from the scientists around the globe, who dedicate their lives to finding new extraction techniques that would make such an outstanding metal more accessible [6], making it the focus of this thesis.

### 1.1.2 Applications

Titanium possesses a high weight to strength ratio that makes it a favourable material in such areas as aerospace, marine, biomedical, and leisure and sport.

In aerospace, titanium is used in engines that require uniquely shaped components like vanes in turbines, and some components of the airframes [7]. It is reported that on average about 15% of an air-plane is made of titanium or its alloy, which is 5% more than steel [8]. However, most of the titanium used in aerospace is in a form of beta alloys as they have even higher strength and lower creep under elevated temperatures compared to pure titanium [9]. Additionally, a number of details were produced by 3D printing and certified for use in an aircraft, which also lead to the development of a few standards regarding titanium additive manufacture for aerospace [10].

Chemical and energy plants utilise titanium for its corrosive resistance in the form of turbine blades, pipes, and vessels [11]. With one of the most important uses in heat exchangers of nuclear and other power generating plants, which is associated with a high corrosion resistivity and 50% higher thermal conductivity compared to steel [8].

Due to titanium's high corrosion resistance, it's a perfect working material for salty waters of sea or oceans. As one of the striking examples titanium is often used as a taper stress-joints on oil platform as it is also flexible enough to allow to account for the stresses within drilling shaft. It is also often used as a part of the ships and submarines for the same reason. Since its discovery titanium submarine hulls increased the depth of submersion from 1800 to 6000 m [8].

Another valuable property of titanium is biocompatibility with the human body, which is a unique property taking into account titanium's lightweight and high strength. In addition, scientists try to synthesise bone matching morphology to match the mechanical properties of the bone and reduce a stress shielding effect [12]. The most common implants made of titanium are hip and knee joints and tooth implants, although more and more complex and unique applications have been seen such as a part of a jaw and skull implants [13]. This aspects of application benefits from the 3D printing the most as those implants are unique to a patient such as tooth implants or joint prosthetics [14].

Titanium is also widely used in other aspects of our lives such as cutlery, sports equipment (bike parts, golf clubs, scuba diving equipment, winter gear), jewellery, musical instruments, etc. [8].

### **1.1.3 Manufacture**

The manufacture of every metal starts with mining and purification of ore. After that, purified ore undergoes a specific metal extraction process that is unique to

some metals such as the Kroll process for titanium and Hall–Heroult process for aluminium [15]. These processes typically of red-ox nature as most of the ore contain metals in oxide forms [16], which are divided into two main types:

- Metallothermic or Carbothermic

These processes utilise other materials (metals or carbon) that would be oxidised at the elevated temperatures resulting in the production of reduced metals.

- Electrochemical

The electrochemical processes utilise electricity to drive those red-ox reactions, which typically happen at a lower temperature or reduced material and energy consumption.

Moving onto the specific case of titanium production, it starts with the mining of typical ilmenite that contains iron, titanium and some other metals [17]. This ore is separated from other materials by a so-called high-intensity magnetic separation that removes materials that are even slightly magnetic [16]. After that separated material undergoes flotation, which forces a density-driven separation where the purified ilmenite is, then, smelted with the addition of petroleum coke as the reductant. At the final stage, before titanium can be produced, the titanium dioxide-rich slag is transformed into  $\text{TiCl}_4$ , which is then further purified in distillation [18]. The reduction of  $\text{TiCl}_4$  happens by reaction with magnesium, which takes the chloride and releases metallic titanium.

As a result of all the transformations, the metal is produced in a shape of chunks or sponge that undergo multiple stages of smelting in vacuum or under an inert atmosphere due to high reactivity of titanium with gases contained in the air at high temperature [5].

At this stage titanium is ready to be manufactured in the desired shape, which is known to be hard due to the following problems [19]:

- Variation of chip thickness

When titanium is cut, it tends to produce chips in a not consistent manner.

- High heat stress

Due to low heat conductivity, it is easy to create a localised expansion of the metal.

- High-pressure loads

Instantaneous loads are induced on a cutting tool.

- Springback

The workpiece tends to flex when is cut.

- Residual stress

Generated due to the low and uneven heat dissipation when titanium is cooled.

Overall, these factors require titanium to be treated especially carefully in order to reduce accelerated wear of cutting tools under the increased amount of coolant to reduce heat accumulation [20, 21].

As a solution to these problems titanium was actively developed into the Powder Metallurgy (PM) that utilises additive techniques to produce parts rather than subtractive [22]. Recently titanium and its alloys had seen a wide range of development to be applied into the Additive Manufacture (AM) [23–26], which typically requires metals to be in the powdered form. All techniques, however, usually require a localised melting of this powder in a predefined pattern layer by layer. This causes one of the main issues that are being looked into by the titanium PM industry, which is an undesired microscopic structure that is created due to this treatment. Particularly it forces grains in metals to grow in  $Z$  direction making products to possess orientation-dependended physical properties [27].

This number of different problems, therefore, requires increased research in order to bring titanium to masses, making our lives safer.

#### **1.1.4 Environmental Impact**

In recent years more and more attention was given to sustainability and environmental protection resulting in an increased number of environment-related legislation [28]. These legislations limit the amount of pollution emitted by any sort of activity to preserve our planet for future generations [29].

Due to this, the work produced for this project has to be heavily assessed on the environmental impact to ensure the reduction in pollution. In order to evaluate the environmental damage and to compare it with the conventional route for titanium manufacturing, the gate-to-gate Life Cycle Assessment (LCA) is conducted following

established international standards.

LCA has been a reliable tool for environmental assessment since 1960 [30]. It also attracts increased attention by being the only environmental assessment tool with well developed databases created in association with numerous European governments [29, 30].

## 1.2 Research Question

This project was set to answer a question:

*”Is it possible to develop a cheap and environmentally friendly titanium 3D printing process using a novel extraction technique?”*

This question was formulated to solve some of the notable problems related with the titanium production:

- High cost
- Complex and outdated process
- High amount of waste
- Emission levels

## 1.3 Aims and Objectives

The aim of this project is set as:

### **1.3.1 Development of the Near-net-shape Electrochemical Metallisation Process**

As a solution to the above-stated problems, it was decided to investigate a possibility to produce a new AM technique that would be able to reduce cost and mitigate a large part of the complexity of the existing processes. The base of the project was the uniqueness of the FFC-Cambridge Process that was shown to be able to produce samples with the predefined structure. To achieve such development of two main aspects of the process will be necessary, which include fabrication and extraction. The overall process will also be tested to establish the overall feasibility and competitiveness for product quality and the level of environmental pollution caused by the process.

#### **1.3.1.1 Rapid Fabrication of Titanium Oxide Precursors with Complex Shapes (fabrication aspect)**

The shaping of the ceramic product is required to be precise and reproducible, thus, it is important to establish and optimise the most suitable AM technique to produce samples that will be applicable for the FFC-Cambridge Process.

This stage requires an extensive study of the properties that the titanium dioxide precursors should possess to be successfully applied to the electrochemical metallisation process.

### **1.3.1.2 Direct Metallisation of Titanium Oxide Precursors via the FFC-Cambridge Process (extraction aspect)**

The reduction of the net-shaped precursors needs to yield a precise replica of the initial shape with minimum to none deviations in dimensions. For this, the development of a consistent way of reducing titanium dioxide samples without any deformation and defects have to be established.

Quality control plays an important role in the production of any kind of product, meaning that the quality of products must be thoroughly studied. This will ensure an in-depth investigation of mechanical properties and composition of the products, which will help to allocate the use area for the products.

## **1.4 Statement of Novelty**

The novelty of this project can be summarised in three points:

1. Titanium dioxide 3D printing

An in-depth rheological evaluation of the titanium dioxide paste was performed for the first time at such a high degree of details.

2. Development of a new additive manufacturing technique

This work resulted in a unique manufacturing technique that opens a new research direction for the applied AM of metals in a form of indirect electrochemical AM. As shown in Figure 1.1 the proposed method changes the

order of the manufacture from “*titanium ore*  $\Rightarrow$  *titanium tetrachloride*  $\Rightarrow$  *titanium sponge*  $\Rightarrow$  *titanium ingot/rod/wire/plate/powder*  $\Rightarrow$  *titanium products*” to “*ore*  $\Rightarrow$  *pre-shaped oxide precursor (with/without purification and ceramic 3D printing)*  $\Rightarrow$  *titanium products*”.

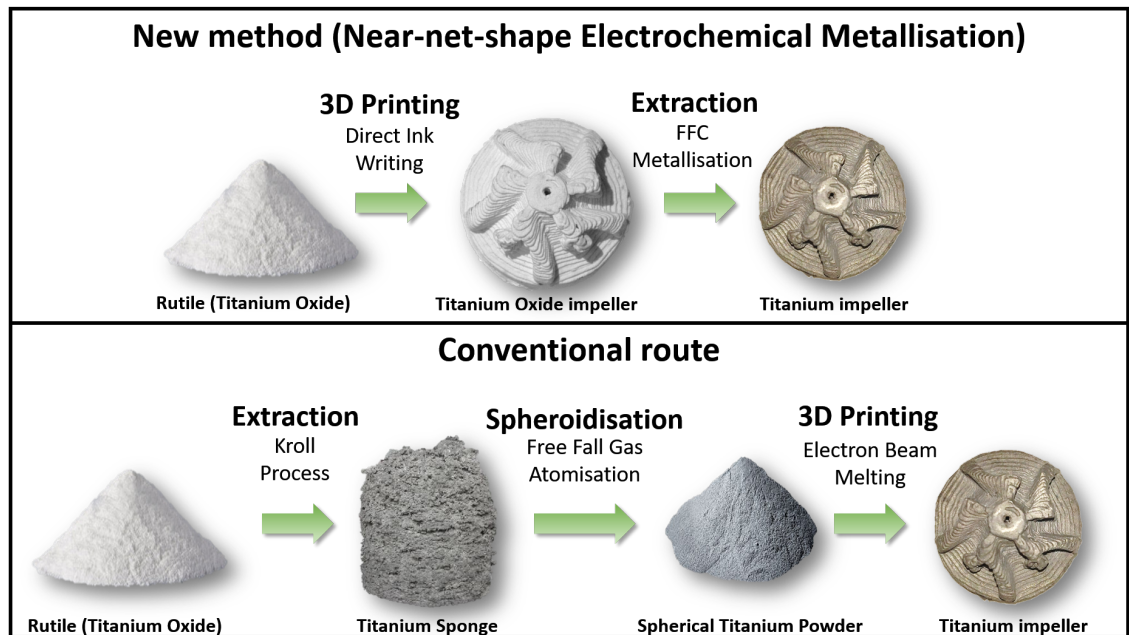


**Figure 1.1:** Comparison of the conventional and proposed routes for AM of titanium components.

Additionally, this development can open a new era for the FFC-Cambridge Process, as for now, it is not feasible enough to be adopted by the industry. With the help of this project, it could find more ways of commercialisation to finally initiate the reduction of the high cost of titanium.

### 3. Environmental evaluation of a newly developed technique

The development of the process was then analysed on the environmental im-

pact that also covered some aspects of the extractive techniques that has not been done before.

# References for Chapter 1

- [1] W. Callister, D. Rethwisch, *Materials Science and Engineering: An Introduction, 8th Edition*, Wiley, **2009**.
- [2] W. Smith, J. Hashemi, *Foundations of Materials Science and Engineering*, McGraw-Hill, **2003**.
- [3] T. E. o. E. Britannica, “Titanium”, **2018**.
- [4] J. Emsley, *The elements / written and compiled by John Emsley*, Oxford : Clarendon Press, Oxford, **1989**.
- [5] M. Donachie, *Titanium: a technical guide*, ASM International, **2000**.
- [6] D. J. Fray, “New Methods for the Production of Titanium”, *International Materials Reviews* **2008**, 53, 317.
- [7] P. Bridges, B. Magnus, “Manufacture of Titanium Alloy Components for Aerospace and Military Applications”, *RTO Applied Vehicle Technology Panel (AVT) Specialists’ Meeting* **2001**.
- [8] C. Leyens, M. Peters, *Titanium and Titanium Alloys: Fundamentals and Applications*, Wiley, **2003**.

- [9] R. R. Boyer, “An overview on the use of titanium in the aerospace industry”, *Materials Science and Engineering: A* **1996**, *213*, 103–114.
- [10] X. Zhang, E. Liang, “Metal additive manufacturing in aircraft: current application, opportunities and challenges”, *IOP Conference Series: Materials Science and Engineering* **2019**, *493*, 012032.
- [11] G. Lütjering, J. C. Williams, *Titanium*, 2nd, Springer, Berlin Heidelberg New York, **2007**.
- [12] M. Niinomi, M. Nakai, “Titanium-Based Biomaterials for Preventing Stress Shielding between Implant Devices and Bone”, *International Journal of Biomaterials* **2011**, *2011*, 836587.
- [13] M. Balazic, J. Kopac, M. J. Jackson, W. Ahmed, “Review: titanium and titanium alloy applications in medicine”, *International Journal of Nano and Biomaterials* **2007**, *1*, 3–34.
- [14] V. V. Popov, G. Muller-Kamskii, A. Kovalevsky, G. Dzhenzhera, E. Strokin, A. Kolomiets, J. Ramon, “Design and 3D-printing of titanium bone implants: brief review of approach and clinical cases”, *Biomedical Engineering Letters* **2018**, *8*, 337–344.
- [15] T. E. Norgate, S. Jahanshahi, W. J. Rankin, “Assessing the environmental impact of metal production processes”, *Journal of Cleaner Production* **2007**, *15*, 838–848.
- [16] C. Bodsworth, *The Extraction and Refining of Metals*, CRC Press, **2018**.

- [17] F. Gao, Z. Nie, D. Yang, B. Sun, Y. Liu, X. Gong, Z. Wang, “Environmental impacts analysis of titanium sponge production using Kroll process in China”, *Journal of Cleaner Production* **2018**, *174*, 771–779.
- [18] C. Nagesh, C. Sridhar Rao, N. Ballal, P. Krishna Rao, “Mechanism of Titanium Sponge Formation in the Kroll Reduction Reactor”, *Metallurgical and Materials Transactions B* **2004**, *35*, 65–74.
- [19] A. Pramanik, “Problems and solutions in machining of titanium alloys”, *The International Journal of Advanced Manufacturing Technology* **2014**, *70*, 919–928.
- [20] M. Darsin, H. A. Basuki, “Development Machining of Titanium Alloys: A Review”, *Applied Mechanics and Materials* **2014**, *493*, 492–500.
- [21] R. Bajoraitis, G. Cadwell, E. Cook, K. Herbert, H. Hollenbach, R. Kaneko, B. Kim, F. Koeller, E. Mild, L. Pionke, P. Russo, J. Schley, J. Solheim, G. Stacher, R. Witt in *ASM Metals Handbook, Vol. 14-Forming and Forging*, **1988**, p. 1836.
- [22] W. E. Frazier, “Metal Additive Manufacturing: A Review”, *Journal of Materials Engineering and Performance* **2014**, *23*, 1917–1928.
- [23] L. E. Murr, S. A. Quinones, S. M. Gaytan, M. I. Lopez, A. Rodela, E. Y. Martinez, D. H. Hernandez, E. Martinez, F. Medina, R. B. Wicker, “Microstructure and mechanical behavior of Ti–6Al–4V produced by rapid-layer manu-

- facturing, for biomedical applications”, *Journal of the Mechanical Behavior of Biomedical Materials* **2009**, *2*, 20–32.
- [24] P.-H. Li, W.-G. Guo, W.-D. Huang, Y. Su, X. Lin, K.-B. Yuan, “Thermomechanical response of 3D laser-deposited Ti–6Al–4V alloy over a wide range of strain rates and temperatures”, *Materials Science and Engineering: A* **2015**, *647*, 34–42.
- [25] R. M. German, “Progress in Titanium Metal Powder Injection Molding”, *Materials (1996-1944)* **2013**, *6*, 3641–3662.
- [26] B. Dutta, F. H. Froes in *Titanium Powder Metallurgy*, (Eds.: M. Qian, F. H. Froes), Butterworth-Heinemann, Boston, **2015**, pp. 447–468.
- [27] M. Arribas, B. López, J. M. Rodríguez-Ibabe, “Additional grain refinement in recrystallization controlled rolling of Ti-microalloyed steels processed by near-net-shape casting technology”, *Materials Science and Engineering: A* **2008**, *485*, 383–394.
- [28] J. M. Allwood, J. M. Cullen, R. L. Milford, “Options for Achieving a 50% Cut in Industrial Carbon Emissions by 2050”, *Environmental Science & Technology* **2010**, *44*, 1888–1894.
- [29] E. Parliament, “Directive 2010/75/EU of the European Parliament and of the Council of 24 November 2010 on industrial emissions (integrated pollution prevention and control)”, *The European Parliament and the Council of the European Union* **2010**, 159–261.

- [30] M. A. Curran, “A Brief History of Life-Cycle Assessment”, *U.S. Environmental Protection Agency* **2006**.

# Chapter 2

## Literature Review

### 2.1 Background

Whenever you hear the word “titanium”, it is always associated with the strongest metal on Earth. This metal fascinates scientists around the globe due to its peculiar set of properties. For its lightweight, high strength and extreme corrosion resistivity, titanium rightfully holds a unique position among the other engineering materials [1]. Indeed, it is clear that there is no such element that can be as light as aluminium and, at the same time, to be as strong as stainless steel. However, one of the most valuable properties of titanium is its great biocompatibility, which grants titanium a unique ability to be implanted in a living body without poisoning it or being rejected. Due to this, tissue happily grows into the titanium implant and thanks to the bone-matching structure and density patients do not feel any difference [2].

Historically titanium was discovered by William Gregor in England in 1791 as

a part of the oxygen-containing compound and only in 1910 titanium was purified to 99.9 % on an industrial scale by Matthew Arnold Hunter [3]. The most common elemental compounds of titanium are ilmenite ( $\text{FeTiO}_3$ ) and rutile ( $\text{TiO}_2$ ). Ilmenite is used to produce titanium metal when synthetic rutile and natural rutile are used as additives for numerous products such as cosmetics, high-quality paper, rubber, toothpaste, sunscreens, etc. Such wide use comes from its white colour, opacity, hardness and unique optical properties [4, 5].

After its discovery, titanium was placed on the 22<sup>nd</sup> position in the periodic table, which allocated it to so-called transition metals. Titanium can be described as a greyish metal [6]. It exists in two elemental crystal structures body-centred cubic (BCC) and hexagonal closed-packed (HCP), which are called beta and alpha respectfully. Important to note that alpha structure is only found under the high temperatures or within an alloyed metal [7].

As a pure metal, titanium is used for implants, jewellery and some specific areas that utilise unique properties such as heat exchanger tubes in nuclear reactors. The broader use comes to titanium when it is applied as an alloy. There are over 30 recognised grades of titanium from unalloyed to alloyed [8]. All of them are divided into 4 groups: alpha, near-alpha, alpha-beta and beta. These groups represent the amount of each of the two phases in a given alloy. As a rule beta phase titanium is more ductile, alpha is relatively stronger and alpha-beta is a mixture of the before-mentioned properties. The most valuable and used alloys, therefore, are alpha-beta alloys, especially Ti-6Al-4V (Ti64). It is used in the aerospace industry for its low

density and high strength [7].

## 2.2 Production of Titanium and Its Alloys

Titanium production, like any other metal production, requires numerous qualitative and quantitative criteria to consider, such as chemical composition, physical properties, scalability and efficiency. Therefore, out of the numerous newly invented production methods, only the most evolved are going to be considered due to the practicality of their application.

### 2.2.1 Conventional Extraction Processes

These extraction processes primarily follow two routes metallothermic, Electrochemical and a combination of these two.

#### 2.2.1.1 Metallothermic Processes

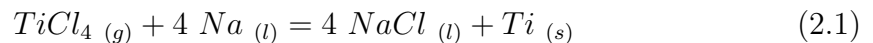
These processes utilise a so-called metallothermic reduction route where metal oxide is reduced under elevated temperature in the replacement reaction with other metal, which is oxidised in the process.

#### **Hunter Process**

The first-ever metallic titanium was obtained by the American metallurgist, born in New Zealand, Matthew Arnold Hunter in 1910 [9]. Method, that was later called the Hunter process, was conducted in a sealed bomb reactor that was heated to a “low

red heat”, the reactor accommodated titanium tetrachloride ( $\text{TiCl}_4$ ) and metallic sodium. After the reaction titanium was found in forms of melted, semi-melted chunks and powder, which resulted in a total yield of 90%. It was found that the reaction was extremely sensitive to oxygen, which concluded that 10 % loss was caused by the oxygen contained within the sodium [10].

Hunter Process follows the replacement reaction between metallic sodium and titanium tetrachloride:



This process pioneered the conventional production of high purity titanium metal and initiated future development in the face of the Kroll and the Armstrong processes.

### **Kroll Process**

Hunter’s discovery made a ground for the metallurgists in the world who were interested in the production of titanium and related elements. One of those people was William J. Kroll from Luxembourg, who, in an attempt to improve the accessibility of Hunter’s process, designed a method where instead of sodium the magnesium was utilised as a reductant (See Figure 2.1) [11]. This was done due to magnesium being a cheaper material, compared to sodium, and being safe to handle in open-air [12]. The process was peaking at 1060 °C and the pressure inside the reactor would reach 1.2 atmosphere [13].

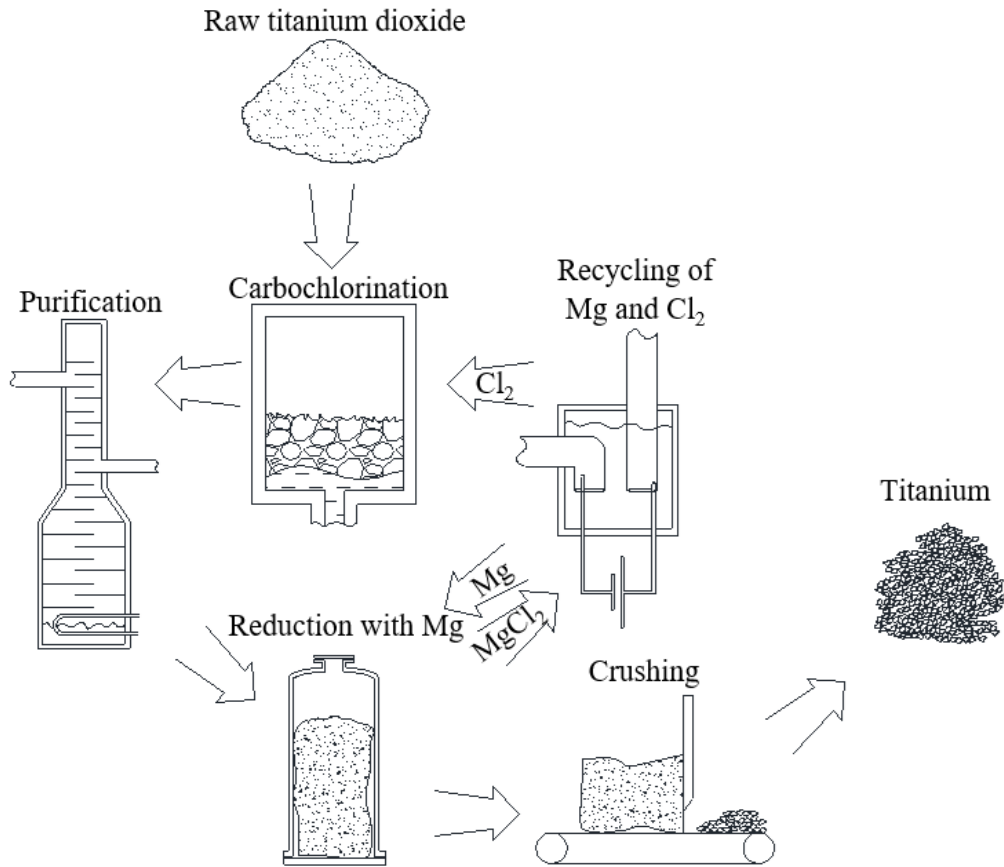
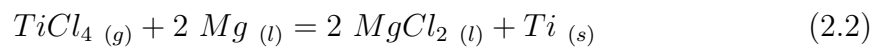


**Figure 2.1:** Schematic process flow diagram of the Kroll process.

After the debut of Kroll, his process became an industry standard for the titanium production and almost completely replaced Hunter process. Even today, despite it being slow and labour intensive, it is a leading manufacturing route for titanium [14].

The Kroll process:

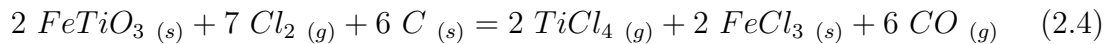


When comparing Equations 2.1 and 2.2 the only visible difference of the two

processes is the replacement of sodium metal to magnesium, releasing necessity of an extreme conditions of handling sodium metal. Notably, these two reactions still utilise titanium in a form of a compound that is derived from titanium ore via the carbochlorination reaction:



Alternatively, this reaction can be applied to ilminate producing iron chloride ( $FeCl_3$ ) together with titanium tetrachloride ( $TiCl_4$ ) (see Equation 2.4). Therefore, this route requires an additional purification stage that is done by distillation.



Both 2.3 and 2.4 are extremely dangerous processes that happen under high temperatures and require the use of such pollutant as the chlorine gas [15]. However, as it can be seen from Figure 2.1, Kroll process utilises an advanced recycling system that reduces the requirement for dangerous gas and improves resource consumption. This advancement, along with other improvements onto an already highly efficient reaction have been made over the last 70 years of the Kroll process' existence to bring it to the stage at which it is used today [16].

Overall, this method carries potential environmental and safety hazards. Additionally, according to Fray, production of titanium tetrachloride takes about 50 % of the final cost of the produced titanium (Figure 2.2) [17].

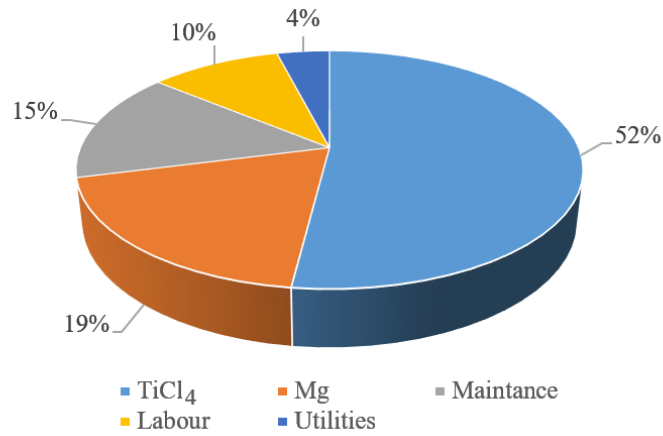


**Figure 2.2:** Cost break down for the manufacture of titanium sponge via the Kroll process [17].

### Armstrong Process

This method was established by International Titanium Powder (ITP) LLC Lockport, Illinois in 2003. Scientists have set a goal to create a continuous production loop for titanium. Which was based on Hunter's idea (Eq. 2.1) of the reaction of titanium tetrachloride with sodium. Included recycling loop contained the flow of unreacted molten sodium that is separated in the distillation process (See Figure 2.3). In this system, the only product that was required to be separated was salt (NaCl). The final metallic titanium product is presented in powdered form [18].

Additionally, the authors proposed the design of direct alloy manufacturing (Figure 2.4), in particular, Ti-64. To achieve this instead of constantly supplying only TiCl<sub>4</sub> the mixture of 3 chlorides is being fed in the reactor (See Figure 2.3). The excess sodium is again being recycled after the distillation step. This, according to creators, resulted in an extremely homogeneous alloy blend, surpassing the conven-

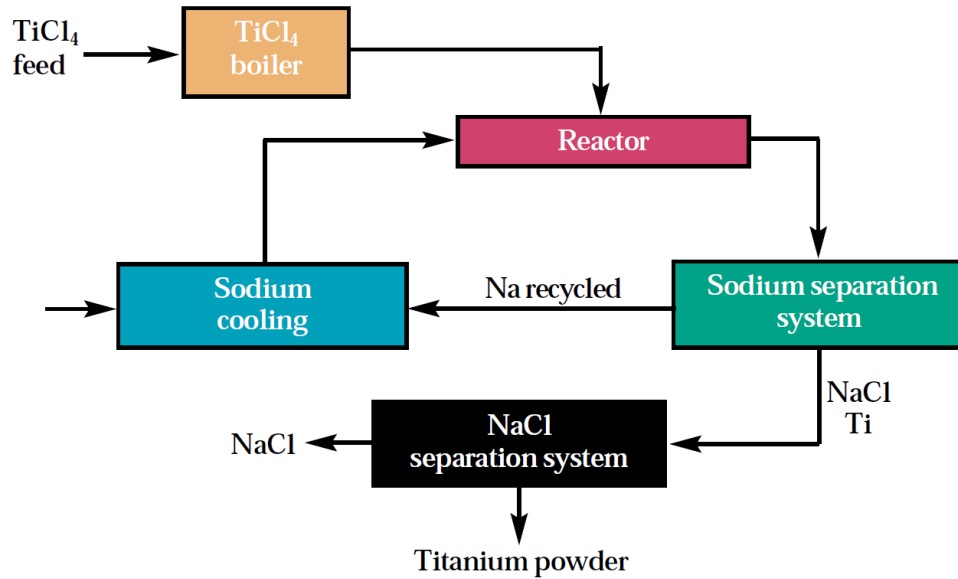
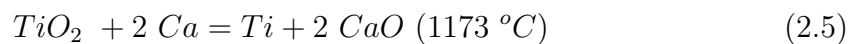


**Figure 2.3:** Process flow diagram of the Armstrong process for the production of the powdered titanium metal [18].

tionally produced alloys. Both systems are reported to be utilised for the production of CP titanium powders and alloys [17, 19, 20].

### Preform Reduction Process

Preform reduction process (PRP) was originally proposed by Okabe et al. in 2004 (Figure 2.5). It is described as a metallothermic process where rutile is reduced by Ca under the elevated temperature and pressure (Equitation 2.5).



However, there is a problem as usually Ca contains impurities that damage the quality of the final product if Ca is mixed within the precursor. To overcome

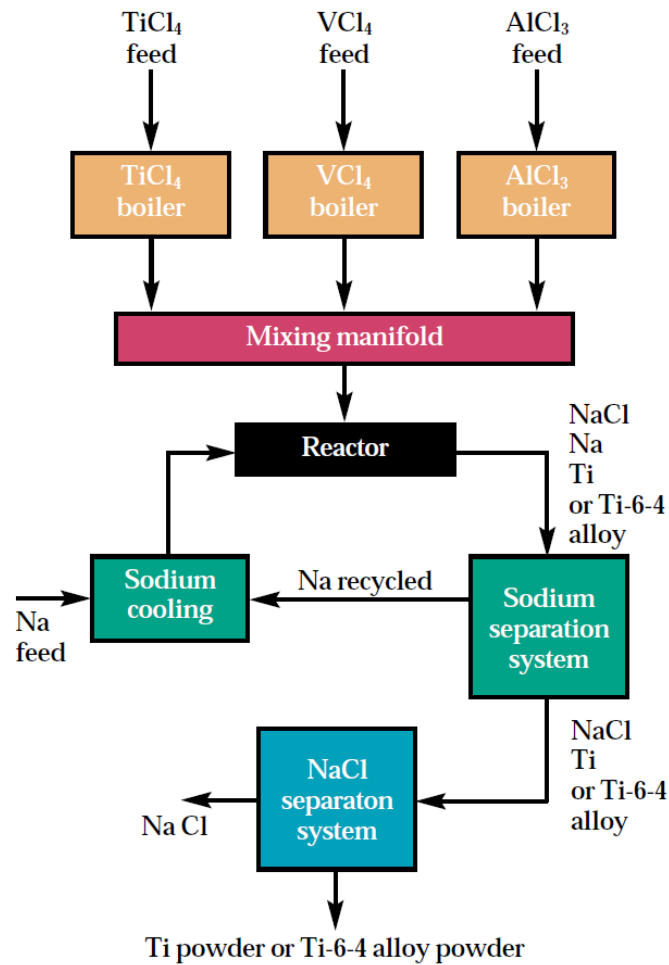


**Figure 2.4:** Process flow diagram of the Armstrong process for the production of the powdered titanium metal [18].

this, it was decided to reduce pre-shaped  $\text{TiO}_2$  by vaporised  $\text{Ca}$ . This process also includes sintering/calcinating of the pre-shapes, which is done in order to remove the initial binder and moisture from the precursor [21]. The last stage is what pulls this method behind, which is extensive and complicated leaching (See Figure 2.5) [14]. Furthermore, the rig that was implemented in the process was required to be welded which was done to seal and contain all the pressure that was building up

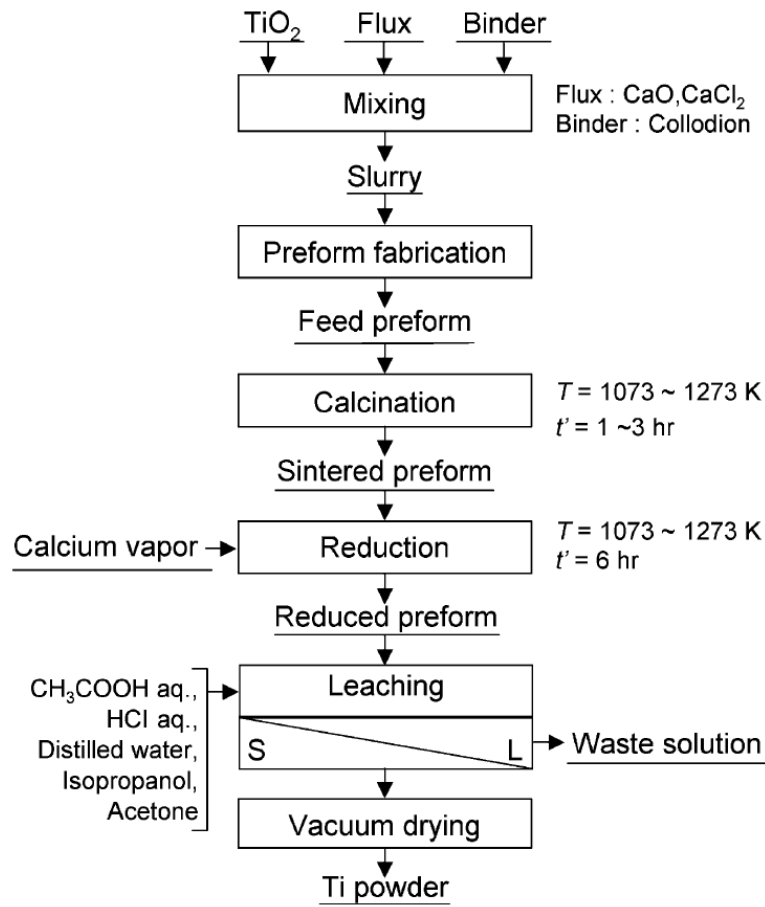


**Figure 2.5:** Process route and parameters involved in the Preform reduction process [21].

inside (Figure 2.6). Even though the final product possesses high quality and is in powdered form, the operating conditions of the PRP such as temperature and pressure cause a high hazard, making it less attractive for the industrial application.

### 2.2.1.2 Electrochemical Process

#### The FFC – Cambridge Process.

The Fray–Farthing–Chen Cambridge Process, named after its inventors, was established in 2000 [22]. Published work raised an enormous interest in the scientific

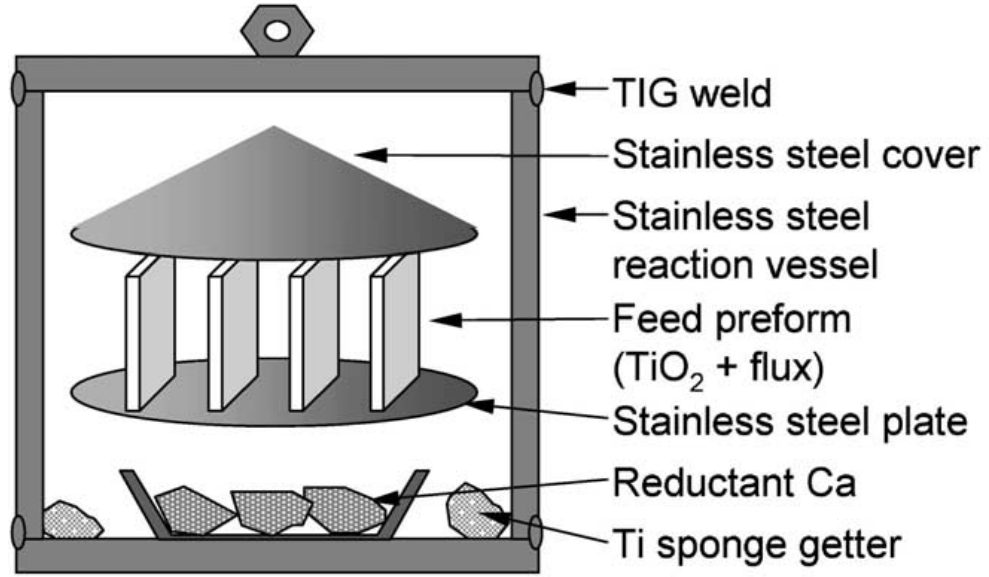


**Figure 2.6:** Schematics of the reactor used in PRP [21].

society due to its green and cost-reducing nature. In that work, the reduction of titanium dioxide was described as an electrochemical process where solid titania ( $\text{TiO}_2$ ) precursor was electrolytically reduced in molten calcium chloride. The kinetics of this process using carbon as an anode was also rigorously studied and the main routes were found to be as following [23]:

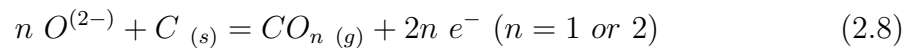
Overall reaction:



Cathodic reaction:



Anodic reaction:



These reactions include M (metal) instead of Ti (Titanium) due to a large number of other metals that were successfully obtained through this electrolytic method [24]. However, this is just the main or desired route, unfortunately, there is one constraint in this process that is the formation of intermediate products so-called perovskites or titanates ( $\text{CaTiO}_3$ ). Such transformation was shown to reduce current efficiency and, therefore, numerous studies were conducted to improve this and the other hindering factors such as feedstock replacement [25], reactor design [26] and electrode material [27]. Alternatively, the FFC-Cambridge Process allowed for the in situ metallisation or so-called solid transformation where product retains the shape of precursor [28].

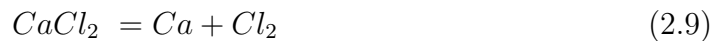
### 2.2.1.3 Combined Process

This method utilises both metallothermic and electrochemical reduction routes, with the dominant part being metallothermic.

#### The Ono-Suzuki Process

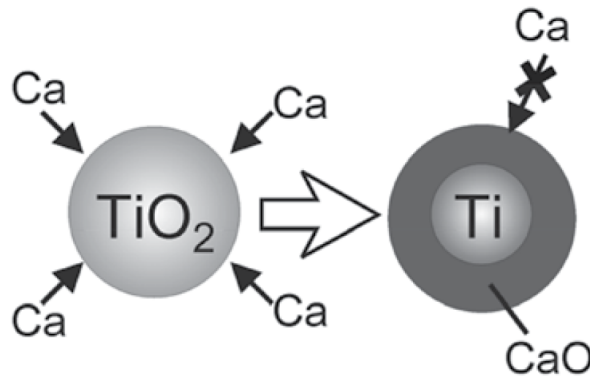
In 2003 group of scientists from Japan proposed a unique calciothermic reduction route for  $\text{TiO}_2$  where a molten salt bath was utilised as a medium to transfer dissolved Ca to the surface of rutile [29]. The method was named The Ono-Suzuki (OS) process after its creators. The decision of using molten salt was established since within the Ca and  $\text{TiO}_2$  system, after reaction 2.5 takes place, the CaO forms a shell around a Ti particle. Which is preventing the further deoxidation as shown in

Figure 2.7. Such hindering, however, is mitigated by molten  $\text{CaCl}_2$  and its ability to dissolve  $\text{CaO}$  to the point where the salt would become oversaturated and stopped dissolving  $\text{CaO}$ . For that Ono and Suzuki decided to implement electrolysis, in order to reduce the amount of oxide and produce new atoms of  $\text{Ca}$ . Figure 2.8 describes the structure of the designed experimental rig in details. There the evolution of 3 gases can be found, which are  $\text{Cl}_2$ ,  $\text{CO}$  and  $\text{CO}_2$ . The first gas is produced during the electrolysis of the molten salt via the reaction:



Which represents the splitting of  $\text{CaCl}_2$  under the applied voltage of 3.3 V and consecutive evolution of the chlorine gas on the surface of an anode. The rest of the gases are generated when oxygen has reached the anode side and begun to consume carbon-based electrode.

The creators also indicated that at some point the mechanisms of the FFC-Cambridge Process happen on the interface between the cathode and the titanium



**Figure 2.7:** Schematic of the  $\text{CaO}$  shell formation around  $\text{Ti}$  particle [30].

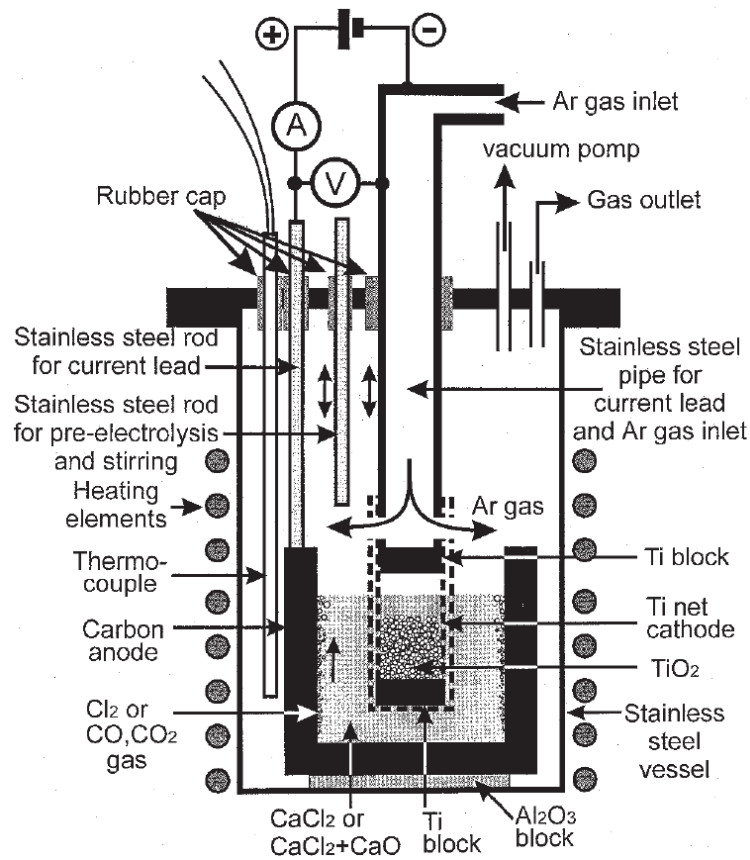


**Figure 2.8:** Schematic representation of the experimental set up used by Ono et al. in the OS process [29].

dioxide, although it accounts for a minor part of the whole process [30].

Overall, the chloride gas evolution creates the main drawback for the described system with the huge benefit in a form of it being a continuous process.

### 2.2.2 Summation

Through the search of a suitable method, the described FFC – Cambridge Process has the desired properties. The FFC – Cambridge Process has a number of advantages over the conventional methods:

- Shape conservation.
- Lower cost.
- Lower energy consumption per kg of titanium.
- Does not utilise toxic or dangerous chemicals.
- Simpler (One-stage process).
- Faster.

The disadvantages, however, are:

- Has only been shown on a pilot scale.
- Has some undesired side reaction.
- Has low current efficiency.

All this, along with the ability to maintain the shape of a precursor, increases the success of the proposed topic by forming a cheap and simple extraction stage.

## 2.3 Fabrication of Titanium and Its Alloys

Traditionally, fabrication of any metal component is done via machining (*i.e.* subtractive fabrication), forming/forging and casting, with more advanced methods of near-net-shape production techniques in the form of rapid prototyping techniques.

### 2.3.1 Conventional Fabrication Methods

Conventional fabrication routes utilise well-established methods of metal forming techniques that were known for centuries. These methods are well studied and optimised and mainly comprised of forging, casting and machining [31–33].

#### 2.3.1.1 Metal Forging

All metals are ductile and, thus, can be shaped by applying sufficient force on it. Such plasticity allows the metal to be shaped in a variety of shapes starting from simple sheets, wires or ingots to complex coins, panels, etc. [31].

Generally forging is divided into two categories: sheet forming and bulk deformation. These can be applied to a cold or heated material with respective naming of cold and hot forging. Sheet forming contains numerous other subdivisions such as rolling, bending, deep drawing and stretch forming techniques as shown in Figure 2.9. In addition to that rolling is used to produce wires, rods and other elongated products.

Bulk deformation operates on the same principle, but at a larger bulk volume due to that, it can produce complex objects such as turbines, shafts, etc. [31].

Metal forming nowadays is used in the production of a wide variety of products from car bodies, to cups and bullets. Titanium and its alloys are readily formed at room temperature, which describes them as easy to form [35].

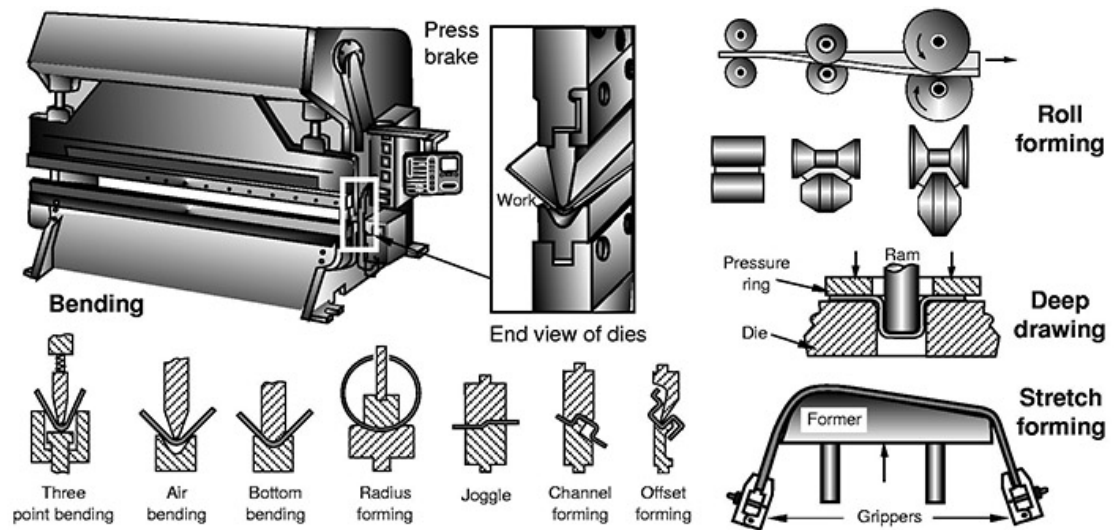


**Figure 2.9:** Examples of the sheet forming techniques [34].

### 2.3.1.2 Casting

The casting of metal has been practised for centuries, thus, its modelling and design has evolved to the highest level [33]. The principle of this process revolves around solidification of molten material and when this liquid material is filled in a mould the shape of the mould can be reproduced. Mould production is considered the hardest part of the process as at the designing stage mould should account for thermal expansion/compressions, air entrapments, etc. Due to this complexity, there is a wide range of defects that are common to a cast product, which include but are not limited to distortion/warp, cracks and tears, mismatches, cavities, etc. [33]. Additionally, the surface finish of the cast product is typically rough and requires additional machining.

The casting of titanium is an extremely challenging process, which requires the complete absence of oxygen and any other reactive gases. This is essential to safely

produce titanium due to its high reactivity [36]. Apart from that, molten titanium is reactive with the mould material, which is typically avoided by implementing a coating inside the mould. Important to notice that due to the low specific heat, the above-mentioned reactions happen on the interface between the mould and titanium and sometimes can be accounted for by using an inexpensive backup material [36].

The most precise casting is done by a so-called investment casting where mould contains another material that is being replaced by the molten titanium [37].

Overall, the casting of titanium can reduce the cost of a product, however, the designing of a mould for titanium casting can be a challenging task.

### **2.3.1.3 Machining**

Machining of metal is the essential part of any metal production as it allows for the extreme level of precision, which is essential when applied to engineering [38]. This precision is achieved by cutting metal down by a harder cutting tool. The cutting procedure can be controlled by a computer, which is the bare bones of Computer Numerical Control (CNC). Typically this process is carried out after forging or casting to bring the product to the desired shape and finish.

Unlike other metals, titanium poses several challenges to machining such as increased lubricant consumption and rapid wear of cutting tools [1, 38, 39]. First of all, due to titanium low heat dissipation, it requires a large amount of coolant, which, additionally, causes titanium to harden (change phase) further reducing the life of cutting tools [1]. Low Young's modulus makes titanium springy causing a

so-called spring back effect, which reduces the precision of matching if not taken into consideration [38].

### **2.3.2 Near-net-shape Methods**

As the solution of the conventional processes the use of Near-net-shape methods, or so-called rapid prototyping, is preferred as it reduces waste and the amount of milling required for the production of a metallic product by fabricating an end of the line product, skipping the conventional post-treatment [40].

Initially created as a non-commercial process for the rapid production of prototypes, near-net-shape methods have been hugely advanced and developed over the past 30 years. Nowadays rapid prototyping is considered a reliable option for the production of final parts in a fast and waste efficient way [41, 42]. Therefore, scientists around the globe express huge interest in this manufacturing idea, triggering the development of numerous rapid prototyping techniques for almost any possible material [43].

In this study, the material of interest is metal that can be treated in the vast variety of rapid prototyping methods, which include well-established processes along with novel ones.

#### **2.3.2.1 Selective Melting/Sintering**

One of the most developed metal AM technique nowadays is considered to be Selective Sintering or Selective Melting. These methods have a common principle of

operation: the powder bed is moved layer by layer into a building chamber and then the selective melting or sintering of the powder particles creates a pattern taken from a CAD file. The melting part of this process happens with the use of either a laser or an electron beam (See Figure 2.10). From this, the naming of a process appears Selective Laser Melting (SLM), Selective Laser Sintering (SLS) and Electron Beam Melting (EBM) [44, 45]. However, due to the novelty and the extreme applicability of these methods, numerous synonyms appeared. Here is an example of Laser Sintering Process' names: Selective Laser Melting (SLM), Direct Metal Laser Sintering (DMLS), LaserCUSING, Laser Metal Fusion (LMF) or industrial 3D printing [46].

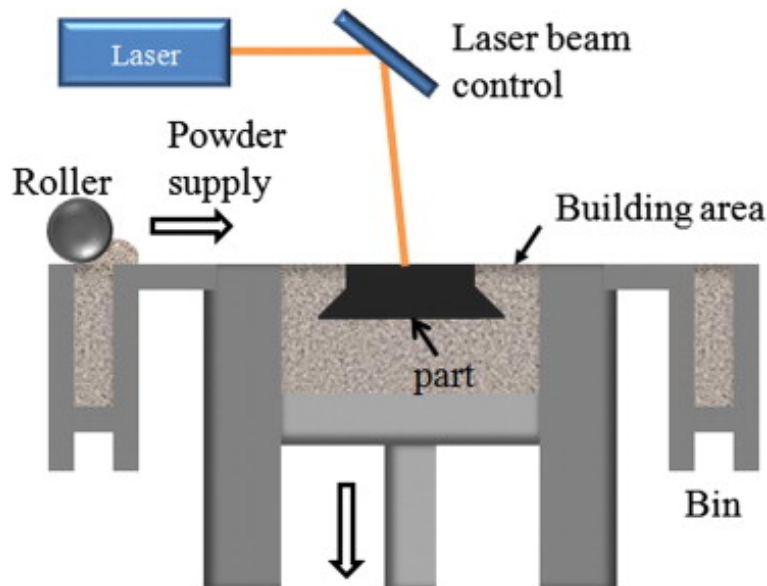


**Figure 2.10:** Schematic of Selective Laser Sintering (SLS) process [47].

Even though, the SLS, SLM and EBM have similar working principles the final product appears to possess different properties. The SLM/SLS tends to produce smoother surfaces but in cost of the slower process which requires the finest particles

and use of argon atmosphere. The latter results in an additional problem of creating closed pores filled with argon. Such a defect affects structural strength and cannot be eliminated using the best post-treatment process, the Hot Isostatic Pressing (HIP) [40]. In comparison, Electron beam melting (EBM) utilizes the high energy and density electron beam, which allows producing products with relatively high speed, compared to other additive manufacturing methods. According to Baufeld, Biest et al. (2010) the final surface finish is not as good as SLM/SLS parts' and the requirement of high vacuum creates a financial drawback comparing with the use of argon atmosphere [48].

### **2.3.2.2 Shaped Metal Deposition**

Another 3D printing technique utilised in the manufacture is Shaped Metal Deposition (SMD). It is very similar to the previous 3 methods but has one major difference: instead of using and melting powder from two chambers that create a bed of powder, it either melts a wire (See Figure 2.11) or a powder which is supplied directly in the melt, created by a heat source (laser or electron beam) [49]. Due to the use of a laser or an electron beam, SMD can also be referred to as SLS and EBM accordingly, inheriting the same problems discussed for SLM and EBM. Such implementation of different feeding methods increases the maximum size of the produced objects as it removes the necessity for powder bed that plays the role of the support.

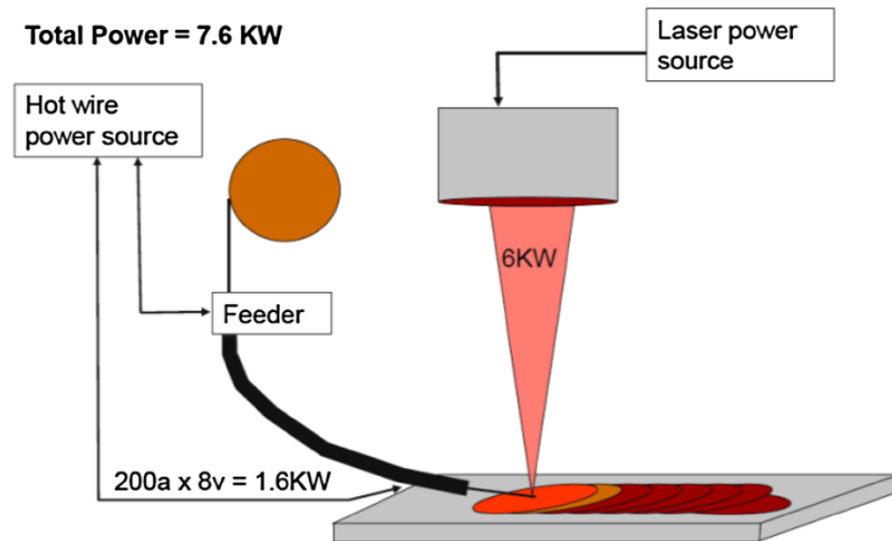


**Figure 2.11:** Schematic of the laser Shaped Metal Deposition (SMD) process [49].

### 2.3.2.3 Hot Isostatic Pressing

Due to the rapid prototyping being in high demand, numerous novel methods are proposed if not already industrialised for metal near-net-shape manufacturing. One of such methods is the Hot Isostatic Pressing (HIP). It is usually used along with additive manufacturing methods to enhance the property of 3D printed products by reaching near 100% density [40]. Moreover, it is also implemented as a standalone method of rapid prototyping. The principle is based on filling a pre-shaped capsule with the metal powder, sealing it and putting in a HIPing machine (See Figure 2.12) [50].

Such a simple process is reported to produce the forged-comparable mechanical properties, with that, however, the level of details remains low [51].

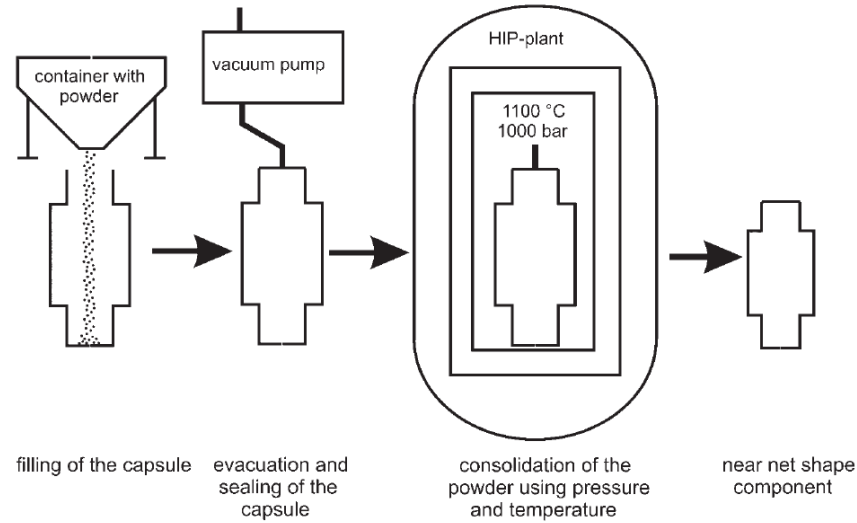


**Figure 2.12:** Schematic of the Hot Isostatic Pressing (HIP) process [50].

#### 2.3.2.4 Metal Injection Moulding

Another novel method was originally adopted from the plastic industry that is Metal Injection Moulding (MIM). The working principle of this method is similar to an industrial plastic injection moulding with the exception of using metal and additionally the use of a binder to hold metal particles together (See Figure 2.13). The described mixture is injected into a mould, which is then followed by a few stages of debinding, which depends on the binder [52]. Finalising sintering brings the product to its final stage. However, such sintering can only produce 95% dense body, application of HIP further increases density up to 99.5% of the theoretical density [53].

Such use of binders interested Scheithauer, Schwarzer et al. (2015), who performed work on 3D printing of a mixture of a waxy binder and a metallic powder

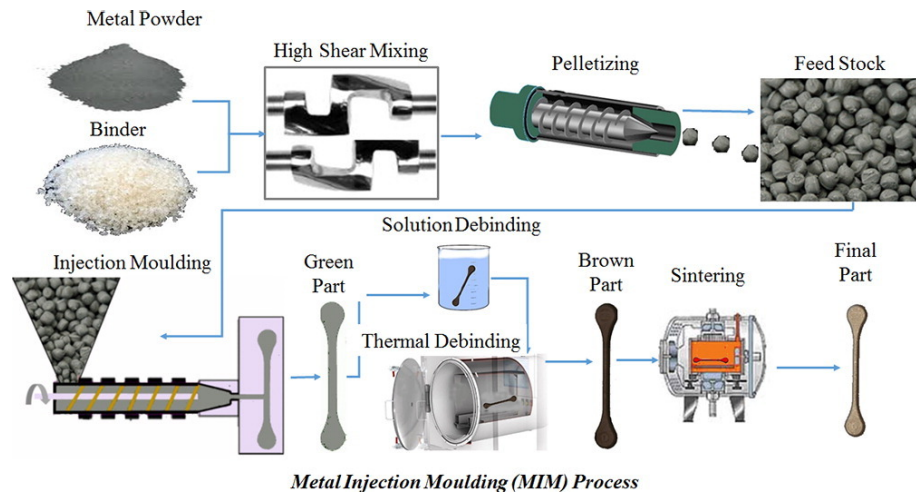


**Figure 2.13:** Schematic of the Metal Injection Moulding (MIM) process [54].

[55]. For this a heated chamber was fixed to a printing head of a 3D printer, the liquefied mixture was then pushed through the nozzle to create a quickly solidifying structure. Debinding process along with the final product's properties is similar to MIM.

### 2.3.2.5 Field Assisted Sintering Technology Forging

The final process in this category is FAST–forge. FAST is a so-called Field Assisted Sintering Technology (FAST) or Spark Plasma Sintering (SPS). As the name states it is a sintering process, the difference from the conventional sintering is the implementation of electric current that penetrates the sample, this in return results not only in lower temperature of the process but also almost 100% density [56]. Weston and Jackson (2017) developed a process that utilizes the FAST method along with forging in order to produce near-net-shaped product [57]. The results are given in the paper state that mechanical properties were similar to ones that commercial

multi-step forged materials have.

### **2.3.2.6 Binder Jetting Printing**

The binder jetting printing has a similar operation with EBM or SLM, however, instead of a laser/electron beam, a binder is deposited on the powder bed using a jet printing dispenser. This provides a high resolution of 0.2 mm, which was applied to producing titanium and other metals [58, 59]. As the product is comprised of metal particles connected with binder the consecutive sintering is required. Such manufacture technique was reported to produce samples of about 3% porosity which compared to other techniques is relatively high and require additional HIP to produce functional products [60].

The advantage of this method lies in its relatively low energy consumption as the whole process takes place in the air atmosphere. The main energy consumption within the process comes from the sintering stage.

### **2.3.3 Summation**

The above-mentioned techniques have a common problem, which is the microstructure and density. Usually small and well-distributed alpha and beta phases are desired for metal or an alloy as they yield the best physical properties. However, due to fast cooling and heating profiles presented in SLS, SLM, EBM and SMD, the growth of elongated granules is inevitable, resulting in a direction-dependent strength of a 3D printed part. This heating profile results in increased energy consumption

and prolonged process time, which creates a drawback for the discussed processes [61, 62]. Providing the ground for the ongoing studies, which are aimed to reduce this impact by adjusting process variables or using the HIP, that additionally brings the density of the final part to almost 100% [2, 44, 63].

### **2.3.4 Powder Spheradisation**

As additive manufacture is a part of powder metallurgy, the feedstock material has to be in a powdered form (true for some of the above-mentioned methods). These powders, typically, are required to have high sphericity with no voids or satellites [64]. Application of high-quality powders is especially important for SLS, EBM and MIM, as it improves the structural integrity and the feed rates during these processes [65].

#### **2.3.4.1 Direct Powder Production**

To produce spherical powder two approaches can be implemented: direct powder production or post-treatment. For direct powder production, only a few methods have been proven feasible namely Armstrong process and the FFC-Cambridge Process. With Armstrong process being designed to produce powder whereas the FFC-Cambridge Process requires an additional grinding stage [18, 66]. The indirect approach includes the utilisation of an additional process that changes the shape of the feedstock powder or pulverises a solid ingot into the powder with desired parameters.

#### 2.3.4.2 Hydride-Dehydride

One of the cheapest but low-quality powder production method utilises the embrittlement of metal hydrides [67]. In the process, called Hydride-Dehydride (HDH), titanium or titanium alloy material is transformed into a hydrate via the reaction with hydrogen (300 °C). This allows the metal to be easily shattered as it loses the initial ductility and, consequently, sieved to a required size. Afterwards, produced hydrate powders are heated up to 750 °C under vacuum that causes the decomposition to occur leaving metal in the shape of a coarse powder [68]. Such process yields in a material desirable for compaction and metal injection moulding [52, 67].

#### 2.3.4.3 Advanced Techniques

The production of spherical powder requires the melting of metal and, thus, can utilise more energy compared to HDH. There are four established methods of spherical powder production: Free Fall Gas Atomization, Electrode Induction Gas Atomization, Plasma Atomization and Plasma Rotating Electrode Process. Each of them operates at the same principle of surface area reduction (spheradisation) of molten metal droplets [65, 69–71]

The difference between those processes lies in the heating mechanism and the feedstock. The Free Fall Gas Atomization (FFGA) utilises conventional arc melting of the metal that flows through the orifice in the crucible [69]. A similar technique is used in Electrode Induction Gas Atomisation (EIGA) where rod-shaped feedstock is melted by the induction heating coil covered in ceramic coating [70]. Resulting

streams from both processes are broken up with the pressurised argon flow and are cooled during the fall. Powders created via FFGA and EIGA tend to agglomerate and have a high amount of satellites, in addition, contamination is inevitable for both of the techniques due to the contact with the crucible and the induction coil [69–71].

More advanced techniques utilise plasma as a heating source to melt titanium. For Plasma Atomisation (PA) a wire is fed into the plasma torch flame, which simultaneously melts and brakes down the molten metal stream [65]. Plasma Rotating Electrode Process (PREP) utilises a cylindrical electrode that is rotated at  $\geq 15000$  RPM and is melted from one end via the plasma torch [72]. These methods yield in the highest sphericity levels with no satellites. Besides, the material is not contaminated as it is never in touch with anything during the melting stage [66].

### **2.3.5 Summation**

Overall, the requirement for the spheradisation stage implies additional energy and material consumption onto the production of titanium components. With the numerous different methods, the quality of those parts can vary to fit the need.

## **2.4 Fabrication of Titanium Oxide Precursors**

The produced literature review brought a conclusion that the combination of the FFC-Cambridge Process with a ceramic shaping technique can yield in the direct

production of titanium components. Therefore, it is necessary to analyse the existing shaping techniques leaning towards the most practical and established ones [28].

The concept of such combination has been shown on 3 examples: near-net-shape production of Ti-6Al-4V components, production of niobium tubes and production of titanium foams [73–75]. These examples showed a small scale production with a slipcasting method as a shaping technique, which is discussed below. Particularly in-depth research of this combination was shown by Hu et al. (2013) in their work on the near-net-shape production of Ti-6Al-4V hollow golf club [73]. This work inspired the name of the method to be Near-net-shape Electrochemical Metallisation with the abbreviation of NEM. The flexibility of this naming also allows for NEM to be addressed to the numerous materials that are possible to produce via the FFC-Cambridge Process, for example, NEM of titanium, NEM of tantalum, etc.

### **2.4.1 Shaping of Ceramics**

Titanium is widely spread in the form of oxide, mostly represented by such minerals as rutile, anatase and brookite. The raw or purified oxide ( $\text{TiO}_2$ ) have similar properties with common ceramics such as aluminium oxide or zirconium oxide, which opens a wide range of applicable shaping techniques.

#### **2.4.1.1 Slip Casting**

The slip casting of ceramics is one of the most used shaping techniques applied prior to the FFC-Cambridge Process. Two studies were reported to utilise the

slip casting procedure in the plaster of Paris mould to shape a precursor with the following reduction in the molten salt. There the mixture of water and the ceramic powder was filled into a plaster mould. After solidification, prepared green ceramic parts had enough of mechanical strength to proceed without sintering or addition of binders. It started with the preparation of Zr or Zr–2.5Nb alloy tubes by Peng, Jiang et al. (2008), who successfully slip cast a tube of  $\text{ZrO}_2$  and then electrolytically reduced it in the molten salt [74]. This work was first to exploit the unique property of the FFC-Cambridge Process, which is described as the solid-state transformation or in situ metallisation. Following this, in 2013 a work was made on the production of near-net-shape titanium and titanium alloys [73]. The author investigated three shapes in particular: a cup, a hollow sphere and a driver golf club. All of them were successfully prepared by the slip casting method from a mixture of oxides and fully reduced to a Ti–6Al–4V alloy. No binders and sintering were used, making such process more cost-effective and environmentally friendly than any metal AM method.

As shapes become more complex the required methods also need to be advanced. This lead to an improved slip casting technique, a so-called gel casting method, that was applied to produce titanium sponge [75]. This technique required the use of toxic organic polymers to solidify a precursor, which brings potential risk to the production process. During the manufacturing, created polymers are burned out in a sintering stage and the 81% porosity can be achieved. Compared to a commercially produced sponge scaffolds, the properties of a product have met the requirements

for a medical titanium scaffold.

Overall, this technique is considered as the best choice for mass production of small precursors such as tooth implants, jewellery, etc.

#### 2.4.1.2 Direct Ink Writing

Given the properties of  $\text{TiO}_2$  to be similar to one of a ceramics, numerous manufacturing routes of ceramics can be applied to shape the precursor. One of the most affordable but the less precise method is an extrusion-based process called Direct Ink Writing (DIW) [76]. It was adopted from the common Fused Deposition Modelling (FDM) of plastic, where a plastic wire (filament) is fed into a heated extruder (printing head). This extruder is controlled by a computer to produce a pattern following a CAD-based route. For ceramics, however, the feedstock is a paste-like, water and ceramics mixture, which is extruded through the nozzle in the same manner as FDM operates (see Figure 2.14). As it was mentioned, such method has a low resolution and a final part has a highly distinguished layered surface. One of the strongest sides of DIW is the production of a hollow confined object as it does not rely on a powdered bed or a bath of polymer that will be discussed later [77, 78].

The similar concept was utilised by the previously mentioned process where along with the metal particles ceramics was introduced into the mixture of a waxy binder, which was melted and extruded (see Figure 2.14). After burning a binder out a ceramic body remained its initial structure [55].

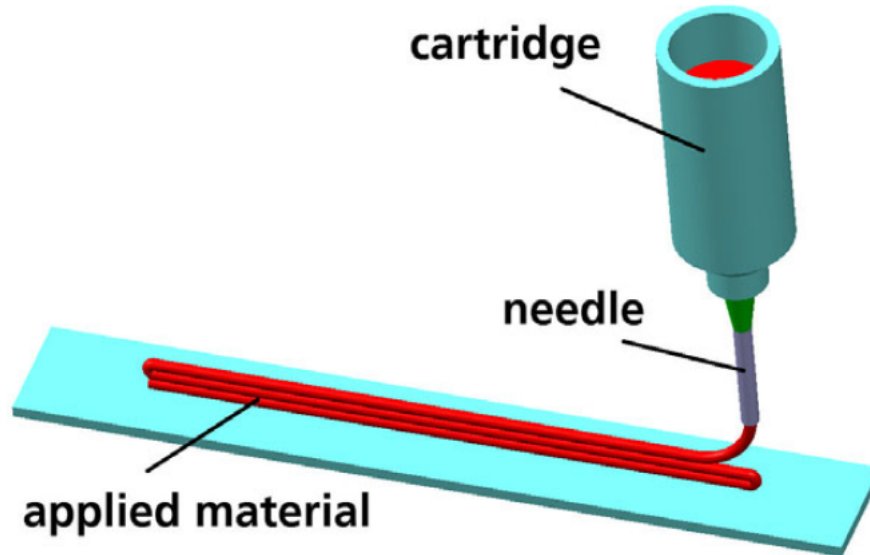


**Figure 2.14:** Schematic of the Direct Ink Writing of ceramics and waxy mixture extrusion [55].

Overall, this method showed to be a reliable and flexible candidate for rapid prototyping of titania pastes, with a major advantage of the creation of hollow objects. However, the utilised ink is required to be specifically tailored in order to be successfully extruded. This is done via the addition of different binders, surfactants, etc., which has the potential of damaging the purity of the final product.

### 2.4.1.3 Indirect Methods

For highly complex shapes, however, slip casting can be enhanced by implementing the use of 3D printers for the production of a mould (See Figure 2.15) [79]. This way the mould has a higher definition of smaller details, the imprint of an object is not required and, therefore, the mould is not damaged during the retraction of

the imprinted object. Another advantage of such a method is an ability to produce porous object via modelling porous structure within the mould. However, after the solidification of a final product, the mould has to be destroyed to retract a product, which implies constant production of such moulds.

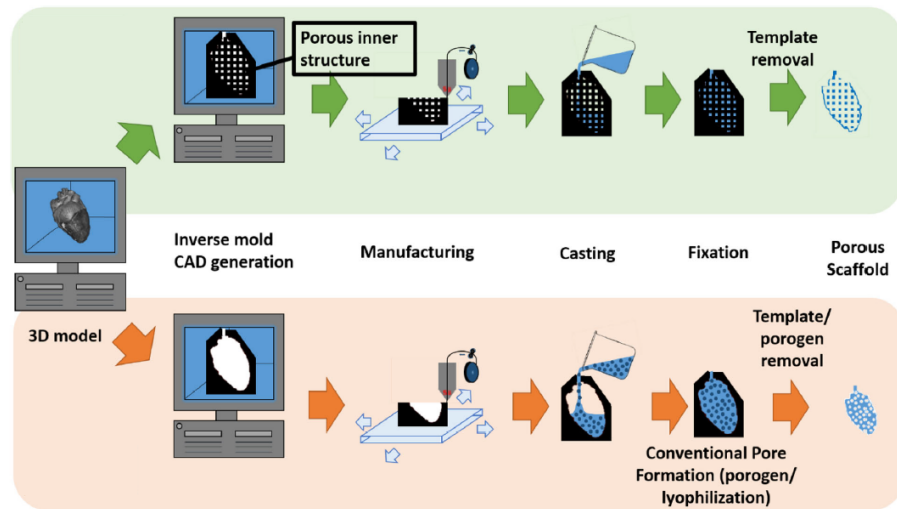


**Figure 2.15:** Production of porous moulds via 3D printing for slip casting of ceramics [79].

This is the latest method that has been applied in conjunction with the FFC-Cambridge Process to produce tantalum scaffold [80]. As the range of mould printing techniques is also wide the complexity and availability of that technique can vary from low to high, accordingly.

#### 2.4.1.4 Selective Laser Sintering

More modern techniques have been developed for the direct rapid manufacturing of ceramic objects, one of them is similar to a metal manufacturing method - SLS.

This technique was reported to work on titania resulting in the small study of the utilisation of the low power laser (10 W) at different scan speed, successfully producing sintered titania powder of different dimensions into 2D layers [81]. There were no further updates on the project, however, SLS was successfully used on all the other commercial ceramic materials [82].

Nevertheless, the SLS method applied to a slurry, rather than powder, found high success within the ceramic enthusiasts. So-called LSD method or Layer-wise slurry deposition is the technique that utilizes deposition of a slurry into thin layers. Combined with SLS, this method allows for the high definition rapid prototyping method for ceramics. Xiaoyong, Dichen et al. (2012) performed a study where the 87 wt% loaded slurry of the binder-free water-based mixture was used to evaluate the reliability of the process and compare properties of the manufactured samples with the products of conventional firing production methods [83]. However, the speed of such a process did not satisfy modern world requirements, as each consecutive layer had to be set to dry for 2 minutes. The results also showed that the overall mechanical properties were worse than the conventionally produced material. From this, another work was proposed on the addition of an additional step to freeze the system, the laser was used to evaporate the frozen liquid and stabilize obtained structures. This method reduces the time needed to dry a layer to 1 sec, the cryogenic plate is kept under  $-50\text{ }^{\circ}\text{C}$  to freeze the slurry instead of drying it [84].

Such advanced techniques have a potential of creating an extremely fine quality object on a smaller than a millimetre scale. However, the power of the laser

is required to be high and the properties of a final product are yet to meet the requirements, making it require more development before it can be commercially applied.

#### **2.4.1.5 Stereolithography**

Originated from the resin stereolithography, this kind of ceramic 3D printing uses a bath filled with a suspension/slurry of a ceramic powder and a photosensitive resin. The building platform moves upwards as a consecutive layer has been solidified and the controlled UV light source is located under the bath. The light passes through the permeable membrane that can prevent polymerisation at some distance above it. The final product is then debinded by firing [54]. The more advanced and recent invention was made by Eckel, Zhou et al. (2015), he synthesised polymeric compound with the ceramic component incorporated into the polymeric chain [85]. This allowed the production of even better quality ceramic products that can withstand extremely high temperatures.

Such methods have been already commercialised for not only industrial applications but also for personal use. Despite the micrometre level of details, the photosensitive resin is a toxic substance that requires careful handling. The post-treatment of the product also requires the use of the alcohol-based solvents to clean the surface from any leftovers. Overall, this process can be considered as the least environmentally friendly process among the discussed methods due to the use of toxic polymers and an excessive burning process of the binding material.

#### **2.4.1.6 Binder Jetting Printing**

This is another process that applies to both metals and ceramics. As described in Section 2.3.2.6 it uses a binder to draw CAD-generated layers on a powder bed. The resulted product has to undergo a sintering stage, which, compared to metals, is done in air [86]. Important to add that this technique has a high dependence on parameters such as wettability, flowability and packing of the printed material, which results in the ongoing development and improvement of this technology, especially related to ceramic fabrication [86].

#### **2.4.2 Summation**

Every method, described above, has a potential to be used for the production of a solid precursor and then to be reduced via the FFC-Cambridge Process, however, only one method have been chosen that is commercialised and remained high affordability, and, thus, is worth to be investigated: the Direct Ink Writing. This method utilises a simple working principle that is capable of sufficing the need of producing functional products and has a high level of support for both hardware and software related obstacles.

### **2.5 Conclusion**

The produced literature review summarises the most established titanium extraction and fabrication methods, exposing their limitations. This search yielded in

the idea of utilising the solid-state transformation, unique to the FFC-Cambridge Process, along with a ceramic shaping technique. Due to the feedstock possessing similar properties with porcelain ceramics, the wide range of ceramic manufacturing techniques has been looked into. Making an accent on the safe, environmentally friendly and simple aspect of the FFC-Cambridge Process it was decided to be combined with an appropriately similar fabrication technique, which was discovered to be Direct Ink Writing. For this, a few sacrifices were made, mainly the increase in resolution.

The literature search also showed that the concept of the conjunction of ceramic shaping technique, mainly slip casting, was successfully achieved. However, the complexity and size of the previous products were relatively low, which is set to be enhanced in this project.

## References for Chapter 2

- [1] A. Pramanik, “Problems and solutions in machining of titanium alloys”, *The International Journal of Advanced Manufacturing Technology* **2014**, *70*, 919–928.
- [2] X. Pei, B. Zhang, Y. Fan, X. Zhu, Y. Sun, Q. Wang, X. Zhang, C. Zhou, “Bionic mechanical design of titanium bone tissue implants and 3D printing manufacture”, *Materials Letters* **2017**, DOI 10.1016/j.matlet.2017.04.128.
- [3] T. E. of Encyclopaedia Britannica, *Titanium*, Encyclopaedia Britannica, inc., **2018**.
- [4] H. Tang, K. Prasad, R. Sanjinès, P. E. Schmid, F. Lévy, “Electrical and optical properties of TiO<sub>2</sub>anatase thin films”, *Journal of Applied Physics* **1994**, *75*, 2042–2047.
- [5] S. Middlemas, Z. Z. Fang, P. Fan, “Life cycle assessment comparison of emerging and traditional Titanium dioxide manufacturing processes”, *Journal of Cleaner Production* **2015**, *89*, 137–147.

- [6] T. E. o. E. Britannica, “Titanium”, **2018**.
- [7] M. Donachie, *Titanium: a technical guide*, ASM International, **2000**.
- [8] *Titanium Alloys*, Titanium Information Group, **2006**.
- [9] M. A. Hunter, “Metallic Titanium”, *Journal of the American Chemical Society* **1910**, *32*, 330–336.
- [10] C. Schaschke, *A Dictionary of Chemical Engineering: Hunter process*, **2014**.
- [11] R. B. Subramanyam, “Some recent innovations in the Kroll process of titanium sponge production”, *Bulletin of Materials Science* **1993**, *16*, 433–450.
- [12] J. Emsley, *The elements / written and compiled by John Emsley*, Oxford : Clarendon Press, Oxford, **1989**.
- [13] C. Nagesh, C. Sridhar Rao, N. Ballal, P. Krishna Rao, “Mechanism of Titanium Sponge Formation in the Kroll Reduction Reactor”, *Metallurgical and Materials Transactions B* **2004**, *35*, 65–74.
- [14] D. v. Vuuren, “A critical evaluation of processes to produce primary titanium”, *The Journal of The Southern African Institute of Mining and Metallurgy* **2009**, *109*, 455.
- [15] J. Andrade Gamboa, A. E. Bohé, D. M. Pasquevich, “Carbochlorination of TiO<sub>2</sub>”, *Thermochimica Acta* **1999**, *334*, 131–139.
- [16] M. Jackson, K. Dring, “A review of advances in processing and metallurgy of titanium alloys”, *Materials Science and Technology* **2006**, *22*, 881–887.

- [17] D. J. Fray, “Novel methods for the production of titanium”, *International Materials Reviews* **2008**, *53*, 317–325.
- [18] E. Technologies, Summary of Emerging Titanium Cost Reduction Technologies, Report, **2004**.
- [19] G. Crowley, “How to Extract Low-Cost Titanium”, *Advanced Materials & Processes* **2003**, 25–27.
- [20] K. Araci, D. Mangabhai, K. Akhtar, *Titanium Powder Metallurgy: Science, Technology and Applications*, Elsevier, Butterworth-Heinemann, **2015**.
- [21] T. H. Okabe, T. Oda, Y. Mitsuda, “Titanium powder production by preform reduction process (PRP)”, *Journal of Alloys and Compounds* **2004**, *364*, 156–163.
- [22] G. Z. Chen, D. J. Fray, T. W. Farthing, “Direct electrochemical reduction of titanium dioxide to titanium in molten calcium chloride”, *Nature* **2000**, *407*, 361–364.
- [23] D. Hu, G. Z. Chen in *Springer Handbook of Electrochemical Energy*, (Eds.: C. Breitkopf, K. Swider-Lyons), Springer Berlin Heidelberg, Berlin, Heidelberg, **2017**, pp. 801–834.
- [24] A. J. Fenn, G. Cooley, D. Fray, L. Smith, “Exploiting the FFC Cambridge Process”, *Advanced Materials & Processes* **2004**, 162.

- [25] C. Wu, M. Tan, G. Ye, D. J. Fray, X. Jin, “High-Efficiency Preparation of Titanium through Electrolysis of Carbo-Sulfurized Titanium Dioxide”, *ACS Sustainable Chemistry & Engineering* **2019**, *7*, 8340–8346.
- [26] M. Hu, Q. Zhengfeng, B. Chenguang, D. Hu, G. Z. Chen, “Effect of the Changed Electrolytic Cell on the Current Efficiency in FFC Cambridge Process”, *Materials Transactions* **2017**, *58*, 322–325.
- [27] C. Schwandt, D. T. L. Alexander, D. J. Fray, “The electro-deoxidation of porous titanium dioxide precursors in molten calcium chloride under cathodic potential control”, *Electrochimica Acta* **2009**, *54*, 3819–3829.
- [28] D. Hu, A. Dolganov, M. Ma, B. Bhattacharya, M. T. Bishop, G. Z. Chen, “Development of the Fray-Farthing-Chen Cambridge Process: Towards the Sustainable Production of Titanium and Its Alloys”, *JOM* **2018**, *70*, 129–137.
- [29] R. Suzuki, K. Ono, K. Teranuma, “Calciothermic reduction of titanium oxide and in-situ electrolysis in molten CaCl<sub>2</sub>”, *Metallurgical and Materials Transactions B* **2003**, *34*, 287–295.
- [30] R. Suzuki, “Direct reduction processes for titanium oxide in molten salt”, *JOM Journal of the Minerals Metals and Materials Society* **2007**, *59*, 68–71.
- [31] K. Lange, *Handbook of Metal Forming*, Society of Manufacturing Engineers, **1995**.
- [32] T. Childs, *Metal Machining: Theory and Applications*, Elsevier Science, **2013**.

- [33] M. Khan, A. Sheikh, B. Al-Shaer, *Evolution of Metal Casting Technologies: A Historical Perspective*, Springer International Publishing, **2016**.
- [34] “SHEET-METAL FORMING”, *Mechanica Technical Solutions* **2014**.
- [35] T. Fuxing, L. Mingzhe, C. Zhongyi, L. Xiangji, “Formability analysis on the process of multi-point forming for titanium alloy retiary sheet”, *The International Journal of Advanced Manufacturing Technology* **2009**, *41*, 1059–1065.
- [36] R. Saha, K. Jacob, “Casting of titanium and its alloys”, *Defence Science Journal* **1986**, *36*, 121–141.
- [37] R. C. S. Rodrigues, A. C. L. Faria, I. A. Orsi, M. d. G. C. d. Mattos, A. P. Macedo, R. F. Ribeiro, “Comparative study of two commercially pure titanium casting methods”, *Journal of applied oral science : revista FOB* **2010**, *18*, S1678-77572010000500010[PII], 487–492.
- [38] M. Darsin, H. A. Basuki, “Development Machining of Titanium Alloys: A Review”, *Applied Mechanics and Materials* **2014**, *493*, 492–500.
- [39] A. R. Machado, J. Wallbank, “Machining of Titanium and its Alloys-a Review”, *Proceedings of the Institution of Mechanical Engineers Part B: Journal of Engineering Manufacture* **1990**, *204*, 53–60.
- [40] B. Erhard, L. Christoph, P. Frank, “Mechanical Properties of Additive Manufactured Ti-6Al-4V Using Wire and Powder Based Processes”, *IOP Conference Series: Materials Science and Engineering* **2011**, *26*, 012004.

- [41] T. Machry, D. Eatock, J. Meyer, A. Antonysamy, A. Ho, P. Prangnell, “Effect of microstructure on the tensile strength of Ti6Al4V specimens manufactured using additive manufacturing electron beam process”, *Powder Metallurgy* **2016**, *59*, 41–50.
- [42] M. K. Thompson, G. Moroni, T. Vaneker, G. Fadel, R. I. Campbell, I. Gibson, A. Bernard, J. Schulz, P. Graf, B. Ahuja, F. Martina, “Design for Additive Manufacturing: Trends, opportunities, considerations, and constraints”, *CIRP Annals - Manufacturing Technology* **2016**, *65*, 737–760.
- [43] J.-Y. Lee, J. An, C. K. Chua, “Fundamentals and applications of 3D printing for novel materials”, *Applied Materials Today* **2017**, *7*, 120–133.
- [44] H. Attar, M. Calin, L. C. Zhang, S. Scudino, J. Eckert, “Manufacture by selective laser melting and mechanical behavior of commercially pure titanium”, *Materials Science and Engineering: A* **2014**, *593*, 170–177.
- [45] K. Yamanaka, W. Saito, M. Mori, H. Matsumoto, A. Chiba, “Preparation of weak-textured commercially pure titanium by electron beam melting”, *Additive Manufacturing* **2015**, *8*, 105–109.
- [46] D. Herzog, V. Seyda, E. Wycisk, C. Emmelmann, “Additive manufacturing of metals”, *Acta Materialia* **2016**, *117*, 371–392.
- [47] N. Guo, M. C. Leu, “Effect of different graphite materials on the electrical conductivity and flexural strength of bipolar plates fabricated using selective

- laser sintering”, *International Journal of Hydrogen Energy* **2012**, *37*, 3558–3566.
- [48] B. Baufeld, O. V. d. Biest, R. Gault, “Additive manufacturing of Ti-6Al-4V components by shaped metal deposition: Microstructure and mechanical properties”, *Materials & Design* **2010**, *31*, *Supplement 1*, S106–S111.
- [49] M. Kottman, S. Zhang, J. McGuffin-Cawley, P. Denney, B. K. Narayanan, “Laser Hot Wire Process: A Novel Process for Near-Net Shape Fabrication for High-Throughput Applications”, *JOM* **2015**, *67*, 622–628.
- [50] C. Broeckmann, “Hot isostatic pressing of near net shape components - process fundamentals and future challenges”, *Powder Metallurgy* **2012**, *55*, 176–179.
- [51] K. Zhang, J. Mei, N. Wain, X. Wu, “Effect of Hot-Isostatic-Pressing Parameters on the Microstructure and Properties of Powder Ti-6Al-4V Hot-Isostatically-Pressed Samples”, *Metallurgical and Materials Transactions A* **2010**, *41*, 1033–1045.
- [52] A. Dehghan-Manshadi, M. J. Bermingham, M. S. Dargusch, D. H. StJohn, M. Qian, “Metal injection moulding of titanium and titanium alloys: Challenges and recent development”, *Powder Technology* **2017**, *319*, 289–301.
- [53] R. M. German, “Progress in Titanium Metal Powder Injection Molding”, *Materials (1996-1944)* **2013**, *6*, 3641–3662.

- [54] M. Dehurtevent, L. Robberecht, J.-C. Hornez, A. Thuault, E. Deveaux, P. Béhin, “Stereolithography: A new method for processing dental ceramics by additive computer-aided manufacturing”, *Dental Materials* **2017**, *33*, 477–485.
- [55] U. Scheithauer, E. Schwarzer, H.-J. Richter, T. Moritz, “Thermoplastic 3D Printing—An Additive Manufacturing Method for Producing Dense Ceramics”, *International Journal of Applied Ceramic Technology* **2015**, *12*, 26–31.
- [56] O. Guillon, J. Gonzalez-Julian, B. Dargatz, T. Kessel, G. Schierning, J. Räthel, M. Herrmann, “Field-Assisted Sintering Technology/Spark Plasma Sintering: Mechanisms, Materials, and Technology Developments”, *Advanced Engineering Materials* **2014**, *16*, 830–849.
- [57] N. S. Weston, M. Jackson, “FAST-forge - A new cost-effective hybrid processing route for consolidating titanium powder into near net shape forged components”, *Journal of Materials Processing Technology* **2017**, *243*, 335–346.
- [58] E. Wheat, M. Vlasea, J. Hinebaugh, C. Metcalfe, “Sinter structure analysis of titanium structures fabricated via binder jetting additive manufacturing”, *Materials & Design* **2018**, *156*, 167–183.
- [59] M. T. Stawovy, K. Myers, S. Ohm, “Binder jet printing of tungsten heavy alloy”, *International Journal of Refractory Metals and Hard Materials* **2019**, *83*, 104981.

- [60] X. L. Huang, T. Bauder, T. Do, H. Suen, C. Boss, P. Kwon, J. Yeom, “A Binder Jet Printed, Stainless Steel Preconcentrator as an In-Line Injector of Volatile Organic Compounds”, *Sensors* **2019**, *19*, 15.
- [61] M. Baumers, C. Tuck, R. Hague, I. Ashcroft, R. Wildman, “A Comparative Study of Metallic Additive Manufacturing Power Consumption”, *Solid Freeform Fabrication Proceedings* **2010**, 278–288.
- [62] L. E. Murr, S. M. Gaytan, A. Ceylan, E. Martinez, J. L. Martinez, D. H. Hernandez, B. I. Machado, D. A. Ramirez, F. Medina, S. Collins, R. B. Wicker, “Characterization of titanium aluminide alloy components fabricated by additive manufacturing using electron beam melting”, *Acta Materialia* **2010**, *58*, 1887–1894.
- [63] P. A. Kobryn, S. L. Semiatin, “The laser additive manufacture of Ti-6Al-4V”, *JOM* **2001**, *53*, 40–42.
- [64] P. Nandwana, M. M. Kirka, V. C. Paquit, S. Yoder, R. R. Dehoff, “Correlations Between Powder Feedstock Quality, In Situ Porosity Detection, and Fatigue Behavior of Ti-6Al-4V Fabricated by Powder Bed Electron Beam Melting: A Step Towards Qualification”, *JOM* **2018**, *70*, 1686–1691.
- [65] G. Chen, S. Y. Zhao, P. Tan, J. Wang, C. S. Xiang, H. P. Tang, “A comparative study of Ti-6Al-4V powders for additive manufacturing by gas atomization, plasma rotating electrode process and plasma atomization”, *Powder Technology* **2018**, *333*, 38–46.

- [66] C. G. McCracken, C. Motchenbacher, D. P. Barbis, “Review of Titanium-Powder-Production Methods”, *International Journal of Powder Metallurgy* **2010**, *46*, 19–26.
- [67] D. P. Barbis, R. M. Gasior, G. P. Walker, J. A. Capone, T. S. Schaeffer in, Elsevier, **2015**, pp. 101–116.
- [68] M. Mitkov, D. Božić, “Hydride-dehydride conversion of solid Ti6Al4V to powder form”, **1996**, *37*, 53–60.
- [69] J. H. Moll, “Utilization of gas-atomized titanium and titanium-aluminide powder”, *JOM* **2000**, *52*, 32–34.
- [70] K. K. Guo, C. S. Liu, H. H. Dong, S. Y. Chen, “Effect of Extension Length of Catheter on Properties of TC4 Powder Prepared by Electrode Induction Melting Gas Atomization”, *Dongbei Daxue Xuebao/Journal of Northeastern University* **2018**, *39*, 797–802.
- [71] M. Smagorinski, G. Tsantrizos, “Proceedings of the 2002 World Congress on Powder Metallurgy & Particulate Materials”, **1989**.
- [72] P. Sun, Z. Z. Fang, Y. Zhang, Y. Xia, “Review of the Methods for Production of Spherical Ti and Ti Alloy Powder”, *JOM* **2017**, *69*, 1853–1860.
- [73] D. Hu, W. Xiao, G. Chen, “Near-Net-Shape Production of Hollow Titanium Alloy Components via Electrochemical Reduction of Metal Oxide Precursors in Molten Salts”, *Metallurgical and Materials Transactions B* **2013**, *44*, 272–282.

- [74] J. Peng, K. Jiang, W. Xiao, D. Wang, X. Jin, G. Z. Chen, “Electrochemical Conversion of Oxide Precursors to Consolidated Zr and Zr-2.5Nb Tubes”, *Chemistry of Materials* **2008**, *20*, 7274–7280.
- [75] R. Singh, P. D. Lee, J. R. Jones, G. Poologasundarampillai, T. Post, T. C. Lindley, R. J. Dashwood, “Hierarchically structured titanium foams for tissue scaffold applications”, *Acta Biomaterialia* **2010**, *6*, 4596–4604.
- [76] E. Peng, D. Zhang, J. Ding, “Ceramic Robocasting: Recent Achievements, Potential, and Future Developments”, *Advanced Materials* **2018**, *30*, 1802404.
- [77] T. Chen, A. Sun, C. Chu, H. Wu, J. Wang, J. Wang, Z. Li, J. Guo, G. Xu, “Rheological behavior of titania ink and mechanical properties of titania ceramic structures by 3D direct ink writing using high solid loading titania ceramic ink”, *Journal of Alloys and Compounds* **2019**, *783*, 321–328.
- [78] S. Tang, Z. Fan, H. Zhao, L. Yang, F. Liu, X. Liu, “Layered extrusion forming—a simple and green method for additive manufacturing ceramic core”, *The International Journal of Advanced Manufacturing Technology* **2018**, *96*, 3809–3819.
- [79] A. Houben, J. Van Hoorick, J. Van Erps, H. Thienpont, S. Van Vlierberghe, P. Dubruel, “Indirect Rapid Prototyping: Opening Up Unprecedented Opportunities in Scaffold Design and Applications”, *Annals of Biomedical Engineering* **2017**, *45*, 58–83.

- [80] G. Zhao, S. Li, X. Chen, X. Qu, R. Chen, Y. Wu, Y. Liu, X. Zou, X. Lu, “Porous tantalum scaffold fabricated by gel casting based on 3D printing and electrolysis”, *Materials Letters* **2019**, *239*, 5–8.
- [81] D. Macri, D. Sofia, D. Barletta, Massimo Poletto, P. Lettieri, “Selective Laser Sintering of Titania Powder: Experiments and Modelling”, **2017**.
- [82] D. Bourell, H. Marcus, J. Barlow, J. Beaman, “Selective laser sintering of metals and ceramics”, *International Journal of Powder Metallurgy (Princeton New Jersey)* **1992**, *28*, 369–381.
- [83] T. Xiaoyong, L. Dichen, G. H. Juergen, “Rapid prototyping of porcelain products by layer-wise slurry deposition (LSD) and direct laser sintering”, *Rapid Prototyping Journal* **2012**, *18*, 362–373.
- [84] G. Zhang, H. Chen, H. Zhou, “Additive manufacturing of green ceramic by selective laser gasifying of frozen slurry”, *Journal of the European Ceramic Society* **2017**, *37*, 2679–2684.
- [85] Z. C. Eckel, C. Zhou, J. H. Martin, A. J. Jacobsen, W. B. Carter, T. A. Schaedler, “Additive manufacturing of polymer-derived ceramics”, *Science* **2015**, *351*, 58.
- [86] X. Lv, F. Ye, L. Cheng, S. Fan, Y. Liu, “Binder jetting of ceramics: Powders, binders, printing parameters, equipment, and post-treatment”, *Ceramics International* **2019**, *45*, 12609–12624.

# Chapter 3

## Equipment and Methods

*This chapter overviews the main principles behind the tests and experiments utilised in the study.*

### 3.1 Manufacturing Routes

This project is built around the premise of an advanced application of the molten salt electrolysis into additive manufacturing, which can be achieved by utilising any ceramic deposition or fabrication techniques with the consecutive reduction into molten salt.

#### 3.1.1 Direct Ink Writing

The Direct Ink Writing (DIW) process was considered the most suitable ceramic 3D printing for its simple nature and low cost. The whole process is divided into

three stages: ink preparation, manufacturing and drying. These three stages were evaluated to have the highest impact on the final quality of a product and undergone modifications that are going to be discussed in the following chapters.

#### **3.1.1.1 Ink Preparation**

The DIW process starts with the ink preparation, which was done using a mortar and pestle. This technique is widely used to prepare stable slurries or pastes of ceramics on a small scale, additionally, the utilisation of a mixer was reported to have similar success [1–3].

The ingredients were carefully weighted to match the desired composition. Then all of the components were transferred into a mortar with thorough mixing of ceramic powders into a liquid via the pestle. The highest attention was given to the breaking of any agglomerates that were being produced during the initial mixing stages. Overall, this process took about 15-30 minutes to homogenise the resulting paste.

#### **3.1.1.2 3D Printing**

The second stage of the DIW process is the 3D printing of the prepared paste, which is done by utilising principles of the conventional Fused Deposition Modelling (FDM) 3D printing. This technique is considered the cheapest on the market, due to its simplicity. The main components of any FDM based 3D printing machine are a frame, a motherboard and software.

**Frame**

The frame consists of multiple stepper motors that are dedicated to move the printing head to the X and Y axis and to lift and lower the printing bed. The printing head is moving along the X and Y rails that have to be lubricated, which is done to prevent the most common quality problems such as jerking, rippling, etc. Every motor is allocated to a sensor that is used to indicate the beginning of any axis or in other words to determine the origin of the printing space.

Along with the mechanical parts, there are a motherboard and a power supply.

**Motherboard**

The used 3D printer utilises the ChiTu FDM motherboard V3.9. This motherboard has several connections as shown in Figure 3.1 in addition to the expansion slot that allows installing a second printing head (indicated by green arrows). Namely, the X, Y and Z axis are used to drive stepper motors to move along those axes with E1 and E2 axis being dedicated for the extrusion on the printing heads one and two, respectively. Additionally, the X, Y and Z axis have a connection for min and max that are used to link a sensor that would stop a stepper motor upon being triggered. Only the min sensors are compulsory for the printer to operate. The hot end is referred to as a printing head one and two with all the necessary safety and quality equipment such as a cooling fan, a thermistor and a thermocouple. If any of the hot ends are connected it has to be linked to a thermistor and a cooling fan, the exception is given to a thermocouple as thermistor may possess a similar function.

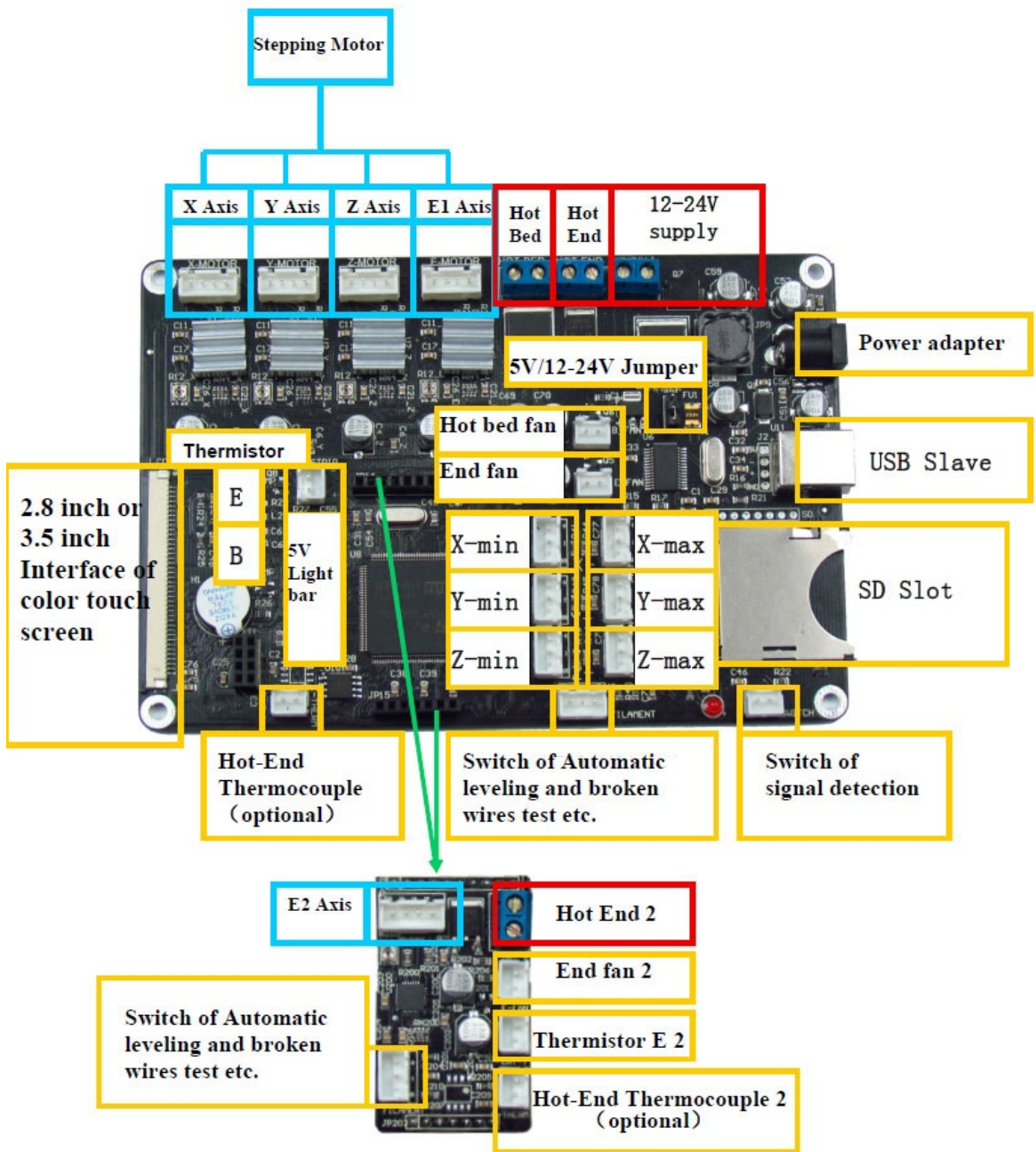


Figure 3.1: ChiTu V 3.9 FDM 3D Printer motherboard.

It is important to note that the printing bed also can be heated up and, thus, it has a similar set of connections as the printing head. Along with this, there is a slot for an SD card, a USB bridge, a power adapter and a power supply connector with an

option to connect a 12-25V or a 5V (connected via the power adapter input) power supplies with the respective jumper to swap between the two.

This motherboard includes the ARM chipset (STM32F103ZET6) that allocates this motherboard to Arduino-based systems meaning the applicability of the higher throughput software firmware.

This information is essential in order to make any kind of modifications to the motherboard such as software or hardware-based for improvement of printing capabilities of the printer.

## Software

A 3D printing process relies on 3 software: a 3D modelling software, a slicing software and a firmware. For this project three modelling software were used:

1. **AutoCAD**

AutoCAD is a 2D/3D drawing software that is produced by Autodesk. It is usually used for a highly precise design with predetermined dimensions. This software produces 3D models in a wide array of formats, which provides great compatibility with other modelling applications.

2. **Blender**

Blender is an open-source software developed by Blender Foundation. It has an intuitive User Interface (UI) , which makes it a solid choice for any non-commercial use. The strongest side of this software is the so-called “freehand” drawing and a rich set of in-build model fixing tools. In this project, it was

used to clean up and modify designs of produced objects.

### 3. Paint 3D

This software is produced by Microsoft and is pre-installed on the recent versions of Windows. It is mainly used for quick fixes of models starting from simplification and finishing at the addition of basic shapes such as boxes, spheres and cylinders.

After a 3D object was created it was saved into the SLT format and was imported into a slicing tool, mainly Cura 3.6.0. Slicing software transforms a 3D model into a so-called g-code that contains a set of commands that will be understood by the 3D printer. This slicing of a 3D model follows several parameters that were required to be tested in order to find the optimal set-up. The list of parameters includes but is not limited by a layer height, a line width, an infill amount, a support generation, a speed of different movements, etc.

The generated g-code has a set of action commands formatted in a line by line style, which means that it is read in an obvious order that allows for simple code analysis. Each line tells the position of a printing head via the X, Y and Z commands and the unique commands such as turn on or off a cooling fan (M106 and M107), pause (P) and so on.

This g-code was then uploaded to an SD card and inserted into the 3D printer. The core software that was connecting g-code commands and electrical signals from the motherboard is called firmware. There are many available firmware on the

market but in general, they have a similar structure. The ChiTu motherboard, in this case, was operating on the Marlin firmware that was pre-installed and modified by the manufacturer.

### DIW

The printing starts when an SD card with a g-code is inserted into the printer and the desired file is selected to print. As was stated before, due to the FDM's accessibility and simplicity it was adopted to print paste-like materials by implementing a feed cylinder instead of the hot end printing head. The material is extruded from the cylinder employing a pneumatic piston or compressed air. In the used set up the conventional air compressor was connected to the feed cylinder. The pressure was controlled via a manual valve (MV) located on a pressure gauge (PG) as seen in Figure 3.2.

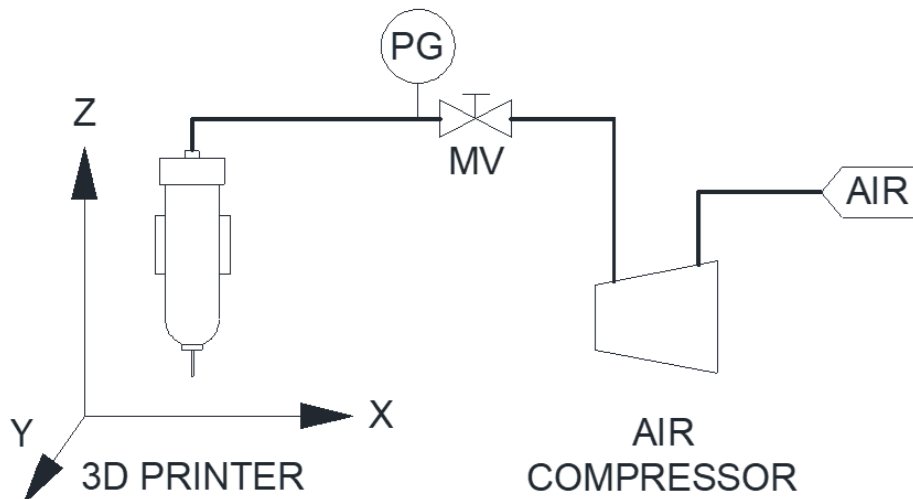


**Figure 3.2:** Schematic of the DIW 3D printer.

### 3.1.1.3 Drying

After an object was printed it was dried in an ambient environment overnight and then it was further dried in the drying oven at 60 °C for 10 hours. This was done to ensure a moisture-free product, which is essential for the molten salt reduction stage.

## 3.1.2 The Electrochemical Reduction Process

The molten salt reduction or so-called the FFC-Cambridge Process is conducted according to the procedure established in 2000 by G.Z. Chen et al. [4]. According to that procedure,  $\text{CaCl}_2$  is used as an electrolyte and carbon rod of HK-3 grade is used as an anode. The cell is closed when the cathodic assembly of a porous metal oxide is placed in the salt. This process is subdivided into three stages:

1. Preparation
2. Electrolysis
3. Post-metallisation treatment

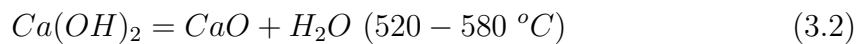
### 3.1.2.1 Preparation

Even though the FFC-Cambridge Process is, seemingly, a simple process in order to conduct it, numerous details have to be taken into consideration. Such details include electrolyte conditions, crucibles, cathodic and anodic assemblies and retort

sealing. The smallest divination form which can inevitably lead to an unsuccessful result.

### Electrolyte

This experiment utilises molten  $\text{CaCl}_2$  as an electrolyte. Before melting, however, it is important to thoroughly dry the salt, because due to the hygroscopic nature it tends to absorb moisture from the air. At high temperatures absorbed moisture leads to undesired formation of  $\text{CaO}$  following reactions 3.1 and 3.2. Even though  $\text{CaO}$  plays an important role in the reduction process by stabilising  $\text{O}^-$  concentration during the initial stage of the reaction, high amounts of  $\text{CaO}$  slow down the transport of oxygen ions, thus, slowing down or stopping the reduction [5]. Additionally,  $\text{HCl}$ , produced during such decomposition, at  $900\text{ }^\circ\text{C}$  imminently attacks any material that is exposed to it. Such active acid tends to attack one of the electrodes resulting in the formation of a huge amount of floating carbon, which becomes one of the reasons of short-circuiting of a current or an increased IR drop [6]. Both of which will prevent a sufficient current from reaching one of the electrodes submerged in the salt and, thus, leaving ceramic oxide unreduced.



For this experiment anhydrous  $\text{CaCl}_2$  was used and dried in a vacuum at  $180\text{ }^\circ\text{C}$  overnight. Prior to the experiment the salt was transferred in a  $60\text{ }^\circ\text{C}$  crucible and placed in a retort within 2 minutes to minimise the absorbed moisture content.

### Crucible selection

Selecting a crucible is the next important step as it affects the structure of a cell.

There are commonly three types of crucibles used for the molten salt reduction:

#### 1. Stainless Steel

Stainless steel (SS) crucible is used when the amount of reduced material is high. This is done due to the ability of steel to conduct current which means that the cathodic assembly becomes the whole crucible. As shown in Figure 3.3 crucible is connected to the negative terminal of a power supply, with the graphite rod to be connected to a positive terminal. This set up means that a ceramic body can be left at the bottom of the crucible. Another pro for SS crucible is that the cooling procedure at the termination stage of the experiment does not require a low cooling rate and, therefore, shortening the duration of the experiment.

However, there are several cons when using a SS crucible. First is the requirement to wash away all the salt after the experiment is done in order to get a sample out, however, this does not play a big role if the reduced object is small and can be attached on an individual SS rod. Another con is the short circuit that happens when floating carbon is being released. This can be mitigated by implementing an insulating shell around the anode usually made of aluminium oxide. Even though this shell can protect the system from the short-circuit it will slowly be reduced as a result of the contact with floating carbon that

passes current.

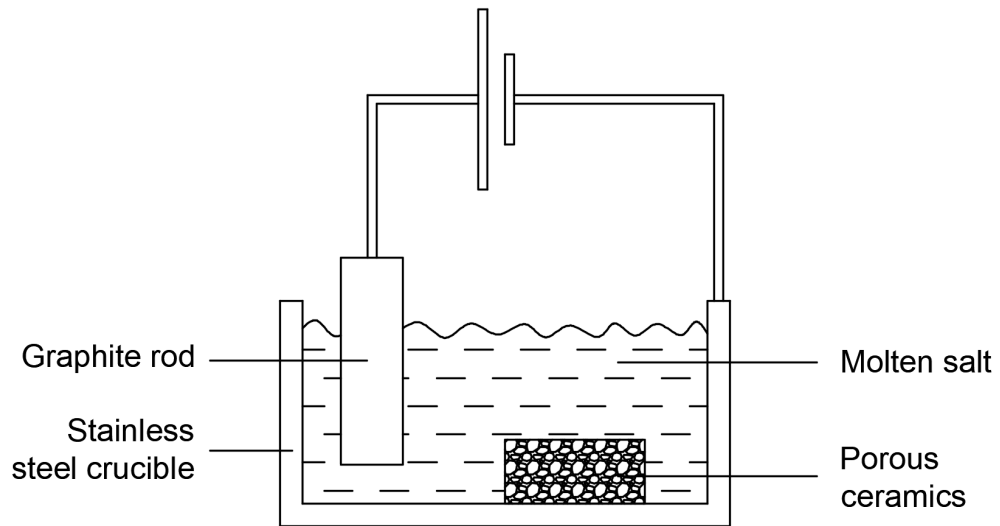


**Figure 3.3:** Cell set up for a stainless steel crucible.

## 2. Ceramic

Even though there is a huge number of inert ceramic materials the most common is aluminium oxide. These crucibles are quite brittle, thus, require special attention when being handled. Figure 3.4 shows a typical cell assembly for a ceramic crucible. The distinction of ceramic crucibles is that they do not conduct current and, therefore, both anode and cathode should be submerged separately. The cons of the aluminium oxide crucible are the requirement for a slow cooling procedure in order to minimise thermal shock-induced cracking, this will prevent the salt from seeping into the retort. A single aluminium oxide crucible can only be used for 2 batches as after the second cooling the crucible inevitably tends to crack. Another con is the fact that the wall of the crucible

can be reduced if, in contact with the cathode, this means that the positioning of cathode requires to be accurately selected. The reduced crucible wall will result in a salt leakage. Overall it is the best choice for Cyclic voltammetry (CV) tests due to a low level of introduced impurities, compared with the SS crucible.

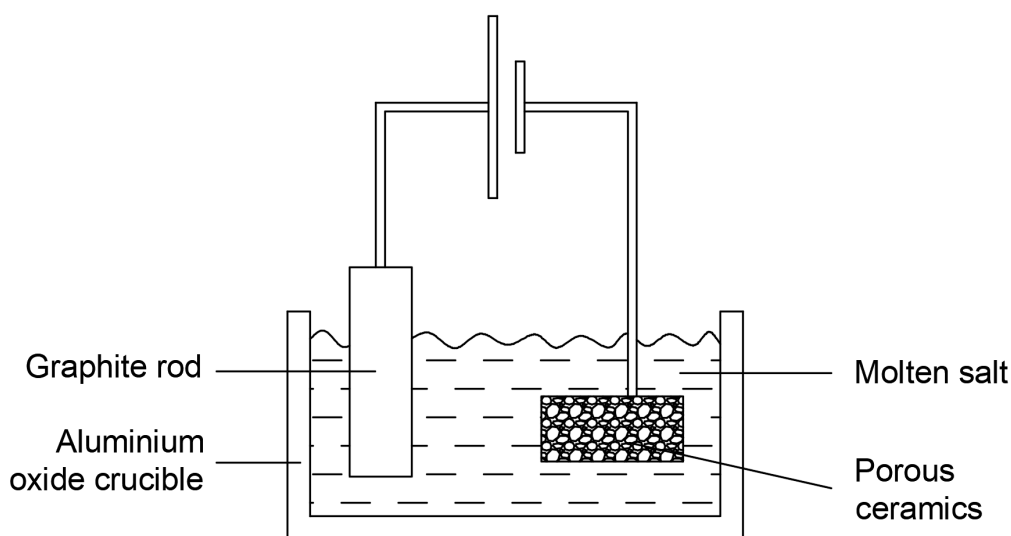


**Figure 3.4:** Cell set up for an aluminium oxide crucible.

### 3. Graphite

Graphite is another commonly used material for crucibles, which is conductive and possesses better tensile strength compared to ceramic crucibles. This crucible is an intermediate between SS and aluminium oxide as it conducts current and can be reused multiple times. However, unlike SS crucible graphite can be connected in all possible setups including those shown in Figure 3.3 and 3.4. Besides, it can also be used as an anode (Figure 3.5), in this case,

the anode has to be placed in the centre to reduce a short-circuit caused by the floating carbon. This type of crucible is extremely versatile, but its use generates a huge amount of floating carbon that not only affects the current flow but also has a tendency to be combined into a metal carbide on the surface of the cathode.

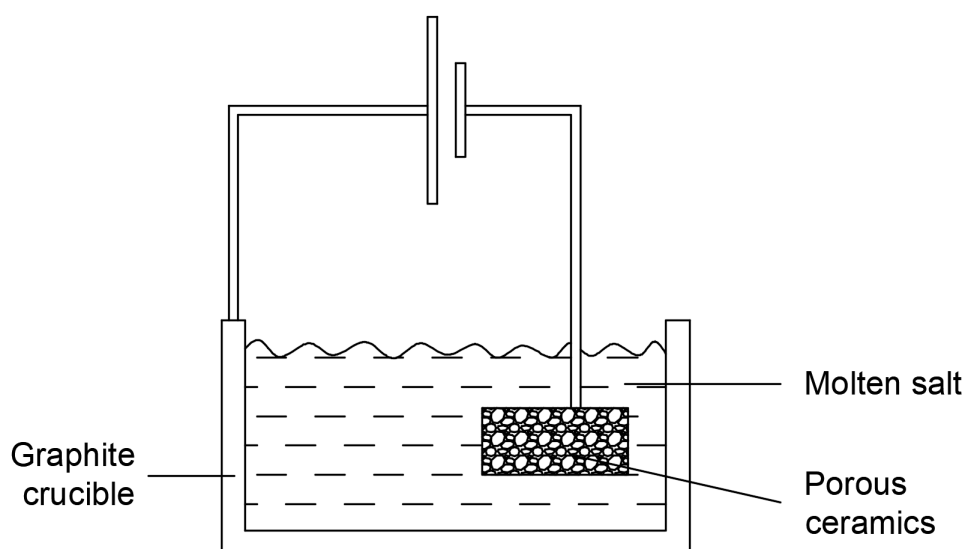


**Figure 3.5:** Cell set up for a graphite crucible.

For the conducted work all of the described setups were used. Prior to the experiment every crucible was washed and dried in the drying oven at 60 °C over 24 hours.

### Cathodic Assembly

The cathode is represented as a metal oxide in powdered or shaped forms. For this project, every cathode was based on SS rods, a molybdenum mesh and a nickel foam. After a sample was wrapped into a nickel foam it was then fixed with a SS wire to

a rod with a molybdenum mesh as a base. Nickel and molybdenum were selected for their flexible and ductile properties that would not interfere with the sample's integrity when applied. It is also important to ensure a sufficient connection between the rod and metal oxides for the completeness of the reduction.

### **Anodic Assembly**

For every test, anodic assembly consisted of a SS rod with an HK-3 grade graphite rod. Every rod was threaded and was screwed onto a threaded part on the SS rod.

### **Retort Preparation**

The molten salt experiment was conducted in a sealed retort under an inert atmosphere. Prior to the experiment it was washed and thoroughly dried at 300° for 6 hours to minimise moisture trapped in the retort. 3 hours into the drying procedure a stand and an insulating brick were placed inside for the same reason. After the retort has dried, a crucible loaded with salt was placed inside and everything was covered with a lid.

Sealing of the retort happened in 2 stages venting and purging with argon, this was repeated 3 times to ensure the oxygen-free atmosphere. During this process, the outlet was connected to a pressure gauge to prevent accidental popping out of bungs when purging with argon. Figure 3.6 shows a schematic of the experimental set up with the indicated heating elements that should be located around the crucible to avoid a non-uniform temperature profile in the crucible. Additionally, the cooling jacket should be connected to a cooling water circulator to prevent an O-ring and

bungs from burning and compromising sealing.

A sealed retort with argon flowing at 0.1 l/min is heated up with a heating rate of up to 20 °/min. Slower heating rates are favourable when the ceramic crucible is utilised. The outlet of the retort is connected to two Dreschel gas washing bottles to prevent oxygen inflow.

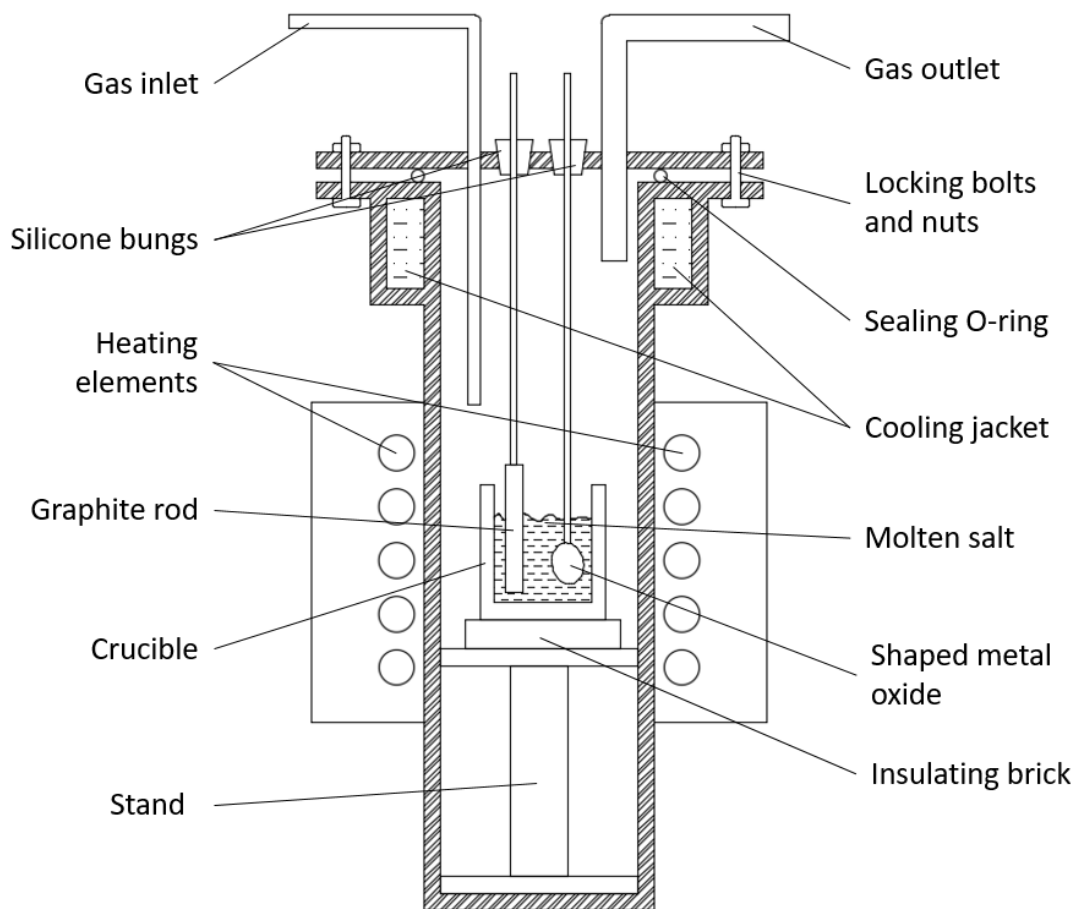


**Figure 3.6:** Experimental set up of the molten salt reduction.

### 3.1.2.2 Electrolysis

The electrolysis process started with testing the temperature of the salt to ensure sufficient heating. This was done with a long high-temperature thermocouple that was submerged in the melt until stabilised readings were observed. After that, the depth of salt was measured by a SS rod and electrodes were adjust accordingly. The anode was placed first and then cathode was slowly lowered in the retort to prevent the sample from cracking due to a possible heat shock. Both of them were connected to a power supply (Gwinstek PSW 30-36) with an applied constant voltage of 3.2 V.

The experiment was terminated upon reaching a set time. The anode was lifted to the top part of the retort to prevent oxidation of the freshly reduced metal. After it was cooled, it was then removed from the retort and washed in tap water for 10 minutes. When required, samples were washed in dilute HCl to dissolve all the impurities. Following that, the anode was removed from the retort and heating was stopped or was set to a low cooling rate to prevent the ceramic crucible from cracking. The cooled retort was opened and washed along with the crucible.

### 3.1.2.3 Post-Metallisation Treatment

After washing the sample was dried in a drying oven at 60 °C overnight. Sand-blasting was utilised as a cleaning technique with the following polishing to uncover metallic shine.

## 3.2 Analytical Techniques

The production of any material requires different levels of quality control. For this project, there were two main products ceramic objects and their metallised alternative. In order to ensure that both materials were produced to the highest standard, their feedstock and final forms were investigated qualitatively and quantitatively.

### 3.2.1 Rheological Tests

A rheological investigation was essential for this study to understand the flow behaviour of produced titanium oxide inks, which were applied into a DIW machine and were extruded through differently sized nozzles.

#### 3.2.1.1 Theory of Rheology

Rheology is a branch of physics that investigates flow behaviours of different materials mainly in liquid form. These materials are subdivided into 2 groups Newtonian and non-Newtonian. With the latter being the base of rheology as non-Newtonian liquids tend to behave in an unpredicted way. These ways are described as a Shear thickening, ideal Newtonian and shear-thinning. Due to a non-Newtonian liquid most of the time behaving in complex ways, it can include all of the three properties depending on the force applied onto a liquid. The shear thickening behaviour occurs when material changes its viscosity when an external force is being applied. The ideal Newtonian behaviour is described as an indifferent reaction to an external

force. Finally, shear-thinning is considered one of the most useful properties as it describes the ability of a material to become less viscous as force is applied. All these parameters can change with time, temperature and with the applied force.

Apart from these flow parameters, rheology investigates viscosity and different kinds or reaction forces that distinguish viscous, elastic and viscoelastic materials.

The complete investigation was built upon three tests that are commonly utilised for testing other ceramic inks and concrete mixtures [7, 8]. These methods were aimed at the investigation of relationships between shear rate against viscosity, elastic reformation and shear rate against shear stress.

1. Shear rate against viscosity.

This test is used to investigate the dependence of viscosity to a range of shear rates. Figure 3.7 demonstrates examples of common trends that can be found on the flow plot. Here a shear thickening material will result in an increased viscosity along with the increased shear rates. The shear-thinning material becomes less viscous as the force applied is increasing and a Newtonian liquid is not affected by the change in the shear rate. Overall this test is used to evaluate the type of the material and to detect any abnormality in the flow during the change of the applied force.

2. Creep and Recovery.

This test is commonly applied for cement, however, it can also provide valuable information about the investigated material's elastic reformation ability. This

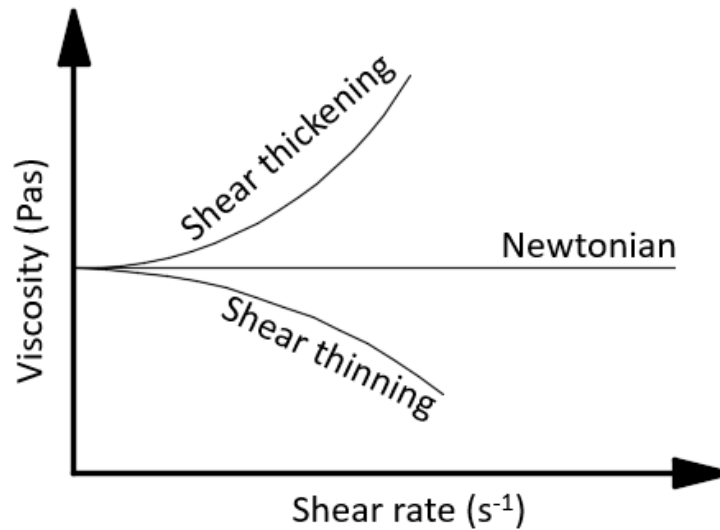


**Figure 3.7:** Typical examples of the shear rate vs viscosity plots [9].

test is conducted by applying a pulse of force for a period time during which a measurement of strain is taken resulting in a graph that is made of a creep phase where force was applied and a so-called relaxation/recovery phase where the force produced by the material is measured after the pulse has ended (Figure 3.8). In this test, viscous material would be shown a linear increase of strain in the creep phase and with no reaction in the recovery phase. This happens due to the liquid's inability to hold any shape or in other words liquid will flow under a force and remain its final position/state when the force is removed. Elastic materials, on the other hand, tend to remain its shape after a not critical amount of a force was applied, thus, the plot will show a constant strain followed by the return to the initial state in the relaxation phase. When combining both of the properties in a so-called viscoelastic material the graph

possesses both changing natures of viscous material in the creep phase and elastic reformative nature of an elastic material in the relaxation phase. As a result, the creep and relaxation graphs contain a wide range of information about elastic and viscous capabilities of the material.

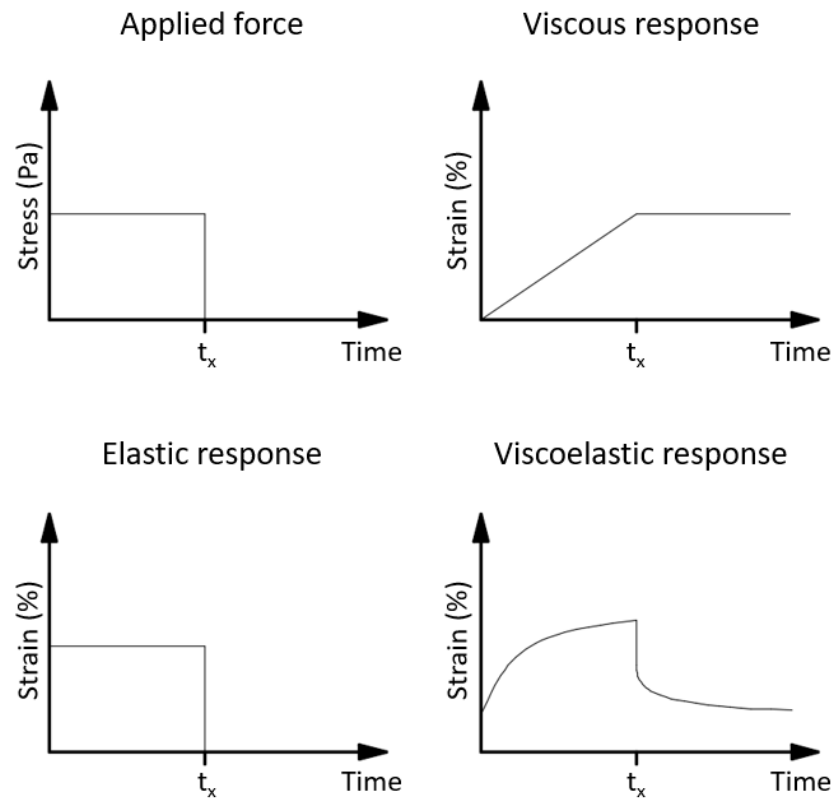


**Figure 3.8:** Typical reaction of a tested materials in the creep and recovery test. With creep phase to be before  $t_x$  and relaxation phase after  $t_x$  [9].

Figure 3.9 indicates the parameters that can be deducted from a creep and recovery graph, such as an instantaneous deformation, a primary creep, a secondary creep, an instantaneous recovery strain, a delayed elastic strain and a residual strain. There an instantaneous deformation shows the compliance

of a material to the deformation, and ideally, this value will be similar to the instantaneous recovery indicating an elastic nature of these segments. The primary creep and delayed elastic strain are related to the mix of elastic and viscous properties with the delayed elastic strain this feature will yield the different strain results when the ratio of viscous and elastic properties is changed. The secondary creep can be considered the indicator of the above-mentioned ratio because as an elastic material the gradient of the secondary creep would be closing to 0, in this case, a material would possess a solid-like elastic response. A viscous material would possess a positive gradient and would be referred to as a steady-state viscous response.

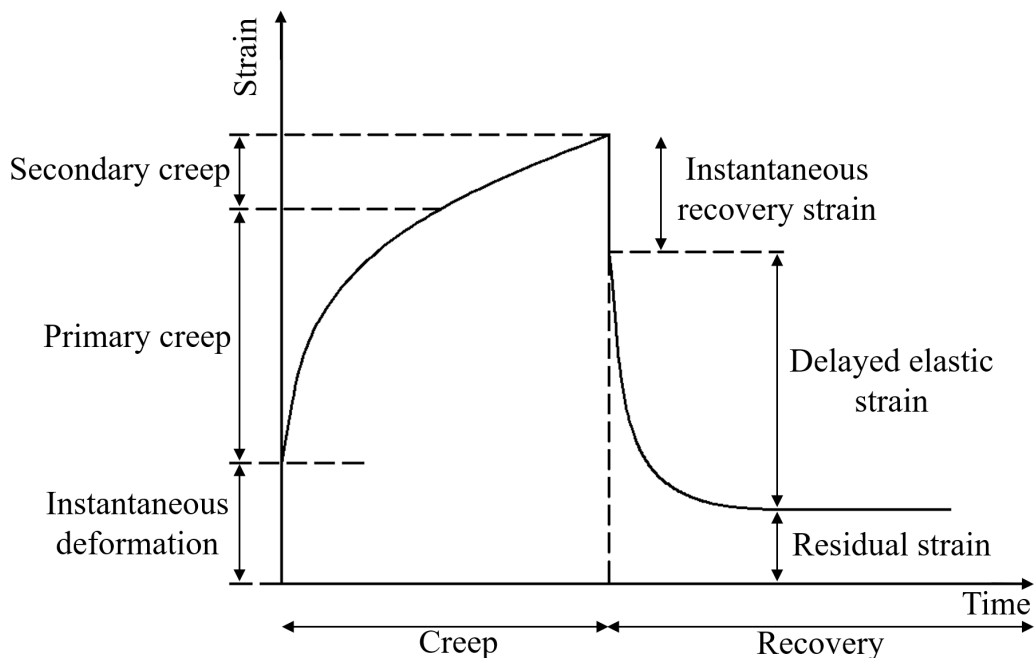


**Figure 3.9:** Main parameters found on a creep and recovery graphs [9].

### 3. Shear rate against shear stress.

This type of plots is also referred to as flow plot and describes a planar distribution of stress occurring parallel to the applied force. The change of shear stress along with the varying shear rate shows the internal struggle of material when particles start to interact with each other, thus, exerting forces on each other. Knowing the cumulative of those forces provides information about such factors as yield point, which shows the minimum force that should be applied on the material before it starts to flow, and shear thinning or thickening abilities.

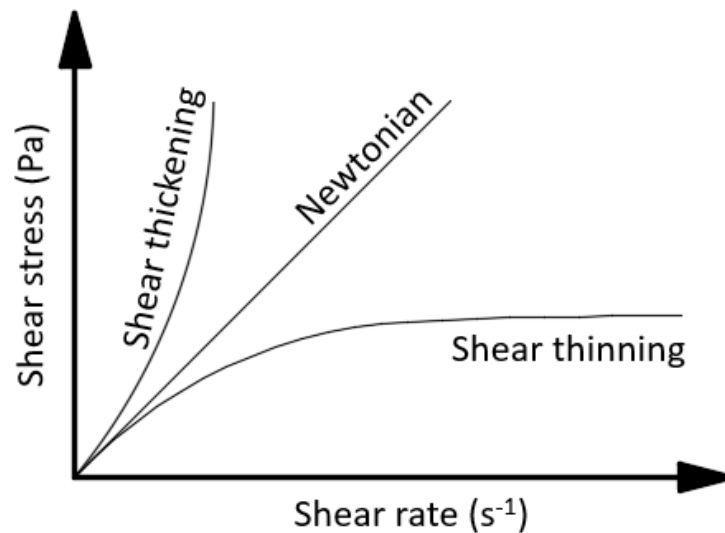


**Figure 3.10:** Typical examples of the shear rate vs shear stress plots [9].

### 3.2.1.2 Methodology of Rheological Tests.

These tests were conducted on a Kinexus rheometer KNX2100 (Malvern Panalytical Ltd) operating on a principle of a single head system. This is one of the most common systems where a motor and a sensor are made as a single unit as shown in Figure 3.11 [9]. It is also referred to as the Combined Motor Transducer (CMT) system. Apart from the motor and the sensor, there is an air bearing utilised in the device, such bearings provide 25000 better sensitivity than mechanical bearings [9]. Figure 3.11 also indicates the presence of temperature control, which is implemented in the form of a liquid bath with a stand-alone cooling reservoir and an internal heating element.

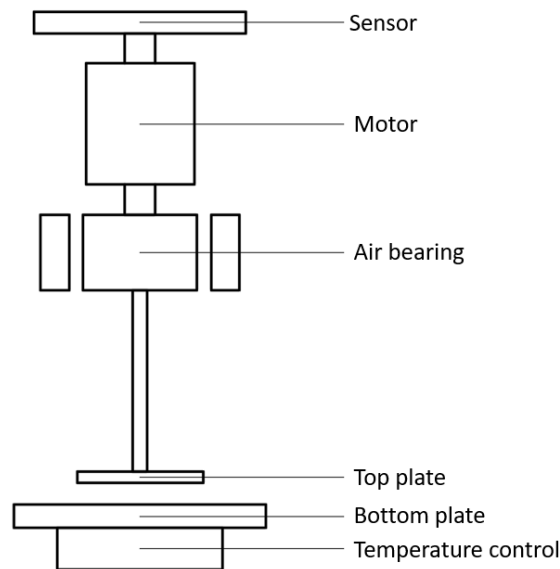


**Figure 3.11:** Schematic drawing of the Kinexus rheometer KNX2100.

Due to such sensitivity, it was important to load a sample in the same ways in order to minimise errors. For start, it is recommended to fill the amount that

would create a 1 mm rim around the top plate (Figure 3.12) [9]. This, however, was not necessary as the installed software was calculating volume, which required an operator to load up to the “Good” state shown in Figure 3.12. When the loading operation was complete the top plate was lowered an additional step that brought a sample to the “Optimal” state.

After a sample was loaded the top plate was lowered to match a set gap distance (distance between the top and bottom plates). For this test, the gap was selected to be 1 mm, which is widely applied for gels, suspensions and other complex systems [9–11]. This gap ensures the structural integrity of the tested material which is formed from a complex mixture of different components.

The two-plate system was selected due to the high viscosity of some of the samples that were impossible to load to a cone and plate system. The top plate was selected to be 2 cm in diameter due to the same reason as stated above.

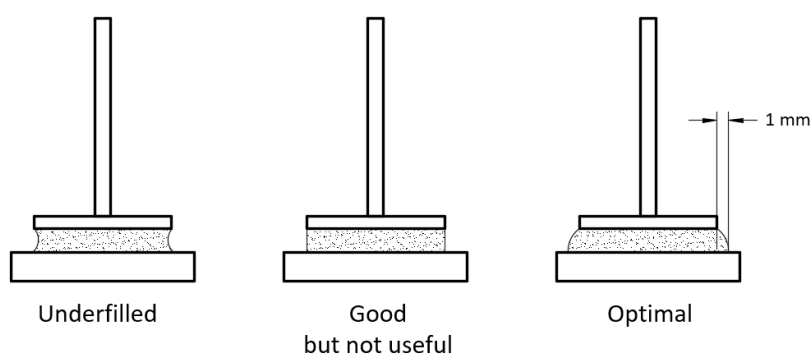


**Figure 3.12:** Types of loading states of a sample [9].

After every test, the sample was removed and plates were washed with a washing liquid that provided a short drying time. The gap was recalibrated and a new sample

was placed following the procedure described above.

### **3.2.2 Scanning Electron Microscope and Energy-Dispersive X-Ray Spectroscopy**

The Scanning Electron Microscope (SEM) is a widely used technique for microstructural evaluation of materials on a nm scale [12]. With the help of a variety of developed techniques, it is possible to distinguish different materials and analyse their boundary interaction.

#### **3.2.2.1 Theory of SEM and EDS**

The SEM operates by directing a beam of electrons onto a material. The beam is emitted by tungsten filament and then is “shaped” or focused into a small point of about 0.4 nm depending on the instrument [13]. This beam is then scattered and those backscattered electrons are caught by the detector, which draws the image just like an old Cathode Ray Tube (CRT) TV. The detector is comprised of a photodiode that is placed above the sample. Along with backscattered electrons (BSE), the sample emits secondary electrons (SE) and Auger electrons with BSE having the highest energy (See Figure 3.13)[14].

Upon reaching the surface of a sample primary electrons (PE) have multiple ways to travel through the material. Firstly, some of PE get reflected in the direction of PE by orbiting a nucleus forming BSE and having the highest remaining energy (Figure 3.13 A). Secondly, PE can excite electrons of the investigated material by

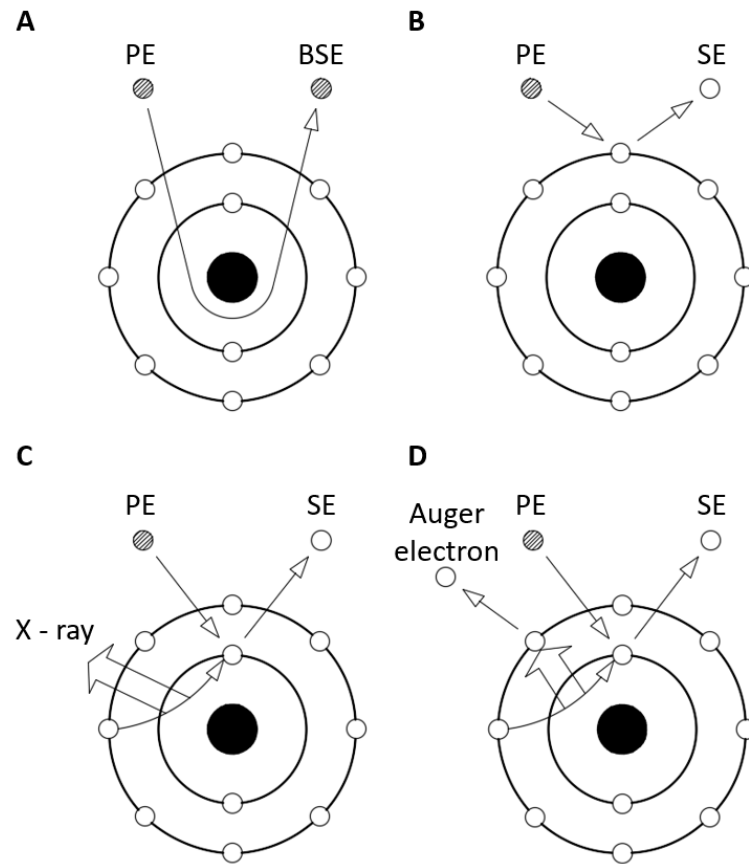


**Figure 3.13:** Scattering of electrons and production of X-rays during SEM and EDS analysis [14]. [A - formation of backscattered electron; B - formation of a secondary electron; C - formation of characteristic x-rays; D - formation of Auger electrons.]

bumping into them and, thus, releasing the forming SE that possesses low energy (Figure 3.13 B). Finally, the de-excitation energy created by filling the vacant place from SE can emit enough energy to excite nearby electrons that can leave their orbitals in a form of Auger electrons (Figure 3.13 D). Important to note that SE and Auger electrons possess just enough energy to leave a very thin surface layer of about 50 - 10 nanometres and due to that comparable low energy these types can be

attracted by a positively charged detector on the side of the chamber and referred as the Everhart - Thornley detector. The respective origins and penetration levels are summarised in Figure 3.14.

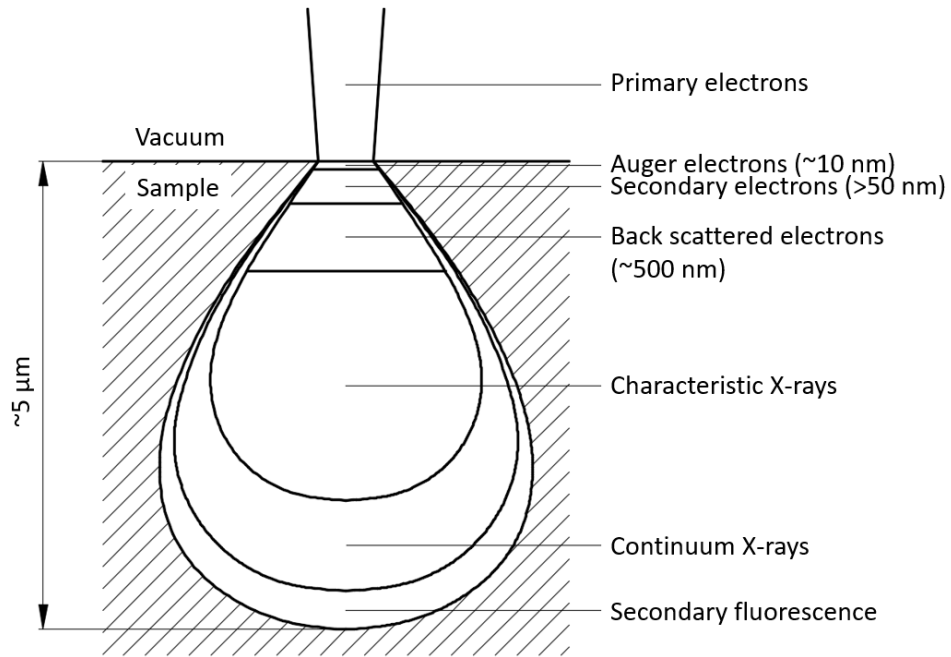


**Figure 3.14:** Cross-section of the area of interaction of primary electron beam and sample [14].

The above-mentioned scattering also results in the emission of x-ray waves that are used to conduct a so-called Energy-Dispersive X-Ray Spectroscopy (EDS), which is a fast, quantitative and qualitative method for analysing the elemental composition (Figure 3.13 C) [14]. However, not all x-rays can be utilised as they do not possess a characteristic nature and only those that were emitted from a jump of an electron from the higher electron shell to a lower one. Emitted waves are collected by another detector that converts them into electrical signals via ionization

on a diode that is kept under low temperature to eliminate noise from the thermally generated electron-hole pairs [15]. The output signals are represented in forms of spectra or peaks with a width of which it is possible to evaluate the relative amount of elements.

### **3.2.2.2 Methodology of SEM and EDS**

For this project a Zeiss SIGMA Scanning Electron Microscope was used to observe a change of morphology of produced samples at 6kV. Additionally, chemical composition was evaluated with the help of an Energy-Dispersive X-ray Spectroscopy installed within the SEM and labelled as X-Act (Oxford Instrument).

### **3.2.3 X-Ray Diffraction**

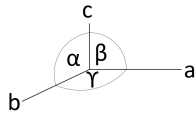
X-Ray Diffraction (XRD) is an analytical technique that allows measuring a distance and an orientation of atoms within a material, thus, rebuilding its crystalline structure. This crystalline structure can be used to determine an unknown material or to ensure the eligibility of a produced sample. Additionally, XRD can be utilised to measure quantitative parameters such as composition and stresses within the material.

#### **3.2.3.1 Theory of XRD**

In the base of the XRD, every material is represented as a structured frame commonly referred to as a lattice [16]. Every chain of that lattice is presented in a

form of ions, atoms or molecules. These lattices were thoroughly investigated and summarised in seven systems as shown in Table 3.1. Additionally, every system is subdivided into so-called Bravais lattices that include Primitive (P), Base-centered (C), Body-centered (I) and Face-centered (F), which are allocated to existing groups in Table 3.1 and examples being shown in Figure 3.15 [17].

**Table 3.1:** Crystal systems and their existing Bravais lattices [17].

			
Name	Sides	Angles	Bravais lattices
Cubic	$a = b = c$	$\alpha = \beta = \gamma = 90^\circ$	P I F
Hexagonal	$a = b \neq c$	$\alpha = \beta = 90^\circ; \gamma = 120^\circ$	P
Trigonal	$a = b = c$	$\alpha = \beta = \gamma \neq 90^\circ$	P
Tetragonal	$a = b \neq c$	$\alpha = \beta = \gamma = 90^\circ$	P I
Orthorhombic	$a \neq b \neq c$	$\alpha = \beta = \gamma = 90^\circ$	P I F C
Monoclinic	$a \neq b \neq c$	$\alpha = \gamma = 90^\circ; \beta \neq 90^\circ$	P C
Triclinic	$a \neq b \neq c$	$\alpha \neq \beta \neq \gamma \neq 90^\circ$	P

In reality, however, crystals can be incomplete and, therefore, it is necessary to indicate the plane within a lattice in order to know the orientation of the whole structure. This is done via Miller indices that are built by taking a crystal structure as a unit coordinate that is then brought to their greatest common divisor of 1

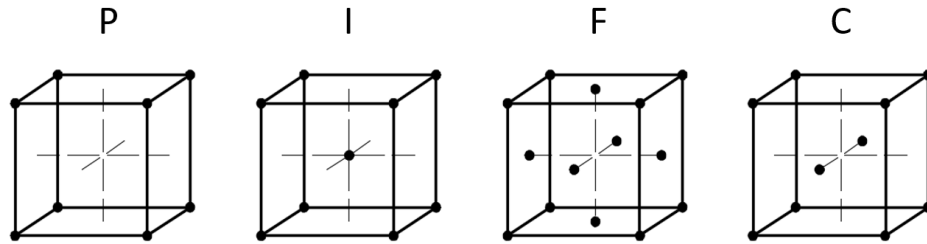


**Figure 3.15:** Example of four types of Bravais lattices [17]. [P - Primitive; I - Body-centered; F - Face-centered; C - Base-centered]

[16]. This builds a system of three coordinates that describes the plane, except for hexagonal and trigonal systems where the modified method called Bravais-Miller indices is used [17]. According to which four indices are used to indicate a plain with the fourth one being used to indicate permutations that happen in those systems.

The measurement of those structures is done via X-rays produced from the excited electrons within a target material, typically copper. The energy to excite those electrons comes from the electron beam emitted from the tungsten filament. However, to analyse a material X-rays have to be distinguishable and contain minimum interference/noise. To ensure that, the created X-rays are filtered by a material with one atomic number lower than the target (nickel for a copper target) making them monochromatic, the produced waves are called  $K\alpha$  and denote a transition of electrons from 2p to 1s (within a copper atom) that have a value of  $\lambda = 0.154 \text{ nm}$  [18]. These X-rays are then directed onto a sample's surface where they are scattered by atoms making them out of phase. The greater the difference in phases the longer distance was between the atoms. Diffracted rays are collected by a photo-diode de-

tector that produces so-called X-ray spectra [18]. During this procedure the emitter and the sensor are rotated to change angles, which helps to measure the spacing between the planes following the Bragg's law:

$$\lambda = 2d \sin^2\theta \quad (3.3)$$

*Where  $\lambda$  is the wavelength of the X-ray wave,  $\theta$  the scattering angle and  $d$  the distance between two plains.*

All this results in a spectrum with a pattern that is unique to a specific element with a specific crystalline structure.

### 3.2.3.2 Methodology of XRD

D8 Advance diffractometer (Bruker) was used in this study. All measurements were taken at the range of  $20^\circ < 2\theta < 80^\circ$  with a step size of  $0.01^\circ$  and step duration of 0.1 seconds. Diffraction data were compared with a PowCod database via QUALX2.0 software.

### 3.2.4 Cyclic Voltammetry

Cyclic voltammetry is a powerful tool for investigating reaction pathways within an electrochemical system. Such a test can show the potential red-ox stages of the studied material with an addition of the interaction of species within an electrolyte.

### 3.2.4.1 Theory of CV

In the core of Cyclic Voltammetry (CV) lies the principle of the electric charge transfer, where electrons or ions transfer charge through the different media (i.e. solid, liquid and gas) [19]. Such migration causes materials to be reduced (gain electrons) or oxidised (lose electrons), creating a red-ox system. Depending on the kinetics of the system, the charge transfer can be spontaneous or forced, both of which create a directional flow of charge that is opposed in direction to electricity. The measure of the charge flow is called current, which is resulted from a charge (C) over time (s) and is measured in A. Movement of the charge requires an applied work, called voltage, which measures a difference between two point's electric potentials within a circuit. The relation between charge and voltage was defined in Ohm's law [20]:

$$I = \frac{V}{R} \quad (3.4)$$

Where  $I$  is the current (A),  $V$  the voltage (V) and  $R$  the resistance (Ohm).

When this principle is applied to a specific system the oxidation happens on an anode and reduction on a cathode. These chemical transformations are referred to as Faradaic reactions and usually happen on the surface of electrodes. To link these chemical and electrical parts of the system a so-called Nernst equation is used. The application of the Nernst equation allows to calculate relative potentials based on a few parameters making it possible to calculate individual and overall potentials

under non-standard conditions [20]:

$$E_i = E_i^0 - \frac{RT}{nF} \ln(\alpha_i) \quad (3.5)$$

Where  $E_i$  is the cell potential,  $E_i^0$  the red-ox potential at a specific temperature,  $R$  the gas constant ( $8.314 \text{ JK}^{-1}\text{mol}^{-1}$ ),  $T$  the temperature,  $\alpha_i$  the chemical activity.

This equation allows to estimate reduction potential of every species in a given system and analyse the likelihood of any stage of the transformation.

Everything combined makes it possible to systematically analyse an electrochemical system. Sweeping the potential allows to analyse reaction mechanism and detect the involved species. Such a method is called voltammetry and can be conducted in two ways: linear and cyclic [19, 21]. The difference between those is that cyclic voltammetry (CV) will have a backwards sweep of the potential and usually is repeated several times/cycles. Due to the repetition, the reversibility of reactions can be determined. When running a CV test cell's response on the change in potential is recorded as a current vs potential. A so-called voltammogram typically has at least one peak that represents a red-ox activity. One peak means that there is no reverse reaction happening, thus, meaning that the investigated system is irreversible. A reversible system, on the contrary, will have at least 2 peaks that happen in the forward and backwards sweep, respectively.

The peaks observed on the voltammogram are formed due to the initiation of a particular reaction that leads to a rise in current. When such a reaction has started to consume the respective reactants, reducing their concentration, the current starts

to drop forming the above-mentioned peaks [21]. Important to notice that some system can be made of multiple materials or have a multi-staged transformation leading to several peaks. As forward and backwards peaks are equivalent in their size it is also possible to observe different kinetics of those stages/species.

The final detail in running a CV is the formation of the double layer, where the surface of an electrode becomes surrounded by species of the opposite charge creating a capacitive region that is weakening with distance. Beyond this region is a diffusion layer that allows for the discussed reactions to complete. Together these layers are referred to as a double layer that affects CV due to the requirement to charge the capacitive part of the structure [21]. The magnitude of such interference is depended on temperature, making the double layer effect negligible under high temperatures.

#### 3.2.4.2 Methodology of CV

The CV was conducted using the AUTOLAB (Metrohm, Autolab PGSTAT302N) with the three-electrode setup. The working electrode was a leaded molybdenum wire with a diameter of 2 mm. The graphite rod was used as a counter electrode and a molybdenum wire was used as a quasi reference electrode. The selection of molybdenum was done to eliminate interference from the molybdenum oxide as it is transformed into a liquid at a high temperature, separated from the tested material.

The tested system was held at 900 °C and the scans of the molten CaCl<sub>2</sub> (electrolyte) were taken for the reference. After that, the tested material was loaded

onto the molybdenum wire and tested by a cycling potential within the measured working potential range of the molten salt.

### 3.2.5 Oxygen Analysis

The production of metals of the highest grade requires for the product to be analysed for the impurity content, which in the majority can be done by EDX. However, when measuring such elements as oxygen and nitrogen, the EDX can not be sufficient due to the low  $K\alpha$  of the elements. To define the concentration of those elements in the metal a method of Carrier Gas Hot Extraction (CGHE) is used.

#### 3.2.5.1 Theory of Oxygen Analysis

Everything starts in the combustion chamber where the analysed sample contained in the graphite crucible is purged with inert gas, in this case, it is argon. After that the crucible is heated up to 2700 °C by the induction heating, this releases all the gases from the materials and lets oxygen to react with graphite crucible resulting in the production of carbon monoxide. The evaporated materials then pass through a dust filter and are then analysed in the infrared (IR) gas analyser [22]. In the IR chamber, the produced gas is irradiated by the infrared light and the detector measures the amount of the absorbed IR strictly in the range of carbon monoxide absorption, producing a spectrum that is the interpreted into the concentration. The rest of the gases are passed over through packed bed columns to separate everything except nitrogen, which then detected using a thermal conductivity detector. This

detector is based on the principle of the Wheatstone bridge that is used to determine very low resistances by balancing the other parts of the circuit as shown in Figure 3.16 [22, 23]. For that, two chambers, one with a carrier gas and another with the tested gas, are arranged in the way of cooling the included heated coils (Represented as R3 and R2 in Figure 3.16). As different gases have different heat transfer capabilities it allows for the Wheatstone bridge to precisely detect the difference in the resistance of those two coils and transform it into the concentration of nitrogen. Allowing for the CGHE to evaluate oxygen and nitrogen concentrations at the PPM scale.

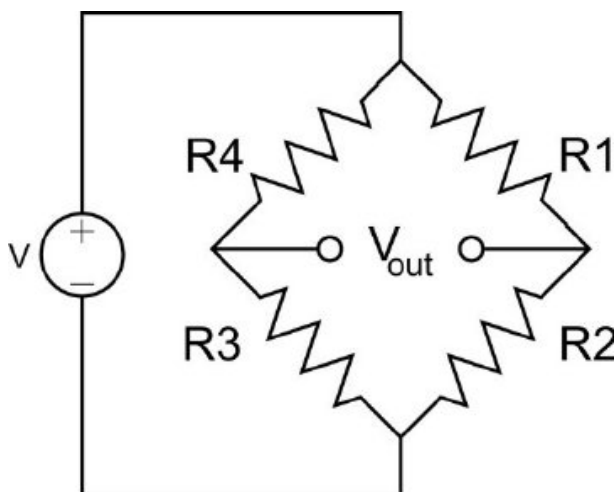


**Figure 3.16:** The Wheatstone bridge [22].

### 3.2.5.2 Methodology of Oxygen Analysis

The test was conducted on HORIBA EMGA 620W Oxygen/Nitrogen Analyser. Metal samples were first etched to remove any contaminants and cleaned with alcohol. After that, the sample in the weight of about 0.8 g was placed in the graphite crucible and inserted in the combustion chamber. The data was received as a wt%

of oxygen.

### **3.2.6 Compressive Strength Testing**

Physical properties of the products are the essential parameters that can help to evaluate the quality of the manufactured products. For this, a compressive test was selected due to small required sample size and importance in some of the areas.

#### **3.2.6.1 Theory of the Compressive Strength Testing**

The compressive strength test is a quasistatic test where a material is subjected to a load that is then linked to the degree of deformation (typically change in the length) [24]. This load is applied until the specimen is completely collapsed or broken. The apparatus contains a familiar Wheatstone bridge (see Figure 3.16) except instead of heat coils there are resistors and one of them (R3) is replaced with a strain gauge, which changes its resistivity based on the induced deformation. The output of this bridge is voltage, which is then converted to the units of force or pressure depending on the setting. The required load is applied using pneumatics or electro motors, depending on the capacity.

#### **3.2.6.2 Methodology of the Compressive Strength Testing**

The barrel-shaped specimens were prepared and placed into the Instron Universal Testing System 9657. Where it was consequently crashed and the data was extracted in the format of the stress-strain curve.

### 3.2.7 Life Cycle Assessment

In the time of sustainability and environmental protection enforcement, every new manufacturing route has to evaluate its impact on the environment to ensure that the new method does not harm our planet more than the conventional one. Thus, the Life Cycle Assessment (LCA) was implemented in this study as it is one of the core methods of environmental impact assessment that has been practised for 80 years [25].

#### 3.2.7.1 Theory of the Life Cycle Assessment

The core principle of the LCA can be described as numerical modelling of the potential emissions that can be produced during the process. The accuracy is closely depended on the quality of the acquired data and the appropriate selection of the numerical method. This data in return consist of two parts: First is the data collected per a specific product. This data includes all inputs and outputs of the system including energy, heat, raw materials, water, etc. This data is then assigned to a product in the specific ratio, which can be mass, volume or cost-based (this is also referred to as allocation). Selection of this method is crucial for the calculation of a scaled-up process [26].

The second part of the data comes from databases that include relative emissions per specific input. These databases are built upon data collected from numerous factories over a long period. This means that the selection of data from this part is important to be done in a region related manner to closely reflect a real-world

situation [27]. As an example this project was based in China, thus, all the materials were selected to be produced in the Asian region.

When the data from the first type is collected and allocated it is then linked with the data from the database [28]. This allows evaluating possible emissions that are reported by commercial producers and arranged in the desired assessment groups such as Global Warming(GW), Water Consumption (WC), etc. Important to notice that based on the numerical method these groups can have different units, which represent different approaches that were undertaken. For example, damage based models provide units in the equivalent of killed species or destroyed lands, whereas impact models show data in the equivalent of the emitted pollutant ( $\text{CO}_2$ ,  $\text{SO}_2$ ,  $\text{NO}_x$ , etc.). This type of data (i.e. damage or impact) is found from the database and sometimes numerically derived from the data following the selected calculation model [29].

The final result represents data sets of impact values and input and outputs of the system, allowing for the in-depth evaluation of the origins of the environmental problems that can be produced by the methods. This, however, can be a rather tedious task as it requires an in-depth knowledge of the upstream processes that take place in the production line of the involved materials.

### **3.2.7.2 Methodology of the Life Cycle Assessment**

For this project, 2 types of LCA was performed: contributor analysis and comparative assessment both of which were produced following a set of British and inter-

national standards (BS EN ISO 14044:2006+A1:2018 and BS EN ISO 14040:2006) [26, 27]. For the comparative assessment, a conventional production method is compared with the NEM Process. From this, a relative impact of both candidates is assessed and compared as a whole. For the contribution analysis, the NEM Process is subdivided onto the subprocesses that are then assessed on their contribution to the overall impact. This detailed LCA allows to indicate the weaknesses of the process and propose potential changes to reduce the impact.

The above-mentioned types were performed identically in 4 stages. The first stage was to identify the goal and the scope of the study and to select a set of tools that is proper to the study. This was crucial to eliminate any unnecessary data and limit the data and is discussed in Chapter 6.

The second stage is the data collection or so-called Life Cycle Inventory Analysis (LCIA), where the data from the laboratory work was recorded in the smallest details but within the set scope. The data for the comparative study is acquired via a rigorous literature search.

The third stage of the analysis can be described as a calculation where the data is inputted into the software and is numerically analysed following the selected model.

The fourth stage is the interpretation of the results. In this stage, the results are compared and linked to the inputs which sometimes requires an additional literature search as the cause of any observation lies in the upstream methods of production, treatment or transportation.

The detailed methodology is discussed in the Chapter 6 as it is an important part

of the LCA, which following standard has to be elaborately stated in the relative section of the produced document.

## References for Chapter 3

- [1] X. Wei, E. Peng, Y. Xie, J. Xue, J. Wang, J. Ding, “Extrusion printing of a designed three-dimensional YBa<sub>2</sub>Cu<sub>3</sub>O<sub>7-x</sub> superconductor with milled precursor powder”, *Journal of Materials Chemistry C* **2017**, *5*, 3382–3389.
- [2] C. Minas, D. Carnelli, E. Tervoort, A. R. Studart, “3D Printing of Emulsions and Foams into Hierarchical Porous Ceramics”, *Advanced Materials* **2016**, *28*, 9993–9999.
- [3] M. A. Torres Arango, D. Kwakye-Ackah, S. Agarwal, R. K. Gupta, K. A. Sierros, “Environmentally Friendly Engineering and Three-Dimensional Printing of TiO<sub>2</sub> Hierarchical Mesoporous Cellular Architectures”, *ACS Sustainable Chemistry & Engineering* **2017**, *5*, 10421–10429.
- [4] G. Z. Chen, D. J. Fray, T. W. Farthing, “Direct electrochemical reduction of titanium dioxide to titanium in molten calcium chloride”, *Nature* **2000**, *407*, 361–364.
- [5] C. Schwandt, G. R. Doughty, D. J. Fray, “The FFC-Cambridge Process for Titanium Metal Winning”, *Key Engineering Materials* **2010**, *436*, 13–25.

- [6] D. Hu, A. Dolganov, M. Ma, B. Bhattacharya, M. T. Bishop, G. Z. Chen, “Development of the Fray-Farthing-Chen Cambridge Process: Towards the Sustainable Production of Titanium and Its Alloys”, *JOM* **2018**, *70*, 129–137.
- [7] B. Huang, P. J. Bártolo, “Rheological characterization of polymer/ceramic blends for 3D printing of bone scaffolds”, *Polymer Testing* **2018**, *68*, 365–378.
- [8] P. R. d. Matos, A. L. d. Oliveira, F. Pelisser, L. R. Prudêncio Jr, “Rheological behavior of Portland cement pastes and self-compacting concretes containing porcelain polishing residue”, *Construction and Building Materials* **2018**, *175*, 508–518.
- [9] T. Mezger, *The Rheology Handbook*, 4th Edition, Vincentz Network, **2014**.
- [10] J. Ahmed, R. Auras, T. Kijchavengkul, S. K. Varshney, “Rheological, thermal and structural behavior of poly( $\epsilon$ -caprolactone) and nanoclay blended films”, *Journal of Food Engineering* **2012**, *111*, 580–589.
- [11] T. Chen, A. Sun, C. Chu, H. Wu, J. Wang, J. Wang, Z. Li, J. Guo, G. Xu, “Rheological behavior of titania ink and mechanical properties of titania ceramic structures by 3D direct ink writing using high solid loading titania ceramic ink”, *Journal of Alloys and Compounds* **2019**, *783*, 321–328.
- [12] J. Newell, *Essentials of Modern Materials Science and Engineering*, Wiley, **2008**.

- 
- [13] J. Goldstein, D. Newbury, D. Joy, C. Lyman, P. Echlin, E. Lifshin, L. Sawyer, J. Michael, *Scanning Electron Microscopy and X-Ray Microanalysis: Third Edition*, Springer US, **2012**.
- [14] L. Reimer, H. Kohl, *Transmission Electron Microscopy: Physics of Image Formation*, Springer New York, **2008**.
- [15] R. Egerton, *Physical Principles of Electron Microscopy: An Introduction to TEM, SEM, and AEM*, Springer US, **2011**.
- [16] R. Gould, W. Borchardt-Ott, *Crystallography: An Introduction*, Springer Berlin Heidelberg, **2011**.
- [17] M. Woolfson, W. M, M. Woolfson, *An Introduction to X-ray Crystallography*, Cambridge University Press, **1997**.
- [18] B. Cullity, S. Stock, *Elements of X-Ray Diffraction: Pearson New International Edition*, Pearson Education Limited, **2013**.
- [19] V. Bagotsky, *Fundamentals of Electrochemistry*, Wiley, **2005**.
- [20] C. Zoski, *Handbook of Electrochemistry*, Elsevier Science, **2007**.
- [21] C. Brett, A. Brett, *Electrochemistry: Principles, Methods, and Applications*, Oxford University Press, **1993**.
- [22] R. Grob, E. Barry, *Modern Practice of Gas Chromatography*, Wiley, **2004**.

- 
- [23] P. Lall, R. Lowe, K. Goebel, “Prognostic health monitoring for a micro-coil spring interconnect subjected to drop impacts”, *2013 IEEE Conference on Prognostics and Health Management (PHM) 2013*, 1–11.
- [24] J. Mark, *Physical Properties of Polymers Handbook*, Springer New York, **2007**.
- [25] M. A. Curran, “A Brief History of Life-Cycle Assessment”, *U.S. Environmental Protection Agency 2006*.
- [26] T. B. S. Institution, “Environmental management - Life cycle assessment - Principles and framework”, **2006**.
- [27] T. B. S. Institution, “Environmental management - Life cycle assessment - Requirements and guidelines”, **2018**.
- [28] Ecoinvent, “Ecoinvent database”, *Ecoinvent 2018*.
- [29] M. Goedkoop, R. Heijungs, M. Huijbregts, A. D. Schryver, J. Struijs, R. v. Zelm, *ReCiPe 2008 Report I: Characterisation*, 1st, National Institute for Public Health, the Environment. Ministry of Health, Welfare, and Sport., The Netherlands, **2013**.

# Chapter 4

## Direct Ink Writing of Titania

*This chapter addresses the optimisation of the Direct Ink Writing technique for titania printing, which includes the investigation into the titania ink rheological properties and redesigning of the ceramic 3D printer.*

### 4.1 Introduction

The titania is an abundant material with great biocompatibility and electrical properties [1–3]. Therefore, it has been utilised in a wide range of applications from a scaffold material for biomedical applications to photocatalysts and solar energy harvesting [3, 4]. Furthermore, it was found that preshaped titania can be reduced to a corresponding metallic form, retaining the initial shape and providing an alternative route for titanium component fabrication [5, 6]. Therefore, additive manufacture (AM) of titania should be investigated in order to further improve the

customisation degree of ceramic titania products. Currently, titania is reported to be shaped using a sol-gel assisted direct ink writing (DIW) method and selective laser sintering (SLS) [3, 7]. However, sol-gel as a binding technique utilises toxic chemicals and SLS is considered to be an expensive technique, giving the need for alternative AM routes [8, 9]. As DIW is a comparably environmentally friendly, simple and cheap method, this chapter is focusing on the implementation of titania in DIW [10]. However, due to the requirement for complex shape production, an investigation into the utilisation of highly loaded titania inks for DIW has yet to be conducted, especially in regards to favourable properties of the ink. Therefore, the goal of this chapter is to adopt the DIW process for printing of highly loaded  $\text{TiO}_2$  paste and produce a rheological investigation of titania inks and evaluate their applicability in DIW process.

## 4.2 Ink Loading Technique

One of the first problems faced upon starting the DIW process was the loading of ceramic ink into a feed cylinder. The transferred paste typically ended up to form a graded density profile with less dense material to be at the nozzle side and more dense to be at the opposite side. Such grading caused the extrusion pressure to be increasing during the duration of the process. This resulted in unextrudible part of the mixture to be left in the feed cylinder at the end of the process.

### 4.2.1 Established Technique

The above-mentioned problem was occurring when the ink was loaded following the technique provided by the manufacturer of the 3D printer. As shown in Figure 4.1 the paste was first loaded into a feed cylinder and then repeatedly knocked on the nozzle side in a vertical orientation. This caused an agglomeration of air in the top part of the cylinder that was later closed off with a rubber bung.

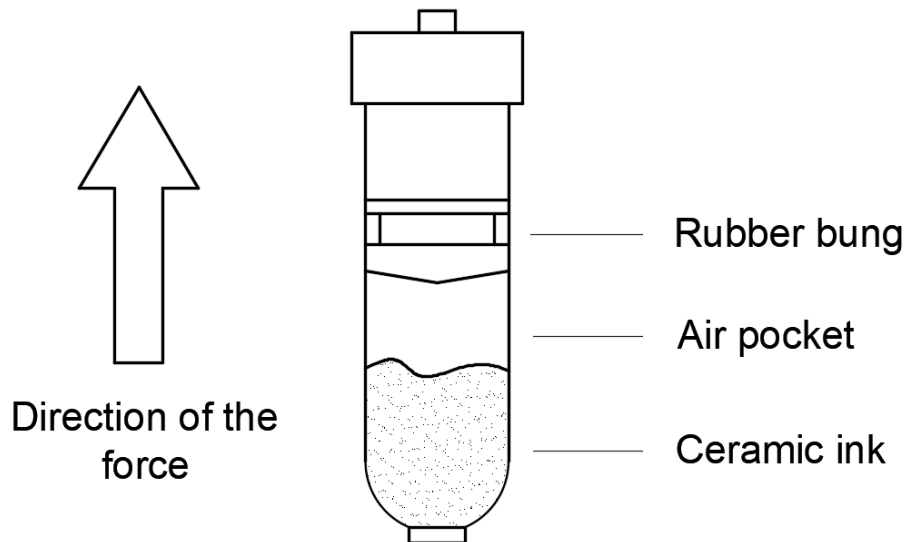


**Figure 4.1:** Ink loading technique proposed by the manufacturer of the 3D printer.

Such a set of actions resulted in a low amount of air bubbles in the bulk of the ink but also in a huge air pocket that was pushing the paste from the top. Upon printing the paste would extrude up until the point where air would burst through the nozzle destroying everything that has been deposited prior.

### 4.2.2 Upgraded Technique

To remove the above-mentioned air pocket it was decided to change the direction of the force. As shown in Figure 4.2 the paste now is loaded in the cylinder and the top part is sealed off with a bung. The cylinder is then flipped over and repeated knocks are allocated on the side of a bung. This results in the absence of air pocket typical for the manufacturer-provided loading technique.

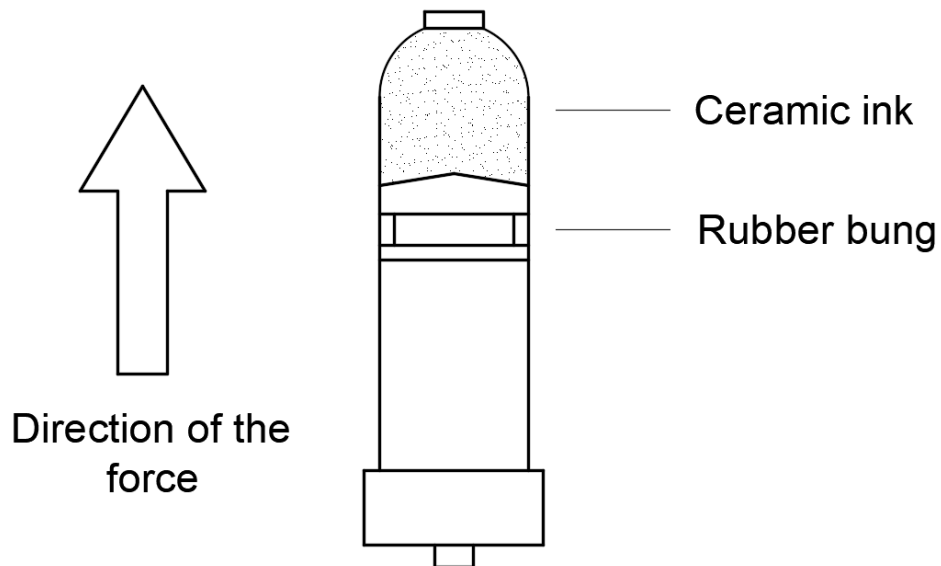


**Figure 4.2:** Different ink loading technique.

This loading technique, however, creates a graded distribution of paste according to density. Such a phenomenon was observed by an extremely big difference in the extrusion pressure, ranging from 0.1 MPa to 0.6 MPa. This inconsistency also affected the flow of the paste which could suddenly increase or stop, thus, requiring an intense pressure control.

In order to avoid it and further homogenise the ink, it was extruded from one feed cylinder into another through an appropriate nozzle. Repeating such process 3 times resulted in a homogeneous paste with negligible density change that is inevitable in the above-mentioned system.

Such a step, however, introduced a huge amount of air bubbles in the paste. These bubbles interrupted the flow of the extruded paste and, due to them being under pressure, damaged an underlying part of a printed object. A solution came from applying the above-mentioned knocks on to the final feed cylinder at an angle (see Figure 4.3). The tilted position was used in order to ensure that the ink would not block the nozzle and would not block the escape of air. Additionally, this positioning ensured a higher surface area where the air would be able to escape from the paste. After approximately a minute the cylinder was slowly rotated so that the conditions of Figure 4.2 could be achieved.

Overall, this change in the proposed by the manufacturer loading technique resulted in a better-homogenised ink with a minimum amount of air. Thus, removing the requirement for a laborious manual extrusion pressure adjustment and improving the reliability of the process.

### **4.3 3D Printer Modification**

Even though DIW is considered a mature ceramic printing technique with printing resolution range from micrometres to meters [11, 12], it has not been applied to

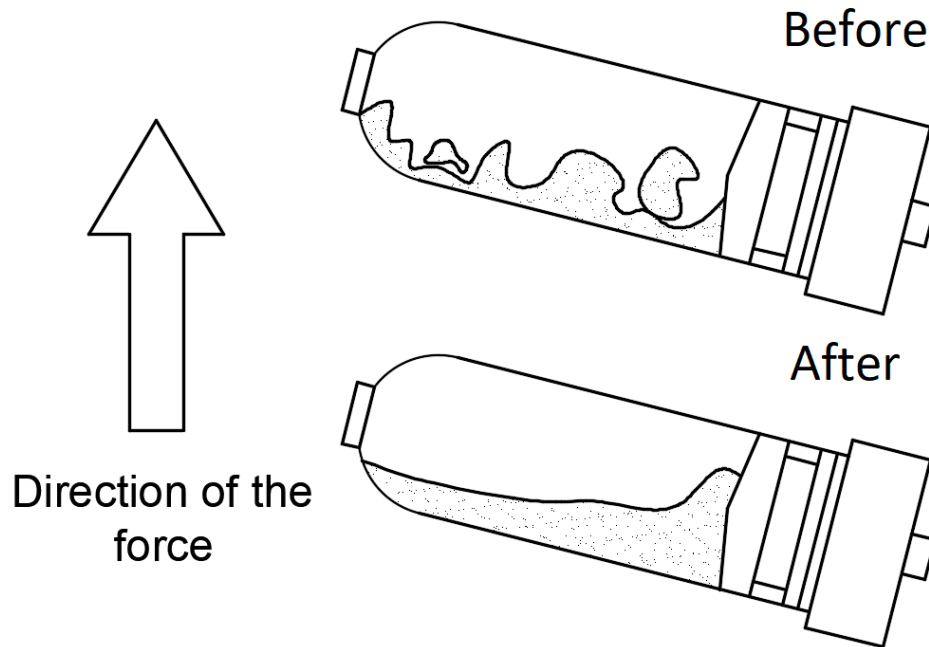


**Figure 4.3:** After loading homogenisation step.

the printing of highly loaded titania slurries. Therefore, an optimisation of the 3D printing machine had to be conducted in order to produce highly defined products.

### 4.3.1 Original Design

The original design of a DIW machine consists of a frame from a conventional desktop FDM 3D Printer with the replaced polymer melting nozzle to a cylinder filled with clay (see Figure 3.2). This design is the most suitable for the continuous extrusion of a material due to the lack of any flow controlling mechanism [10]. Due to such an uninterrupted flow, products tend to have artefacts shown in Figure 4.4, which affect the quality and integrity of any complex shaped product. These artefacts have a form of an upward standing pillars of paste that were formed when

the nozzle was lifted above the printing area before it is moved to the next point without stopping the material extrusion.

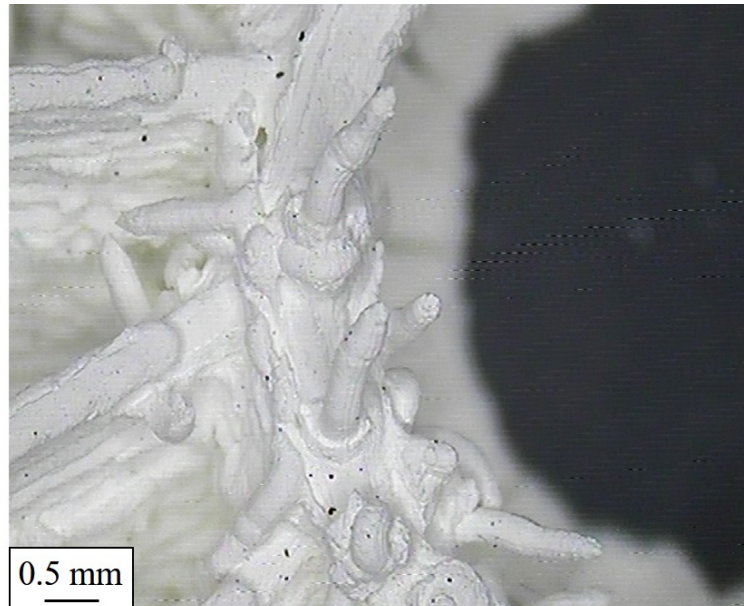


**Figure 4.4:** Artefacts caused by uninterrupted extrusion of paste.

### 4.3.2 Screw-head Design

As a measure of flow control, it is common to see an implementation of a screw valve that is fixed to a frame instead of a feed cylinder as shown in Figure 4.5. This screw head design was adopted from adhesive dispensing machines, which provides highly precise extrusion of a material [13]. The screw head utilises an auger screw that creates a positive drag for material when is rotating clockwise and stopping the flow when not rotating or rotating in an opposite direction. However, with the utilisation of an additional component in the system, the pressure drop becomes noticeable increasing initial pressure required to extrude material. Due to the selected

material being water-based paste such increase in applied pressure was discovered to increase the rate of water migration from the paste, regardless of paste's stability. With the reduced amount of liquid, the material becomes unextrudible leading to a requirement to prematurely terminate a 3D printing process. Dried pastes or pastes with a low liquid composition also tend to increase friction between auger screw and its case to the point where a motor connected to the auger screw can not rotate (see Figure 4.5). Replacing the motor would require the addition of a power supply to drive such a higher power motor. Furthermore, pastes that are applied for the screw head design are typically contain more liquid to reduce the load on the before-mentioned motor. This in return limits the amount of liquid within the paste, thus, reducing the material load that increases the chance of cracks during drying. It is also important to notice that when a feed cylinder is empty there is

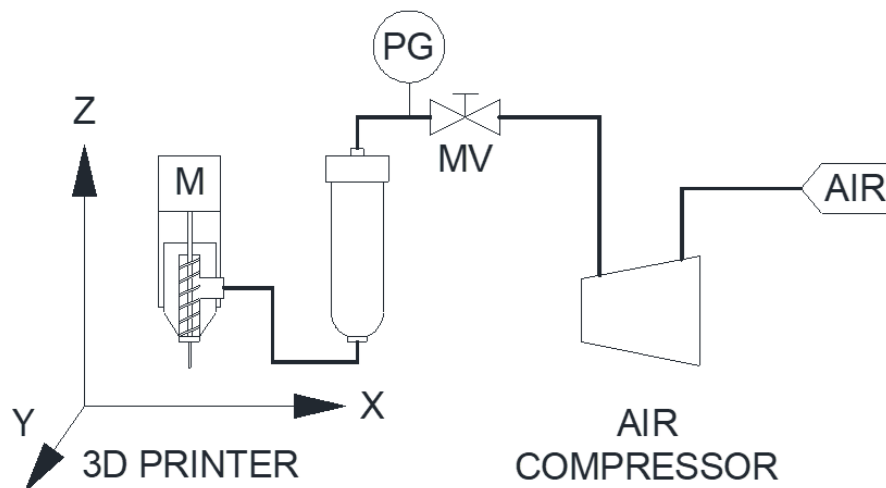


**Figure 4.5:** Schematic drawing of the screw head Direct Ink Writing 3D printer.

always a considerable amount of material left in the screw head that can not be further extruded and is treated as waste.

### 4.3.3 Updated Design

The observed restrictions and problems demanded an enchantment to the above-mentioned designs. Modifications were undertaken in two stages:

1. Reducing pressure drop
2. Improving flow controlling system

These two points were addressed in the nozzle size change and implementation of a pressure relief system, respectfully.

#### 4.3.3.1 Nozzle Change

As was mentioned before the screw head design was adopted from the adhesive dispensers, along with that the nozzle was taken from the conventional extruder, so-called needle. However, during the investigation of the used systems, it was noticed that adhesive extruders also happen to use cone-shaped nozzles. This finding made the application of the needle questioned and required to be analysed and compared to evaluate its applicability for the extrusion of ceramic pastes as it was theorised to have a potential reduction on the pressure required for the extrusion. To prove that it was decided to first calculate pressure drops that occur along the narrow needle and cone-shaped nozzle. This was done by applying the Bernoulli equation to both

geometries [14]:

$$\frac{P_1}{\rho g} + \frac{v_1^2}{2g} + z_1 + h_p - h_L = \frac{P_2}{\rho g} + \frac{v_2^2}{2g} + z_2 \quad (4.1)$$

Where  $\frac{P}{\rho g}$  is the initial head,  $\frac{v^2}{2g}$  the head due to superficial velocity,  $z$  the vertical position,  $h_p$  the head that is produced by a pump work and  $h_L$  the friction-related head loss.

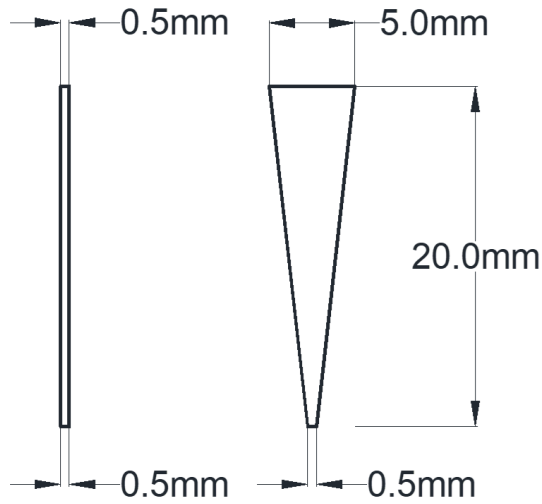


**Figure 4.6:** Drawing of analysed nozzles.

The friction related head loss is calculated following the equation below [15]:

$$h_L = f \frac{L}{D} \frac{v_{average}^2}{2g} \quad (4.2)$$

Where  $f$  is the pipe friction factor,  $L$  the pipe length,  $D$  the pipe diameter,  $v$  the flow velocity,  $g$  the acceleration due to gravity.

To produce a set of equations two assumptions were made:

1. Nozzles are positioned horizontally

2. Friction coefficients are the same for both geometries.

This resulted in following equation for the needle:

$$\Delta P_{needle} = h_L = f\rho \frac{L}{D} \frac{v^2}{2} \quad (4.3)$$

And for the cone shaped nozzle:

$$\Delta P_{cone} = \frac{\rho v_2^2}{2} - \frac{\rho v_1^2}{2} + f\rho \frac{L}{D_{average}} \frac{v_{average}^2}{2} \quad (4.4)$$

Plugging known parameters in the equations 4.3 and 4.4 results in  $\frac{\Delta P_{cone}}{\Delta P_{needle}}$  to be 0.11 which means that the pressure drop within the cone shaped nozzle is almost 10 times lower than the pressure drop across the needle. Knowing this the needle nozzle was replaced with cone-shaped, which immediately removed majority of blockages.

#### 4.3.3.2 Pressure Relief System

As was mentioned before, it is impossible to produce extremely precise objects using the original design. Furthermore, utilisation of the screw head design can imply additional material waste limiting the number of solid particles within the paste. Therefore, the alternative way of controlling the flow was to remove the screw head and instead to manipulate pressure supplied by the compressor. As shown in Figure 4.7 two solenoid valves were installed in between the feed cylinder and the compressor. First valve (SV1) isolates the pressure from the air compressor when this happens the second valve that is normally closed (SV2) is activated releasing pressure from the feed cylinder, thus, stopping the flow of the paste.

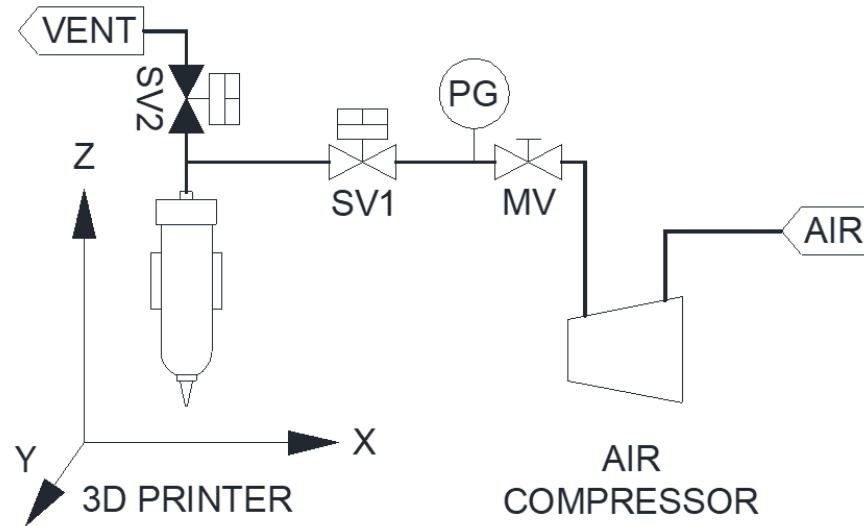


**Figure 4.7:** Schematic drawing of the modified Direct Ink Writing 3D printer.

Valves were connected to one of the cooling fans pins on the motherboard, this was done due to the following reasons:

1. Fan had the same parameters as every solenoid valve (12V-DC).

This ensured compatibility of the installed valves, plus it removed the necessity for any kind of hardware modification on the 3D printer's frame site. The current supplied by the pin was sufficient to drive 2 of those valves.

2. Fan could be controlled from within a g-code.

This means that it was possible to modify g-code in order to switch on and off the above-mentioned fan on demand.

While the physical implementation of solenoid valves did not require any modifications, the software adaptation took place in the form of a Matlab script (see

Appendix B). This script was run on a pre-generated g-code adding stop and start commands for a fan. However, it was discovered that valves were closing and opening extremely quickly creating a delay in the paste flow which resulted in a gap in the extruded paste as shown in Figure 4.8. From the diagram, it is clear that the actual starting point of printing (A2 compared to A1) has been delayed leaving a space, which resulted in an incomplete shape fill. Therefore, it was necessary to include delays between the stop and start commands to let the feed cylinder to get back to the extrusion-sufficient pressure.



**Figure 4.8:** Delayed deposition of material compared with the programmed path.

As seen from the g-code example below the script would compare lines of g-code and establish whether there is a so-called filament extrusion action represented in “E\*\*,\*\*\*\*” command. Whenever line below has no “E” the script would insert two lines: M106 - which turns off the fan and G4 P150 - which sets a wait time of 150 milliseconds before the 3D printer moves on to the next line of commands. If the opposite happens meaning the line below has “E” the script would paste another two lines into the code: M107 - which turns on the fan and G4 P220 - which sets a wait time of 220 milliseconds to recover the released pressure.

```

G1 X8.986 Y6.11 E12.33703

M106                                     } Valve close sequence
G4 P150                                 }

G0 F7200 X9.891 Y6.558

M107                                     } Valve open sequence
G4 P220                                 }

G1 F1200 X10.23 Y6.153 E12.3867

```

This allowed producing necessary movement of the printing head without extruding any material. Overall these two modifications (*i.e* the nozzle replacement and the relief valve system implementation) resulted in dramatical quality improvement of the DIW process by stabilising flow control, reducing waste material and removing the necessity for the screw head set up (See Figure 4.9).

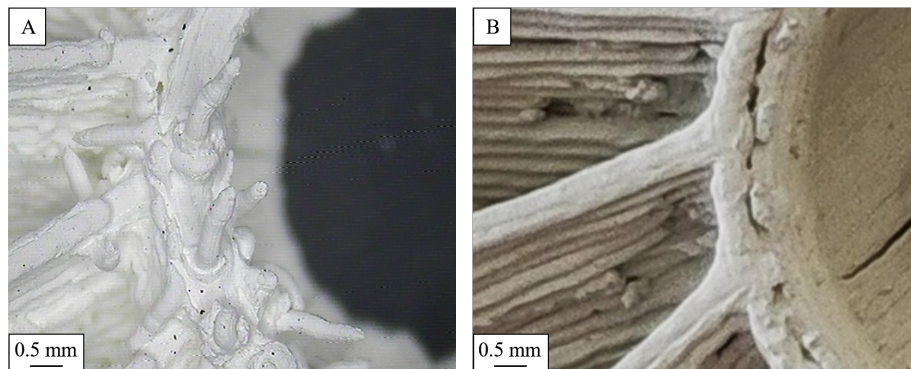


**Figure 4.9:** The comparison of the quality of A - before optimisation and B - after optimisation.

## 4.4 Ink Preparation and Analysis

Due to the high loaded  $\text{TiO}_2$  paste being a novel material to be applied in DIW, it is important to understand its flow behaviour in order to improve the quality of the final product.

### 4.4.1 Experimental

The complete experimental procedure is described in Figure 4.10. With detailed descriptions given below.

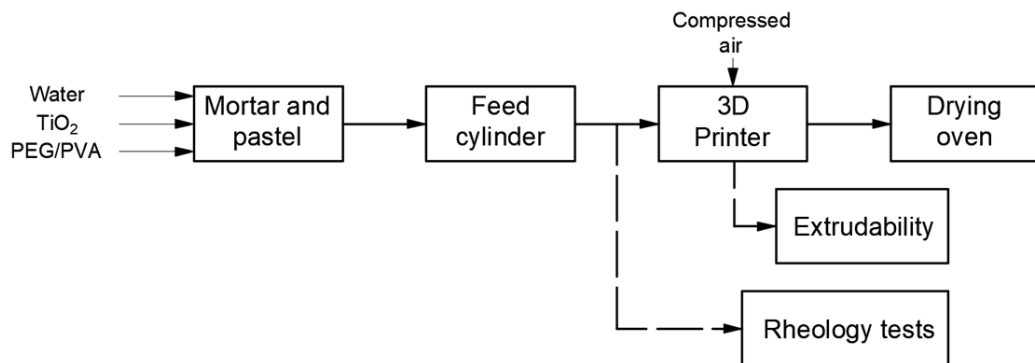


**Figure 4.10:** Flow diagram for the experimental set-up.

#### 4.4.1.1 Feedstock

To produce a titania ink, titania (99.5%  $\text{TiO}_2$  Aladdin, 60 nm, rutile) was mixed with deionised water or a solution of selected additives in the mortar for 10 minutes. Two rheological modifiers were applied in this study for their binding and dispersive properties and their composition: polyethylene glycol (PEG) (SCR, Average

molecular weight: 6000) and polyvinyl alcohol (PVA) (Aladdin, 87 - 89 mol%, 3.2 - 3.6 mPa.s). PEG was dissolved in water at room temperature, while PVA required heating of 60 °C in order to be fully dissolved. These mixtures were then mixed with titania in a specified weight ratio denoted as X:Y (for example PEG 1:0.9) where X is the ratio of TiO<sub>2</sub> and Y is the ratio of the solution (PEG, PVA or H<sub>2</sub>O). The concentration of the solution is going to be evaluated for PEG 0 wt%, 5 wt% and 10 wt% and for PVA 0 wt%, 2.5 wt% and 5 wt%. These concentrations were selected due to the consistency of the slurries that would show to be incompatible when outside of that range. The produced paste/slurry was then transferred into the feed cylinder.

#### 4.4.1.2 Rheological Tests

Rheological tests were conducted using Kinexus rheometer KNX2100 (Malvern Panalytical Ltd) using 20 mm stainless steel disc and a gap of 1 mm. All experiments were done at 25 °C. Two types of test were performed:

- Rotational

The test was performed for a shear sweep of 100 to 0.01.

- Creep and relaxation

The test was performed to end at a time of 5 seconds for both creep and relaxation parts with 1 Pa shear stress applied.

#### 4.4.1.3 Extrudability

For this work, extrudability is defined as an ability to be extruded through the selected nozzle with a thickness of 0.5 mm. This means that the result can be described according to the following criteria:

1. **Uncontrollably extrudable.**

The paste possesses high fluidity and cannot retain its shape.

2. **Controllably extrudable.**

The paste can be extruded without any deviations in the flow.

3. **Extrudable with occasional inconsistencies.**

The paste possesses inconsistency in the flow.

4. **Unextrudable** – Cannot be extruded.

Extrudability tests were conducted in two phases. Firstly, a rivet with 10x10x10 mm dimensions was printed. Based on the results of the first phase, the second phase focused on the production of an impeller with the dimensions of 40x40x18 mm. This is done in order to test the material for the production of larger objects and eliminate criteria 1 and 4. The whole process takes place on a modified Fused Deposition Modelling (FDM) 3D printer (LUOBO, China) connected with the conventional air compressor with a working pressure range of 0.1-0.6 MPa and a maximum output of 0.8 MPa.

## 4.4.2 Results and Discussion

### 4.4.2.1 Effect of Additives

The main focus for this test was given to the viscosity change when adding an additive to the paste. As a rule of thumb, viscosity must be as low as possible in order to prevent any problems during the DIW process. Important to notice that to reduce any complex flow behaviour of a highly loaded slurry the particle load was reduced to about 30 %. Figure 4.11 compares the effects of different amounts of PVA and PEG and their degrees.

From Figure 4.11 it is clear that both of the selected additives increase the viscosity of the paste, however, PVA has a larger effect on viscosity compared to PEG. Increasing the concentration of PEG shows a linear increase in viscosity compared to the exponential for PVA. Such an effect is caused by two factors. Firstly the size of the polymer chains of PEG compared to PVA, which tend to entangle creating a less viscous slurry. Secondly, it was reported that PVA is mostly used as a binder with some exception of a surfactant when PEG is solely used as a surfactant, meaning that binder would tend to be less viscous in order to hold particles upon drying [16–18]. From the test, however, it is not clear whether PEG or PVA have any thinning effect, as according to the results viscosity keeps increasing when adding more of any of the polymers.

Nonetheless, this test pointed out that the concentration of 10% is the most suitable for PEG and 2% is the best for PVA before it makes ink too thick. It is

not necessary to move above 10% PEG as the increased amount of organics can negatively affect the integrity of the final product.

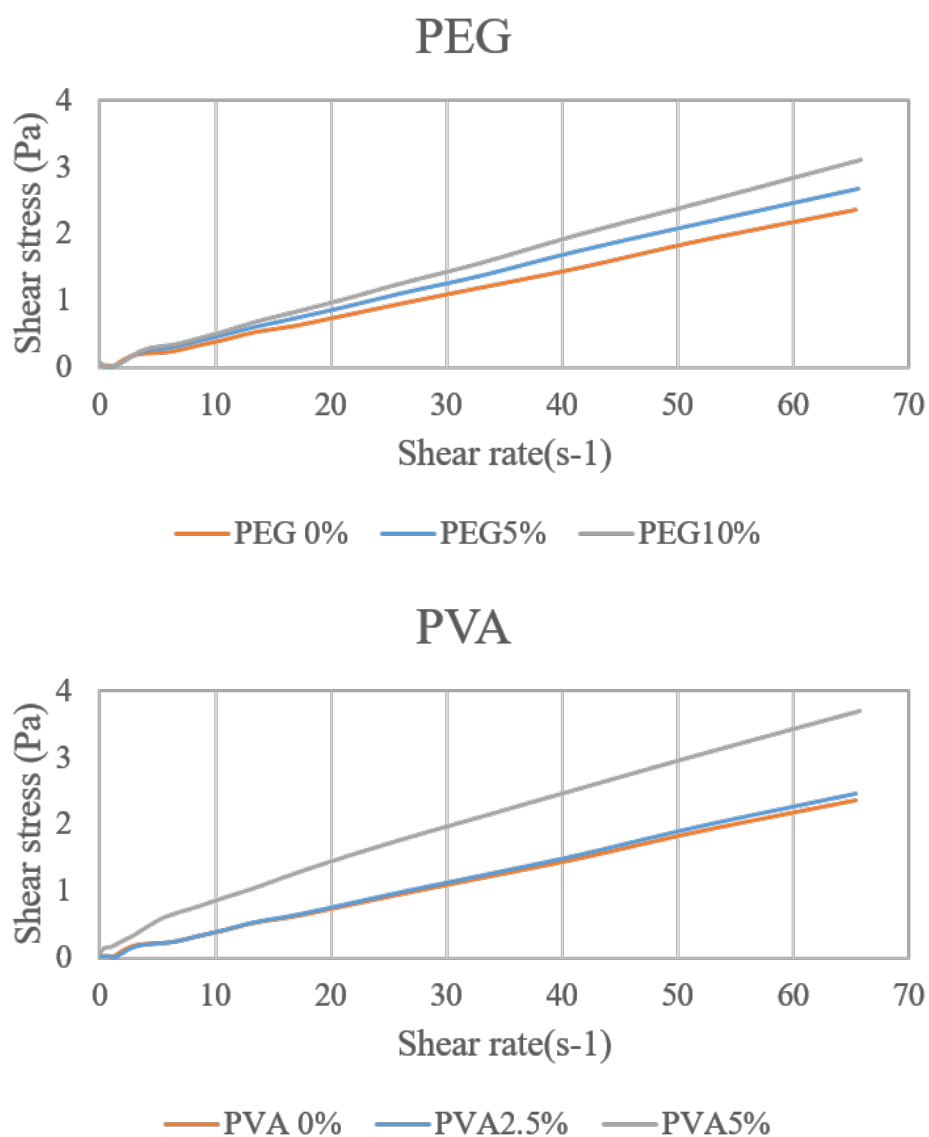


**Figure 4.11:** Shear stress vs shear rate comparison for PEG and PVA containing water-based  $\text{TiO}_2$  slurries.

#### 4.4.2.2 Rheological Evaluation

An evaluation of the relationship between shear rate and shear viscosity showed the shear thinning behaviour across all the samples. Figure 4.12 indicates that with increasing shear rate shear viscosity reduces, which is an indicator of a shear-thinning response and pseudo-plastic behaviour.

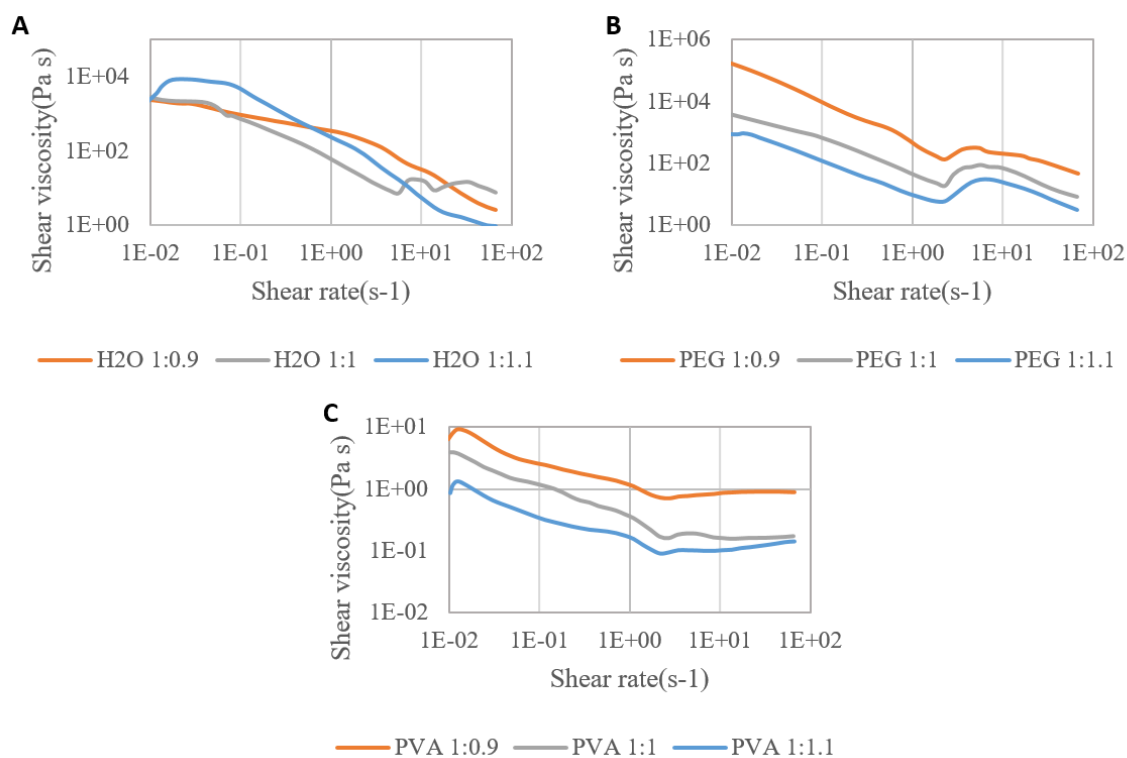


**Figure 4.12:** Shear rate vs Viscosity. A – water-based inks; B – PEG-based inks; C – PVA based inks. With the ratio representing X:Y, where X is the weight ratio of TiO<sub>2</sub> and Y the weight ratio of respective additive (2% aqueous solution of PVA and 10% aqueous solution of PEG)

Inks without any additives showed highly unstable behaviour that affected rhe-

ological readings, as they do not follow any trend compared to other samples (see Figure 4.12 A). It was not possible to achieve a stable suspension of titania without additives for samples H<sub>2</sub>O 1:1 and 1:1.1. Therefore, there are random peaks appear on the graph, which implies signs of segregation and relatively higher loading across the samples (as seen in Figure 4.12 A). Addition of PEG to an ink resulted in a shear thickening region in the range of 2 to 7 s<sup>-1</sup> (as shown by the increase in shear viscosity in Figure 4.12 B). This was previously observed and discussed by Ge, et al. [19]. Such a phenomenon is caused by the interaction of spherical particles suspended in solutions containing polymers with relatively long polymer chains [20], resulting in the agglomeration of particles at a particular shear rate. As the agglomeration of particles increases, an inevitable risk of clogging occurs in the nozzle of the DIW 3D printer. Samples with PVA presented a sensible reduction in viscosity, shown by a plateau at higher shear rates, making them behave as a viscous slurry (see Figure 4.12 C). Therefore, produced graphs in Figure 4.12 C can be divided into two parts shear thinning (at 0.01 to 2 s<sup>-1</sup>) and slightly shear-thickening region (at 2 to 100 s<sup>-1</sup>). This second part can occur as a result of a reformed morphology of the ink due to the binding properties of PVA. At higher loads of TiO<sub>2</sub> particles ink was showing obvious shear thickening behaviour, which unfortunately could not be tested on the rheometer due to the ink being tightly packed.

Creep and recovery tests were conducted to investigate the viscoelastic properties of the inks, as seen in Figure 4.13.

Overall Figure 4.13 displays mostly viscoelastic behaviour with dominant viscous

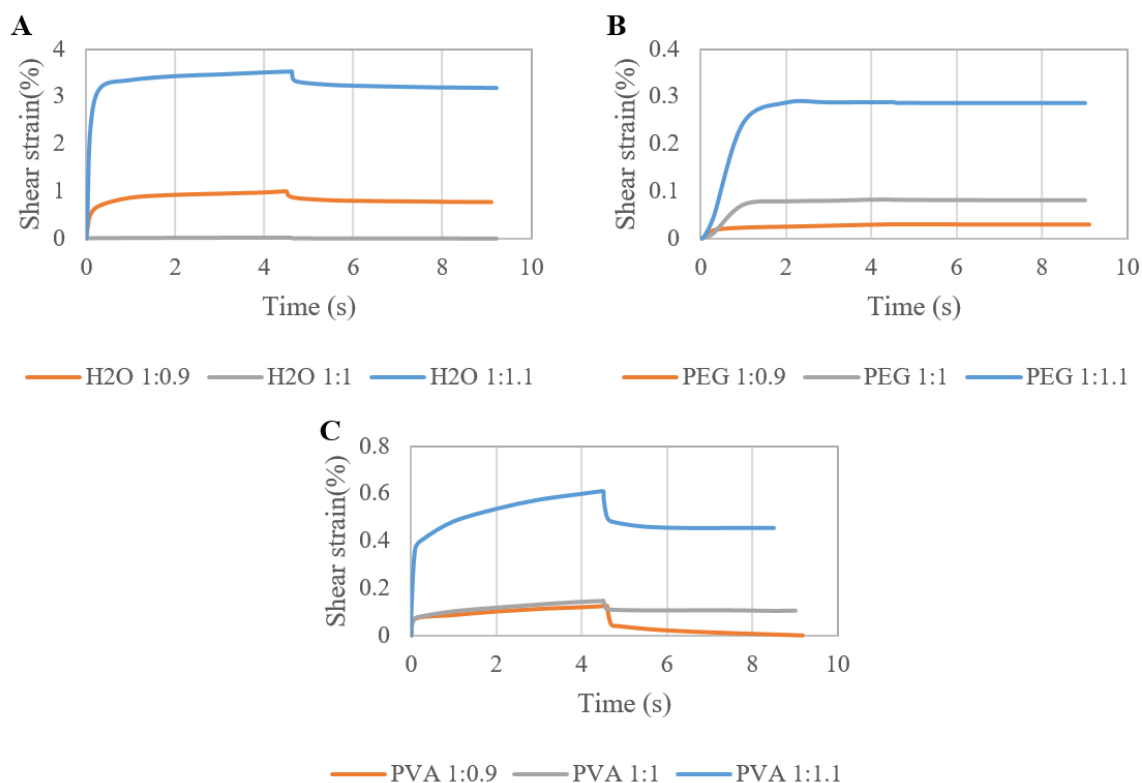


**Figure 4.13:** Creep and recovery test. A – water-based inks; B – PEG-based inks; C – PVA based inks. With the ratio representing X:Y, where X is the weight ratio of TiO<sub>2</sub> and Y the weight ratio of respective additive (2% aqueous solution of PVA and 10% aqueous solution of PEG)

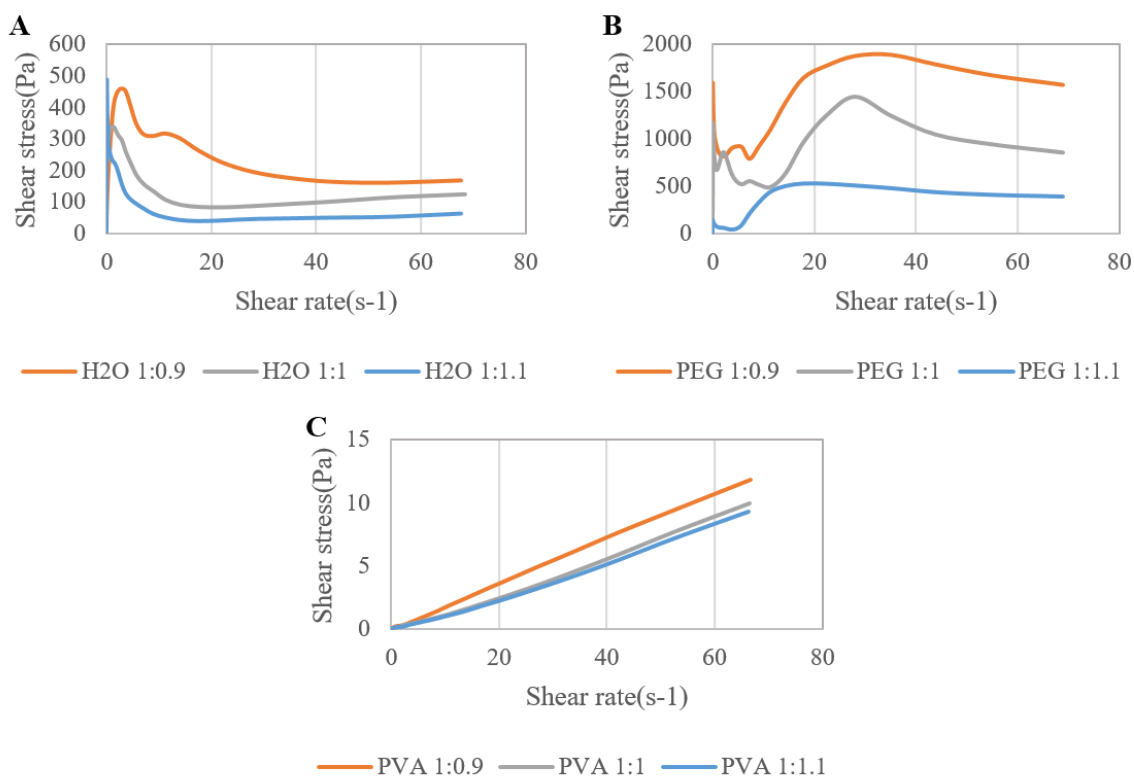
side across all samples, which is represented by a relatively small reduction of strain after about 5 seconds (recovery phase). In addition, samples with a lower content of titania followed trends of increased strain (as seen from Y-axis on Figure 4.13). Alternatively, this results in the ability of inks with higher amount of titania to withstand higher loads when applied to DIW.

Figure 4.13 C shows that on average PVA based inks had a 30% reformation abil-

ity with water fluctuating between 10% and 80% (see Figure 4.13 C). This means that the ink tends to remain part of its shape and structure. Applying such inks in extrusion can be beneficial for shape conservation, but also may theoretically constrain extrusion process due to the additional resistance stored in the ink. Important to notice that PEG samples in Figure 4.13 B show almost viscous behaviour with negligible elasticity, as demonstrated by the lack of the elastic reaction after the creep phase has ended. This behaviour is linked to the surfactant effect of PEG. It allows ink to flow better and reduce the viscoelastic component of an ink. However, DIW inks are expected to have viscoelastic nature and, therefore, PEG may possess unsuitable properties.

Testing shear stress (Figure 4.14) showed that most of the inks followed a shear-thinning trend that is represented by a stabilisation of the shear stress value, however, it is not that obvious due to an elastic reaction at the beginning of curves in Figure 4.14 A and B. This reaction is represented in initial spikes of shear stress that can be associated with the stable structure that forms during the idle state. This structure creates a resistance to flow and, therefore, has increased shear stress. When repeating the tests all peaks persist meaning that the formation time of the resistant structure is extremely small. In addition to that, Figure 4.14 B shows that samples with PEG show fluctuation before the logarithmic increase. The fluctuation has appeared in the dilatancy peaks range ( $2$  to  $7 \text{ s}^{-1}$ ), observed in shear viscosity vs shear rate tests (see Figure 4.12 B). Overall, this means that when applied to DIW, the inks will become stable soon after it is extruded. Samples with PVA once again

showed almost ideal viscous behaviour, which means that these samples will most likely not be able to be implemented into the DIW process due to their fluid nature and, thus, uncontrollable extrusion (see Figure 4.14 C).



**Figure 4.14:** Shear rate vs shear stress plots. A – water-based inks; B – PEG-based inks; C – PVA based inks. With the ratio representing X:Y, where X is the weight ratio of TiO<sub>2</sub> and Y the weight ratio of respective additive (2% aqueous solution of PVA and 10% aqueous solution of PEG)

#### 4.4.2.3 Extrudability

When using the variations of inks discussed above as inks for DIW printing, only PEG 1:0.9 and 1:1 were able to be extruded without any clogging through 0.5

mm nozzle. Table 4.2 contains a summarised extrudability evaluation with images where it was appropriate. PVA based inks were determined to be too fluid to maintain any shape and most of the water-based samples were not extrudable at any composition. As seen from the Table 4.2 only samples containing PEG in a ratio of 1:0.9 and 1:1 produced relatively good results. PEG 1:1.1, however, could not be printed consistently due to blockages that resulted in a sudden and uncontrollable extrusion. It is important to note that increasing the nozzle size to 1 mm allowed every ink to be extruded, however, this limits the resolution of the product.

**Table 4.2:** Extrudability results from a 0.5 mm nozzle. (1 - too fluid to be controlled during the extrusion; 2 - can be adequately controlled during the extrusion; 3 - can be extruded with occasional blockage; 4 - cannot be extruded)

Ink	Compositions			Model
TiO <sub>2</sub> to H <sub>2</sub> O	1:0.9	1:1	1:1.1	
Extrudability	4	4	4	
TiO <sub>2</sub> to PEG	1:0.9	1:1	1:1.1	
Extrudability	 2	 2	 3	
TiO <sub>2</sub> to PEG	1:0.9	1:1	1:1.1	
Extrudability	1	1	1	

#### 4.4.2.4 Investigation of the Best Performing Ink

It was found that the best performing ink was PEG 0.9, therefore, to further investigate the properties that PEG containing ink possesses its storage and loss moduli were assessed to enhance the understanding of its behaviour in elastic and viscous way.

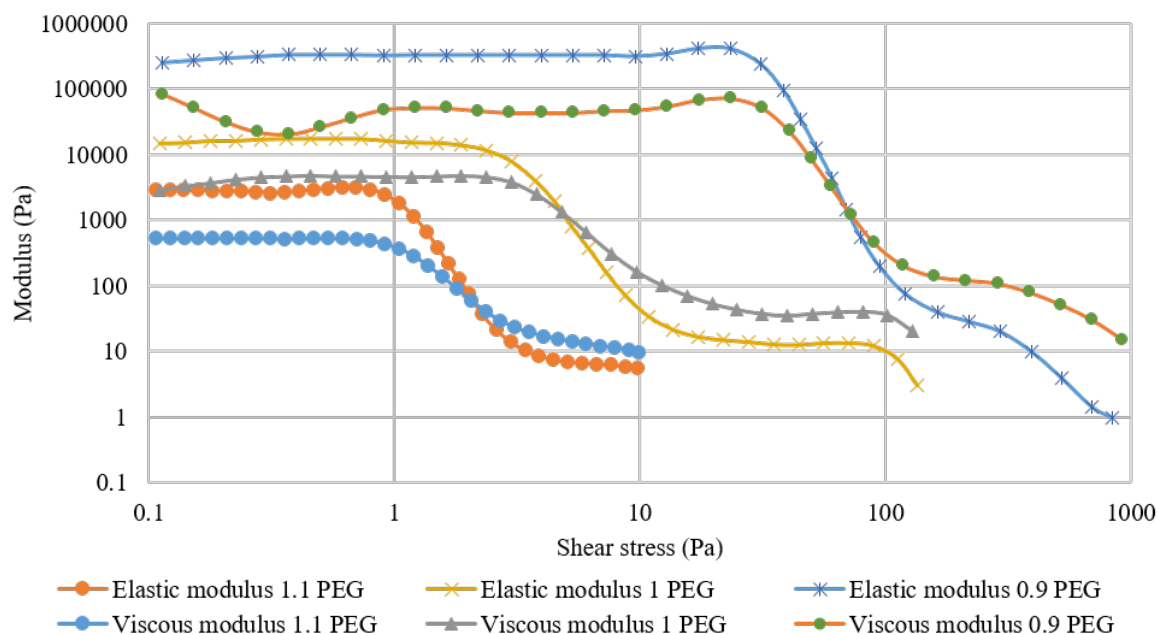


**Figure 4.15:** The effect of solution content on the storage and loss moduli. With the ratio representing X:Y, where X is the weight ratio of  $\text{TiO}_2$  and Y the weight ratio of 10% aqueous solution of PEG

From Figure 4.15 it is clear that with increasing ratios of PEG solution resulted in a reduction in both moduli. However, the sample with a 0.9 PEG ratio also shows a slight peak near the end of the Linear Viscoelastic (LVE) plateau (seen in Figure 4.15 at shear stress between 10 and 100 Pa). This can be correlated to an

increased modulus with increasing deformation that is, potentially, associated with the interaction between ceramic particles and polymeric chains of PEG, due to the lack of the solution that separates particles [21]. Such an interaction means that the system may express a unique behaviour when extruded under extreme conditions (i.e. a very narrow nozzle). Another noticeable characteristic change is the shift of the yield and the corresponding flow points in all samples with the increased content of the PEG solution. This indicates that as more solvent is introduced into the ink, less force is required to make it flow (see Table 4.3).

**Table 4.3:** The ink composition and its relative Yield and Flow points.

Sample	0.9 PEG	1 PEG	1.1 PEG
Weight Ratio PEG:TiO <sub>2</sub>	0.9:1	1:1	1.1:1
Yield point (Pa)	41.7	1.8	0.7
Flow point (Pa)	72.4	4.8	2.1

When applied to DIW with 1 mm nozzle, the use of 0.9 PEG was found to be the most suitable, which was confirmed by the yield point of 41.7 Pa; close to a value of 42 Pa previously described to be suitable for ceramic inks applied in DIW [22]. However, the 1 PEG ink ratio was also shown to have the potential for extrusion, for the printing of smaller products with a smaller nozzle ( $\pm 0.5$  mm) even though a relatively low viscosity meant that it could not sustain its weight during large prints. This is due to the increased maximum shear rate that the paste experiences

when extruded through a nozzle. Following the equation:

$$\gamma = \frac{4Q}{\pi r^3} \quad (4.5)$$

Where  $Q$  is the volumetric flow rate and  $r$  the nozzle radius.

When changing the nozzle size from 1 mm to 0.5 mm the shear rate increases from  $15.4 \text{ s}^{-1}$  to  $50.9 \text{ s}^{-1}$  [22]. Such an increase makes inks with lower PEG solution content harder to extrude when thinner pastes would require less force to be extruded and have a less chance of clogging the nozzle [21].

Overall, 0.9 PEG showed all desirable characteristics for a DIW ink such as a yield point and shear thinning behaviour and was successfully used to produce a wide variety of different shapes.

#### 4.4.2.5 Further Optimisation

Combining findings from rheological tests and extrudability evaluation, PEG-based inks with the ratio of 1:0.9 were proven to have the most suitable rheological parameters (shear thinning and almost viscous) for the DIW. However, the shear thickening region for the PEG-based inks was discovered to be the final factor for the inconsistency of the flow, especially when prints were scaled up. Moving from 10 mm wide shape to 40 mm resulted in the observed inconsistency of the ink's flow, similar to that of PEG 1:1.1 sample. By applying a surface lubricant in the weight ratio of 1  $\text{TiO}_2$  to 0.1 mixed cooking oil the flow became more stable, meaning that particles were not constrained by chains of PEG at higher shear rates due to reduced friction

between the components of the ink. This was proven by a rheological investigation, which pointed out that the dilatancy peak at the range of 2 to 7  $\text{s}^{-1}$  was reduced (See Figure 4.16). Application of the updated formula to the complex shape of an impeller resulted in better surfaces finishing and higher precision of final dimensions as seen from Figure 4.17.

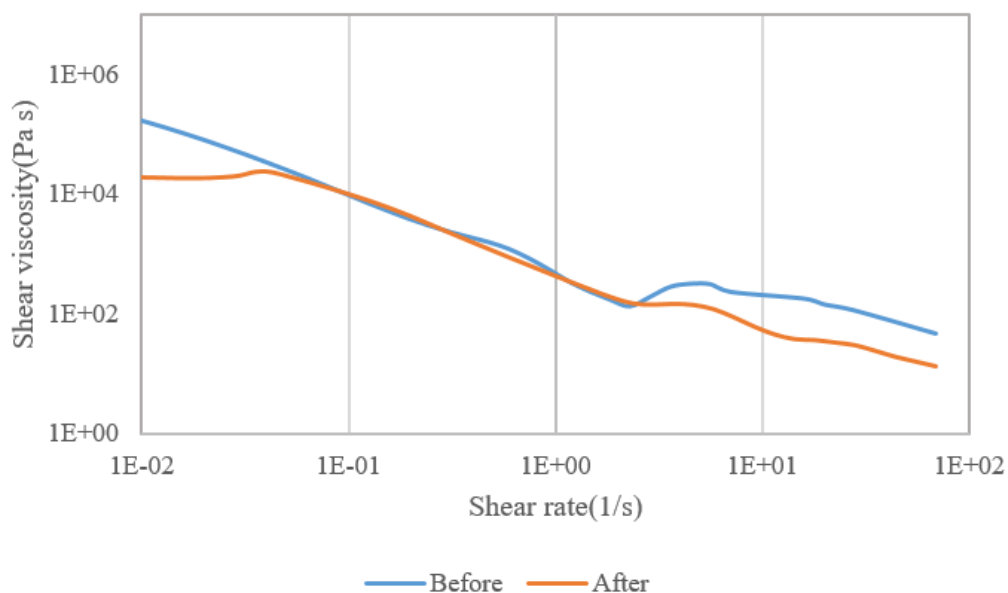


**Figure 4.16:** Shear rate vs viscosity comparison of ink (PEG 1:0.9) with and without boundary lubricant (Composition before: 1:0.9 -  $[\text{TiO}_2]$ : [10% PEG solution] and After: 1:0.9:0.1 -  $[\text{TiO}_2]$ : [10% PEG solution]: [Lubricant]).

#### 4.4.3 Effects of Additives

From the previous investigation, it was found that the 1:0.9 PEG ink along with the implemented boundary lubricant (1:0.9:0.1 -  $[\text{TiO}_2]$ : [10% PEG solution]: [Lubricant]),



**Figure 4.17:** TiO<sub>2</sub> impeller produced before (left) and after (right) adding the boundary lubricant (Composition before: 1:0.9 - [TiO<sub>2</sub>]:[10% PEG solution] and After: 1:0.9:0.1 - [TiO<sub>2</sub>]:[10% PEG solution]:[Lubricant]).

produced the best result for the DIW process. As was stated before the system of PEG and titanium dioxide was stable compared to the plain mix of water and titanium dioxide. This is due to the hydrophilic properties of the polymer, coordinating with water, which causes the long polymeric chains of PEG to become entangled among the solid particles of titanium dioxide, creating a stable system without separation of the liquid (see Figure 4.18 A and B). The proposed system structure also matches the one described in the jamming theory that was applied to a PEG-based system mentioned earlier.

SEM images of the samples demonstrate that PEG had a medium binder effect on the structural integrity, as shown in Figure 4.18 C and D. This makes the product

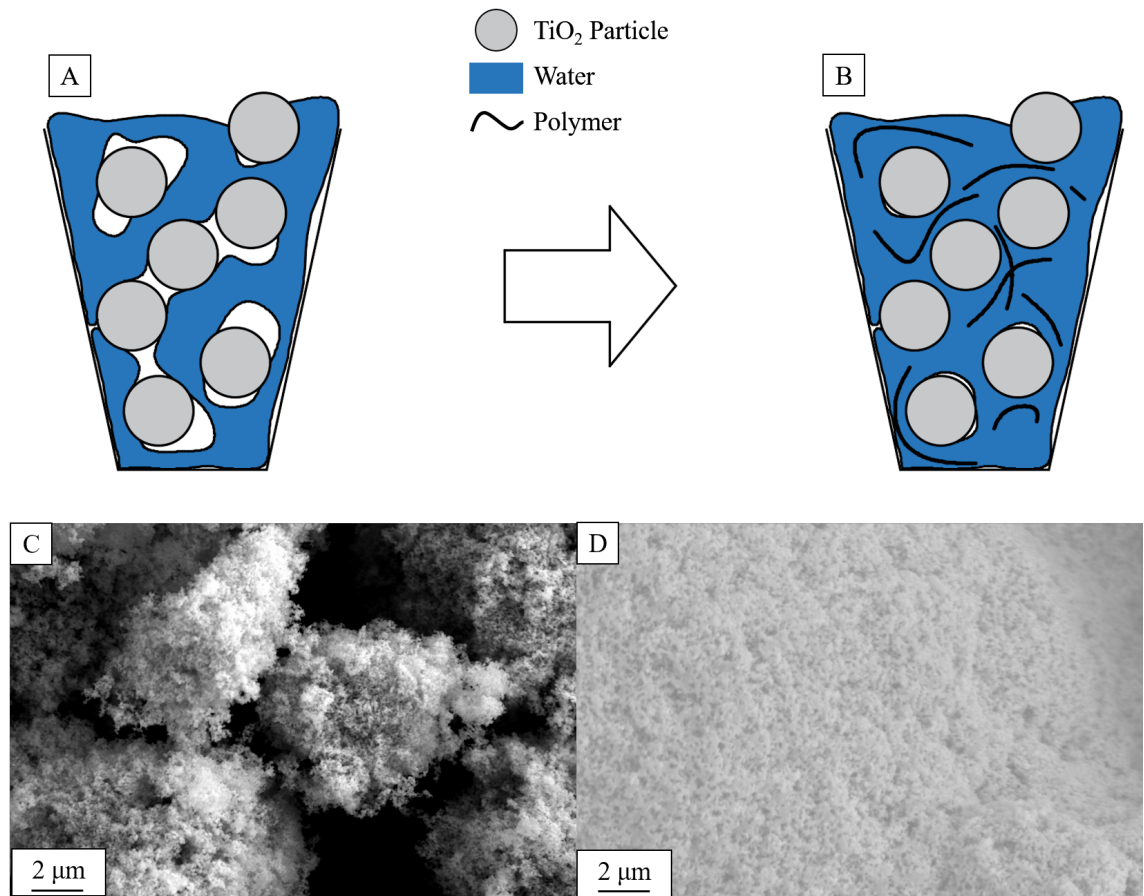


**Figure 4.18:** The effect of PEG onto the ink. A: The system schematics before the addition of PEG; B: The system schematics with PEG added; C: SEM image of dried water-based ink (1:0.9 - [TiO<sub>2</sub>]:[Water]); D: SEM image of the dried PEG-based ink (1:0.9:0.1 - [TiO<sub>2</sub>]:[10% PEG solution]:[Lubricant]).

less brittle and produce less of the residue powder when handled. It is also visible that particles are linked with solidified PEG after its application (Figure 4.18 D). This finding removes the necessity for an additional binder that is typically required for a green body to maintain its shape [23].

Besides, such entrapment of water reduces the migration of water molecules from

the paste during the DIW process as shown in Figure 4.19. This conclusion was made due to the increased viscosity of the paste before and after the DIW process, which has resulted in the requirement to increase the extrusion pressure as the DIW process continued [24].

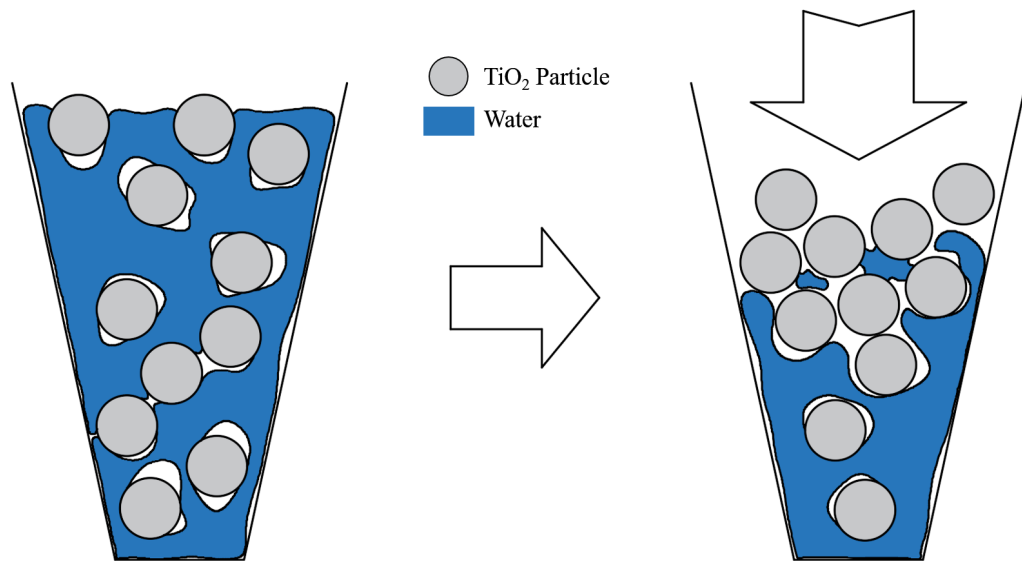


**Figure 4.19:** The migration of water under the applied pressure in the unstable ink.

#### 4.4.4 Drying Behaviour

After the extrusion, it was found that produced samples tend to shrink, which was associated with drying. This shrinkage was measured to be around 10 % of the original dimensions, happening uniformly in all directions and causing samples to crack if printed directly on the printing bed. To mitigate the cracking every sample was printed on a 3 mm tall support. This technique not only removed the necessity for additional treatment of the printing bed [25], but also removed the requirement

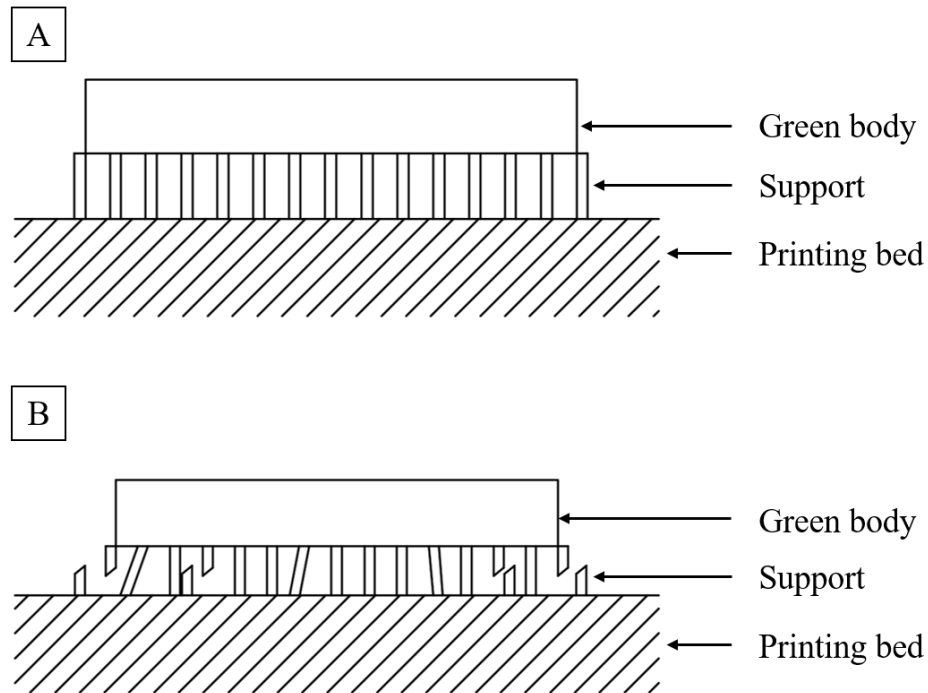


**Figure 4.20:** The effect of the drying-induced shrinkage on the support. A: After printing; B: After drying and shrinking.

of a binder or any gelling agent that are widely used in ceramic DIW [10, 18, 23]. Figure 4.20 implies three parallel processes that happen upon drying. First is the snapping of the support structure that compensates shrinkage. The second occurs due to the low contact area of the printing bed and supports reduced, compared to the area of the whole sample, which allows some of the support to easily separate from the printing bed and accompany the drying induced shrinkage without any cracks. The third process is represented as leaning of the support, where the support structure is following the shrinking green body but is still attached to the printing bed. The third type is typically observed around the outer side of the product and usually follows the second type as due to the stretch and deformation it becomes

more susceptible for separation from the printing bed.

#### 4.4.5 Summation

The produced investigation, on the titania inks, resulted in a comprehensive parameter collection for the paste to be utilised in DIW. Different paste compositions were rheologically tested and then applied to the DIW in order to link rheological behaviour and extrudability potential. As a result, it was discovered that pastes that display a shear-thinning behaviour and high extent of remained deformation after the creep are the best candidates for DIW process based on the consecutive extrudability tests. Additionally, the results produced for the PEG-based pastes indicated the presence of a dilatancy peak in a region of 2 to 7 s<sup>-1</sup>. This peak appeared due to the jamming phenomenon that happens in systems of spherical particles and long polymeric chains. The peak, however, was almost eliminated after the implementation of the surface lubricant. This lubricant reduced the friction between particles, which reduced their agglomeration at the above-mentioned shear rate region. Eliminating the peak resulted in a better flowing paste and, therefore, increased the quality of the final object. Additionally, the new technique of printing was developed with the utilisation of support structures, which allow printing of pastes with any degree of shrinkage without any cracks or deformation, removing the requirement for any specific treatment of the printing bed.

## 4.5 Conclusion

This chapter was set to adopt the Direct Ink Writing (DIW) technique to additively manufacture titania products to their final or near-net shape. The investigation in the feasibility of the DIW process was done in two phases: DIW optimisation and rheological investigation of highly loaded titania pastes.

Typically desktop DIW 3D printers are developed to work with clay, which, unlike other ceramic mixtures, possess great level of stability. Therefore, in order to apply a new material to this 3D printer, the modification was inevitable. Commercial DIW machines are available in two types: direct extrusion of clay through the feed cylinder and a screw head that is used after feed cylinder to create an additional driving force to extrude the material. However, both of these designs were established to be unsuitable for titania 3D printing. The first design extruded more material than required creating an undesirable defect in a product. The Screw head design resulted in an increased extrusion pressure and generated waste.

To optimise the DIW 3D printer its design was reworked to ensure best flow control of the extruded material. This was done by implementing two solenoid valves: one normally open and another normally closed. The principle was to stop pressure supply when the material was not required to be deposited with the first valve and then vent the remaining pressure from the feed cylinder with the help of the second valve. However, along with the physical implementation, it was necessary to modify software code in order to activate previously installed valves. As a result,

a Matlab script was compiled that scanned pre-generated g-code and looked for the lines where extruder needed to stop and start. This modification ensured the constant flow of the material.

Another modification was done to the nozzle that was used in the DIW machine. The shape of that nozzle was the so-called needle that according to observation was a cause of constant blockages. An alternative shape of the nozzle was investigated to be cone-shaped nozzle. The preliminary calculation showed that along with the conical geometry pressure drop was almost 10 times less when compared to the one generated across the needle. This meant that with the replacement of needle to cone it was possible to reduce required pressure for the process and negate blockages.

After the 3D printer was ready to work with new material, mainly titanium dioxide, it was important to understand the flow behaviour of the material. For this titania inks with varied composition have been tested on their rheological properties such as viscosity, elasticity, thinning or thickening behaviour. Obtained results were connected with the extrudability results that showed that the only ink that could be printed was PEG 1:0.9. This ink possesses mostly viscous properties with no elastic reformation happening in the creep and recovery test. The remained test showed that PEG 1:0.9 was a shear-thinning material which is common for the materials applied in DIW. However, it was also found that all mixtures of PEG, water and  $\text{TiO}_2$  were creating a dilatancy peak in the range of 2 to 7  $\text{s}^{-1}$ . Such peak meant that ink became more viscous within that shear rates. This was found to be the cause of occasional blockages that were occurring from time to time. In order to eliminate

such behaviour, it was decided to implement a surface lubricant that according to the results eliminated the above-mentioned peak.

Additionally, the further investigation of the best performing ink showed that the yield point was 41.7 Pa, which means that the ink will react fast enough onto the forces that drive the ink to flow or to stop flowing. This parameter is essential to all inks applied in DIW and, therefore, ensures the best properties of the final product.

All of the above improvements resulted in the consistent and highly precise DIW of titania.

## References for Chapter 4

- [1] Y. Wang, C. Wen, P. Hodgson, Y. Li, “Biocompatibility of TiO<sub>2</sub>nanotubes with different topographies”, *Journal of Biomedical Materials Research Part A* **2014**, *102*, 743–751.
- [2] H. Tang, K. Prasad, R. Sanjinès, P. E. Schmid, F. Lévy, “Electrical and optical properties of TiO<sub>2</sub>anatase thin films”, *Journal of Applied Physics* **1994**, *75*, 2042–2047.
- [3] M. A. Torres Arango, D. Kwakye-Ackah, S. Agarwal, R. K. Gupta, K. A. Sierros, “Environmentally Friendly Engineering and Three-Dimensional Printing of TiO<sub>2</sub> Hierarchical Mesoporous Cellular Architectures”, *ACS Sustainable Chemistry & Engineering* **2017**, *5*, 10421–10429.
- [4] H. Haugen, J. Will, A. Köhler, U. Hopfner, J. Aigner, E. Wintermantel, “Ceramic TiO<sub>2</sub>-foams: characterisation of a potential scaffold”, *Journal of the European Ceramic Society* **2004**, *24*, 661–668.

- 
- [5] R. Singh, P. D. Lee, J. R. Jones, G. Poologasundarampillai, T. Post, T. C. Lindley, R. J. Dashwood, “Hierarchically structured titanium foams for tissue scaffold applications”, *Acta Biomaterialia* **2010**, *6*, 4596–4604.
- [6] D. Hu, W. Xiao, G. Chen, “Near-Net-Shape Production of Hollow Titanium Alloy Components via Electrochemical Reduction of Metal Oxide Precursors in Molten Salts”, *Metallurgical and Materials Transactions B* **2013**, *44*, 272–282.
- [7] D. Macri, D. Sofia, D. Barletta, MassimoPoletto, P. Lettieri, “Selective Laser Sintering of Titania Powder: Experiments and Modelling”, **2017**.
- [8] A. E. Danks, S. R. Hall, Z. Schnepp, “The evolution of ‘sol-gel’ chemistry as a technique for materials synthesis”, *Materials Horizons* **2016**, *3*, 91–112.
- [9] J.-Y. Lee, J. An, C. K. Chua, “Fundamentals and applications of 3D printing for novel materials”, *Applied Materials Today* **2017**, *7*, 120–133.
- [10] E. Peng, D. Zhang, J. Ding, “Ceramic Robocasting: Recent Achievements, Potential, and Future Developments”, *Advanced Materials* **2018**, *30*, 1802404.
- [11] R. A. Buswell, W. R. Leal De Silva, S. Z. Jones, J. Dirrenberger, “3D printing using concrete extrusion: A roadmap for research”, *Cement and Concrete Research* **2018**, *112*, 37–49.
- [12] J. A. Lewis, G. M. Gratson, “Direct writing in three dimensions”, *Materials Today* **2004**, *7*, 32–39.

- [13] X. B. Chen, J. Kai, M. Hashemi, “Evaluation of Fluid Dispensing Systems Using Axiomatic Design Principles”, *Journal of Mechanical Design* **2006**, *129*, 640–648.
- [14] J. Wang, “Theory of flow distribution in manifolds”, *Chemical Engineering Journal* **2011**, *168*, 1331–1345.
- [15] P. S. Bernard, “Fluid dynamics / Peter S. Bernard”, **2015**.
- [16] F. Yu, H. Wang, J. Yang, J. Gao, “Effects of organic additives on microstructure and mechanical properties of porous Si<sub>3</sub>N<sub>4</sub> ceramics”, *Bulletin of Materials Science* **2010**, *33*, 285–291.
- [17] X. Wei, E. Peng, Y. Xie, J. Xue, J. Wang, J. Ding, “Extrusion printing of a designed three-dimensional YBa<sub>2</sub>Cu<sub>3</sub>O<sub>7-x</sub> superconductor with milled precursor powder”, *Journal of Materials Chemistry C* **2017**, *5*, 3382–3389.
- [18] C. Minas, D. Carnelli, E. Tervoort, A. R. Studart, “3D Printing of Emulsions and Foams into Hierarchical Porous Ceramics”, *Advanced Materials* **2016**, *28*, 9993–9999.
- [19] J. Ge, Z. Tan, W. Li, H. Zhang, “The rheological properties of shear thickening fluid reinforced with SiC nanowires”, *Results in Physics* **2017**, *7*, 3369–3372.
- [20] R. S. Farr, J. R. Melrose, R. C. Ball, “Kinetic theory of jamming in hard-sphere startup flows”, **1997**, *55*, 7203–7211.
- [21] T. Mezger, *The Rheology Handbook*, 4th Edition, Vincentz Network, **2014**.

- 
- [22] S. Tang, Z. Fan, H. Zhao, L. Yang, F. Liu, X. Liu, “Layered extrusion forming—a simple and green method for additive manufacturing ceramic core”, *The International Journal of Advanced Manufacturing Technology* **2018**, *96*, 3809–3819.
- [23] R. Riedel, I. Chen, *Ceramics Science and Technology, Volume 3: Synthesis and Processing*, Wiley, **2011**.
- [24] X. P. Chi, S. Yang, J. R. G. Evans, “Extrusion Pressure Generated in High Alumina Content Paste Extrusion”, DOI 10.1109/icma.2010.28.
- [25] L. Chen, X. Tang, P. Xie, J. Xu, Z. Chen, Z. Cai, P. He, H. Zhou, D. Zhang, T. Fan, “3D Printing of Artificial Leaf with Tunable Hierarchical Porosity for CO<sub>2</sub> Photoreduction”, *Chemistry of Materials* **2018**, *30*, 799–806.

# Chapter 5

## Optimisation of the Near-net-shape Electrochemical Metallisation Process

*This chapter addresses the main reasons behind the shape deformation that happens during the molten salt electrolysis and investigates possible solutions to mitigate such deformation. Furthermore, the properties and the cost evaluation are analysed to evaluate the conventional feasibility.*

### 5.1 Introduction

Chapter 2 established the most demanding challenges associated with the extraction and fabrication of titanium. These challenges are mostly caused by the chemical

and mechanical properties that metallic titanium possesses, including low Young's modulus, low heat dissipation, high reactivity, etc [1, 2]. To account for these properties, conventional production routes were made complex due to the requirement of an inert atmosphere, increased amount of coolant, increase wear of milling tools, etc [3–5]. Increased complexity inevitably sets the price of titanium to be high, limiting the wider use and accessibility of such a light and strong metal as titanium [6].

In order to mitigate the effects of the above-mentioned challenges, a new method was developed where the manufacturing stage is done before the extraction, which reduces the amount of work done with the metallic titanium. To achieve this the in situ metallisation phenomenon of the FFC-Cambridge Process is exploited that allows the preshaped feedstock material to maintain its shape [7, 8]. Such an approach has already been applied to produce different shapes from different materials, ranging from zirconium alloys and tantalum to titanium and its alloys [8–11]. However, all previous studies have one common shaping stage which is a slip casting. Slip casting requires a ceramic slurry to be filled into a mould that can be produced by different means. In this work, the Direct Ink Writing (DIW) of titanium dioxide is utilised as a shaping method that, when connected with the FFC-Cambridge Process, forms the Near-net-shape Electrochemical Metallisation (NEM) Process. The selection of the DIW was done for its simplistic nature and affordability. This, however, means that the quality of the product can only be suitable for near-net-shape fabrication. Application of more advanced techniques such as selective laser sintering, binder jetting printing or stereolithography can increase the final quality

to match and even surpass that of the conventional titanium AM methods [12–14]. Therefore, this work is aimed at the development of the NEM Process, which was proven to be more environmentally friendly than conventional alternatives and also capable of reducing the cost of such expensive metal like titanium.

## 5.2 Characterisation of Feedstock

### 5.2.1 Electrochemical Characterisation

In order to ensure the optimal parameters and to understand the mechanism of the reduction of the used feedstock (99.5% TiO<sub>2</sub> Aladdin, 60 nm, rutile), cyclic voltammetry was used, which, additionally, may point on the potential obstacles for the complete reduction. For this, a notched molybdenum wire was first analysed via CV method described in Section 3.2.4 to achieve the baseline reading. After that, a similar wire was loaded with TiO<sub>2</sub>, which resulted in Figure 5.1.

On the obtained CV three forward and four reverse peaks are visible (Figure 5.1 R1, R2, R3 and O1, O2, O3, O4, respectively). The forward peaks (cathodic peaks) represent the reduction of the analysed material, which in this case is TiO<sub>2</sub>, and the reverse (anodic peaks) are the subsequent oxidation of the material. As the cyclic voltammogram of TiO<sub>2</sub> is thoroughly investigated the reaction behind every peak can be found [15, 16]. Therefore, the first peak can be allocated to the initial stage of reduction where titanium (IV) is transformed into titanium (III):

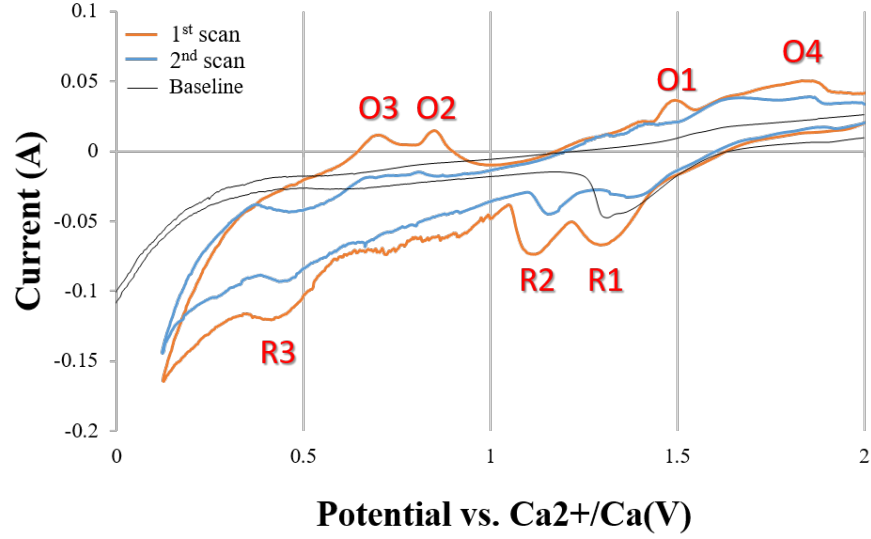
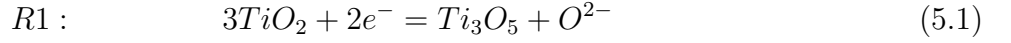
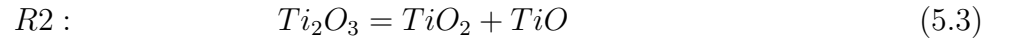
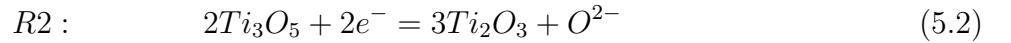


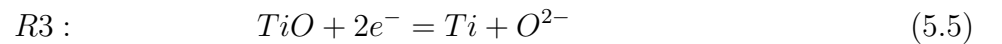
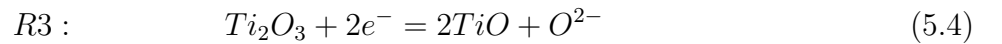
**Figure 5.1:** CV of the notched Mo electrode loaded with  $TiO_2$ , recorded at the scan rate of 1 mV/sec.

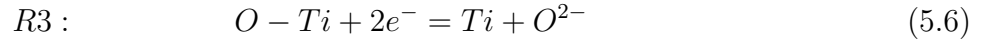


Following this the next transformation, which is associated with the peak 2, is dedicated to the formation of  $Ti_2O_3$  and its immediate decomposition to  $TiO_2$  and  $TiO$ :

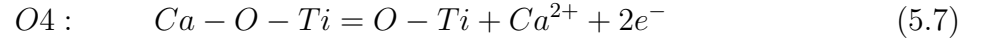


The third peak consists of the final transformation of oxides into titanium and an additional desorption of oxygen from the surface of titanium (O-Ti) [16]:





When the current is reversed the oxidation happens within the described reactions. Therefore, the peaks that are labelled in Figure 5.1 as O# represent the reverse reactions from their respective forward reactions. The additional peak O4 represents the removal of calcium ions from the intermediate compound of Ca-O-Ti following the reaction 5.7.



Allocation of the reaction to a specific potential allows to understand the selection of the voltage value for the reduction of precursors. According to the previous studies, the reduction at the potentials close to peaks R1 and R2 can produce perovskites [15]. This was described to happen due to the high concentration of oxygen in the pores around the precursor and the contact with the hot  $CaCl_2$ , leading to the formation of the before mentioned perovskites [17].

Important to notice that during the reduction oxygen ions will diffuse in the salt and reach the surface of the anode. Where oxygen ions have two routes: one is to react with carbon (Anode) and produce  $CO_2/CO$ , and another is to combine and form  $O_2$  with the first pathway to be predominant. Due to this combination, the anodic material is being consumed, which is a considerable issue in the field of molten salt electrolysis. The produced  $CO_2/CO$  have a chance to further be dissolved into the melt and upon the migration to the cathode can be reduced to carbon, which tends to form carbides with the product (i.e. unwanted side-

products). This reduction, however, has not been shown to play an important role as most of the carbides are produced from the floating carbon. Such floating carbon is formed when oxygen ions combine with anode thus deteriorating its surface and releasing some amount of carbon particles into the molten salt.

From this evaluation, it became clear that the reduction of  $\text{TiO}_2$  is a multi-step process that is required to be completed in order to achieve a complete reduction. As was stated before the reduction at an insufficient potential can result in the formation of intermediate products. Therefore, it is important to ensure that the system is not susceptible to an IR drop, or a reduction of potential or vantage due to a weak connection or high resistance. Due to this, every experiment was thoroughly prepared, all the connections were checked to be tight.

## 5.2.2 SEM

The morphological evaluation is essential for the prediction of physical properties of the product and its association with the initial state makes it possible to observe a morphological transformation.

### 5.2.2.1 Powder

The direct reduction of the feedstock in powdered form was conducted to observe morphological change within the structure of the precursor under the constant voltage (3.2 V) electrolysis in molten  $\text{CaCl}_2$  at 900 °C as discussed in Chapter 3. For this, SEM images were taken for raw feedstock and reduced samples that can be

found in Figures 5.2 and 5.3, respectively.

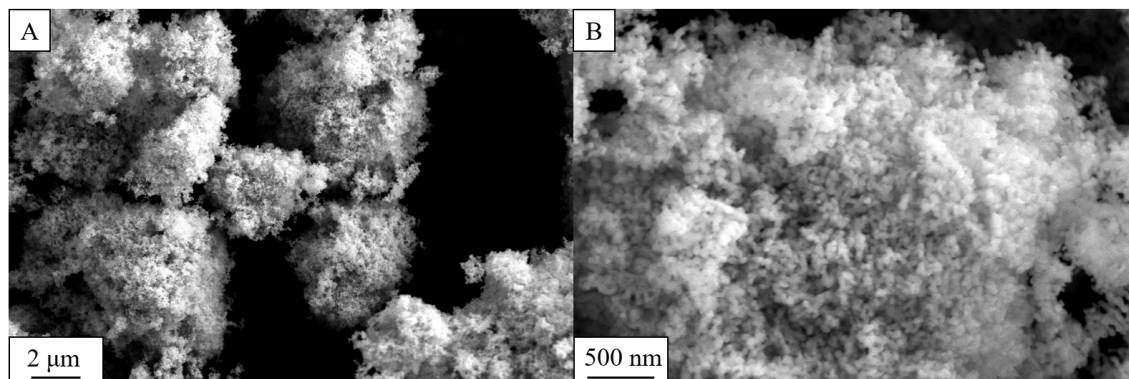


**Figure 5.2:** The SEM image of the powdered TiO<sub>2</sub>; A: at the scale of 2 μm; B: at the scale of 500 nm.

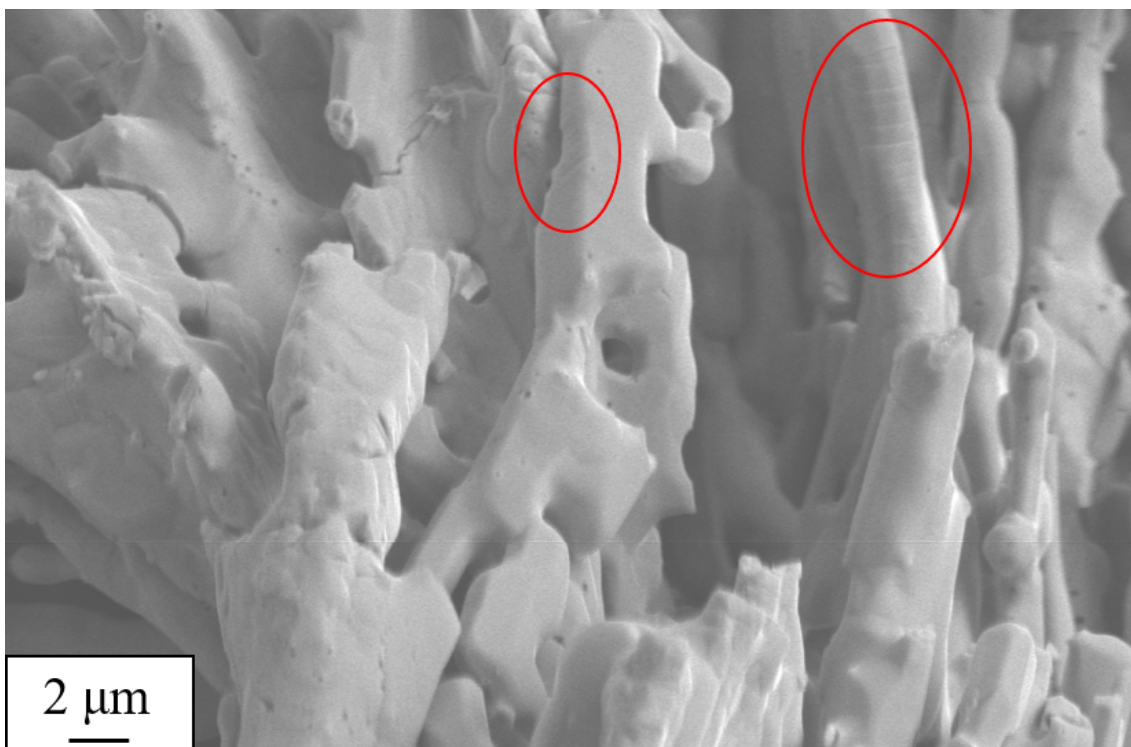


**Figure 5.3:** The SEM image of Ti derived from 60 nm TiO<sub>2</sub>. Red ovals indicate the areas with crystal growth steps.

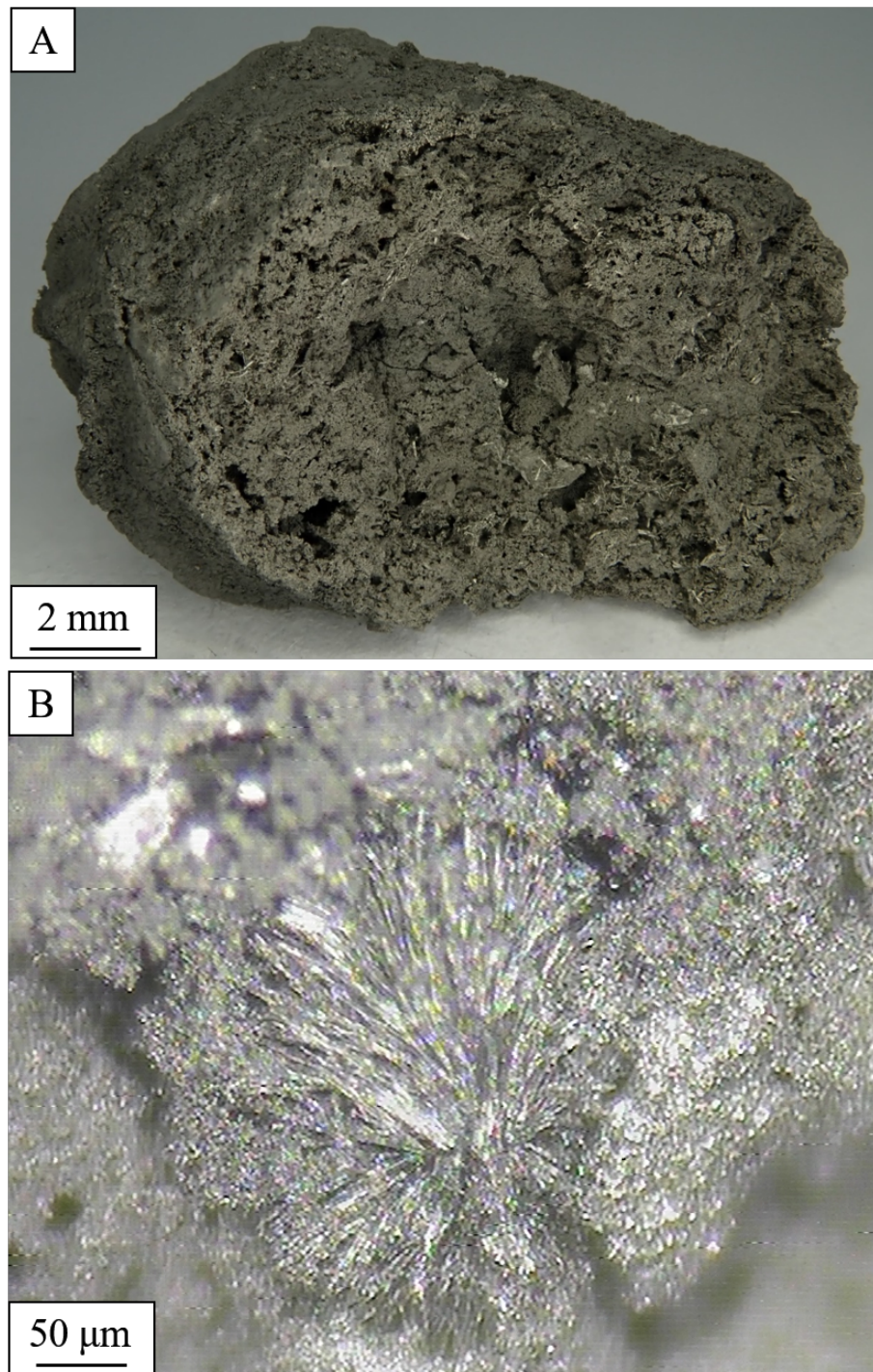


**Figure 5.4:** The optical images of A: the whole titanium sponge (Macro scale) and B: the individual crystals (Micro scale).

Figure 5.2 shows that powder is arranged in big agglomerates that are made of nano-sized oval-shaped granules. When reduced, however, the loose powder particles form an interconnected titanium sponge, which, as shown in Figure 5.4 A, includes visible shiny spikes all over the inside area. A closer look at an SEM (Figure 5.3) or an optical microscope (Figure 5.4 B) images revealed the structure of those spikes. Such transformation has not been reported before and deserves further study. However, some theories were proposed regarding the observation after the results were reproduced:

- The dissolution of Ti into the solution and local saturation that led to the consecutive crystallisation.

This theory is originated from the fact that those structures were localised in pockets of salt inside the packed powder. The creation of those pockets can also indicate on the reformation of the structure as it develops a structure with the relatively low surface area from the typically observed sponge. Another factor for this theory is the presence of the crystal growth steps on the produced pillar (Highlighted in red ovals in Figure 5.3) [18].

- The transformation of some of the feedstock into perovskites with the following reduction.

The observed shapes make it clear that the produced structure has some similarities as seen in Figure 5.5. In addition, due to this phenomenon being observed only in the centre part of the packing, it can be assumed that the

hindering in the diffusion of oxygen created a zone of high oxygen concentration in the salt, which usually helps the production of perovskites [19].

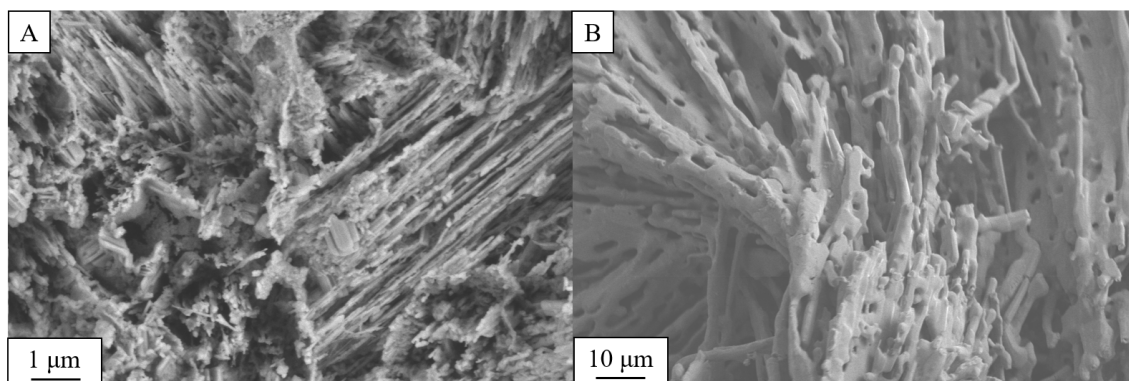


**Figure 5.5:** The SEM images of A: Perovskite spikes; B: Titanium spikes.

This finding has a great potential as reducing the surface area means the reduction of the persistent oxide layer, which in return reduces the amount of oxygen in the product. Such reduction can allow the FFC-Cambridge Process to reach higher efficiency in the production of ultra-pure titanium.

### 5.2.2.2 DIW

The addition of binder dramatically changes the structure of both the precursor and the reduced product. Figure 5.6 A shows that when PEG is added in the weight ratio of 1  $\text{TiO}_2$  to 0.9 of 10% aqueous solution of PEG, the particles are arranged in bulk but still have high porosity. When reduced this takes a shape of a typically observed nodular structure showed on Figure 5.6 B [7, 20].

This, however, changed when the precursor was made in the shape of a hollow sphere. As seen from Figure 5.7 A the inside surface of the sphere was produced into

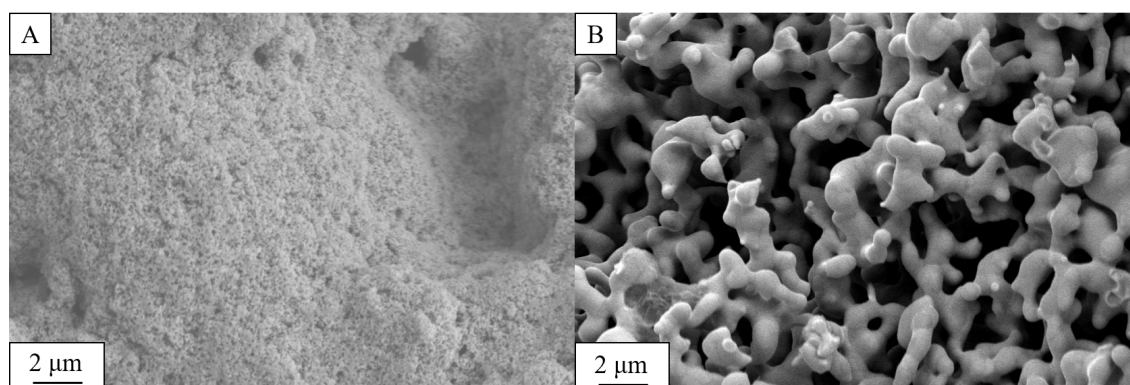


**Figure 5.6:** The SEM images of A: the precursor after the DIW process (1:0.9 PEG); B: the reduced precursor.

a solid layer of titanium. This was again associated with the spiking phenomenon described before, due to the location of this side being in an enclosed  $\text{TiO}_2$  body. Such surface had a shiny glance due to the dramatically reduced porosity as shown in Figure 5.7 B.

These observations made it clear that the metallic substance, produced during the reduction of the nano-sized  $\text{TiO}_2$ , is sintered together creating larger globules making the nodular structure. This along with the removal of oxygen reduces the size of the final product. Also, it was found that the used feedstock could produce the larger than normal structure (Figure 5.6 B compared to Figure 5.5 B and Figure 5.7 A) opening an opportunity for further research of such a phenomenon.

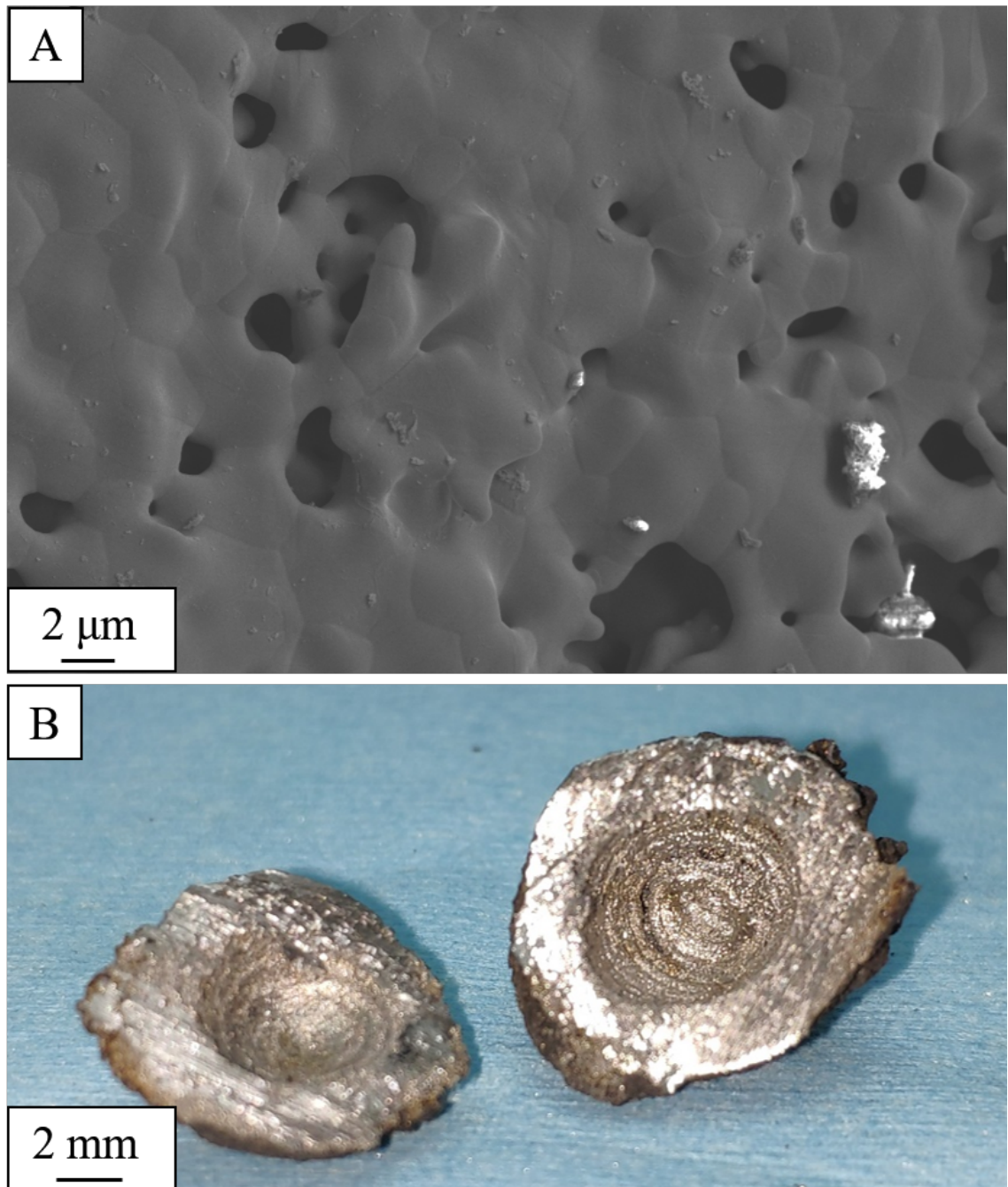


**Figure 5.7:** The inside of hollow titanium sphere. A - The SEM image of the internal surface of the reduced hollow titanium sphere. B - The photo of the internal section of the hollow titanium sphere.

### 5.3 Sintering and Porosity

The dried green products after DIW possessed low physical strength, which made them highly susceptible to braking during transportation and/or the attachment to the electrode before the reduction. This issue was addressed via the sintering process. The applied heating profile was adapted from the work of Tang, Fan et al. (2018) [21], where a sample was slowly heated up to 600 °C and held there to ensure that all additives were decomposed. Further heating and cooling were more rapid but still within the 1 °C/min region. The application of the greater heating rates caused samples to express high warping and crack formation. For the test 3 temperatures were selected 900 °C, 1100 °C and 1300 °C, the SEM images of the cross-section is presented in Figure 5.8.

Figure 5.8 A-D shows the almost exponential growth of grains, which indicates a form of stronger bonding of the material making it easier to handle. However, this also indicates the fact that the resulted product possesses lower porosity.

Due to the purpose of the additive manufacturing of titania was the consecutive reduction in the molten salt, it was necessary to maintain some degree of porosity for it is one of the driving factors of the complete reduction process [17, 22, 23]. Table 5.1 summarises the porosity of the produced green and sintered samples. When reduced the samples showed comparable porosity of around 50% with a slight increase in density from “not sintered” to “1100 °C” (Figure 5.8 A' - C'). This, however, was different for samples sintered at 1300 °C that appeared to be more porous than the

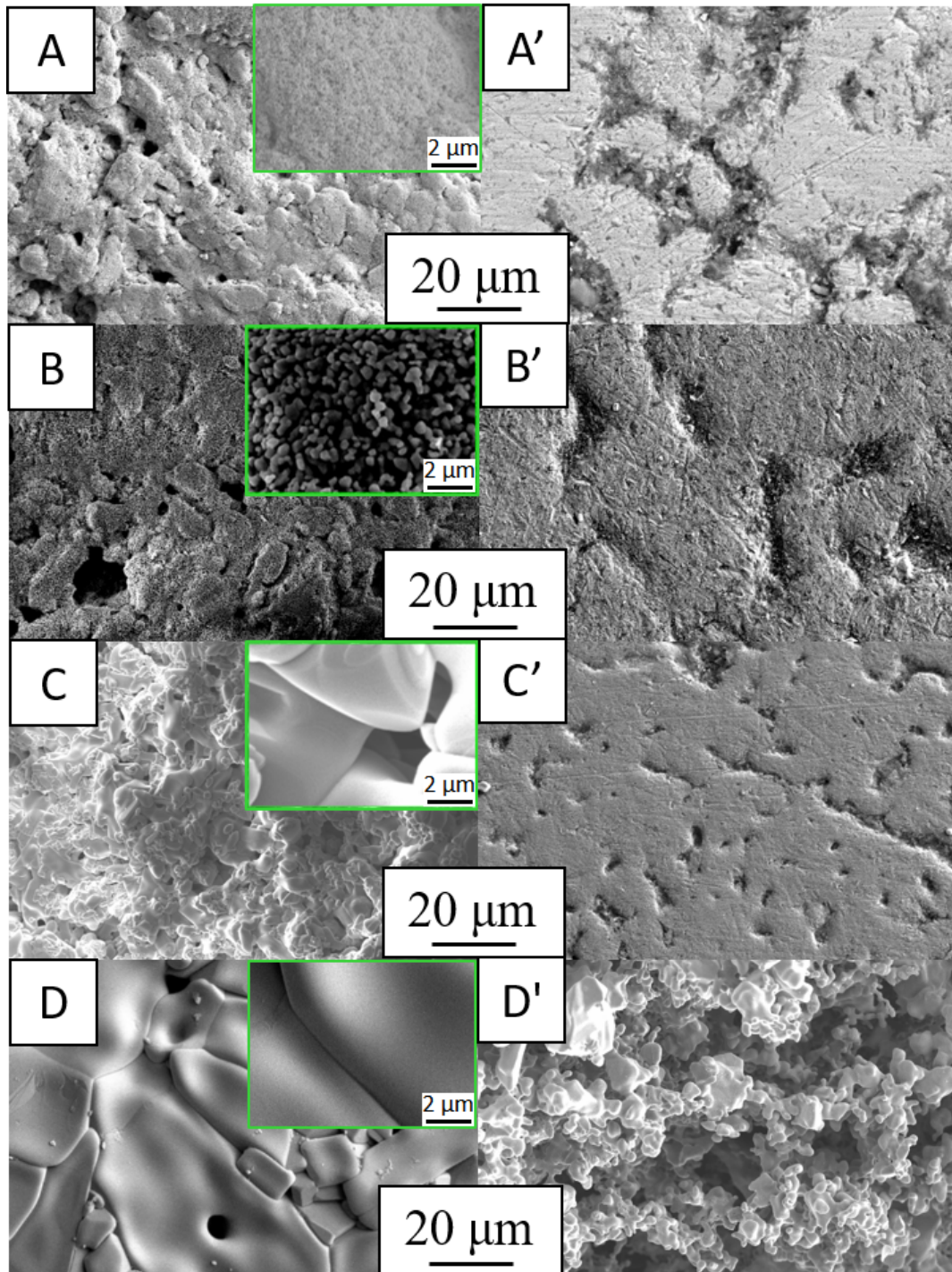


**Figure 5.8:** SEM images of titanium dioxide samples sintered at different temperature (A–not sintered; B–900 °C; C–1100 °C; D–1300 °C) and their respective morphology after reduction (A'–not sintered; B'–900 °C; C'–1100 °C; D'–1300 °C).

rest, which is seen from Figure 5.8 A' - D'. The samples were comprised of less sintered particles, which can be associated with the slower reduction speed induced by the low porosity of the precursors. This slow reduction process reduced the time that newly produced metal would be sintering inside the reactor, thus, generating such a morphology.

**Table 5.1:** The measurement of porosity for titanium and titanium oxide samples produced via the NEM Process.

		Sintering Temperature (°C)			
		Not sintered	900	1100	1300
Porosity	TiO <sub>2</sub>	71%	59%	40%	34%
	Electrolytic Ti	53%	50%	45%	49%

## 5.4 Deformation

Upon reaching the reduction stage of the NEM Process it was noted that the products possess a high degree of deformation. This deformation had a different degree depending on the scale of the desired product and their shape. As seen from Figure 5.9 the deformation of the logo of the University of Nottingham (C-D) precursors was dramatic when the tooth implants (A-B) were undamaged. Additionally, the hollow samples with a complex internal structure like a hydrocyclone (Figure 5.9 E-F) expressed a slight change in the middle part of the sample, which overall seemed

more resistant against deformation than the logo. In order to compete with the commercially available methods, it is important to reduce or mitigate such defects within the products.

After the reduction, it was found that samples were warped and/or cracked. The potential causes were divided into chemical and physical. With chemical to be caused by the material transformation that happens within the molten salt, which is mostly allocated to the volumetric expansion during the formation of perovskites [22]. The perovskitisation has been a hindering factor in the improvement of current efficiency as it was shown to happen in the initial hours of the reduction and to form within the product whenever the diffusion of oxygen was not sufficient [19, 24]. It was reported that the expansion varies from 10 to 23 % compared to the precursor [22]. In order to investigate the effect of such expansion onto larger scale samples, two experiments were performed. First, the sample was left in the molten salt for 10 hours and then was reduced over another 24 hours. This was done to let  $\text{TiO}_2$  precursor to react with all  $\text{Ca}^{2+}/\text{CaO}$  from the salt. The second test was to apply low cell voltage (2 V) to form perovskite electrochemically just as was described by Mohanty, Mishra et al. (2012) [25]. None of the tests, however, had any effect onto the final shape. This can be associated with the relatively high porosity that mitigates the change in the volume or a negligible amount of  $\text{Ca}^{2+}/\text{CaO}$  within the salt.

Physical deformation can happen on two occasions: First is caused by the difference in density, which inevitably happens during the first stages of the reduction

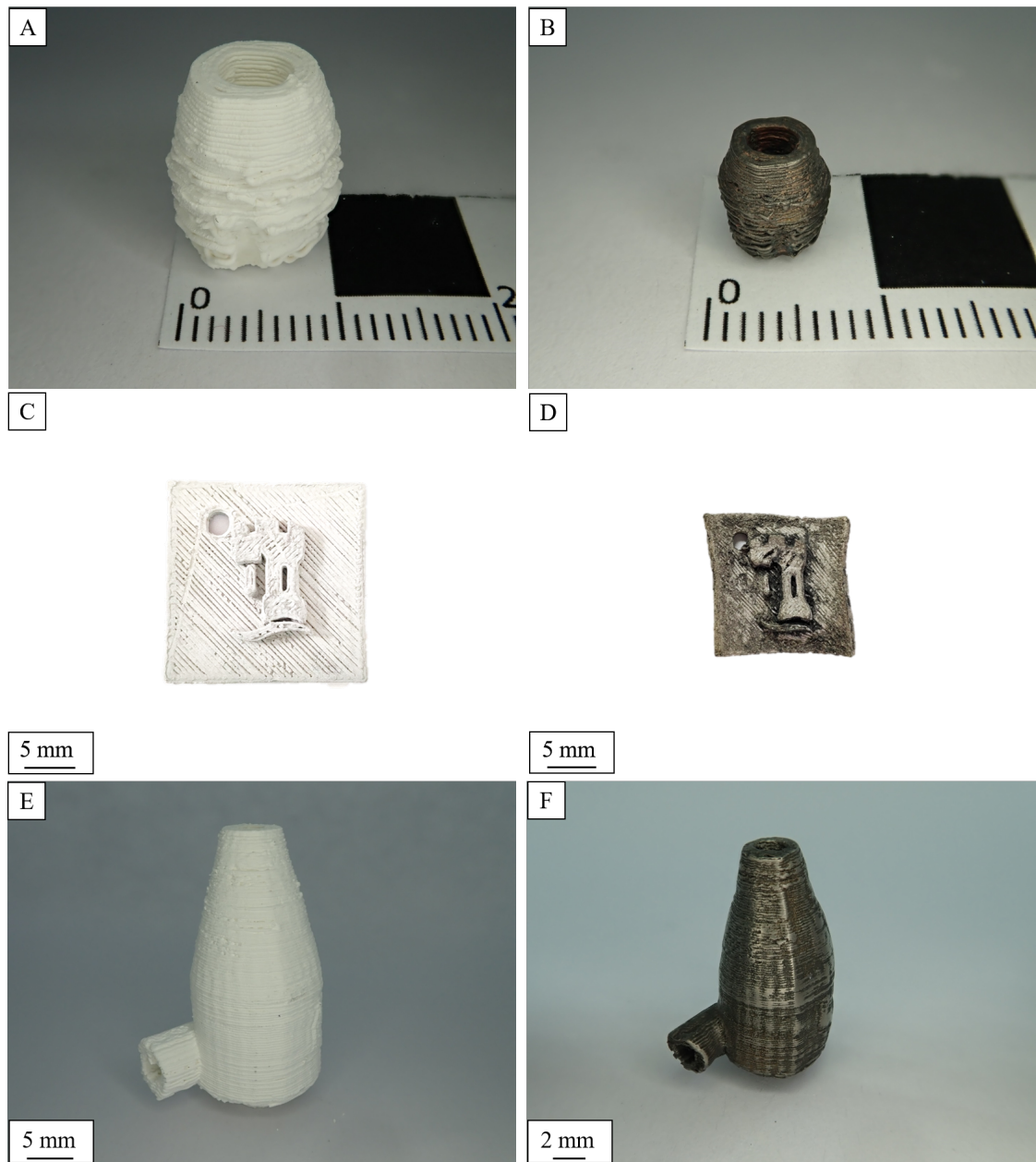


**Figure 5.9:** Examples of the precursors and the respective titanium counterparts produced via the NEM Process: A: TiO<sub>2</sub> tooth implant; B: Titanium tooth implant; C: TiO<sub>2</sub> logo of the University of Nottingham; D: Titanium logo of the University of Nottingham; E: TiO<sub>2</sub> Hydrocyclone; F: Titanium Hydrocyclone. [Precursor ink composition 1:0.9 PEG; Metallisation parameters: constant 3.2V, 900 °C CaCl<sub>2</sub>]

(i.e.  $\text{TiO}_2$  and Ti). Such difference at such elevated temperature as 900 °C causes materials to sinter at a not even rate, due to materials with different density express different expansion properties. This is more visible on flat samples that are hard to produce flat as they tend to warp due to the above-mentioned phenomenon [26]. During the reduction of a complex structure, however, the above principle yields in a complete deformation and tearing of adjacent features. The second reason is the sintering itself, which when done at an accelerated rate causes the material to uncontrollably shrink. This especially crucial for structures with high porosity as described in Table 5.1. This criterion is important as the total shrinkage of the metallised body can reach 50% compared to the green part.

In order to eliminate any effect on the product from the first factor, a not sintered plate sample was prepared and wrapped in Ni foam to ensure that the sample's surface would metallise simultaneously from the whole area ensuring the nullifying effects of the forces induced through the sintering. This, however, did not improve the final shape of the product that was warped. Nonetheless, when samples were sintered prior to the experiment and wrapped as described above, the sample was successfully metallised with negligible shape change. This indicated that the second cause of physical deformation had a predominant nature in the observed defects. To investigate the effect of this phenomenon a more complex shape was utilised to allow for a more complex force distribution and match the real-world production requirements. The centrifugal impeller was designed and printed for this purpose as shown in Figure 5.10.

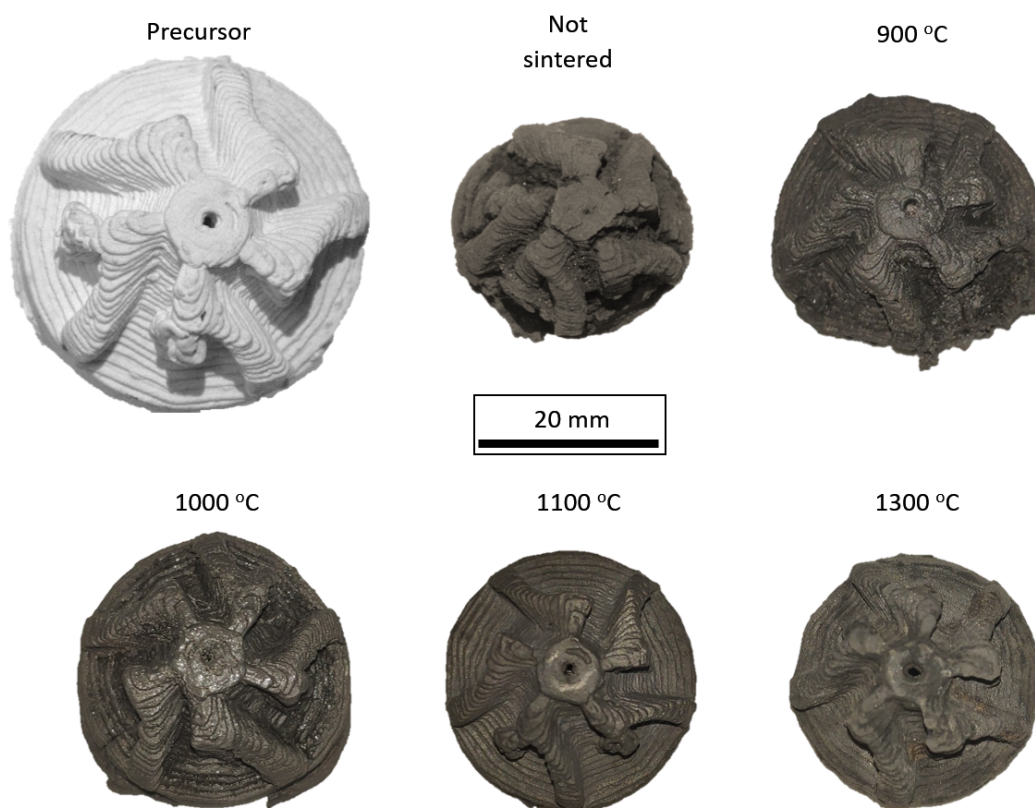


**Figure 5.10:** Product deformation comparison after 24h of  $\text{TiO}_2$  samples with different degree of sintering during constant voltage reduction (3.2 V) in molten  $\text{CaCl}_2$  (900 °C).

As seen from Figure 5.10 the deformation of the product is reduced along with the increased sintering temperature. The sample without sintering possessed the highest degree of deformation with torn marks at the connection of vanes and the main body. Following the increase of sintering temperature, it was noted that sample sintered at 1100 °C stopped having any signs of distortion. At 1300 °C, however, the reduction process was slowed due to the changed morphology of the precursor as discussed previously, which resulted in a weaker product with high oxygen content (See Figure 5.11). This indicated the only option of sintering at 1100 °C.

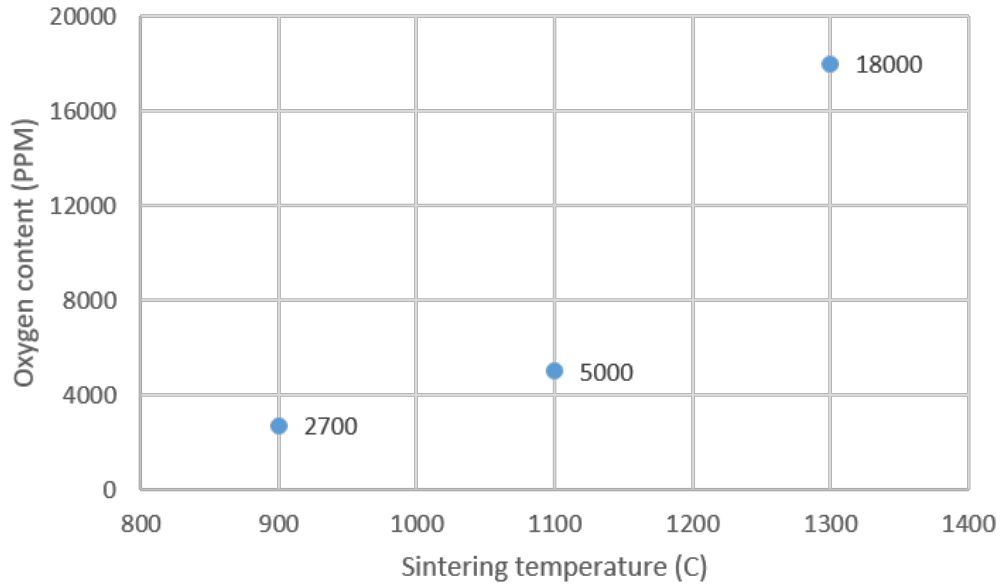


**Figure 5.11:** Oxygen content of titanium impellers produced via the NEM Process (Constant voltage of 3.2 V in 900 °C CaCl<sub>2</sub>) from TiO<sub>2</sub> precursors sintered at 900 °C, 1100 °C or 1300 °C.

As was stated before, the additional sintering occurs during the reduction, therefore, the adjustment of reduction parameters such as time and temperature can reduce the effect of the reduction. From these two parameters, time is directly linked to the final oxygen content [27]. The improvement is exponentially reducing leading to the huge efficiency problems that require a trade-off point, which is typically taken as 24 hours [28]. The temperature of reduction, however, has a higher impact on the system including reduced sintering and kinetics. To analyse the effect of electrolysis temperature on the final shape deformation a thin-walled titanium dioxide turbine was reduced at 600, 700, 800, 900 and 1000 °C. The lower temperature was achieved via the implementation of the eutectic salt mixture of lithium

and calcium chlorides. The following salt mixtures were used for the respective temperatures:  $\text{CaCl}_2$  (800-1000 °C);  $\text{LiCl}+\text{CaCl}_2$  (0.6  $\text{LiCl}/\text{LiCl}+\text{CaCl}_2$  - 600 °C; 0.27  $\text{LiCl}/\text{LiCl}+\text{CaCl}_2$  - 700-800 °C). All the experiments were conducted under the constant voltage of 3.2 V, against a graphite anode. Results can be seen in Figure 5.12 where samples reduced at 600 °C could not maintain its integrity and fell apart during washing. Starting from 700 °C and onwards the reduction produced solid

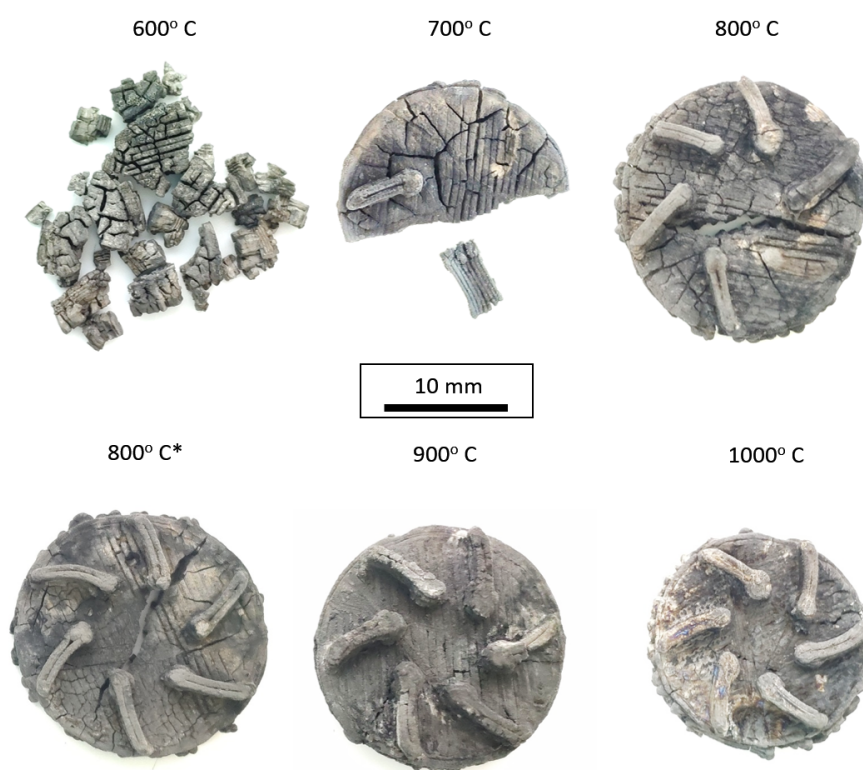


**Figure 5.12:** The effect of electrolysis temperature on the integrity of titanium turbines. (Constant voltage electrolysis (3.2 V) in  $\text{CaCl}_2$  (800-1000 °C);  $\text{LiCl}+\text{CaCl}_2$  (0.6  $\text{LiCl}/\text{LiCl}+\text{CaCl}_2$  - 600 °C; 0.27  $\text{LiCl}/\text{LiCl}+\text{CaCl}_2$  - 700-800 °C)) \*-test was reproduced in pure  $\text{CaCl}_2$ .

samples with gradually increased physical strength and reduced cracks on the sur-

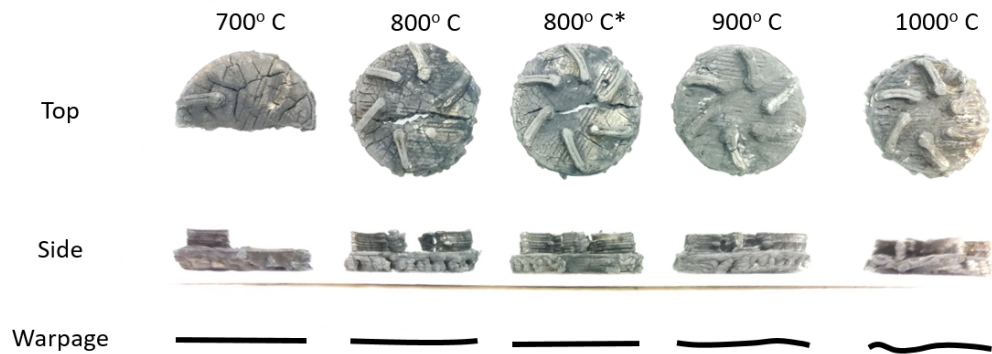


**Figure 5.13:** The effect of reduction temperature on complex deformation. (Constant voltage electrolysis (3.2 V) in  $\text{CaCl}_2$  (800-1000 °C);  $\text{LiCl}+\text{CaCl}_2$  (0.6  $\text{LiCl}/\text{LiCl}+\text{CaCl}_2$  - 600 °C; 0.27  $\text{LiCl}/\text{LiCl}+\text{CaCl}_2$  - 700-800 °C)) \*-test was reproduced in pure  $\text{CaCl}_2$

face. In order to evaluate the difference of reduction mechanism between pure  $\text{CaCl}_2$  and binary salts (i.e.  $\text{CaCl}_2$  and  $\text{LiCl}$ ) reduction was conducted at 800 °C for both of them with no observable difference in quality, which leads to an assumption that the selected salts (i.e.  $\text{CaCl}_2$  and  $\text{LiCl}$ ) and their mixtures affect the deformation in the same manner and, thus, can be compared. Figure 5.13 shows that warpage is increasing as the temperature of reduction increases. This is especially important as the selected design has a thin wall that has spaced vanes on top and closely packed support lines on the bottom, inducing different stresses on each side. All this shows that the sintering of metal particles plays an important role in the NEM Process, and the reduction temperature should be in a range of 800-900 °C.

The final crucial factor of the shape deformation was the design of the model itself. The initial test showed a consistent crack along the vanes of the turbine after sintering that were greatly expanded after the metallisation stage. Observation made

from Figure 5.14 indicated that the above-mentioned force distribution should be taken into account prior to the experiment to avoid any material waste. This defect was mitigated by increasing the thickness of the base of the impeller (See Figure 5.14 C).

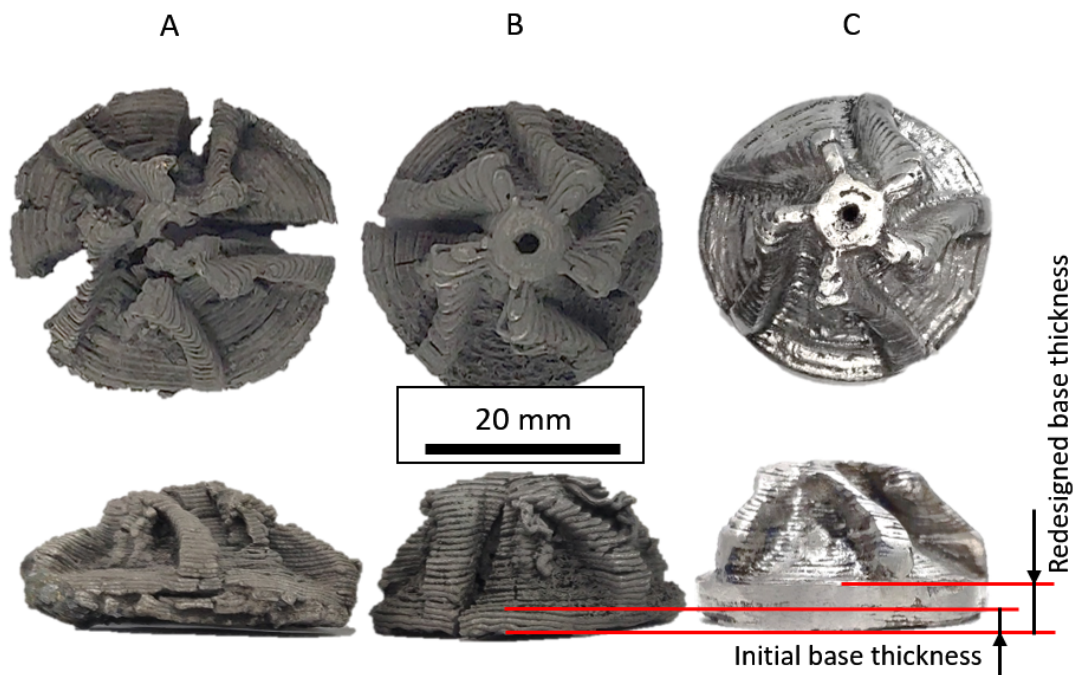


**Figure 5.14:** Design depended defects. A - not sintered; B - sintered at 1100 °C; C - sintered at 1100 °C with changed design (polished); Constant voltage electrolysis (3.2 V) in 900 °C  $\text{CaCl}_2$

Overall, it was found that in order to mitigate deformation and cracks of the metallised product the green bodies have to be sintered at 1100 °C for 1 hour. This sintering reduces the degree of shrinkage that happens when oxygen is removed from the precursor and was measured to be around 40% without sintering and only 5-10% after sintering. The formation of cracks was found to be mitigated by increasing

the reduction temperature that affected the softness of metal allowing it to release formed stress without being cracked.

## 5.5 Product Tests

The near-net-shaped samples were produced with the final accuracy of  $\pm 0.5$  mm. This is due to the consistency in shrinkage degree that was measured to be 40% in all directions. The final shrinkage consisted of 3 stages drying, sintering and reduction, which were 10/5%, 35/30% and 40/40% respectively in XY/Z coordinates. This orientation-dependent and uneven rate of shrinkage were observed for an impeller that had most of its bulk volume spread across the XY axis. The relatively high porosity of the products meant that the density of the sample was lower than the theoretical value, which made sample to be less strong compared to solid material. This was also visible from the SEM images where the typical nodular structure for the electrochemically produced titanium was observed.

The compression stress test showed that produced samples had Compressive strength of 111.4 MPa and Young's modulus of 1.39 GPa, which was found to be comparable with the porous titanium produced by Metal Injection Moulding (MIM) with controlled porosity of about 50% [29]. This consistency shows a similar quality between NEM and MIM produced products with MIM being a well-established manufacturing technique.

When allocating the material to a standard-defined grade (i.e. ASTM standards)

oxygen content plays an important role. From the produced samples this content was found to fluctuate in the range from 1000 to 5000 ppm of oxygen, depending on the geometry of the final product. This potentially limits the possible commercialisation of this technique as grade 4 pure titanium is limited to 4000 ppm [30]. It is clear that in order to improve the route to commercialisation the process that causes this fluctuation has to be thoroughly researched.

The XRD pattern after the reduction shows peaks typical for alpha titanium (Figure 5.15). Further tests with EDX showed that no other elements can be detected but titanium, which was different for the dark spots on the surface of some of the samples (See Figure 5.12 “800 °C\*”) that additionally contained carbon as shown in Figure 5.16. This carbon contamination was found only on the surface of some of the samples and could be cleaned mechanically via polishing or sandblasting.

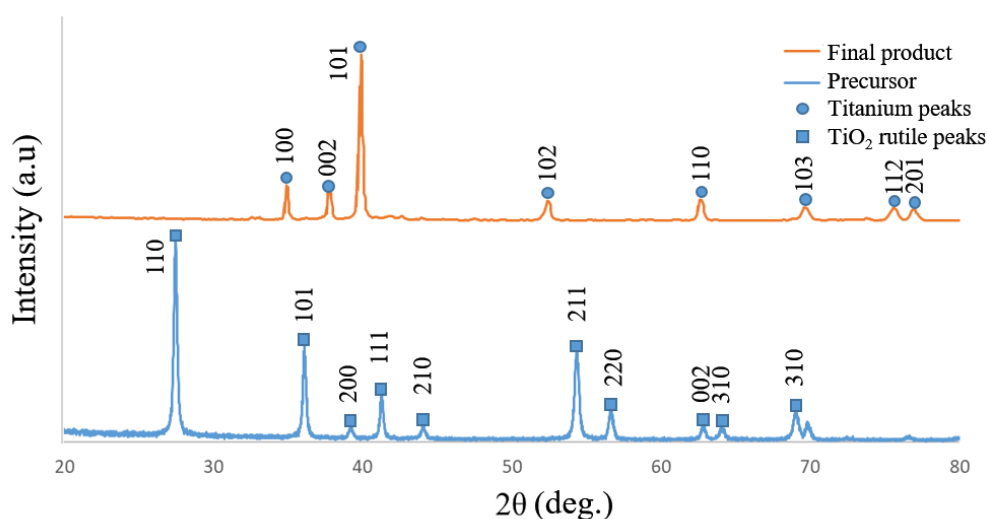


**Figure 5.15:** The XRD spectra of titanium dioxide feedstock and consequently reduced titanium.

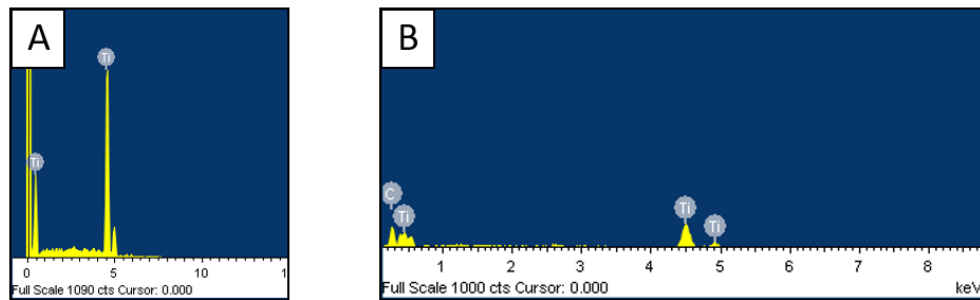


**Figure 5.16:** The EDX results for A – the bulk of a reduced sample; B – black spots on the surface of the reduced samples such as on Figure 5.12 “800 °C\*”.

## 5.6 Financial Analysis

When considering a novel process it is important to properly evaluate the financial impact it has compared to the conventional technique. This study evaluates the price for fabricating a titanium tooth implant, using the NEM Process. For this evaluation, a few assumptions were made:

- All data were taken from a non-optimised laboratory-scale setup.
- All used prices represent real values for Ningbo, China.
- The payback period for the equipment was set to 1 year.
- The salary was set to be 5000 Chinese Yuan/month, which is above the typical range of 2500 to 4000 Chinese Yuan/month. (Based on the junior level engineering jobs in Ningbo, China)

The local cost of a commercially produced titanium tooth implant is set to 400 Chinese Yuan, which is comparable with the one presented by Syam et al. (2011) [31], who estimated the cost of a titanium alloy coping to be 48.3 USD or approximately 340 Chinese Yuan. This price reflects the state of the Electron Beam Melting Process that provides a relatively high speed of production [32]. When compared to products fabricated using the NEM Process it was found that the implementation of this novel technique can yield a potential reduction of the net cost of more than 4 times. This is due to the net price of a single tooth implant (1.5 g titanium) was estimated to be 68 Chinese Yuan.

### 5.6.1 Data Collection

Net cost calculation consists of the equipment, human labour, miscellaneous, materials and electricity.

#### Electricity

Energy cost per product was calculated by multiplying the wattage of selected equipment by the time used. As the power consumption of all electrical equipment can fluctuate, it was decided to use its maximum rated wattage, which means that the calculated value will indicate the peak energy consumption for individual equipment. In addition to that, equipment such as tube furnace that required heating up and cooling down is assumed to operate constantly and switched off only during weekends or when optimised would work almost 24/7. This assumption makes the

energy consumption during the heating up and cooling procedures to be very small compared to the overall working period, which additionally can be argued to be covered by the use of maximum wattage in the calculation. The maximum power consumption was then multiplied by the electricity rate set in the Yinzhou district of Ningbo, China. To get the final cost on electricity per one tooth implant every power consumption was divided by the batch size that the specific equipment can process in one batch.

**Table 5.2:** Electricity related calculation.

Power cost			Electricity cost: (RMB/kWh)	0.5
Item	Wattage (Wh)	Working time (h)	Batch size (number of products)	Cost/per product (RMB)
Tube furnace	4000	24	10	4.8
Chamber furnace	8000	12	80	0.6
Power supply	125	24	10	0.15
PC	200	24	10	0.24
Pump	1000	0.5	30	0.008
Air compressor	1500	1	1	0.75
Water circulator	1000	24	10	1.2
3D Printer	50	0.5	1	0.0125

	Total	7.76
--	-------	------

## Materials

Material cost represents the price of all the chemicals involved in the production.

**Table 5.3:** Price of the raw materials.

Material cost	Price/g (RMB)	Weight ratio	Final cost
TiO <sub>2</sub>	0.8	1	2.4
PEG	0.08	0.12	0.0288
Oil	0.04	0.2	0.024
Mass of precursor (g)	3	Total	2.4528

The used ratio of the materials was established experimentally and then converted to RMB by multiplying the price by ratio by the mass of the precursor.

## Miscellaneous

Miscellaneous materials and equipment include all the additional things used in the experiment such as Argon gas, an electrolyte (CaCl<sub>2</sub>), a crucible, graphite rods, stainless steel electrodes, the nickel foam, tap water.

The price of these materials was estimated from a weekly price found by the total price divided by the average consumption rate, which varies for every material:

- 1 argon cylinder per 1 week;

- 1 kg of CaCl<sub>2</sub> per 1 week;
- 1 crucible per 1 week;
- 1 graphite rod per 3 weeks;

**Table 5.4:** Data collected for the calculation of the prices of miscellaneous materials.

Item	Price per week (RMB)	Production capacity per week	Price per item (RMB)
Argon	133	30	4.4333
CaCl <sub>2</sub>	40	30	1.3333
Crucible	100	486	0.2058
Graphite rod	10	30	0.3333
Ni foam	30	30	1.0000
SS electrodes	5	30	0.1667
Water	2	30	0.0667
		Total	7.5388

- 1 sheet of nickel foam per week (30\*30 cm);
- 2 SS electrodes per 2 months;
- 1 m<sup>3</sup> of tap water per week.

From there this weekly price was divided by the production capacity per week.

## Equipment

The equipment price is stated as received.

**Table 5.5:** Prices of the used equipment.

Name	Price (RMB)	Name	Price (RMB)
Tube furnace	12000	Power supply	8000
Chamber furnace	20000	Pump	1000
Water circulator	4000	Air compressor	1000
PC	4500	3D Printer	4000
Total (RMB)		54500	

## Labour Cost Estimation

The labour cost for a single worker was estimated from a monthly salary, which within Ningbo, China ranges from 2500 – 4000 RMB for a technician job. To make this imaginary position more competitive the price was set to 5000 RMB, which would attract fresh graduates based on their expectation. This value was then divided by the monthly production rate to achieve a per-item cost represented in the RMB/1 tooth implant.

## Payback Period

The payback period was calculated as the last step after the cost of everything except equipment was summed up. After that, the total equipment cost was divided

by the amount of produced items produced in a desired number of years (1 for the original estimation).

### Net Cost Calculation

All the produced values were then added up and used in the cost break down analysis.

$$\text{Net cost} = \text{“Total electricity cost”} + \text{“Total Material cost”} +$$

$$\text{“Total Miscellaneous cost”} + \frac{\text{“Equipment price”}}{\text{“Payback period production”}} + \text{“Labour cost”} =$$

$$7.76 + 2.4528 + 7.5388 + \frac{54500}{6240} + 41.6 = 68.0855 \text{ RMB}$$

### 5.6.2 Cost Break Down

This financial evaluation allows for the breakdown of cost associated with the NEM-produced implant, as shown in Figure 5.17 the largest part of the cost is comprised of the equipment and labour cost (81%). The equipment cost is accounted to have up to 38%, which is a common value for a commercial product [31]. This cost is depended on the desired payback period and sometimes is calculated using a life span of the equipment [33]. Therefore, to reduce the impact the equipment has on the cost of the implant it is possible to increase the payback period up to the life

span of the equipment, to make a profit before the equipment reaches its end-of-life (5-10 years) [34].

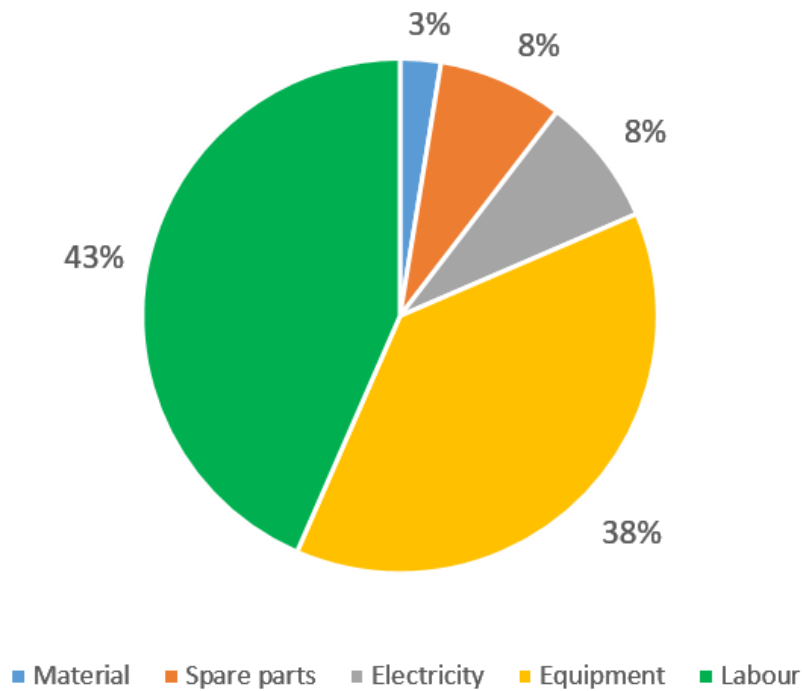


**Figure 5.17:** Cost break down of a titanium tooth implant produced by the NEM Process on the Lab-scale.

The labour cost, however, is fixed, taking up to 43% for our lab-scale production. This cost depends on the production volume, meaning that the production volume can alter the impact of the labour cost. The limit of such reduction reflects the ability of a worker to process a set amount of products, which is estimated to be 3 times larger than the studied laboratory scale (Lab scale: 120 implant/month). By implementing all the proposed changes (production: 360 implants/month; pay-back period: 5 years) it was possible to reduce the net cost of a titanium tooth

implant from 68 to 26.5 Chinese Yuan, producing a different cost break down (See Figure 5.18). There the equipment cost was reduced to 9% due to the extended pay-back period, with an increased share of a labour cost making it the most dominant contributor to the overall cost (56%).

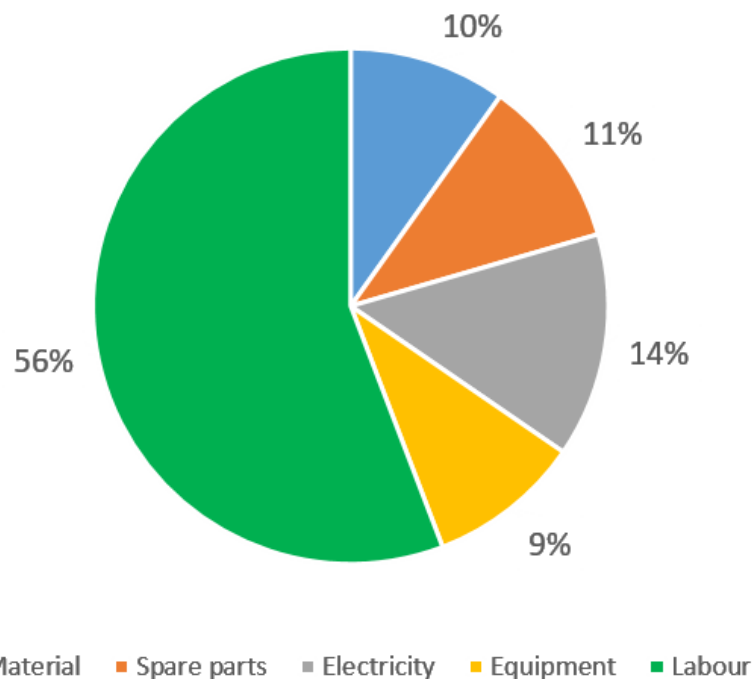


**Figure 5.18:** Cost break down of the optimised production of a titanium tooth implant produced by the NEM Process.

Furthermore, while 3D printing allows for more flexibility in design, products with set dimensions (copping or tooth implants) can be slip-cast, which dramatically increases production rates, thus, further lowering the price. Combined with the above discussion, it is clear that the NEM Process has the potential for further optimisation, leading to further cost reductions.

## 5.7 Critical Evaluation

The development of a novel technique is always an overwhelming endeavour as it can show an outstanding result on paper. Therefore, this section is dedicated to addressing all the minor details that have to be mentioned and elaborated on to establish the feasibility of the designed process.

Firstly, the NEM Process is built on a relatively simplistic and cheap AM technique that utilises ceramic slurries as the filament, which brings two main issues:

1. Ceramic ink

Even though the ink was precisely tailored to for the NEM process, it still possesses a random nature. Particularly it was noted that a lot of atmospheric factors affect its performance such as humidity and temperature. These factors affect the ink making it harder to extrude or slower to dry, increasing the complexity of the process as additional factors have to be taken into consideration.

Another problem is associated with the reduction of nozzle size, which accelerates water separation due to the increased load required for the extrusion. This means that when the paste performs well with 1 mm nozzle it can start clogging 0.5 mm nozzle or enhance the water migration, which in return was found to require a complex pressure control to amend the flow.

Furthermore, as the deposited ink remains wet some of the details can not be maintained due to the deposition path or simply lack of the strength. This

was found especially impactful on the tall or thin structures.

## 2. Deposition path

The G-code generated from a CAD model makes an approximation of tool-path that the nozzle will travel to fill the shape with the ink. This issue forces two potential results that are unfilled spaces or overfilled areas. The unfilled part crates void in the product that compromises the integrity of the functional part, which affects its durability and performance. An example of such zones can be seen in Figure 5.19 which are indicated in circles along with the areas that will be filled during the printing (arrows). The overfilled areas reduce the accuracy of the product as the extruded ink is pushed from its desired position by the excess ink.

Secondly, the molten salt metallisation process brings a few limitations that are the size and the porosity. It was found that at the current stage it is hard to reduce samples with the walls of  $>7$  mm due to the hindering of the oxygen diffusion that forces the inside part of the wall to form titanates. Such a formation tends to expand and destroy the integrity of the product during the washing and drying steps. Figure 5.20 shows a comparison of the products made from the precursors with varied thickness from 12 to 3 mm along with an effect of the increased anode surface area. It was found that with low anode surface area it was almost impossible to reduce anything around the thickest sample, however, as seen from the metallic glance the increased anode allowed to produce a better quality titanium shell, however, it did

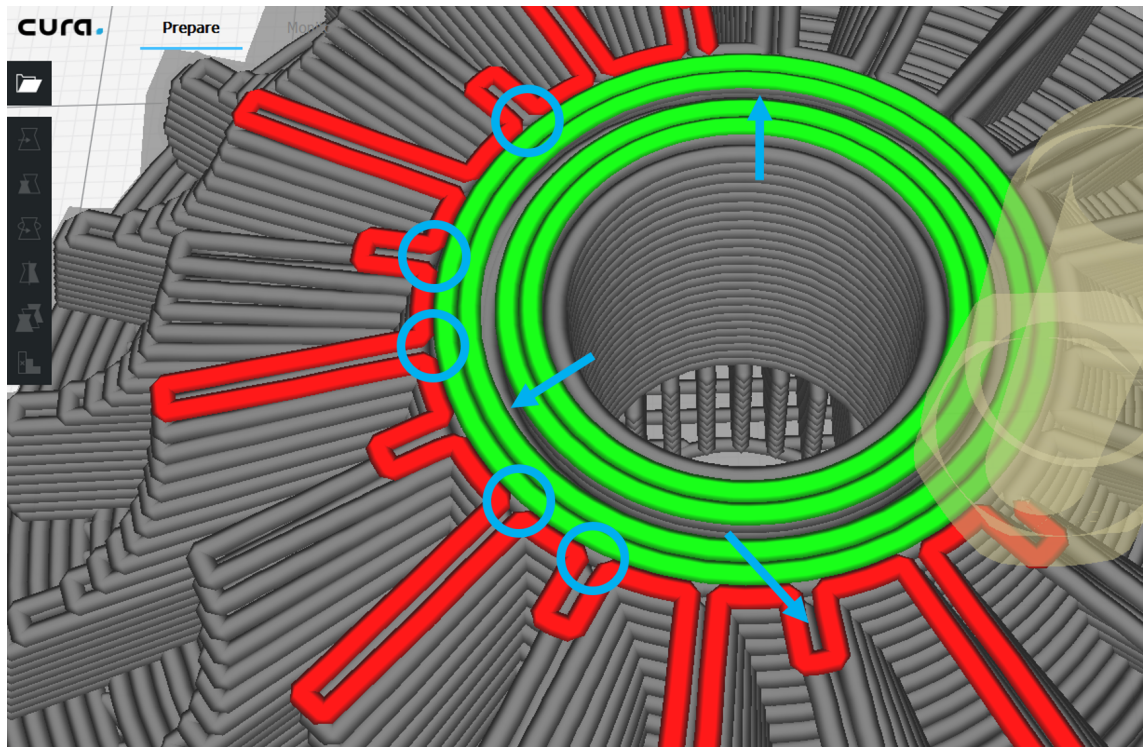


**Figure 5.19:** An example of the G-code predefined problem areas. Blue circles indicate potential unfilled zones; Blue arrows show gaps that are not affected.

not remove the titanates (core) completely. Additionally, it was found that samples with a thickness of  $<5$  mm were able to metallise completely without any difference. As these experiments were done for 5 samples simultaneously the separate reduction with low anode surface area still did not reach the results showed on the Figure 5.20 B. Finally, the high porosity makes the sample more brittle than solid titanium products.

All this means that the applicability of the NEM Process is limited to small products such as implants, which also benefit from being porous. However, it is possible to apply another ceramic AM process that has been proven to produce specimens

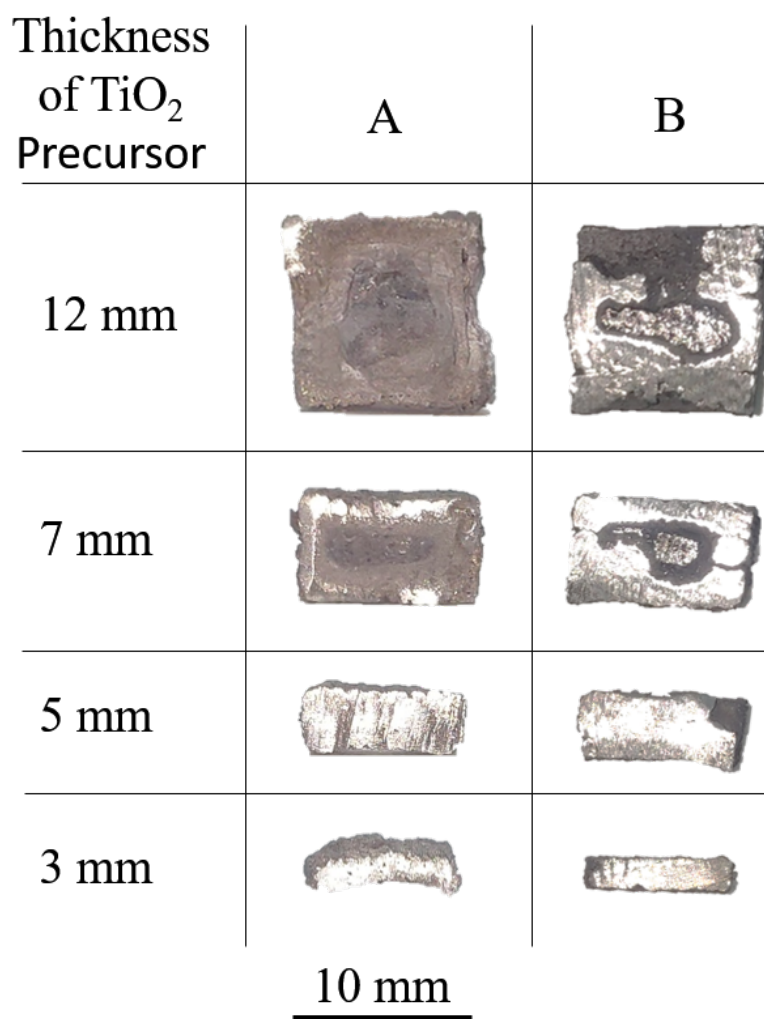


**Figure 5.20:** The reduction ability of samples with different thickness (Cross-section).

A - with anode surface area of 54 cm<sup>2</sup>; B - With anode surface area of 520 cm<sup>2</sup>.

with completely different properties such as binder jetting, selective laser sintering or stereolithography, which would again require optimisation and evaluation. The solution for the molten salt reduction-related issues, however, lies in the further research and potential utilisation of a larger reactor.

Some of the produced samples can be seen in Figure 5.21.



**Figure 5.21:** Examples of the titanium products produced via the NEM Process. A- the Terracotta warrior; B - the “UNNC” labelled ring; C - the impeller with thin vanes/blades; D - the simple polished ring.

## 5.8 Conclusion

This chapter concluded the development of the NEM Process as a novel additive manufacturing technique for titanium products. This was done by investigating the

feedstock, solving deformation issues and evaluating the cost of one of the products manufactured via the NEM Process.

The first stages of the feedstock evaluation resulted in the unique behaviour of the used material. Even though the reduction and CV represented a standard set of reverse and forward peaks, the produced bulk reduction of the titanium dioxide powder was yielding in a unique morphology. This morphology was represented in the shape of elongated and interconnected rods when the typical product has a so-called nodular structure. This finding, however, was outside of the scope of the planned project and only was proposed to happen based on 2 pathways: perovskatisation and recrystallisation. Which were not proven nor disproven at the time of writing of this thesis. Additionally, when this feedstock was applied to the DIW process it was found that some of the products were susceptible to produce low surface area chunks that resulted in as low oxygen content as 1000 PPM, which allocates these products to the level of the 1<sup>st</sup> grade titanium.

Further investigation was conducted on the sintering of precursors, which was then linked to the final porosity of the reduced samples. This resulted in a linear dependence of the porosity and sintering temperature where a not sintered precursor possessed 71% porosity and consecutive sintering at 900, 1100 and 1300 °C produced the reducing porosity of 59%, 40% and 34% respectively. The porosity of the prepared samples was essential due to the consecutive reduction that requires the highest possible value to achieve the most efficient and complete reduction. Thus, the balanced sintering temperature was set to be 1100 °C and was used for the rest

of the samples.

The main obstacle in the complete optimisation of the NEM Process was the deformation that happened during the molten salt electrolysis. This deformation was established to be of two main categories: chemical and physical. The chemical origin was dis-proven by a set of established experiments, which did not result in an increase or decrease of the extent of deformation. The physical deformation theory was harder to prove, however, it was confirmed to affect the products' shape. The investigation was conducted after the initial tests where 40% shrinkage was established that was theorised to be the cause of the deformation. For this, it was decided to “pre-shrink” the samples via sintering in air. This showed a dramatic effect on the shape of the final product with the temperatures above 1100 °C being the most successful. However, when samples have been sintered at 1300 °C the reduction was constrained by reduced porosity and resulted in a brittle product with the highest oxygen content of 18000 PPM. After this, it was clear that the sintering that occurs in the melt plays an important role in the deformation. The temperature of the electrolysis was varied from 600 to 1000 °C, which showed that it indeed affects the quality. First, it was found that samples reduced at 600 °C could not maintain any shape and would fall apart into small chunks. As the temperature increased the obvious and deep cracks would disappear yielding a solid sample from 800 to 1000 °C. This, however, also had a negative effect as the deformation, particularly warpage, was increasing along with the temperature. This allowed establishing the best reduction temperature of 800 - 900 °C.

Production of the near-net-shape products allowed to evaluate the net cost of the manufactured sample and compare it with the alternative product produced via the conventional Electron Beam Melting process. This cost analysis resulted in the net cost of a tooth implant (1.5 g of titanium) to be 68 RMB, with the reduced cost of 26 RMB if the process would be optimised. This demonstrated an enormous potential in cost reduction as the market price of the EBM produced implant was sourced to be 400 RMB.

Overall the main outcome of the work discussed in this chapter is the optimisation of the NEM process for the production of near-net-shape titanium products.

## References for Chapter 5

- [1] F. Borgioli, E. Galvanetto, A. Fossati, G. Pradelli, “Glow-discharge and furnace treatments of Ti-6Al-4V”, *Surface and Coatings Technology* **2004**, *184*, 255–262.
- [2] N. V. Muravyev, K. A. Monogarov, A. N. Zhigach, M. L. Kuskov, I. V. Fomenkov, A. N. Pivkina, “Exploring enhanced reactivity of nanosized titanium toward oxidation”, *Combustion and Flame* **2018**, *191*, 109–115.
- [3] R. B. Subramanyam, “Some recent innovations in the Kroll process of titanium sponge production”, *Bulletin of Materials Science* **1993**, *16*, 433–450.
- [4] W. Zhang, Z. Zhu, C. Y. Cheng, “A literature review of titanium metallurgical processes”, *Hydrometallurgy* **2011**, *108*, 177–188.
- [5] M. Darsin, H. A. Basuki, “Development Machining of Titanium Alloys: A Review”, *Applied Mechanics and Materials* **2014**, *493*, 492–500.
- [6] S. J. Oosthuizen, “In search of low cost titanium: the Fray Farthing Chen (FFC) Cambridge process”, *Journal of the South African Institute of Mining and Metallurgy* **2011**, *111*, 199–202.

- [7] G. Z. Chen, D. J. Fray, T. W. Farthing, “Direct electrochemical reduction of titanium dioxide to titanium in molten calcium chloride”, *Nature* **2000**, *407*, 361–364.
- [8] D. Hu, W. Xiao, G. Chen, “Near-Net-Shape Production of Hollow Titanium Alloy Components via Electrochemical Reduction of Metal Oxide Precursors in Molten Salts”, *Metallurgical and Materials Transactions B* **2013**, *44*, 272–282.
- [9] J. Peng, K. Jiang, W. Xiao, D. Wang, X. Jin, G. Z. Chen, “Electrochemical Conversion of Oxide Precursors to Consolidated Zr and Zr-2.5Nb Tubes”, *Chemistry of Materials* **2008**, *20*, 7274–7280.
- [10] R. Singh, P. D. Lee, J. R. Jones, G. Poologasundarampillai, T. Post, T. C. Lindley, R. J. Dashwood, “Hierarchically structured titanium foams for tissue scaffold applications”, *Acta Biomaterialia* **2010**, *6*, 4596–4604.
- [11] G. Zhao, S. Li, X. Chen, X. Qu, R. Chen, Y. Wu, Y. Liu, X. Zou, X. Lu, “Porous tantalum scaffold fabricated by gel casting based on 3D printing and electrolysis”, *Materials Letters* **2019**, *239*, 5–8.
- [12] S. C. Cox, J. A. Thornby, G. J. Gibbons, M. A. Williams, K. K. Mallick, “3D printing of porous hydroxyapatite scaffolds intended for use in bone tissue engineering applications”, *Materials Science and Engineering: C* **2015**, *47*, 237–247.

- [13] M. Zhou, W. Liu, H. Wu, X. Song, Y. Chen, L. Cheng, F. He, S. Chen, S. Wu, “Preparation of a defect-free alumina cutting tool via additive manufacturing based on stereolithography – Optimization of the drying and debinding processes”, *Ceramics International* **2016**, *42*, 11598–11602.
- [14] D. Macri, D. Sofia, D. Barletta, Massimo Poletto, P. Lettieri, “Selective Laser Sintering of Titania Powder: Experiments and Modelling”, **2017**.
- [15] K. Dring, R. Dashwood, D. Inman, “Voltammetry of Titanium Dioxide in Molten Calcium Chloride at 900 °C”, *Journal of The Electrochemical Society* **2005**, *152*, E104–E113.
- [16] G. Z. Chen, D. J. Fray, “Voltammetric Studies of the Oxygen-Titanium Binary System in Molten Calcium Chloride”, *Journal of The Electrochemical Society* **2002**, *149*, E455–E467.
- [17] C. Schwandt, D. T. L. Alexander, D. J. Fray, “The electro-deoxidation of porous titanium dioxide precursors in molten calcium chloride under cathodic potential control”, *Electrochimica Acta* **2009**, *54*, 3819–3829.
- [18] G. Z. Chen, D. J. Fray, “A morphological study of the FFC chromium and titanium powders”, *Mineral Processing and Extractive Metallurgy* **2006**, *115*, 49–54.
- [19] K. Jiang, X. Hu, M. Ma, D. Wang, G. QIU, X. Jin, G. Z. Chen, “”Perovskitization”- Assisted Electrochemical Reduction of olid TiO<sub>2</sub> in Molten CaCl<sub>2</sub>”, *Angewandte Chemie International Edition* **2006**, *45*, 428–432.

- [20] D. Fray, “Emerging molten salt technologies for metals production”, *JOM Journal of the Minerals Metals and Materials Society* **2001**, *53*, 27–31.
- [21] S. Tang, Z. Fan, H. Zhao, L. Yang, F. Liu, X. Liu, “Layered extrusion forming—a simple and green method for additive manufacturing ceramic core”, *The International Journal of Advanced Manufacturing Technology* **2018**, *96*, 3809–3819.
- [22] D. T. L. Alexander, C. Schwandt, D. J. Fray, “The electro-deoxidation of dense titanium dioxide precursors in molten calcium chloride giving a new reaction pathway”, *Electrochimica Acta* **2011**, *56*, 3286–3295.
- [23] H. Chen, Y. Zeng, W. Li, J. Peng, X. Jin, G. Z. Chen, “A PRS model for accurate prediction of the optimal solid oxide cathode structure for the preparation of metals in molten chlorides”, *Electrochemistry Communications* **2013**, *26*, 33–36.
- [24] D. Hu, A. Dolganov, M. Ma, B. Bhattacharya, M. T. Bishop, G. Z. Chen, “Development of the Fray-Farthing-Chen Cambridge Process: Towards the Sustainable Production of Titanium and Its Alloys”, *JOM* **2018**, *70*, 129–137.
- [25] J. Mohanty, K. G. Mishra, R. K. Paramguru, B. K. Mishra, “Formation of Calcium Titanate During Electroreduction of TiO<sub>2</sub> in Molten CaCl<sub>2</sub> Bath”, *Metallurgical and Materials Transactions B* **2012**, *43*, 513–518.

- [26] E. A. Olevsky, V. Tikare, T. Garino, “Multi-Scale Study of Sintering: A Review”, *Journal of the American Ceramic Society* **2006**, *89*, 1914–1922.
- [27] M. Ma, D. Wang, W. Wang, X. Hu, X. Jin, G. Z. Chen, “Extraction of titanium from different titania precursors by the FFC Cambridge process”, *Journal of Alloys and Compounds* **2006**, *420*, 37–45.
- [28] R. Centeno-Sánchez, D. Fray, G. Chen, “Study on the reduction of highly porous TiO<sub>2</sub> precursors and thin TiO<sub>2</sub> layers by the FFC-Cambridge process”, *Journal of Materials Science* **2007**, *42*, 7494–7501.
- [29] L.-j. Chen, T. Li, Y.-m. Li, H. He, Y.-h. Hu, “Porous titanium implants fabricated by metal injection molding”, *Transactions of Nonferrous Metals Society of China* **2009**, *19*, 1174–1179.
- [30] “ASTM B265-20a, Standard Specification for Titanium and Titanium Alloy Strip, Sheet, and Plate”, *ASTM International* **2020**, DOI <https://doi.org/10.1520/B0265-20A>.
- [31] P. da Silva Bartolo, *Innovative Developments in Virtual and Physical Prototyping: Proceedings of the 5th International Conference on Advanced Research in Virtual and Rapid Prototyping, Leiria, Portugal, 28 September - 1 October, 2011*, Taylor & Francis, **2011**.
- [32] D. Herzog, V. Seyda, E. Wycisk, C. Emmelmann, “Additive manufacturing of metals”, *Acta Materialia* **2016**, *117*, 371–392.

- [33] R. Gustavson, *Production Systems Engineering: Cost and Performance Optimization*, McGraw-Hill Education, **2010**.
  
- [34] K. Humphreys, A. A. o. C. Engineers, *Jelen's Cost and Optimization Engineering*, McGraw-Hill, **1991**.

## Chapter 6

# Environmental Assessment of the NEM Process

*This chapter evaluates and compares the environmental impact of the NEM Process and proposes the potential ways of optimising and reducing its effect on the environment.*

The material from this chapter has been published in the journal of Green Chemistry under the title of “Environmental Assessment of the Near-net-shape Electrochemical Metallisation Process and the Kroll – Electron Beam Melting Process for Titanium Manufacture” (February 2020)

## 6.1 Introduction

Titanium is extensively used in numerous industries such as biomedical [1, 2], architectural [3], aerospace [4] and etc. [5–7]. This high demand is caused by the wide range of unique properties of titanium including biocompatibility, low density and high strength [8]. However, the extraction and fabrication of titanium are energy and labour-intensive processes. Therefore, severe optimisation is required to lower both energy utilisation and material waste generated by these processes. Furthermore, fabrication steps require an inert environment and strict temperature control during the operation [9, 10], due to titanium’s low Young’s modulus, low heat dissipation, high reactivity at temperatures exceeding 600 °C and high affinity to other elements [11, 12]. Additionally, these high demanding titanium components often have complex shapes, which are difficult to produce using conventional methods, create a large amount of waste and reduce the lifespan of the milling tools [13, 14]. In order to reduce the quantity of waste and the energy requirements of titanium fabrication, several industrial processes have been investigated. For example, it was demonstrated that Powder Metallurgical (PM) methods solve many problems associated with machining titanium. One of these problems is the rapid wearing out of cutting and milling tools due to thermally induced phase change of titanium, which hardens the material [15–17]. There are many PM processes that have been adapted for the fabrication of titanium components such as Metal Injection Moulding (MIM) [18], Selective Laser Melting (SLM) [19], Electron Beam Melting (EBM)

[20], Hot Isostatic Pressing (HIP) [21] and etc. [22–24]. Within those processes, this study will focus on EBM as it is considered a standard for the relatively high-speed and highly flexible fabrication of titanium components [25]. This method, however, utilises high-quality spherical titanium powder as a feedstock, which inevitably adds an additional pretreatment step to the production chain [26]. To produce these high-quality powders the raw titanium has to be treated using additional steps such as Free Fall Gas Atomization (FFGA) [27, 28], Electrode Induction Gas Atomization [29], Plasma Atomization [30] and Plasma Rotating Electrode Process [30]. Between the above-mentioned methods, FFGA has emerged as the most suitable process, due to the high sphericity and narrow size distribution of the particles that, additionally, do not agglomerate and represent separate spheres with no internal voids and, therefore, it will be utilised in the assessment described in this work [31, 32]. Moreover, the extraction of the unprocessed titanium for the use in EBM is considered as one of the main hindering factors in the fabrication chain, taking up to 53% of the cost due to the materials applied [33]. Currently, the majority of titanium is extracted via the Kroll Process [34], which was established in 1940 and has not seen major advances since the original implementation of this technique [35]. The Kroll Process, being slow, high energy and resource-demanding process, has, therefore, been drawing the attention of the metallurgical community. Substantial efforts have been made in order to develop simpler, faster and more efficient extraction methods such as the Armstrong Process [36], Preform reduction method [37], the Solid-Oxide-Membrane (SOM) Process [38], the Ono-Suzuki Process [39] and

the Fray-Farthing-Chen (FFC)-Cambridge Process [40]. Among these methods, the FFC-Cambridge Process shows great potential, especially due to its unique ability of in-situ reduction that allows for the direct titanium powder production [41] and even near-net-shape manufacture [42, 43]. Therefore, this feature can be exploited to minimise above-mentioned hindering factors associated with titanium extraction and component fabrication. Instead of producing and melting titanium powder in EBM, it has been investigated to shape the feedstock (titanium dioxide) and then utilise Near-net-shape Electrochemical Metallisation (NEM) to deoxidise it to the respective titanium component [42, 43]. The shift of the feedstock for titanium fabrication from metal to metal oxide and its corresponding in-situ electrochemical reduction can dramatically reduce both of the energy and material costs, as well as potentially their related environmental impacts [44]. However, this new technique has not been quantitatively assessed for its relative environmental impacts, therefore, it is crucial to conduct a quantitative environmental assessment of the NEM Process in comparison to the commonly adopted fabrication process (i.e. Kroll - EBM Process) to determine the potential benefits of this method. This is especially important due to new policies, such as emission trading scheme, drawing increased attention of multiple governments in recent years, which could potentially make this technique more favourable for the industry [45–47]. Therefore, for the first time, the Life Cycle Assessment (LCA) of the NEM Process was performed in order to quantify its environmental impact and compare it to the current fabrication process (Kroll Process-Electron Beam Melting). Moreover, the relative contribution of

NEM process production steps (i.e., extraction and fabrication) was investigated to determine which steps could be further improved. Especially when an LCA evaluation of the electrochemical process for titanium extraction (i.e., FFC-Cambridge Process) in combination with the downstream/upstream processes has not yet been produced, which may disclose a potential benefit for its commercialisation [48].

## 6.2 Methodology

This LCA was conducted according to the principles described in BS EN ISO 14044:2006+A1:2018 and BS EN ISO 14040:2006 [49, 50]. Accordingly, the systematic approach used for this study was divided into four main phases. First is the goal and scope definition, where the main goal is established, the level of detail and the system boundaries are set. Here the assumptions and limitations of the study are also stated. The second phase is the Life Cycle Inventory Analysis (LCIA). For this phase, the data sources are analysed and the required inputs and outputs are collected. The last two phases are the impact analysis and the interpretation of the gathered results. These are the finalising stages of an LCA study that summarise all the data prepared in the first two phases.

### 6.2.1 Goal and Scope

Two main objectives were set for this study. Firstly, to determine the environmental impact of the proposed NEM Process in comparison with the conventional Kroll -

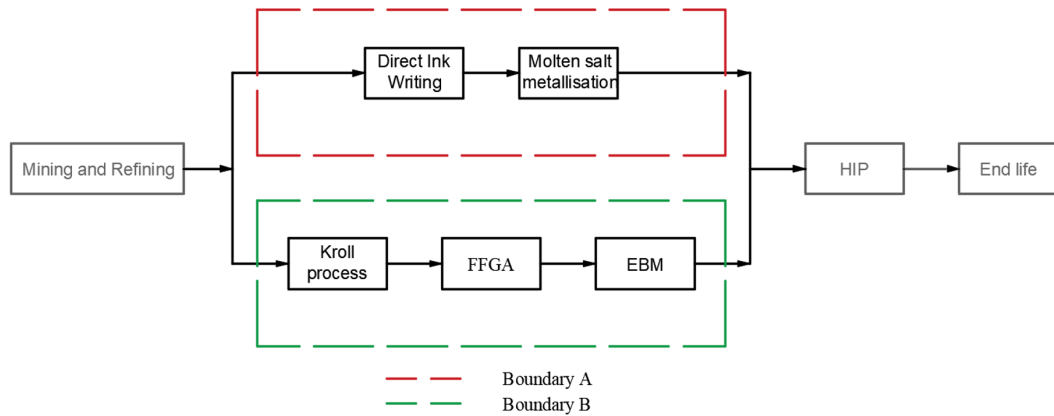


**Figure 6.1:** Manufacture routes of an additively produced (i.e. 3D-printed) titanium product; FFGA – Free Fall Gas Atomisation; EBM – Electron Beam Melting; HIP – Hot Isostatic Pressing.

EBM Process. Secondly, to define the environmental impact of the NEM Process in order to propose adjustments that could further reduce the environmental impact. For this study, the capability of producing one impeller has been selected as a Functional Unit (FU). This FU was set due to the scaling up that may happen in the future. In addition, the cut-off of 2% on environmental impact was selected to show the most relevant contributors. The system boundaries are presented in Figure 6.1. This leads to two boundaries (Figure 6.1 Boundary A and B) that both have a manufacturing technique (DIW and EBM) and the transformation of synthetic rutile into titanium (Molten salt reduction and Kroll process) [51]. As the extraction and purification methods for the titanium dioxide (synthetic rutile) are shared between the two investigated processes, it is assumed that they do not have an impact on the comparative study. Furthermore, the same assumption can be made for the end

life period and a life span of the produced items, the implementation of the Hot Isostatic Pressing (HIP) was applied after both processes in order to bring them to the highest relative density [52]. Boundary B (Figure 6.1), however, also includes an intermediate process of spheroidisation of titanium powder as this production step is essential to increase the quality of the product to the required level [30]. The data used in this study were allocated by mass.

## 6.2.2 Case Study

This work is considering two different production routes conventionally referred to as the NEM (Figure 6.3) and the Kroll - EBM (Figure 6.4) routes.

### 6.2.2.1 The NEM Process

The NEM Process consists of two main stages, with a fabrication time of roughly three days (See Figure 6.3). Figure 6.2 describes all inputs and outputs, along with a detailed list of sub-processes included in the NEM Process.

1. Direct Ink Writing.

This is an Additive Manufacturing (AM) method that utilises pastes or slurries as ink, which are extruded through a nozzle. Extrusion is facilitated via compressed air pressure, which pushes ink from the feed cylinder. Inks are prepared by mixing the solution of PEG and water with titanium dioxide powder. After printing, the oxide precursor is dried for 24 hours. This process takes about 27 hours.

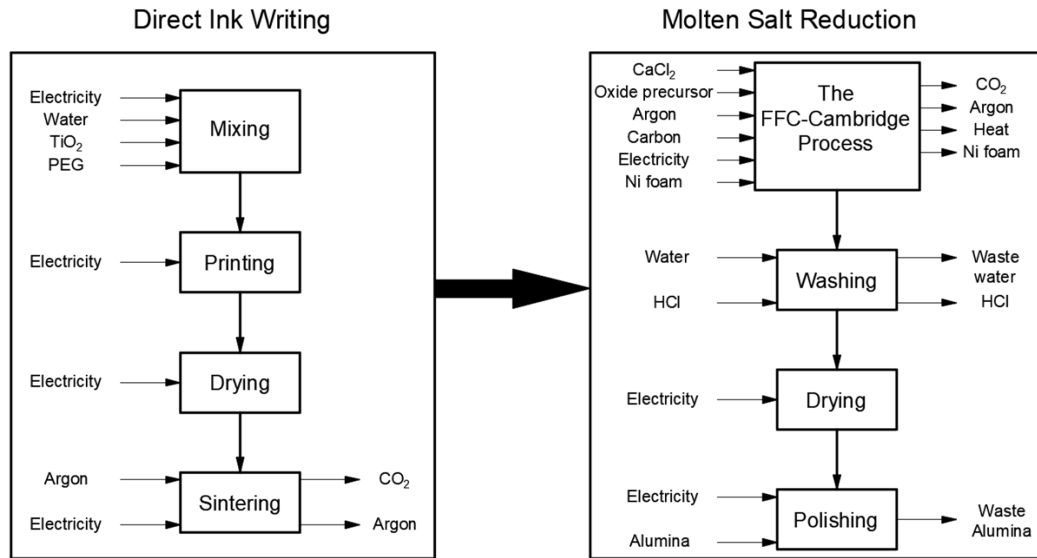


**Figure 6.2:** Detailed material and energy flow within the boundary A (the NEM Process).

- The printing technology utilised in this step is modified from the Fused Deposition Modelling (FDM) Process, which allows for high-resolution printing and also is widely considered to be one of the cheapest 3D printing technique on the market [53].

## 2. Molten Salt Reduction.

The titanium oxide precursor is *in-situ* metallised to metallic titanium by electrochemical reduction using molten salt as the electrolyte, also known as the FFC-Cambridge Process [10, 40]. Firstly, the precursor is attached to the cathode and wrapped in a nickel foam, in order to increase the connection area for electron conduction. The whole cathodic assembly is then placed in a sealed retort that has been kept at 900 °C and continuously flushed with argon. A graphite rod is used as the anode. When a voltage, which is high

enough to split the metal oxide but low enough to avoid the decomposition of the molten salt electrolyte (i.e., molten  $\text{CaCl}_2$ ), is applied between the cathode and the anode, the following electrochemical reactions happen:



After a 24 hour electrolysis under the constant voltage of 3.2 V, the product is washed in water and dilute HCl, then dried and polished by abrasive blasting. Overall, this stage takes about 30 hours and has numerous advantages over the Kroll process:

- Electrochemical reduction uniquely allows for the *in-situ* reduction of a metal oxide precursor to its metallic counterpart without major shape degradation [43]. Therefore, titanium extraction and shaping can be integrated into one step. This ability is the core of the NEM Process, allowing for the shape retention of the 3D structure of a metal oxide precursor after reduction [10].
- It has also been demonstrated that it is possible to lower the overall environmental impact associated with the extraction of titanium by implementing the FFC-Cambridge Process instead of the conventionally applied Kroll process [48].
- Additionally, the FFC-Cambridge Process has been demonstrated to be able to produce alloyed metals without using a complex alloying proce-

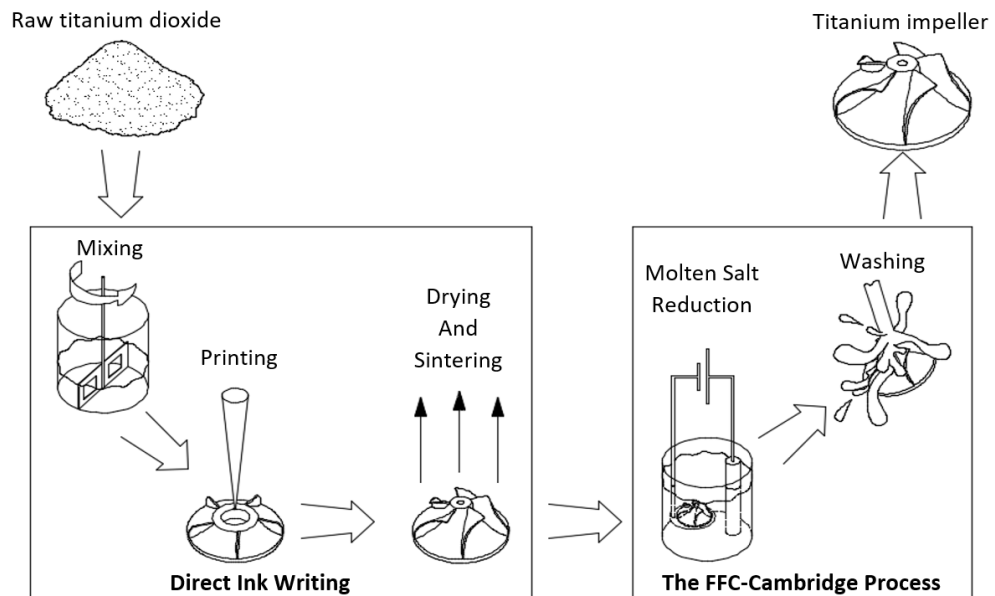


**Figure 6.3:** The NEM Process, showing the two stages used for fabricating a titanium impeller from raw titanium dioxide.

ture that would be required to manufacture metal alloys prior to the EBM process [42, 54].

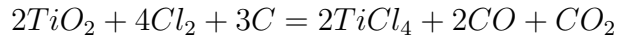
- The integrity of the produced items makes it the promising candidate to be implemented in the medical implants without post-treatment due to the porous nature of the product that is achieved after the FFC-Cambridge Process [55].

### 6.2.2.2 The Kroll Process-Electron Beam Melting

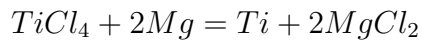
The Kroll - EBM route consists of three main stages and has a fabrication time of at least two weeks (See Figure 6.4):

1. The Kroll process.

At this stage, synthetic rutile is transformed into intermediate chemical ( $TiCl_4$ ) in the carbochlorination reaction:



After purification, it is reduced using molten magnesium metal under vacuum.



The mixture is then distilled under vacuum in order to remove all  $MgCl_2$ .  $MgCl_2$  is then recycled and purified using an electrolytic process. This stage recovers  $Cl_2$  and  $Mg$  that is reused in the process. The produced titanium sponge is crushed at the end of the process. Overall, the Kroll process takes about 2-3 weeks to produce a batch of titanium [34].

2. Free-Fall Gas Atomisation.

This process is used to transform the titanium powder produced by the Kroll process into a spherical shape, which offers the necessary flowability and packability required for the following EBM process. In FFGA, titanium is converted into a molten phase and the resulting flow is broken down to small droplets via a stream of pressurised argon gas. The whole process takes about 3 hours to produce 50 kg of powder with the efficiency of 92.5% [9].

3. Electron Beam Melting.

At the beginning of the EBM process, the chamber is vacuumed and preheated to about 750 °C. After that 3000W electron beam is utilised to melt

the titanium powder spread in thin layers and create a 2D pattern that is produced from the CAD model of an object [56]. The powder that has not been melted plays a role of the support, and after the process, it is reused. This process requires a considerable amount of energy due to the heating and melting involved [57].

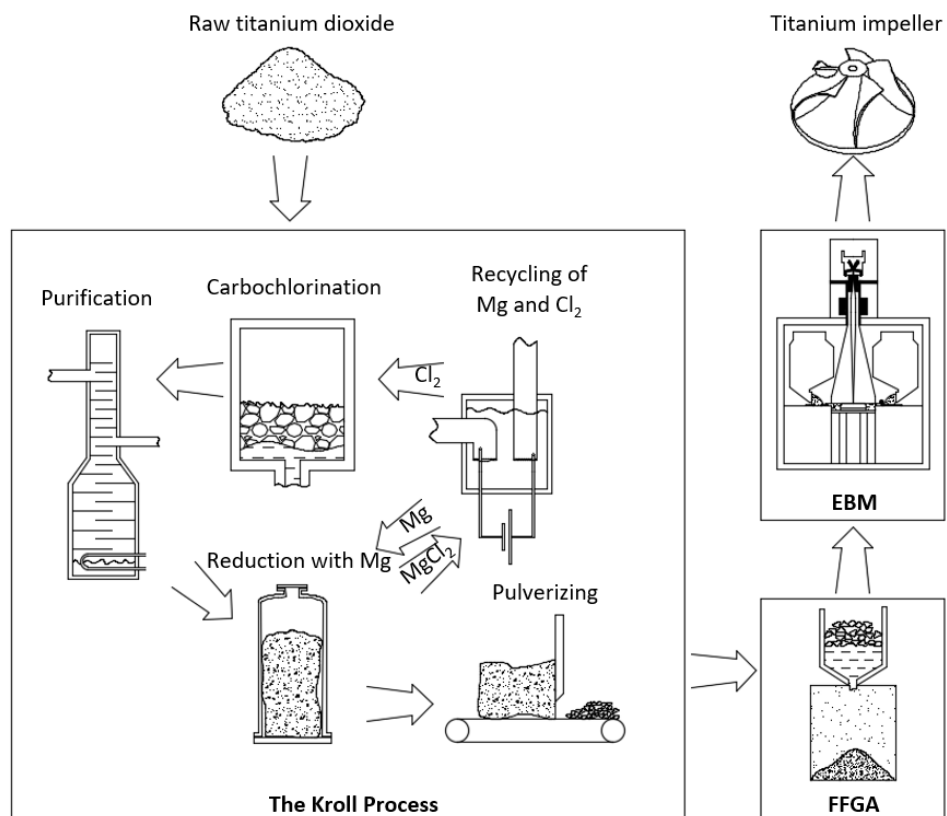


**Figure 6.4:** The AM-assisted Kroll Process, showing the three stages used for fabricating a titanium impeller from raw titanium dioxide.

Figures 6.3 and 6.4 show the simplicity of the NEM Process over the Kroll - EBM route. In addition, this process dramatically reduced the production time from about 2 weeks to 3 days, for the Kroll - EBM route and the NEM Process respectively.

### 6.2.3 Life Cycle Inventory

Data used to evaluate the NEM Process were collected at pilot-scale and are summarised in Table 6.1. As described in the case study section the synthetic rutile is mixed into a paste and extruded in the DIW into the required shape. During drying and sintering, all water is evaporated and PEG from the green body is decomposed to  $\text{CO}_2$ . Following the sintering stage, the FFC Metallisation converts synthetic rutile into titanium metal, which is done following the stoichiometry of the related reactions. There, graphite is consumed and combined with oxygen, generating more  $\text{CO}_2$ . All additional outputs are treated as waste (except for the product), gases are emitted to the atmosphere and metal scrap is sent to a recycling factory. Operation data, describing the conventional process, were acquired from the following relevant studies. Information on the Kroll process was covered by Gao et al. in the in-depth evaluation of the process commonly used in China, but only metal conversion stages were utilised (See Appendix A) [34]. Data for the FFGA process were discussed in the work of Serres et al. who compared a new AM method (MESO-CLAD) with conventional machining [9]. Finally, information for the EBM process was taken from work that compared EBM with conventional machining, conducted by Le et al. [58]. The data summarised in Table 6.2 shows a huge energy consumption of the EBM process compared with the Kroll process and FFGA. This is the time required for the EBM to form a product, which can reach 12 hours for one part [58]. Table 6.2 contains summarised data for the FFGA and EBM. Materials and background pro-

cesses used to model described production processes were taken from the Ecoinvent 3.0 database [59].

A sensitivity analysis was performed by varying electricity consumption of  $\pm 5\%$  in order to establish the stability of the model and made assumptions.

#### **6.2.4 Interpretation**

Impact for a single functional unit is produced for every impact criteria and completed using SimaPro software version 8.5.2.0 [60].

#### **6.2.5 Impact Assessment and Categories**

All of the Life cycle impact assessments described in this study were performed according to the ReCiPe method at midpoint level, to achieve a higher degree of accuracy for the calculation and also produce a clearer picture about the investigated processes [61]. Impact categories considered by this method (summarised in Table 6.3) include Global Warming (GW), Stratospheric Ozone Depletion (SOD), Ionizing Radiation (IR), Ozone Formation on Human Health (OFHH), Fine Particulate Matter Formation (FPMF), Ozone Formation on Terrestrial Ecosystems (OFTE), Terrestrial Acidification (TA), Freshwater Eutrophication (FE), Marine Eutrophication (ME), Terrestrial Ecotoxicity (TET), Freshwater Ecotoxicity (FET), Marine Ecotoxicity (MET), Human Carcinogenic Toxicity (HCT), Human Non-carcinogenic Toxicity (HNCT), Land Use (LU), Mineral Resource Scarcity (MRS), Fossil Resource Scarcity (FRS) and Water Consumption (WC). Endpoint characterization

**Table 6.1:** Inputs and outputs for the NEM Process to produce one titanium impeller (0.23 kg).

	Name	Unit	DIW	FFC Metallisation	Total	
Inputs	Synthetic rutile	kg/FU	0.4	n/a	0.4	
	Synthetic rutile impeller	kg/FU	n/a	0.4	0.4	
	PEG	kg/FU	0.08	n/a	0.08	
	Calcium chloride	kg/FU	n/a	0.8	0.8	
	Argon	kg/FU	0.01	0.49	0.5	
	Graphite	kg/FU	n/a	0.06	0.06	
	Nickel foam	kg/FU	n/a	0.005	0.005	
	Water	kg/FU	0.4	1.2	1.6	
	Alumina	kg/FU	n/a	0.002	0.002	
	HCl	kg/FU	n/a	0.0007	0.0007	
	Electricity	3D Printing	kWh/FU	0.215	n/a	8.05
Sintering		0.015		n/a		
Metallisation		n/a		7.76		
Misc.		0.03		0.03		
Outputs	Titanium impeller	kg (i.e. FU)	n/a	0.23	0.23	
	Calcium chloride	kg/FU	n/a	0.8	0.8	
	CO <sub>2</sub>	Metallisation*	kg/FU	n/a	0.22	0.38
		PEG		n/a	0.16	
	Argon	kg/FU	0.01	0.49	0.5	
	Nickel foam	kg/FU	n/a	0.005	0.005	
	Alumina	kg/FU	n/a	0.002	0.002	
	HCl	kg/FU	n/a	0.0007	0.0007	
	Heat	kJ/FU	n/a	655	655	
Water	kg/FU	0.4	1.2	1.6		

**Table 6.2:** LCI of boundary 2. \* - For the complete list of the LCI for the Kroll Process refer to Appendix A.

	Name	Unit	Kroll Process*	FFGA	EBM	Total
Inputs	Synthetic Rutile	kg/FU	8.7	n/a	n/a	8.7
	Titanium sponge	kg/FU	n/a	0.247	n/a	0.247
	Titanium Powder	kg/FU	n/a	n/a	0.23	0.23
	Argon	kg/FU	n/a	0.07	n/a	0.07
	Water	kg/FU	0.1	35.6	n/a	35.7
	Electricity	kWh/FU	5.4	0.45	11.39	17.24
Outputs	Titanium metal	kg/FU	0.247	n/a	n/a	0.247
	Titanium impeller	kg (i.e. FU)	n/a	n/a	0.23	0.23
	Titanium Waste	kg/FU	n/a	0.017	n/a	0.017
	Titanium Powder	kg/FU	n/a	0.23	n/a	0.23
	Argon	kg/FU	n/a	0.07	n/a	0.07
	Water	kg/FU	n/a	35.6	n/a	35.6

summarises damage from the above 18 criteria into three main groups: ecosystem, human health and resources. This summarisation increases statistical uncertainties but shows the overall picture in a concise manner.

**Table 6.3:** Summarised abbreviations.

GW	Global warming
OD	Stratospheric ozone depletion
IR	Ionizing radiation
OFHH	Ozone formation on Human health
FPMF	Fine particulate matter formation
OFTE	Ozone formation on Terrestrial ecosystems
TAC	Terrestrial acidification
FE	Freshwater eutrophication
ME	Marine eutrophication
TET	Terrestrial ecotoxicity
FET	Freshwater ecotoxicity
MET	Marine ecotoxicity
HCT	Human carcinogenic toxicity
HT	Human non-carcinogenic toxicity
LU	Land use
RES	Mineral resource scarcity
FRS	Fossil resource scarcity
WC	Water consumption

## 6.3 Results and Discussion

### 6.3.1 Contribution Analysis

The proposed NEM Process consists of two main processes: DIW and the molten salt reduction (i.e. the FFC-Cambridge Process). Based on the calculation results shown in the Figure 6.5 molten salt reduction emerged as the main contributor in 14 out of 18 impact categories (62.6% for GW, 53.5% for SOD, 56% for IR, 63.8% for OFHH, 64.9% for FPMF, 63.6% for OFTE, 67.6% for TA, 53.8% for TET, 62.1% for FET, 60.7% for MET, 61.4% for HCT, 51.3% for HNCT, and 58.4% for FRS). In addition, most of the energy consumed in the process is dedicated to the molten salt reduction stage. Furthermore, for the FR, ME, LU and MRS impact categories the DIW process was shown to be the main contributor. This can be linked to the refining and mining of titanium dioxide used in the process, which produce solid waste and require considerable land use [51]. Figure 6.6 displays the source of high contributors to the allocated categories. The majority of impacts are allocated to electricity and the feedstock. However, for IR and WC impact of argon's use overcomes that of electricity. This happened due to the nature of the production process of argon. During this process coproducts, such as krypton and xenon are formed, which are considered radionuclides in ReCiPe [62]. Another area of the interest is nickel's influence. It has relatively high impacts of 10.6%, 14.9% and 13.7% for FPMF, TA and HNCT, respectively. The impact on FPMF is originated from the crushing step of the nickel ore refining process and excavation

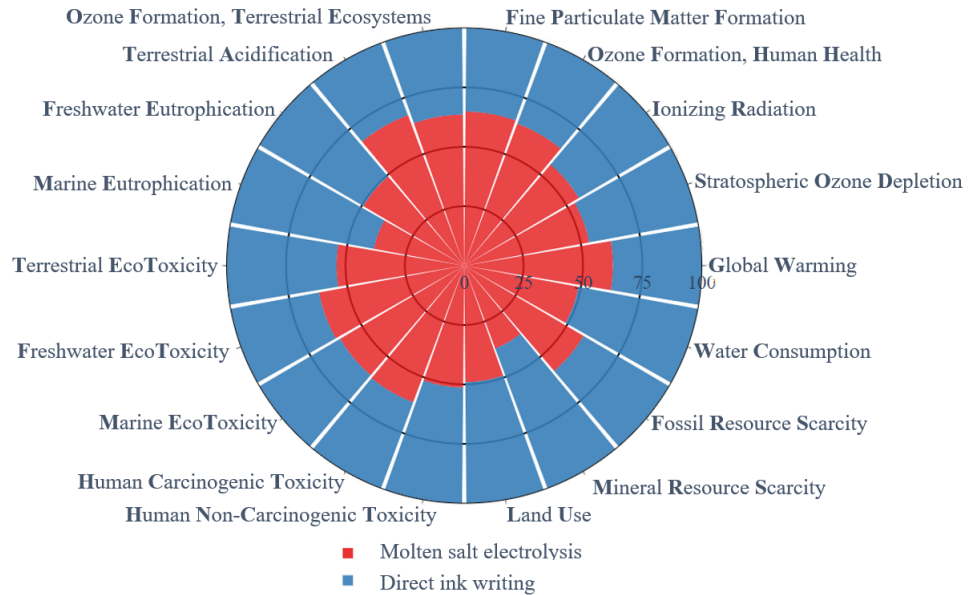


**Figure 6.5:** Impact analysis of contribution of the sub-processes for the NEM Process.

processes, thereby forming fine matter particles [63]. TA is affected due to the acid leaching stages implemented during the metal refining stages of nickel, which in turn results in the increased acid consumption and disposal [63]. In the case of HNCT, the coproducts that are extracted during leaching are cobalt, copper, and gases like  $\text{SO}_2$  and  $\text{CO}_2$ . Both cobalt and copper have been reported to be a non-carcinogenic toxic material and, thus, are considered as the factors affecting HNCT [64]. In addition, both  $\text{SO}_2$  and  $\text{CO}_2$  gases are classified as toxic materials according to the Environmental Protection Agency (EPA) classifications [65]. Analysis of midpoint impacts of DIW process (see Figure 6.7) shows that utilisation of titanium dioxide dominates in every category. This is directly linked to the amount of material used on this stage. Based on the acquired results it is clear that the DIW process

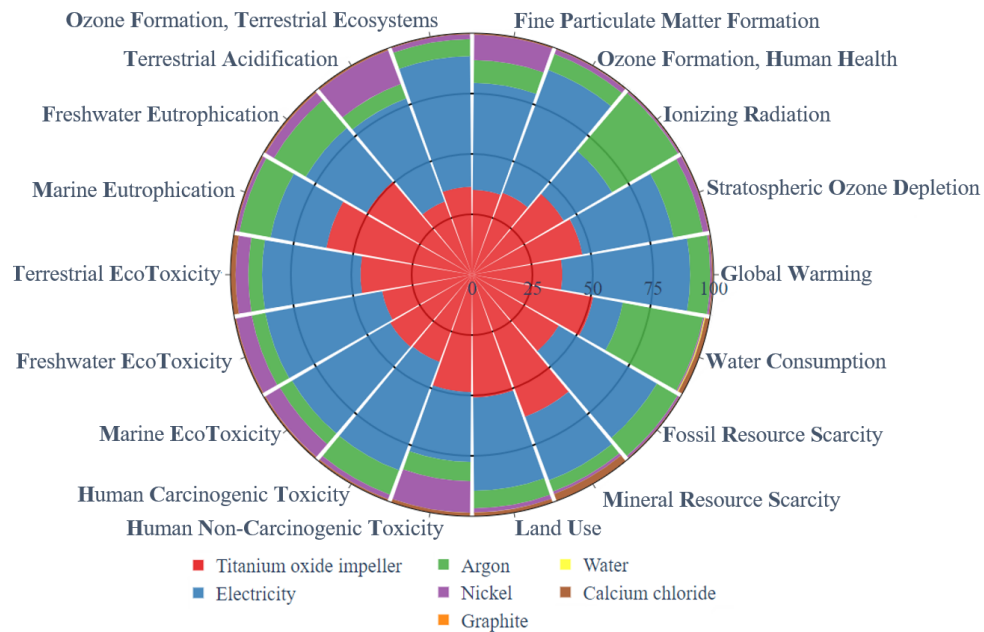


**Figure 6.6:** Environmental impact contribution for the impeller production by the NEM Process.

cannot be improved due to the contributors that are involved, as the amount of titanium dioxide utilised cannot be reduced. However, due to the versatility of the metallisation process, it is possible to replace synthetic rutile with titanium ore. This would reduce the physical properties of the final product but become less environmentally damaging as the refining would be dramatically simplified. On the contrary, the impact of molten salt reduction could be lowered significantly by reducing argon consumption and reusing electrode materials. Argon is essential for the process as it vents produced gasses (i.e.  $\text{CO}_2$  and/or  $\text{CO}$ ) out from the reactor, however, its flow could potentially be reduced by optimising the design of the reactor. Reduction of argon flow from 0.2 l/min to 0.1 l/min can potentially

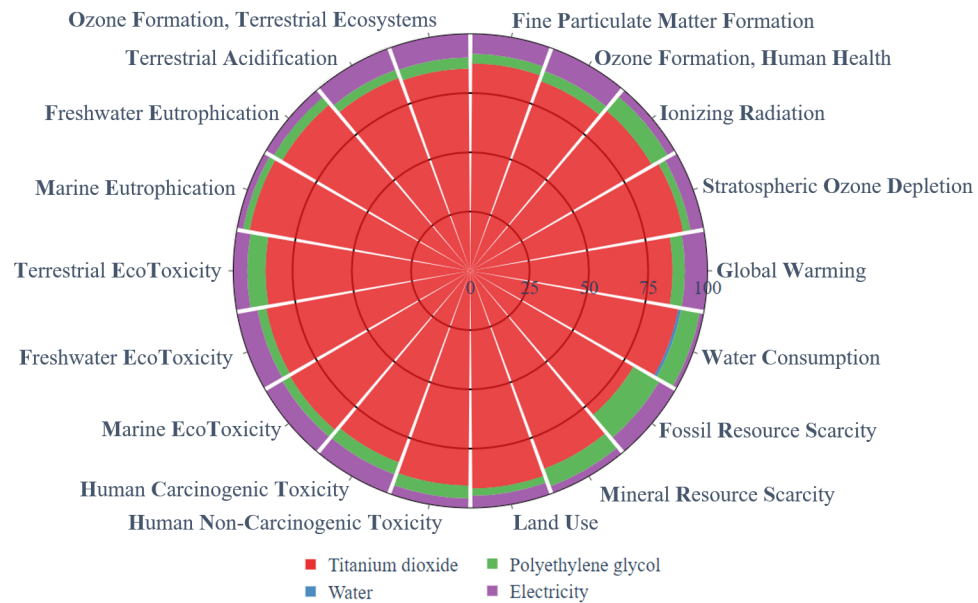


**Figure 6.7:** Environmental impact contributors for the DIW process.

reduce the impact of some categories up to 10 % (SOD, IR, FE, ME and WC). In addition, it is possible to implement a non-constant flow rate for the argon as the production of abovementioned gases reduces exponentially during the metallisation process, thus, requiring less argon to vent them after about 10h from the beginning of the process. Moreover, nickel is used in the process to ensure a high surface connection between the metal oxide precursor and the electrode. In the current process, the nickel foam cannot be reused after the electrolysis due to it becoming brittle, and is, therefore, disposed of after each electrolysis cycle, adding to the environmental impact. This can be improved in two ways:

1. Using another material.

- Stainless steel – Cheap and resistant.

- Titanium - Minimum impurities.
- Molybdenum – Chemically stable in molten  $\text{CaCl}_2$ .
- Tantalum - High temperature and corrosion resistive.
- Carbon/low alloy steel and cast iron - Cheap.

2. Implement a reusable assembly.

- Develop a design that withstands molten  $\text{CaCl}_2$  and survives multiple batches.

From these two suggested improvements, it can be stated that implementing a reusable assembly is more effective. Since the relative impact nickel has on the system is small, replacing it reflects only in a minor reduction for every category. Additional investigation (see figure 6.8) showed that nickel has a comparable environmental impact with titanium, however, the use of titanium would reduce the possibility of nickel forming an alloy with the produced titanium. Furthermore, replacing nickel with stainless steel 316, Carbon steel, low alloy steel and cast iron have the potential to reduce the environmental impact by nearly four times, while additionally reducing the cost. A more detailed comparison of these implementations is discussed later in the Parametric and Sensitivity Analysis section.

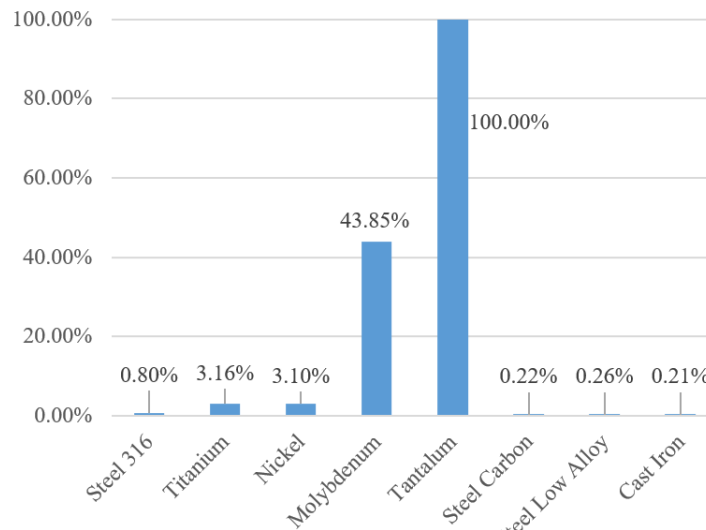


**Figure 6.8:** Endpoint comparison of the replacement material candidates.

### 6.3.2 Parametric and Sensitivity Analysis

An analysis of the stability of the produced model is done via changing the main contributor (Electricity), established during the LCI stage, by 5%. This shows the effect of the LCI values on the environmental impact. Increasing the energy consumption inevitably increased the carbon footprint from 10.05 to 10.31 kg CO<sub>2</sub> eq, a 3% change from the initial state. Improvement in the energy consumption showed that the environmental impact of the described model was indeed heavily relying on the emissions caused by electricity as the reduction in consumption of 5% resulted in the reduction across all the categories by 1-3% (See Figure 6.9 A). Such a response confirms that electricity is a key contributor, however, the reduction of electricity consumption is a complex task, which has been a hot topic among the metallurgical researchers [10]. Following electricity, the sensitivity of the synthetic

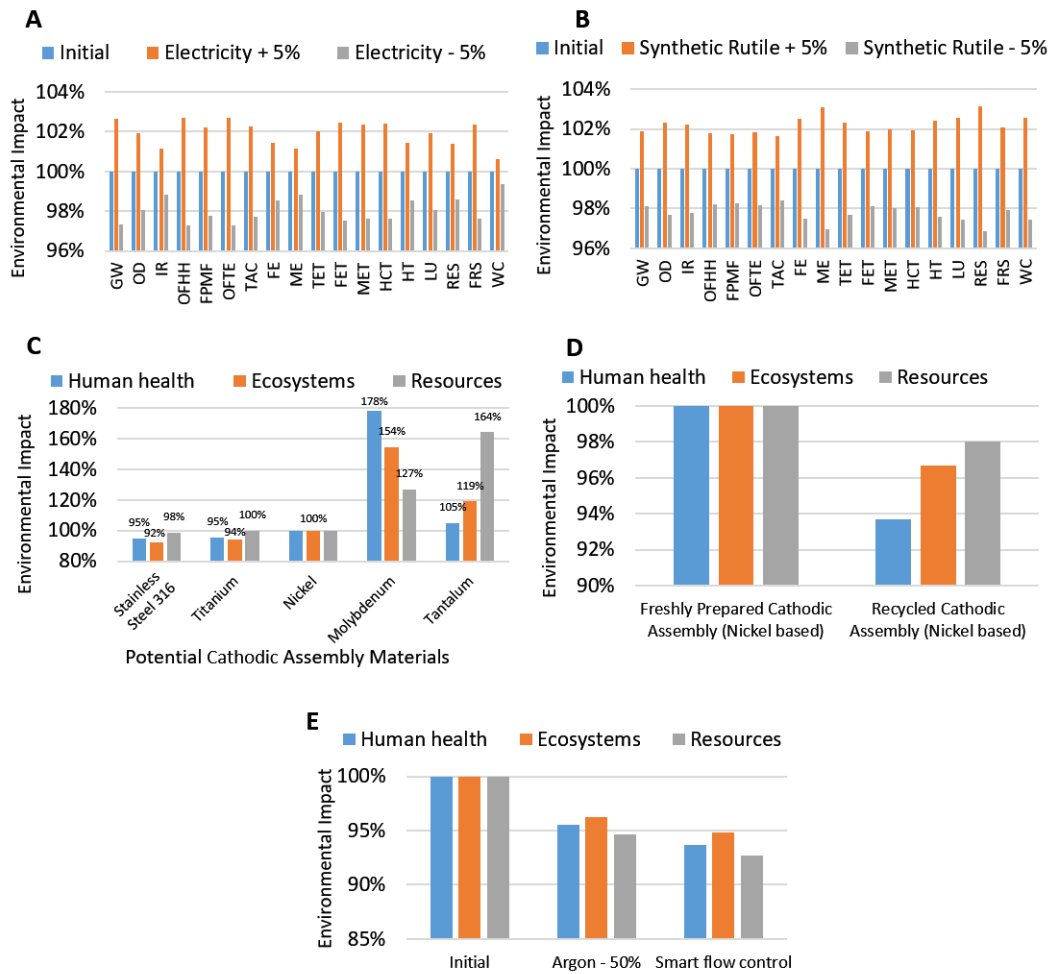


**Figure 6.9:** Parametric and Sensitivity Analysis. A – Sensitivity results for electricity change. B – Sensitivity analysis for Synthetic rutile change. C – Relative impact change on the endpoint criteria for the NEM process due to the replaced cathode-wrapping material. D – Effect of the implementation of the reusable cathodic assembly. E – Relative impact of the improved Argon use scenarios.

rutile was conducted showing the similar fluctuation of around 2-3% for the reduction or increase in the consumption by 5%, demonstrating the stability of the built model. Figure 10 B shows the especially high fluctuation of ME and RES that is closely

tied to the mining and purification stages of synthetic rutile production [66]. These factors represent the formation of particulates that affect ME and the increased mineral consumption, which is in a direct connection to RES. Additionally, the investigation results of the proposed replacement of the current cathodic assembly material, i.e., nickel, are summarised in Figure 6.9 C. Tantalum and molybdenum were selected and investigated here as they have been considered to be chemically and thermally stable materials that are suitable for molten salt electrolysis. From Figure 6.9 C it is clear that the implementation of Stainless Steel 316 as the cathodic assembly material is most beneficial for all three of the endpoint criteria, potentially due to the well-developed technologies in the steel manufacturing industry. The improvement of such implementation was estimated to be 5, 8 and 2% for Human health, Ecosystems and Resources respectively, which is only accounted to a total reduction of the environmental impact of the NEM process of about 0.5%. Such a replacement is not yet applicable due to the physical properties of Stainless Steel 316, which is stiffer compared to nickel foam, an important consideration for wrapping synthetic rutile precursors. Nonetheless, the produced evaluation can be used as a guideline when selecting a cathodic material. The implementation of a recyclable assembly shows the total reduction of 6, 3 and 2% for Human health, Ecosystems and Resources respectively, as seen from Figure 6.9 D. It is important to notice that a proposed assembly is reused and is assumed to not affect the system. The effect of argon was fully assessed, as seen in Figure 6.9 E, showing that the reduction of the flow of 50% yields a total improvement of roughly 5%, which is further reduced

by 1% when implementing smart flow control as discussed earlier. This indicates that argon plays a more significant role than the cathodic assembly and is worth investigating into for environmental and financial concerns.

### **6.3.3 Comparison of Conventional Kroll - EBM Route and the NEM Process**

In this study, the proposed NEM Process was described as an alternative to the Kroll - EBM route. From the data presented in Figure 6.10, it is possible to infer that the NEM of titanium has the potential to reduce environmental impact by 3 times compared to the conventional Kroll - EBM route. Figure 6.10 also shows the relative impacts on the endpoint criteria, where a 70 % reduction of the impacts for human health and ecosystem compared to Kroll - EBM. Resources are slightly lower, with a 63 % reduction. This difference was expected due to the previous work that compared the Kroll Process and the FFC-Cambridge Process or titanium extraction only, as it was previously reported that the latter was up to 35% greener [48]. To fully understand the midpoint impact difference between the two manufacturing routes, the comparison of the core processes is necessary. Figure 6.11 represents the life cycle impacts of the two titanium extraction processes that are implemented into the investigated systems. As seen from Figure 6.11, five categories have a significant difference in that comparison: SOD, IR, FE, ME and FRS. Impacts on the IR and SOD are reduced due to the chemicals involved in the process. This is

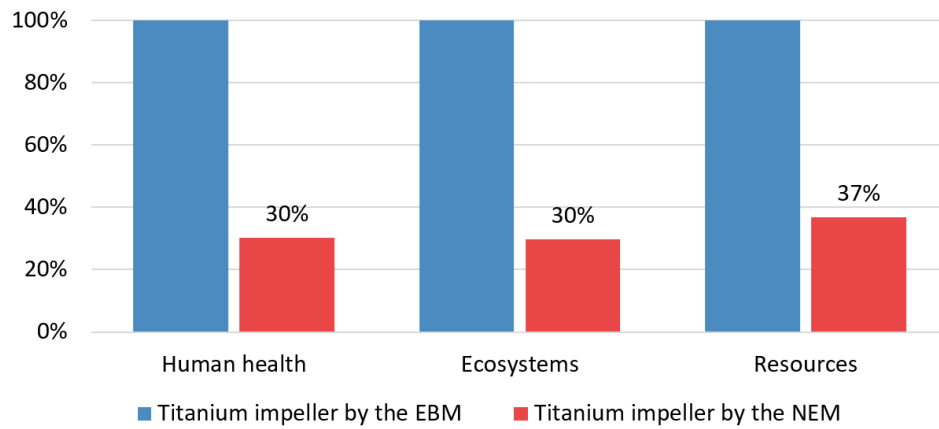


**Figure 6.10:** Endpoint comparison of the Kroll - EBM and the NEM Process.

primarily due to chlorine used in the Kroll Process, a substance known to deplete the ozone layer and increase ionizing radiation [35, 67]. FE and ME differences are probably related to the nature of the carbochlorination step, which is necessary to transform titanium dioxide into the main reagent of the Kroll Process:  $\text{TiCl}_4$ . This step also results in the production of  $\text{CO}_2$  and solid waste that is known to induce excessive growth of plants and algae in both fresh and marine water sources, resulting in depleted oxygen content of the water [34, 68]. The impact of FRS is associated with the magnesium metal involved in the Kroll Process, used in the reduction of  $\text{TiCl}_4$ . Magnesium production requires enormous amounts of resources due to the outdated manufacturing technique [69]. Noticeably, the impact of The FFC-Cambridge Process on MRS is about 3% higher than that of the Kroll Process, most likely due to the advanced recycling system of both  $\text{Cl}_2$  and Mg used in the Kroll Process. The rest is mostly associated with the different nature of the two processes, one being a metallothermic extraction (the Kroll Process), and another

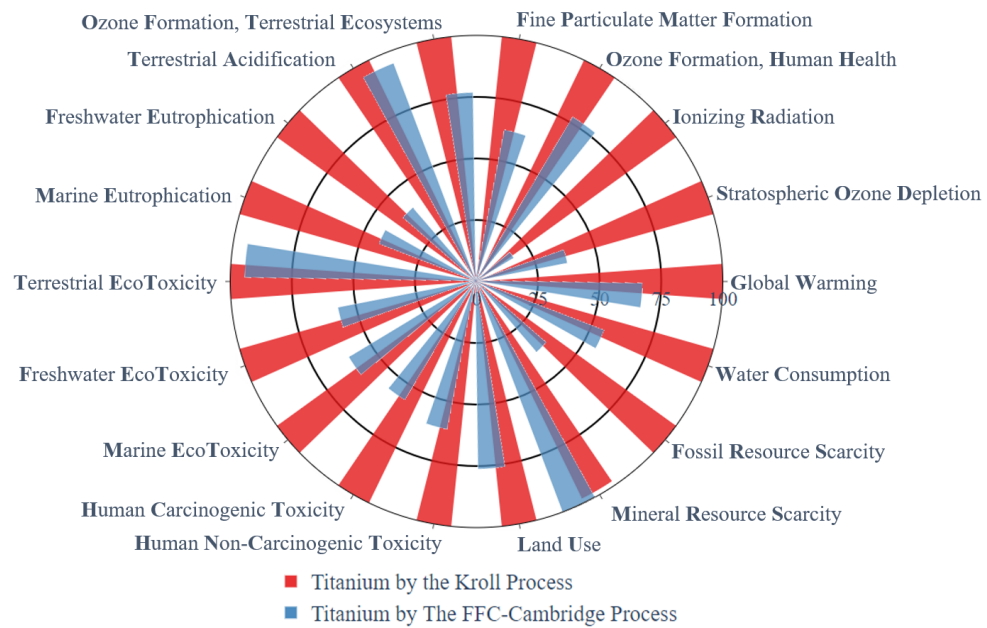


**Figure 6.11:** Midpoint comparison for the Kroll and the FFC-Cambridge Processes for titanium extraction only.

is an electrochemical reduction (the FFC-Cambridge Process) [33]. Due to the principles of the reduction discussed in the case study section, indicating different resource allocation. Midpoint comparison of the two complete routes shows a clear picture of the advantages of the NEM Process (see in Figure 6.12). The most affected criteria are GW, SOD, IR, OFHH, FPMF, OFTE, TA, FE, ME, HCT, LU and FRS. The main cause, in this case, is the dramatic reduction in electricity consumption on the DIW stage. Additionally, SOD, IR, FE, ME and FRS are reduced during the final stage of the process with the implementation of the FFC-Cambridge Process, as discussed for Figure 6.11. Overall, there is a consistent trend of reducing environmental impacts by applying the NEM Process.

This work not only demonstrates a quantitative assessment on the environmental

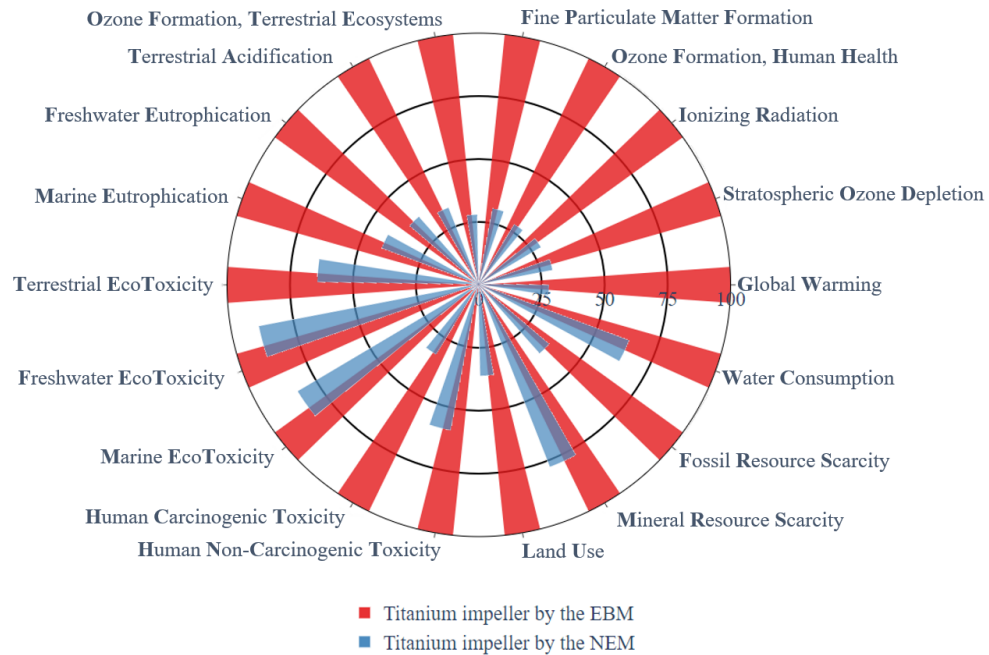


**Figure 6.12:** Midpoint comparison of the NEM Process with the Kroll - EBM route.

impact from one of the evolving titanium fabrication processes but also would exert a far-reaching impact for the greener metallurgy and manufacturing techniques, considering that progressively more countries and regions have proposed and implemented new policies like emission trading scheme for energy-intensive sectors.

### 6.3.4 Legislations

Following the example of the laws enforced by the EPA on the territory of the US and the legislation adopted by the EU regarding the emissions, it was important to look at the parameters indicated in those entities. In the US, the EPA in the Clean Air Act and Air Enforcement allocated high importance to such pollutant as  $\text{NO}_x$ ,  $\text{SO}_2$  and  $\text{PM}_{2.5}$  [70]. Comparing with the EU the list contains  $\text{CO}_2$ , which is

also commonly considered the indicator of the greenhouse effects and degradation of the environment [71]. Therefore, Table 6.4 summarises the main contributors to the emission of those materials. Following the data, the dramatic reduction of the emissions of the above-stated pollutants means that, upon the implementation of the NEM Process, established thresholds for any pollutant can be reduced twofold with no effect on the production volumes. Therefore, the proposed method has a huge potential to replace the established conventional route in case of further restrictions within the future law enforcing acts.

**Table 6.4:** Legislation cantered emissions

	Unit	Kroll-EBM Process	The NEM Process	Percentage reduction
Global warming	kg CO <sub>2</sub> eq	244.21	63.75	74%
Terrestrial acidification	kg SO <sub>2</sub> eq	0.94	0.29	69%
Fine particulate matter formation	kg PM <sub>2.5</sub> eq	0.41	0.12	71%
Ozone formation	kg NO <sub>x</sub> eq	1.09	0.28	74%

## 6.4 Conclusion

This study has compared the Near-net-shape Electrochemical Metallisation (NEM) Process with the conventionally utilised Kroll Process for titanium extraction and the Electron Beam Melting (EBM) for titanium fabrication (i.e., the Kroll-EBM Process). According to the Life Cycle Analysis (LCA), when using the Kroll-EBM Process as the benchmark, the reduction of the impact for the ecosystem and human health achieved by the NEM Process was established to be 70%. In addition, it was pointed out that using the same starting point of synthetic rutile the NEM Process takes three days to complete, while the Kroll-EBM Process takes roughly two weeks. Furthermore, the results from this comparative impact assessment clearly demonstrated that the NEM Process can significantly improve the sustainability of titanium fabrication by about 67% when using the Kroll-EBM Process as the benchmark. The contribution analysis indicated potential improvements that can be done to further reduce the observed environmental impacts of the NEM Process. Significant improvements could be achieved from the optimisation of the FFC Metallisation stage, where the use of nickel and the amount of spent argon contribute to a relatively high impact. It was proposed that the use of nickel foam could be mitigated by replacing it with stainless steel or titanium. Furthermore, utilisation of the reusable nickel foam-based cathode assembly was shown to have the highest reduction in environmental impacts, measuring up to 10%. Argon use was observed to impact 5 of the 18 categories, which is possible to be reduced by 5% by implementing

a better reactor design or utilising a smart flow control. Due to the simplistic nature of the DIW method, there is not much space for further optimising the current shaping process involved in the NEM Process. Overall, for the first time, this work demonstrates a quantitative assessment on the environmental impact from one of the evolving titanium fabrication processes, i.e., the NEM Process and compares it with the conventionally used Kroll-EBM Process. This could exert a far-reaching impact for the cleaner metallurgy and manufacturing techniques, considering that progressively more countries and regions have proposed and implemented new environmental policies like emission trading scheme for energy-intensive sectors.

## References for Chapter 6

- [1] G. Ryan, A. Pandit, D. P. Apatsidis, “Fabrication methods of porous metals for use in orthopaedic applications”, *Biomaterials* **2006**, *27*, 2651–2670.
- [2] M. J. Grimm in *Handbook of Materials Selection*, (Ed.: M. Kutz), John Wiley & Sons, New York, **2002**, Chapter 37.
- [3] T. I. Group, “Titanium for Architectural Applications”, **2006**.
- [4] T. I. Group, “Titanium for Aerospace Alloys & Applications”, **2002**.
- [5] T. I. Group, “Titanium for Automotive Applications”, **2006**.
- [6] I. V. Gorynin, “Titanium alloys for marine application”, *Materials Science and Engineering A* **1999**, *263*, 112–116.
- [7] R. W. Schutz, H. B. Watkins, “Recent developments in titanium alloy application in the energy industry”, *Materials Science and Engineering A* **1998**, *243*, 305–315.
- [8] M. Donachie, *Titanium: a technical guide*, ASM International, **2000**.

- [9] N. Serres, D. Tidu, S. Sankare, F. Hlawka, “Environmental comparison of MESO-CLAD® process and conventional machining implementing life cycle assessment”, *Journal of Cleaner Production* **2011**, *19*, 1117–1124.
- [10] D. Hu, A. Dolganov, M. Ma, B. Bhattacharya, M. T. Bishop, G. Z. Chen, “Development of the Fray-Farthing-Chen Cambridge Process: Towards the Sustainable Production of Titanium and Its Alloys”, *JOM* **2018**, *70*, 129–137.
- [11] F. Borgioli, E. Galvanetto, A. Fossati, G. Pradelli, “Glow-discharge and furnace treatments of Ti-6Al-4V”, *Surface and Coatings Technology* **2004**, *184*, 255–262.
- [12] N. V. Muravyev, K. A. Monogarov, A. N. Zhigach, M. L. Kuskov, I. V. Fomenkov, A. N. Pivkina, “Exploring enhanced reactivity of nanosized titanium toward oxidation”, *Combustion and Flame* **2018**, *191*, 109–115.
- [13] V. T. Le, H. Paris, “A life cycle assessment-based approach for evaluating the influence of total build height and batch size on the environmental performance of electron beam melting”, *The International Journal of Advanced Manufacturing Technology* **2018**, *98*, 275–288.
- [14] M. Darsin, H. A. Basuki, “Development Machining of Titanium Alloys: A Review”, *Applied Mechanics and Materials* **2014**, *493*, 492–500.

- [15] B. Erhard, L. Christoph, P. Frank, “Mechanical Properties of Additive Manufactured Ti-6Al-4V Using Wire and Powder Based Processes”, *IOP Conference Series: Materials Science and Engineering* **2011**, *26*, 012004.
- [16] A. Pramanik, “Problems and solutions in machining of titanium alloys”, *The International Journal of Advanced Manufacturing Technology* **2014**, *70*, 919–928.
- [17] A. R. Machado, J. Wallbank, “Machining of Titanium and its Alloys-a Review”, *Proceedings of the Institution of Mechanical Engineers Part B: Journal of Engineering Manufacture* **1990**, *204*, 53–60.
- [18] A. Dehghan-Manshadi, M. J. Bermingham, M. S. Dargusch, D. H. StJohn, M. Qian, “Metal injection moulding of titanium and titanium alloys: Challenges and recent development”, *Powder Technology* **2017**, *319*, 289–301.
- [19] P. A. Kobryn, S. L. Semiatin, “The laser additive manufacture of Ti-6Al-4V”, *JOM* **2001**, *53*, 40–42.
- [20] L. E. Murr, S. A. Quinones, S. M. Gaytan, M. I. Lopez, A. Rodela, E. Y. Martinez, D. H. Hernandez, E. Martinez, F. Medina, R. B. Wicker, “Microstructure and mechanical behavior of Ti-6Al-4V produced by rapid-layer manufacturing, for biomedical applications”, *Journal of the Mechanical Behavior of Biomedical Materials* **2009**, *2*, 20–32.

- [21] Q. Ma, “Cold Compaction and Sintering of Titanium and Its Alloys for Near-net-shape or Preform Fabrication”, *International Journal of Powder Metallurgy* **2010**, *46*, 29–44.
- [22] B. Baufeld, O. V. d. Biest, R. Gault, “Additive manufacturing of Ti-6Al-4V components by shaped metal deposition: Microstructure and mechanical properties”, *Materials & Design* **2010**, *31*, Supplement 1, S106–S111.
- [23] M. Kottman, S. Zhang, J. McGuffin-Cawley, P. Denney, B. K. Narayanan, “Laser Hot Wire Process: A Novel Process for Near-Net Shape Fabrication for High-Throughput Applications”, *JOM* **2015**, *67*, 622–628.
- [24] N. S. Weston, M. Jackson, “FAST-forge - A new cost-effective hybrid processing route for consolidating titanium powder into near net shape forged components”, *Journal of Materials Processing Technology* **2017**, *243*, 335–346.
- [25] D. Herzog, V. Seyda, E. Wycisk, C. Emmelmann, “Additive manufacturing of metals”, *Acta Materialia* **2016**, *117*, 371–392.
- [26] P. Nandwana, M. M. Kirka, V. C. Paquit, S. Yoder, R. R. Dehoff, “Correlations Between Powder Feedstock Quality, In Situ Porosity Detection, and Fatigue Behavior of Ti-6Al-4V Fabricated by Powder Bed Electron Beam Melting: A Step Towards Qualification”, *JOM* **2018**, *70*, 1686–1691.
- [27] J. H. Moll, “Utilization of gas-atomized titanium and titanium-aluminide powder”, *JOM* **2000**, *52*, 32–34.

- [28] M. Smagorinski, G. Tsantrizos, “Proceedings of the 2002 World Congress on Powder Metallurgy & Particulate Materials”, **1989**.
- [29] K. K. Guo, C. S. Liu, H. H. Dong, S. Y. Chen, “Effect of Extension Length of Catheter on Properties of TC4 Powder Prepared by Electrode Induction Melting Gas Atomization”, *Dongbei Daxue Xuebao/Journal of Northeastern University* **2018**, *39*, 797–802.
- [30] G. Chen, S. Y. Zhao, P. Tan, J. Wang, C. S. Xiang, H. P. Tang, “A comparative study of Ti-6Al-4V powders for additive manufacturing by gas atomization, plasma rotating electrode process and plasma atomization”, *Powder Technology* **2018**, *333*, 38–46.
- [31] C. G. McCracken, C. Motchenbacher, D. P. Barbis, “Review of Titanium-Powder-Production Methods”, *International Journal of Powder Metallurgy* **2010**, *46*, 19–26.
- [32] P. Sun, Z. Z. Fang, Y. Zhang, Y. Xia, “Review of the Methods for Production of Spherical Ti and Ti Alloy Powder”, *JOM* **2017**, *69*, 1853–1860.
- [33] D. J. Fray, “Novel methods for the production of titanium”, *International Materials Reviews* **2008**, *53*, 317–325.
- [34] F. Gao, Z. Nie, D. Yang, B. Sun, Y. Liu, X. Gong, Z. Wang, “Environmental impacts analysis of titanium sponge production using Kroll process in China”, *Journal of Cleaner Production* **2018**, *174*, 771–779.
- [35] W. Kroll in Transactions of the Electrochemical Society, *Vol. 78*, pp. 35–47.

- [36] E. Technologies, Summary of Emerging Titanium Cost Reduction Technologies, Report, **2004**.
- [37] T. H. Okabe, T. Oda, Y. Mitsuda, “Titanium powder production by preform reduction process (PRP)”, *Journal of Alloys and Compounds* **2004**, *364*, 156–163.
- [38] U. B. Pal, D. E. Woolley, G. B. Kenney, “Emerging SOM technology for the green synthesis of metals from oxides”, *JOM* **2001**, *53*, 32–35.
- [39] K. Ono, R. O. Suzuki, “A New Concept for Producing Ti Sponge: Calciothermic Reduction”, *JOM* **2002**, *54*, 59–61.
- [40] G. Z. Chen, D. J. Fray, T. W. Farthing, “Direct electrochemical reduction of titanium dioxide to titanium in molten calcium chloride”, *Nature* **2000**, *407*, 361–364.
- [41] D. S. Maha Vishnu, N. Sanil, L. Shakila, R. Sudha, K. S. Mohandas, K. Nagarajan, “Electrochemical reduction of TiO<sub>2</sub> powders in molten calcium chloride”, *Electrochimica Acta* **2015**, *159*, 124–130.
- [42] D. Hu, W. Xiao, G. Chen, “Near-Net-Shape Production of Hollow Titanium Alloy Components via Electrochemical Reduction of Metal Oxide Precursors in Molten Salts”, *Metallurgical and Materials Transactions B* **2013**, *44*, 272–282.

- [43] J. Peng, K. Jiang, W. Xiao, D. Wang, X. Jin, G. Z. Chen, “Electrochemical Conversion of Oxide Precursors to Consolidated Zr and Zr-2.5Nb Tubes”, *Chemistry of Materials* **2008**, *20*, 7274–7280.
- [44] S. J. Oosthuizen, “In search of low cost titanium: the Fray Farthing Chen (FFC) Cambridge process”, *Journal of the South African Institute of Mining and Metallurgy* **2011**, *111*, 199–202.
- [45] F. Jotzo, V. Karplus, M. Grubb, A. Löschel, K. Neuhoff, L. Wu, F. Teng, “China’s emissions trading takes steps towards big ambitions”, *Nature Climate Change* **2018**, *8*, 265–267.
- [46] S. Bakhtiari, “Coming Out Clean: Australian Carbon Pricing and Clean Technology Adoption”, *Ecological Economics* **2018**, *154*, 238–246.
- [47] B. Murray, N. Rivers, “British Columbia’s revenue-neutral carbon tax: A review of the latest “grand experiment” in environmental policy”, *Energy Policy* **2015**, *86*, 674–683.
- [48] T. E. Norgate, S. Jahanshahi, W. J. Rankin, “Assessing the environmental impact of metal production processes”, *Journal of Cleaner Production* **2007**, *15*, 838–848.
- [49] T. B. S. Institution, “Environmental management - Life cycle assessment - Principles and framework”, **2006**.
- [50] T. B. S. Institution, “Environmental management - Life cycle assessment - Requirements and guidelines”, **2018**.

- [51] S. Middlemas, Z. Z. Fang, P. Fan, “Life cycle assessment comparison of emerging and traditional Titanium dioxide manufacturing processes”, *Journal of Cleaner Production* **2015**, *89*, 137–147.
- [52] K. Zhang, J. Mei, N. Wain, X. Wu, “Effect of Hot-Isostatic-Pressing Parameters on the Microstructure and Properties of Powder Ti-6Al-4V Hot-Isostatically-Pressed Samples”, *Metallurgical and Materials Transactions A* **2010**, *41*, 1033–1045.
- [53] E. Peng, D. Zhang, J. Ding, “Ceramic Robocasting: Recent Achievements, Potential, and Future Developments”, *Advanced Materials* **2018**, *30*, 1802404.
- [54] J. Sure, D. S. M. Vishnu, C. Schwandt, “Direct electrochemical synthesis of high-entropy alloys from metal oxides”, *Applied Materials Today* **2017**, *9*, 111–121.
- [55] M. Ma, D. Wang, W. Wang, X. Hu, X. Jin, G. Z. Chen, “Extraction of titanium from different titania precursors by the FFC Cambridge process”, *Journal of Alloys and Compounds* **2006**, *420*, 37–45.
- [56] M. Baumers, C. Tuck, R. Hague, I. Ashcroft, R. Wildman, “A Comparative Study of Metallic Additive Manufacturing Power Consumption”, *Solid Freeform Fabrication Proceedings* **2010**, 278–288.
- [57] L. E. Murr, S. M. Gaytan, A. Ceylan, E. Martinez, J. L. Martinez, D. H. Hernandez, B. I. Machado, D. A. Ramirez, F. Medina, S. Collins, R. B. Wicker, “Characterization of titanium aluminide alloy components fabricated by addi-

- tive manufacturing using electron beam melting”, *Acta Materialia* **2010**, *58*, 1887–1894.
- [58] V. T. Le, H. Paris, G. Mandil, “Environmental impact assessment of an innovative strategy based on an additive and subtractive manufacturing combination”, *Journal of Cleaner Production* **2017**, *164*, 508–523.
- [59] Ecoinvent, “Ecoinvent database”, *Ecoinvent* **2018**.
- [60] PRÉ, “SimaPro”, *PRÉ CONSULTANTS B.V.* **2018**.
- [61] M. Goedkoop, R. Heijungs, M. Huijbregts, A. D. Schryver, J. Struijs, R. v. Zelm, *ReCiPe 2008 Report I: Characterisation*, 1st, National Institute for Public Health, the Environment. Ministry of Health, Welfare, and Sport., The Netherlands, **2013**.
- [62] G. Weir, T. Muneer, “Energy and environmental impact analysis of double-glazed windows”, *Energy Conversion and Management* **1998**, *39*, 243–256.
- [63] T. Schmidt, M. Buchert, L. Schebek, “Investigation of the primary production routes of nickel and cobalt products used for Li-ion batteries”, *Resources Conservation and Recycling* **2016**, *112*, 107–122.
- [64] L. Leyssens, B. Vinck, C. Van Der Straeten, F. Wuyts, L. Maes, “Cobalt toxicity in humans—A review of the potential sources and systemic health effects”, *Toxicology* **2017**, *387*, 43–56.
- [65] EPA, “CompTox Chemicals Dashboard”, **2018**, *2018*.

- [66] W. Zhang, Z. Zhu, C. Y. Cheng, “A literature review of titanium metallurgical processes”, *Hydrometallurgy* **2011**, *108*, 177–188.
- [67] W. Steinbrecht, M. I. Hegglin, N. Harris, M. Weber, “Is global ozone recovering?”, *Comptes Rendus Geoscience* **2018**, *350*, 368–375.
- [68] P. J. G. Henriksson, A. Rico, W. Zhang, S. Ahmad-Al-Nahid, R. Newton, L. T. Phan, Z. Zhang, J. Jaithiang, H. M. Dao, T. M. Phu, D. C. Little, F. J. Murray, K. Satapornvanit, L. Liu, Q. Liu, M. M. Haque, F. Kruijssen, G. R. De Snoo, R. Heijungs, P. M. Van Bodegom, J. B. Guinée, “Comparison of Asian Aquaculture Products by Use of Statistically Supported Life Cycle Assessment”, *Environmental Science & Technology* **2015**, *49*, 14176–14183.
- [69] F. Gao, Z.-R. Nie, Z.-H. Wang, X.-Z. Gong, T.-Y. Zuo, “Assessing environmental impact of magnesium production using Pidgeon process in China”, *Transactions of Nonferrous Metals Society of China* **2008**, *18*, 749–754.
- [70] EPA, “the Clean Air Act”, *United States* **1970**, *42 U.S.C. Par.7401 et seq.*
- [71] E. Parliament, “Directive 2010/75/EU of the European Parliament and of the Council of 24 November 2010 on industrial emissions (integrated pollution prevention and control)”, *The European Parliament and the Council of the European Union* **2010**, 159–261.

# Chapter 7

## Conclusions and Future Work

*This chapter summarises all the work done toward the establishment of the NEM Process and highlights the future work that could be done to further strengthen the commercialisation of the developed AM technique.*

### 7.1 Concluding Remarks

This project has been aimed at the development of a novel additive manufacture technique, which has been achieved with relative success. As was stated in Chapter 1, the manufacture of titanium has seen a lot of research dedicated to the mitigation of the problems introduced by a set of physical and chemical properties that titanium has. It was further established that the powder metallurgy has great potential for reducing the effects of those properties. However, as discussed in Chapter 2, the production of titanium powder and the applicable PM forming techniques are still

under development and that industry is extremely careful when deciding to utilise AM for the manufacture of different products. Due to this, a new AM technique has to be evolved to eliminate time, cost, and environmental constraints that are inevitable for the metallurgical industry.

This project was carried out in three main directions, including optimisation of the Direct Ink Writing (DIW) of titania, combining it with the molten salt reduction and consecutive environmental assessment.

The DIW machine as received had been designed to extrude clay and, therefore, was found to be unusable for the successful 3D Printing of titania ink. This issue required a redesign of the printing equipment touching two main aspects of the printing method and printing head. The most appropriate technique was found to be direct extrusion via the compressed air. To precisely control the flow of the extruded matter, a set of solenoid valves was implemented that would cut off the pressure supply when needed and release the remaining pressure from the feed cylinder to stop the ink from flowing. These implementations also required additional parameters to be included in the G-code for the printer to manipulate added valves. The tuning was essential to start and stop extruding at the desired intervals as there was a delay between the code and ink's flow. The investigation into the printing head productivity showed that the nozzle provided by the manufacturer had a high-pressure drop, especially when trying to extrude something as thick as ceramic ink. As a solution, it was decided to replace a needle-shaped nozzle for the gradually shrinking conical nozzle. According to the calculations, the pressure drop across the

nozzle was reduced 10 folds, which reduced total pressure induced on the ink. This reduction of pressure was also found to positively affect the stability of the ink.

Noticeably, the stability change pointed at the complex interactions that were happening in the ink. To understand the ink's properties a rheological study was conducted resulting in a discovery of the most suitable additives, which had to contain no metals to reduce titanium to the highest purity. This led to the selection of polyethylene glycol (PEG) and polyvinyl alcohol (PVA), which were established to be applied at 10 wt% and 2 wt% respectively. A further in-depth study showed a dependence of those two additives onto the interaction and behaviour of the ink. Furthermore, it was established that a water-based ink did not possess appropriate stability, which meant that the water would agglomerate in an uneven distribution or would separate from the ink at an uncontrollable rate. The addition of additives increased the stability, which was theorised based on the interaction of water, polymeric chains, and titanium dioxide particles. Such interaction was especially noted for the PEG-based inks, which possessed a dilatancy peak of increased viscosity at increased shear rates. This was due to a known phenomenon of so-called jamming that happens in complex systems of polymeric chains and spherical particles.

Additionally, conducting a creep test on produced inks showed that PVA would increase the reformation ability of the ink when the addition of PEG reduced it almost to 0. This meant that paste would be able to maintain its shape after extrusion, which was considered to be a positive property. However, all these observations were yet to be linked with the printability of the studied compositions. The extrud-

ability test showed that lower elastic reformation was positively affecting the flow of the ink. Meaning that PEG was creating an ideal case for the additive of choice.

This test, however, was conducted on small scale samples, which when increased demonstrated a rather noticeable fluctuation in the flow making impossible to precisely 3D print any products. A closer look at the rheological results showed that it was due to the dilatancy peak. The solution for that was to introduce a so-called boundary lubricant that would not only reduce the stickiness of the paste to the feed cylinder and the nozzle but also reduce the increased stresses that ink had during an increased shear. The addition of this boundary lubricant was found to remove the dilatancy peak, dramatically improving the stability of the ink's flow. The further investigation of the 1:0.9 PEG ink showed that it had the appropriate value of the yield point of around 42, which is considered to be the most important for a ceramic ink for the DIW process.

The final investigation was also performed on the most suitable printing bed material due to the unique requirement of the ink to stick during printing and not during drying. This problem was solved by first printing support under the product, which would stick to a surface and also would brake or slip when the green product would start to shrink due to drying.

When DIW was optimised, the products were subjected to test reductions, which showed that samples tend to shrink up to 40% and also possessed a high degree of deformation and defects. An investigation into the dependency of those deformations was conducted against electrolysis parameters, precursor sintering, and design.

These three parameters were established to be the most dominant. Although it is known that on the initial stages of the reduction process titanium dioxide transforms into an intermediate product of stoichiometric and not-stoichiometric titanates of calcium, the test proved this effect wrong. Following this, it was found that the temperature of the electrolysis affects the integrity of the sample and should not be lower than 700 °C. The further increase in the temperature showed the disappearance of surface cracks, which were common for the product reduced at 700 - 800 °C. Even though this increase in the temperature positively affected the surface quality of the products it also increased the warping of the products. Summarising all the results, it was discovered that the optimal reduction temperature should lie between 800 °C and 900 °C to achieve the best surface quality and the least warping.

Additionally, since the samples were extremely distorted due to the above-mentioned shrinkage, it was decided to sinter samples to establish whether “pre-shrinkage” can reduce the degree of the distortion. It was found that when sintered at 1100 °C samples preserve their shape the best, however on the first glance samples that were sintered at 1300 °C didn’t lose any of their shapes. The consecutive analysis showed that these samples could not be reduced completely and contained 3 times more oxygen than samples produced with 1100 °C. This indicated that all samples had to undergo the sintering stage, which made them stronger for handling and better withstanding temperature-induced deformation when reduced.

Lastly, it was established that the initial design of the produced samples played an important role as it would create undesired stress within the object that would

cause them to crack regardless of the applied techniques and used parameters.

Upon the finalisation of the NEM process, the product was analysed and was established to be of the 1<sup>st</sup>-grade titanium. The morphology, however, was typical to the samples reduced in molten salt, which compromised some of the solid titanium strength but was appropriate for implants, jewellery and others. This allocated products to a unique niche that unfortunately was not strong enough to be applied to the aerospace industry.

The process itself was also evaluated on financial and environmental impacts. Financially it showed an outstanding cost reduction even on the lab scale. The comparison was made on a tooth implant production, which even though doesn't require a user to user modification, still showed high feasibility to be produced by additive manufacturing. The local market analysis showed that the developed method was capable of reducing the cost from 400 RMB to just over 25 RMB, keeping in mind the unoptimised production line. Additionally, the cost breakdown of the process was produced, which showed potential weak areas in the build business model that heavily relied on the human labour contributing 56% of the final cost.

The environmental assessment of the process was essential to establish it against the conventionally applied processes. For this, the NEM process was compared against the conventional route consisting of the Kroll process, Free Fall Gas Atomisation and the Electron Beam Melting process. Such a comparison showed that the investigated method had an enormous head over the conventional route, which is represented by 60-70 % lower emissions. This was mainly due to such chemicals

as  $\text{Cl}_2$  and magnesium utilised in the Kroll process. Additionally, the Kroll - EBM process ended up to be more energy-consuming compared to the NEM process, 17.24 kWh/kg of product and 8.05 kWh/kg of product respectively.

The results of the study were then overlaid the legislations established in the US and EU, both of which only produce a limit of emission that every plant can emit. The legislations mainly focused on such pollutants as  $\text{CO}_2$ ,  $\text{SO}_2$ ,  $\text{NO}_x$  and  $\text{PM}_{2.5}$ . As it was established from the built model, our process would only produce 40% of the emission that the conventional route produces, making it a great candidate for the future commercialisation.

The assessment of the main contributors to the environmental impact showed a few important findings. First is the consumption of argon, which was unnecessarily high and could be reduced. Alternatively, it was proposed to implement a “smart” argon supply because argon requirement drops as the reduction progresses. Such an implementation was reducing the overall argon impact by 10%. Another factor was noted from the different cathodic assemblies scenarios. These scenarios included a wide variety of materials. From there it was established that the use of steel 316 would be the most feasible and less polluting, however, the concern of the impurities made the use of nickel predominant. Additionally, a scenario of a reusable assembly was considered and found reducing the allocated impact by 70%.

Overall, an in-depth development and evaluation of a new titanium additive manufacturing method were conducted, resulting in a process that can be utilised in the areas of bioengineering, food and jewellery manufacturing. This method, as

the name stated, is mainly focused on the manufacture of near-net-shape products that will require some minimal post-treatment with noticeable environmental and financial benefits.

## 7.2 Significance in the Field

The produced work can be allocated to a niche area of indirect AM of titanium via an electrochemical process. Although the combination of 3D printing and electrochemical metallisation was a novel concept, three projects have already pioneered in this direction. These projects were based on slip casting (instead of 3D printing), which is a simple method that could provide a small number of possible shapes (namely a cup, a golf club, a tube and a structured foam) with relatively small sizes of up to 2 cm.

In this project, the products of complex shapes were only limited by the size of a reactor that can be further expanded to produce large samples. Following upscale, however, is still limited by the thickness of an individual wall that can be electrochemically reduced as was indicated in Chapter 5. The whole process also allowed to dramatically reduce the cost of titanium AM.

Along the way, a novel formula for titania ink was devolved to precisely 3D print titanium dioxide into the desired shape. Which, as compared to the previous work in Chapter 4, uses non-toxic additives and produces ceramic material with porosity ranging from 50 to 71%.

Another novelty was done in the field of the Environmental process assessment. For the first time, a detailed LCA was conducted for the FFC-Cambridge process, which can help the industry to accept it as a commercial method for titanium production. The major impact was done by completing a comprehensive study and comparison between the NEM process and the currently applied Kroll-EBM method that can be taken as an example for LCA study of a novel, complex or indirect methods of any kind of manufacture.

## **7.3 Future Work**

This section is dedicated to discussing possible research directions for the further development of the NEM process.

### **7.3.1 Fabrication of Other Metallic and Inter-metallic Materials**

First, the whole project was focused on the AM of titanium. This focus can be further widened to produce other transnational metals, alloys and composites, which is possible due to the molten salt metallisation stage. This direction is important as some of the materials that are possible to produce with the molten salt electrolysis can be difficult to conventionally produce into the desired shape.

### **7.3.2 Enhancement of the Properties of the Product**

Second is the work directed towards the widening of the product application. For this, it is important to investigate ways of post-treatment that can yield in near-solid or completely solid products. Additionally, it can be useful to evaluate methods of surface treatment to increase the durability and toughness of the specimens.

### **7.3.3 Development of the 4D Printing**

Due to the wide range of metals that can be extracted via the FCC-Cambridge Process, the NEM Process can be further developed to produce complex products with graded elemental composition, which at this stage is not possible with the conventional processes and would be extremely valuable, especially when combining materials with high strength and extreme hardness for example titanium with tantalum or tungsten. This elemental grading can be referred to as the fourth dimension on top of 3D printing.

### **7.3.4 Reduction of the Surface Area of the Produced Metal**

Following the discovery of the unique structures showed in Chapter 5, the process of the formation of those structures should be further investigated in details. These structures may positively affect all the properties of the metal, making it contain less oxygen that is mostly found in the form of the oxide layer or enhance physical properties by forming larger structures. Overall, the reproduction of these struc-

tures can yield in a boost of the quality of produced titanium especially when the production was shown to be cheaper than via conventional routes.

### **7.3.5 Computer Simulation of the Deformation**

It was found impossible to predict a design-dependent deformation during the metallisation stage. This, however, can be developed into the computer-assisted modelling of such deformation making the process even less wasteful by predicting any possible inconsistencies in shape preservation.

# Appendix A

## Life Cycle Inventory for the Kroll Process

	Item	Unit	Chlorination and refining	Reduction and distillation	Electrolysis of MgCl <sub>2</sub>
Inputs	Titanium dioxide	kg	3.53E+04		
	Fresh water	kg	4.40E+02		
	Petroleum coke	kg	6.51E+02		
	Sodium hydroxide	kg	4.52E+03		
	Magnesium (make up)	kg		4.10E+01	
	Chlorine (make up)	kg	1.62E+03		
	Sulfuric acid	kg			6.98E+01
	Raw coal	kg	3.53E+03		

Appendix A

	Crude oil	kg	8.51E+02		
	Natural gas	m3	9.16E+01		
	Electric power	kWh	2.55E+03	4.85E+03	1.45E+04
Outputs	CO2	kg	8.42E+03	4.00E+03	1.19E+04
	SO2	kg	5.17E+01	2.71E+01	8.11E+01
	NOx	kg	4.60E+01	1.84E+01	5.51E+01
	CO	kg	6.15E+02	5.62E+00	1.68E+01
	CH4	kg	1.66E+01	5.31E-02	1.59E-01
	N2O	kg	3.96E-02	7.33E-02	2.19E-01
	NMVOC	kg	1.60E+01	1.47E-01	4.40E-01
	HCl	kg			3.92E+00
	HF	kg			6.36E-01
	As	kg	4.03E-03	7.56E-03	2.26E-02
	Cd	kg	2.75E-05	4.81E-05	1.44E-04
	Cr	kg	3.40E-04	6.38E-04	1.91E-03
	Hg	kg	1.77E-04	3.32E-04	9.92E-04
	Ni	kg	5.29E-04	9.47E-04	2.83E-03
	Pb	kg	3.61E-03	6.63E-03	1.98E-02
	V	kg	5.82E-03	1.09E-02	3.26E-02
	Zn	kg	4.84E-03	9.08E-03	2.71E-02
Particulates	kg	7.95E-01	1.51E+00	4.52E+00	

Appendix A

---

	COD	kg	1.53E-01	2.81E-01	8.41E-01
	Spent alkali liquor	kg	4.60E+03		
	Other residue	kg		9.30E+01	1.62E-01
	Hydrochloric acid (concentration: 20%) byproduct	kg	5.13E+02		

**Table A.1:** Inputs and outputs for Kroll process. Production of 1 tonne of titanium.

# Appendix B

## Matlab Scrip for G-code

### Modification

```
f = fopen('C:\RR\3d models\FileName.gcode');  
fout1 = fopen('C:\RR\3d models\FileNamerew.gcode', 'w');  
s1=fgetl(f);  
k=1;  
Y1='M107';    %stop  
Y2='G4 P0';  
Z1='M106';    %start  
Z2='G4 P150';  
while ~feof(f)  
    A{k}= s1;
```

```
s2 = fgetl(f);

k1 = strfind(s1, 'E');

k2 = strfind(s2, 'E');

if isempty(k1)

    if isempty(k2)

        fprintf(fout1, '%s\r\n',A{k});

        disp([num2str(k),' and ',num2str(k+1),' have no E']);

    else

        fprintf(fout1, '%s\r\n',A{k});

        fprintf(fout1, '%s\r\n',Y1);

        fprintf(fout1, '%s\r\n',Y2);

        disp(' end');

    end

else

    if isempty(k2)

        fprintf(fout1, '%s\r\n',A{k});

        fprintf(fout1, '%s\r\n',Z1);

        fprintf(fout1, '%s\r\n',Z2);

        disp(' start ');

    else

        fprintf(fout1, '%s\r\n',A{k});
```

```
        disp([num2str(k),' and ',num2str(k+1),' have an E']);
    end
end
s1 = s2;
k=k+1;
disp(k);
end
fclose(f);
fclose(fout1);
```

double layer  

 全部  图片  视频  更多  设置  工具

找到约 334,000,000 条结果 (用时 0.54 秒)

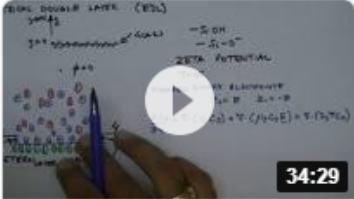
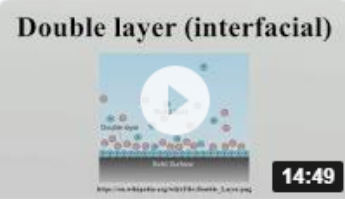
### Double layer (surface science) - Wikipedia

[https://en.wikipedia.org/wiki/Double\\_layer\\_\(surface\\_science\)](https://en.wikipedia.org/wiki/Double_layer_(surface_science))  [翻译此页](#)

A **double layer** is a structure that appears on the surface of an object when it is exposed to a fluid. The object might be a solid particle, a gas bubble, a liquid ...

[Development of the ...](#) · [Helmholtz](#) · [Grahame](#) · [Mathematical description](#)

### 视频

 <p>34:29</p> <p>Lecture 22: Electrical Double Layer (EDL)</p> <p>Bahga Lab IIT Delhi YouTube - 2017年3月26日</p>	 <p>14:49</p> <p>Double layer (interfacial)</p> <p>WikiAudio YouTube - 2016年1月23日</p>	 <p>2:50</p> <p>Double Layer Pumpkin Cheesecake Video</p> <p>Allrecipes - 2018年2月28日</p>
--	--	--

*Many obstacles were overcome, but some were overwhelming...*